



**HAL**  
open science

# Hydrodynamic instabilities in microfluidic magnetic fluid flows

Guntars Kitenbergs

► **To cite this version:**

Guntars Kitenbergs. Hydrodynamic instabilities in microfluidic magnetic fluid flows. Physics [physics]. Université Pierre et Marie Curie - Paris VI; Latvijas universitāte, 2015. English. NNT: 2015PA066311 . tel-01254461

**HAL Id: tel-01254461**

**<https://theses.hal.science/tel-01254461>**

Submitted on 12 Jan 2016

**HAL** is a multi-disciplinary open access archive for the deposit and dissemination of scientific research documents, whether they are published or not. The documents may come from teaching and research institutions in France or abroad, or from public or private research centers.

L'archive ouverte pluridisciplinaire **HAL**, est destinée au dépôt et à la diffusion de documents scientifiques de niveau recherche, publiés ou non, émanant des établissements d'enseignement et de recherche français ou étrangers, des laboratoires publics ou privés.

**THÈSE DE DOCTORAT  
DE L'UNIVERSITÉ PIERRE ET MARIE CURIE  
ET DE L'UNIVERSITÉ DE LETTONIE**

**Spécialité : Physique**

**École doctorale : "Physique en Île-de-France"**

réalisée

à **PHENIX - Physicochimie des Electrolytes et Nanosystèmes interfaciaux**  
et  
**MMML - Laboratory of Magnetic Soft Materials**

présentée par

**Guntars KITENBERGS**

pour obtenir le grade de :

**DOCTEUR DE L'UNIVERSITÉ PIERRE ET MARIE CURIE  
ET DE L'UNIVERSITÉ DE LETTONIE**

Sujet de la thèse :

**Instabilités hydrodynamiques de fluides magnétiques  
en écoulements microfluidiques**

soutenue le 16/07/2015

devant le jury composé de :

M.	Georges BOSSIS	Rapporteur
M.	Agris GAILĪTIS	Rapporteur
M <sup>me</sup>	Florence ELIAS	Examineur
M.	Isaak RUBINSTEIN	Examineur
M <sup>me</sup>	Régine PERZYNSKI	Directrice de thèse
M.	Andrejs CĒBERS	Directeur de thèse



Thesis of  
the UNIVERSITY of PIERRE and MARIE CURIE  
and the UNIVERSITY of LATVIA

Subject : Physics

Doctoral School in France : “Physique en Île-de-France”

performed in

**PHENIX - Physicochimie des Electrolytes et Nanosystèmes interfaciaux**  
and  
**MMML - Laboratory of Magnetic Soft Materials**

presented by

**Guntars KITENBERGS**

to obtain a title :

**DOCTOR of the UNIVERSITY of PIERRE  
and MARIE CURIE and the UNIVERSITY of LATVIA**

Title of dissertation :

**Hydrodynamic instabilities  
in microfluidic magnetic fluid flows**

defended in 16/07/2015

in front of a jury :

Mr.	Georges BOSSIS	Reviewer
Mr.	Agris GAILĪTIS	Reviewer
Mrs.	Florence ELIAS	Examiner
Mr.	Isaak RUBINSTEIN	Examiner
Mrs.	Régine PERZYNSKI	Advisor
Mr.	Andrejs CĒBERS	Advisor



# Acknowledgements

This work would not be possible without a direct and indirect influences of numerous people and institutions. Here I will try to express my gratitude towards them all, which is very difficult to be put in strong enough words.

First of all, I am extremely grateful to both of my advisors prof. Régine Perzynski and prof. Andrejs Cēbers for giving me the opportunity to work on this very interesting topic. I thank them for being reachable when I had questions and sharing their knowledge and opinion, for introducing me to the international world of science and helping in organization and mobility and for being always interesting to talk to!

Sincere gratitude must be expressed to my colleagues in Riga (Mihails, Kaspars, Oksana, Jānis C., Artis, Andrejs T., Jānis R. and many others) and Paris (Jean, Emmanuelle, Veronique, Ali, Michael, Franciscarlos, Rafael, Cleber, Fernando, Mansour, Amandine and others). Without them working at the MMML lab of the Univeristy of Latvia and at the PECSA/PHENIX lab of the UPMC would not have been as pleasant.

I also acknowledge the help from colleagues in other institutions, in particular M. Maiorov from the IPUL for magnetic measurements, E. Nitišs from the ISSP for the common interest in creating molds on silicon and D. Erts and J. Prikulis from the ICP for the collabrative work within the common ESF project.

Arigato to the Bio-Nano Electronics Research Center in Toyo University for the warm welcome during my research visit to Japan, in particular to the director prof. Toru Maekawa and colleagues Takahiro, Hasumura and Anila. Arigatou gozaimasu!

I am thankful to Georges Bossis and Agris Gailītis for agreeing to be the reviewers of this work and Elias Florence and Isaak Rubinstein for joining the jury of my defense.

Happiness is only real when shared, therefore I am most grateful to my friends and family. I thank my parents Ineta and Jānis for letting me choose this path and supporting while pursuing it, my sisters Anitra and Ieva for refreshing my otherwise very scientific view and grandparents for enjoying my humble tries to explain them what I am working on. I promise Jānis and Pēteris finally to be able to have a cold beer when we agree instead of from time to time. And I thank my friends from all around Europe and even further, for the good wishes, useful discussions and the fun time spent together while working on this study. But, without doubt, my largest gratitude goes to my dear Māra. I thank you for supporting me better than possible at all times, even when I was staying long in the office or working far away in Paris.

This joint PhD between Latvia and France was only possible because of a cooperation agreement between the University of Latvia and the UPMC and, most importantly, a scholarship for co-tutelle studies, awarded by the French embassy in Latvia, which I highly acknowledge. In particular, I thank S. Urtāne and her colleagues from the Institut français de Lettonie and people from Campus France in Paris.

I am also very grateful for the financial support during last 18 months of this study from the European Social Fund project Nr.2013/0028/1DP/1.1.1.2.0/13/APIA/VIAA/054.

---

Daļa no šīs disertācijas tapusi Eiropas Sociālā fonda līdzfinansēta projekta “Jaunas starpdisciplināras zinātniskās grupas izveide nanostrukturētu daudzslāņu materiālu pielietojumu attīstīšanai” ietvaros.

*Nr.2013/0028/1DP/1.1.1.2.0/13/APIA/VIAA/054*



**EIROPAS SAVIENĪBA**



**IEGULDĪJUMS TAVĀ NĀKOTNĒ**

# Résumé français

## Table des matières

<b>Introduction</b>	<b>iv</b>
<b>1 Liquides magnétiques</b>	<b>vi</b>
1.1 Préparation . . . . .	vii
1.2 Propriétés . . . . .	vii
<b>2 Micro-convection magnétique</b>	<b>ix</b>
2.1 Observations expérimentales . . . . .	x
2.2 Possibilités de développement en microfluidique . . . . .	xiv
<b>3 Diffusion de particule dans les fluides magnétiques</b>	<b>xiv</b>
3.1 Estimation du champ critique de micro-convection magnétique . . . . .	xv
3.2 Evolution de l'interface d'un ferrofluide en réponse à une marche de concentration . . . . .	xv
3.3 Effet de la gravité . . . . .	xvi
<b>4 Instabilités de ferrofluides démixés en deux phases liquides</b>	<b>xix</b>
4.1 Système de bobines pour explorer sous microscope les propriétés des fluides magnétiques démixés, soumis à des champs dépendant du temps . . . . .	xx
4.2 Expériences réalisées avec des micro-gouttes issues de la séparation de phase d'un ferrofluide . . . . .	xx
4.2.1 Propriétés de la phase concentrée issue de la séparation de phase . . .	xxi
4.2.2 Micro-gouttes magnétiques en champ tournant et en champ précessant	xxii
<b>Bibliographie</b>	<b>xxvi</b>

## Introduction

Le titre de cette dissertation combine un ensemble de concepts scientifiquement forts comme "l'Hydrodynamique", "les Fluides Magnétiques", "les Instabilités" et "la Microfluidique". Chacun d'entre eux représente un domaine important de la Physique. Les trois premiers ont été largement étudiés depuis de nombreuses années, tandis que le domaine de la microfluidique est lui, plus "jeune" et est actuellement en plein développement [1]. Par ailleurs, le monde moderne évolue rapidement, il est continuellement en demande d'une meilleure compréhension et d'un meilleur contrôle de phénomènes complexes et très variés pour leur prédiction et leur exploitation.

Ce travail est, en premier lieu, dédié à des études expérimentales de Fluides Magnétiques et à leur comportement sous champ appliqué. Les Fluides Magnétiques portent en leur sein des nanoparticules magnétiques colloïdales. Ces matériaux sont simultanément liquides et magnétiques à la température ambiante. Ce sont des matériaux intrigants aux propriétés fascinantes [2]. Quand ils sont exposés à des champs magnétiques, le jeu croisé de leurs propriétés produit des instabilités tout à fait inattendues, deux d'entre elles sont discutées ici en détails. D'une part, la micro-convection magnétique [3] est ici étudiée à l'interface entre deux fluides miscibles. D'autre part, l'instabilité de forme d'une micro-goutte magnétique [4] est obtenue avec un fluide Magnétique démixé en deux phases liquides. Ce sont des phénomènes qui dépendent du champ appliqué. Ils sont principalement intéressants d'un point de vue fondamental. Ils ont cependant de proches connections avec des domaines importants en pleine expansion, tels que la biomédecine [5], les nanotechnologies [6] et la microfluidique. Ces connections conduiront très certainement à des applications à l'avenir. Plusieurs de ces applications sont proposées dans ce travail.

Les avancées récentes en termes de développements technologiques du point de vue des techniques expérimentales et de l'analyse de données, permettent de réaliser des études expérimentales de manière beaucoup plus quantitatives que par le passé. Les résultats obtenus conduisent à des critiques solides des modèles existants et aident à leur amélioration. Un excellent exemple est donné ici, montrant qu'en développant parallèlement les approches théoriques, des simulations numériques et des observations expérimentales, on peut atteindre une compréhension profonde des phénomènes étudiés.

Les objectifs et tâches suivants ont été proposés pour ce travail :

- *Objectifs* : Réaliser une étude expérimentale de différentes instabilités dans des systèmes à base de fluides magnétiques; Améliorer et développer de nouvelles méthodes d'étude en choisissant les systèmes de façon à comprendre les principes physiques sous-jacents; comparer aux prédictions théoriques et numériques appropriées.

- *Tâches* :

1. Réaliser une caractérisation complète du système expérimental étudié;
2. Etudier et caractériser la micro-convection magnétique pour une interface de fluides miscibles;

3. Trouver les raisons physiques de la diffusion effective très rapide rencontrée dans la tâche précédente;
4. Développer un montage expérimental pour l'étude de gouttes de fluides magnétiques démixés en deux phases liquides;
5. Observer et décrire leurs instabilités de forme sous champ magnétique précessant et sous champ tournant.

L'ensemble de ces tâches a été réalisé dans le cadre de ce travail. Elles sont présentées dans ce mémoire dans quatre chapitres différents, qui sont condensés ici en quatre sections. Les fluides magnétiques, utilisés dans les expériences sont présentés et caractérisés dans la section 1. La section 2 regroupe les principaux résultats de l'étude extensive qui a été menée sur la micro-convection magnétique au niveau d'une interface entre fluides miscibles. Cette section inclut une comparaison quantitative des mesures du champ critique, de la taille des digitations observées et de la dynamique développée, aux résultats de simulations numériques menées par des collègues. La diffusion effective, très rapide, des nanoparticules mesurée au niveau de l'interface dans l'expérience de micro-convection, est explorée expérimentalement par d'autres techniques dans la section 3. L'influence dominante d'effets de gravité est mise en évidence par des simulations numériques, puis est confirmée expérimentalement. La section 4 présente un montage expérimental construit au cours de ce travail et spécialement dédié à l'étude sous microscope de systèmes de fluides magnétiques démixés en deux phases. Ses capacités sont ici démontrées avec des expériences réalisées sur des micro-gouttes liquides de phase concentrée, issues d'une démixion, pour caractériser leurs propriétés. Puis des observations de gouttes soumises à un champ magnétique précessant à l'angle magique sont comparées à des mesures en champ tournant horizontalement.

L'ensemble de ces résultats a jusqu'ici conduit à 3 publications et 12 communications présentées à des conférences.

#### *Un commentaire sur le système d'unités*

Ce travail utilise principalement le système d'unités CGS, parce que les personnes du laboratoire de Riga, travaillant sur les aspects théoriques et les simulations numériques, préfèrent avoir les constantes  $\epsilon_0$  et  $\mu_0$  égales à l'unité. De façon à rendre les comparaisons aussi simples que possible, les résultats expérimentaux sont aussi présentés en unités CGS. Il est important de noter que les lois physiques sont indépendantes du système d'unités et que la conversion est très simple dans beaucoup de situations. C'est lorsqu'on manipule des grandeurs magnétiques qu'il faut être très attentifs, parce que la définition de l'induction magnétique est différente dans les deux systèmes d'unités. On a dans le système CGS,  $B^{CGS} = H^{CGS} + 4\pi M^{CGS}$  tandis que dans le système international cette relation s'écrit :  $B^{SI} = \mu_0 (H^{SI} + M^{SI})$ . Une façon de se repérer est de regarder le nom des unités utilisées, cependant c'est beaucoup plus compliqué quand on parle de grandeurs adimensionnées comme la susceptibilité magnétique  $\chi$  ou la perméabilité  $\mu$ . Pour permettre une conversion rapide, lorsque c'est nécessaire, quelques formules sont données dans le tableau 1.

Une large bibliographie existe (voir par exemple [7]) pour résoudre des questions additionnelles.

Tableau 1: Formules pour convertir les unités magnétiques du système CGS en unités magnétiques du système SI.

Quantité	Formule de conversion
Champ Magnétique	$H^{\text{SI}}[\text{A/m}] = \frac{10^3}{4\pi} H^{\text{CGS}}[\text{Oe}]$
Aimantation	$M^{\text{SI}}[\text{A/m}] = 10^3 M^{\text{CGS}}[\text{G}]$
Induction Magnétique	$B^{\text{SI}}[\text{T}] = 10^{-4} B^{\text{CGS}}[\text{G}]$
Susceptibilité magnétique	$\chi^{\text{SI}} = 4\pi \chi^{\text{CGS}}$
Perméabilité magnétique	$\frac{\mu^{\text{SI}}}{\mu_0} = \mu^{\text{CGS}}$

## 1 Liquides magnétiques

Un liquide magnétique est une dispersion colloïdale stable de nanoparticules solides dans un milieu liquide. Ce type de système est usuellement appelé "Ferrofluide". Ces nanoparticules magnétiques sont au premier ordre des mono-domaines magnétiques, un moment magnétique leur est associé, et elles sont suffisamment petites pour résister à la sédimentation à température ambiante grâce au mouvement Brownien.

Les liquides magnétiques, tels qu'on les entend actuellement, ont été inventés aux USA dans les années 60. Leurs tout premiers développements ont été réalisés dans des huiles et des solvants organiques, plus tard des ferrofluides aqueux à base de ferrite de fer, ou par exemple de cobalt, ont eux aussi été développés. Des joints magnétiques, des haut-parleurs à bobine mobile ou des amortisseurs ont été parmi les premières applications technologiques développées avec succès. Plusieurs autres applications ont été proposées, ainsi des encres magnétiques ont été aussi avancées [2]. De multiples effets physiques, inattendus et intéressants, ont été décrits dans plusieurs livres [8, 9, 10]. Les impressionnants développements des nanosciences et nanotechnologies au cours des 15 dernières années ont apporté un nouvel intérêt aux ferrofluides dans une perspective différente, celle des nanoparticules magnétiques comme éléments individuels. Dans le domaine de la biomédecine, ces nanoparticules individuelles sont utilisées en tant que bon agent de contraste en Imagerie par Résonance Magnétique, pour le tri cellulaire, la délivrance de médicaments, la vectorisation magnétique et l'hyperthermie magnétique [5, 11]. Cela a été rendu possible grâce à un travail extensif sur les méthodes de préparation qui permettent de contrôler le matériau des nanoparticules, leur taille, leur forme, leur structure et leur état de surface [6, 12].

Pour faciliter ces progrès, des études supplémentaires sur le comportement de fluides magnétiques, associés à des dispersions de nanoparticules dans des milieux plus complexes sont nécessaires. Ici nous nous focalisons sur l'utilisation de ferrofluides conventionnels, parce que leurs méthodes de préparation ont été perfectionnées à un tel niveau que plusieurs de leurs paramètres essentiels peuvent être contrôlés avec une très grande précision.

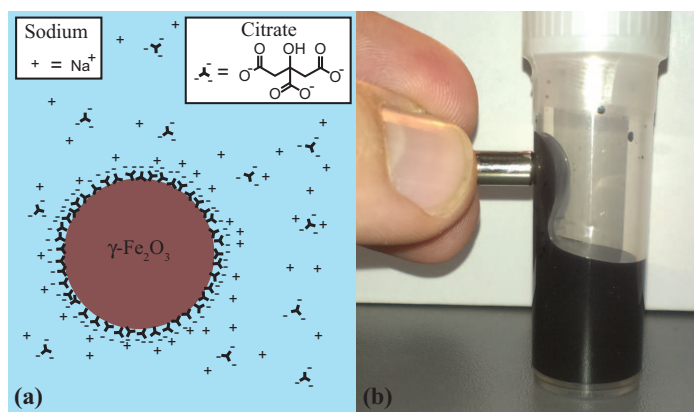


Figure 1: Ferrofluide. (a) Schéma d'une nanoparticule individuelle dans un fluide magnétique, stabilisé avec des ions citrate. (b) Un ferrofluide est attiré par un gradient de champ magnétique.

## 1.1 Préparation

Si des nanoparticules magnétiques peuvent être trouvées dans des bactéries magnétotactiques [13], les ferrofluides pour leur part n'existent pas dans la nature, ils doivent être créés artificiellement. Pour produire un "bon" ferrofluide, les particules doivent résister à la sédimentation, impliquant un diamètre  $d \leq 25$  nm, tandis que leur agglomération est empêchée via des interactions électrostatiques répulsives obtenues grâce à une densité superficielle de charge en surface des nanoparticules [9]. Pour être utilisable dans le domaine biomédical, ce qui est un domaine d'intérêt important, la dispersion colloïdale doit être aqueuse et normalement stable à  $pH = 7$ . Cela peut être réalisé en produisant un ferrofluide à base de nanoparticules de maghémite ( $\gamma - Fe_2O_3$ ) par la méthode mise au point par R. Massart [14], qui est devenue une méthode standard pour stabiliser électrostatiquement des ferrofluides avec des ions citrates, comme l'illustre la figure 1 (a). Les interactions entre particules dépendent fortement des caractéristiques physico-chimiques de la solution, qui peuvent être imposées par dialyse [15]. La distribution de taille, assez polydisperse, obtenue à l'issue de la synthèse peut être affinée par un tri en taille, par une méthode colloïdale [16]. Le processus de fabrication est mené par des spécialistes à la fois au laboratoire MMML - Riga et au laboratoire PHENIX-Paris. Il conduit à des fluides, de couleur rouge sombre, qui peuvent être attirés par un aimant (voir la figure 1 (b)).

Il est aussi possible de préparer des ferrofluides à base de solvants organiques, où le mécanisme de stabilisation est basé sur un tapissage de la surface des nanoparticules par de petites chaînes de surfactant, masquant les attractions à courte portée entre particules. Un ferrofluide à base de nanoparticules de magnétite *DF105*, stabilisé par des chaînes d'acide oléique dans le tétradécane [17], a été fourni par l'Institute of Physics (Salaspils, Latvia) pour réaliser des mesures complémentaires.

## 1.2 Propriétés

Il n'est possible de comparer des expériences quantitatives à des prédictions théoriques que si les caractéristiques des objets étudiés sont connues. La détermination de ces caractéristiques physiques et physico-chimiques (force ionique, fraction volumique, distribution en tailles, aimantation à saturation, susceptibilité magnétique) est expliquée en détails dans

le texte du mémoire. La table 2 regroupe, pour les échantillons utilisés ici, la fraction volumique moyennée en poids  $\Phi^W$ , les grandeurs déduites de mesures magnétiques (la fraction volumique en matériau magnétique  $\Phi^M$ , la susceptibilité magnétique  $\chi$  et l'aimantation à saturation  $M^S$ ) et celles déduites de mesures de diffusion de lumière (le diamètre hydrodynamique  $d_H$ , l'index de polydispersité PDI).

Tableau 2: Propriétés essentielles des ferrofluides utilisés dans les expériences.

Nom	$\Phi^W$ , %	$\Phi^M$ , %	$\chi$	$M_s$ , G	$d_0$ , nm	$\bar{d}_H$ , nm	PDI
<b>D107</b>	2.8	2.9	0.016	8.4	7.1	17.2	0.13
<b>KTF09-13</b>	2.0	3.3	0.064	10	14.0	79.1	-
<b>DF105</b>	6.9	-	-	14.2	7.3	65.0	0.52
<b>p146</b>	$\approx 1$	1	0.009	3.1	10.4	32.0	0.12

On considère que les nanoparticules magnétiques du ferrofluide sont sphériques et que leur diamètre  $d$  est distribué selon par une distribution log-normale, de densité de probabilité :

$$P(d; d_0, \sigma) = \frac{1}{\sqrt{2\pi}\sigma d} e^{-\frac{(\ln d/d_0)^2}{2\sigma^2}}. \quad (1)$$

Celle-ci est caractérisée par deux paramètres : un diamètre médian  $d_0$  (tel que  $\ln(d_0) = \langle \ln d \rangle$ ) et une polydispersité  $\sigma$ . Ces paramètres peuvent être déterminés de multiples façons, par exemple par Microscopie Electronique par Transmission (MET), par diffusion dynamique de la lumière (DLS), par mesures d'aimantation ou de biréfringence magnéto-optique. Une étude extensive de la distribution de tailles des nanoparticules de l'échantillon *D107* a été réalisée. La table 3 regroupe les valeurs des paramètres  $d_0$  and  $\sigma$  définis dans l'équation (1), à coté de la méthode, la fraction volumique à laquelle la mesure a été réalisée est indiquée, en unités de la fraction volumique initiale  $\Phi_0$ . Les résultats sont globalement cohérents entre eux et les quelques différences sont discutées dans le texte du mémoire.

Tableau 3: Comparaison des deux paramètres de la distribution en tailles du ferrofluide *D107*, mesurés par différentes méthodes. Les mesures de diffusion de lumière (DLS) sont réalisées avec deux appareils commerciaux différents identifiés respectivement comme Malvern et Vasco $^\gamma$ .

Method	$d_0$ , nm	$\sigma$
<b>MET</b> , $0.001\Phi_0$	5.7	0.20
<b>DLS, Malvern</b> , $0.3\Phi_0$	8.7	0.35
<b>DLS, Malvern</b> , $\Phi_0$	9.3	0.43
<b>DLS, Vasco<math>^\gamma</math></b> , $\Phi_0$	9.6	0.40
<b>Aimantation</b> , $\Phi_0$	7.1	0.32
<b>Biréfringence</b> $0.3\Phi_0$	9.2	0.25

## 2 Micro-convection magnétique

Les ferrofluides possèdent, à la fois, des propriétés magnétiques et des propriétés hydrodynamiques. En conséquence ces fluides peuvent, non seulement, répondre à un champ magnétique, mais peuvent modifier celui-ci par "feed-back" en modifiant l'écoulement du liquide magnétique et/ou en provoquant des instabilités, qui sont parfois observables avec des fluides non-magnétiques via un écoulement instable. Les ferrofluides sont associés à un grand nombre d'instabilités de forme ou d'écoulement, ce travail s'intéresse à l'instabilité magnétique micro-convective, qui a été mise en évidence au début des années 80 par Maiorov et Cebers [3], en élargissant le concept des instabilités pilotées par le champ magnétique auto-induit [18], dans le cas de fluides miscibles en écoulement de Hele-Shaw. La convection magnétique est provoquée par une force pondéromotrice agissant sur le fluide magnétique en champ appliqué homogène. Cette force est proportionnelle à la concentration locale en nanoparticules et au gradient de champ magnétique local dû au champ magnétique auto-induit dans le ferrofluide. De plus, cette force dérive d'un potentiel seulement si le gradient de concentration est colinéaire au gradient de champ magnétique. Un écoulement est donc créé par n'importe quelle perturbation locale de concentration qui détruit cette colinéarité et qui induit alors un écoulement, conduisant à des digitations.

Le modèle de base pour décrire ces phénomènes s'appuie sur l'équation de Darcy, où la force magnétique pondéromotrice est prise en compte [19] via le potentiel magnétostatique [20, 21]. Sur cette base, plusieurs caractéristiques de la micro-convection magnétique ont été trouvées par une analyse de stabilité linéaire, montrant l'importance de l'étalement initial de l'interface [22, 23, 24], et par simulations numériques [25, 26]. Les premières expériences qui ont exploré cette instabilité, l'ont fait avec une interface circulaire formée par une goutte de ferrofluide plongée dans un fluide miscible non-magnétique [27, 28, 29]. Elles ont été rapidement suivies par une étude beaucoup plus détaillée, réalisée avec une interface plane [30]. La micro-convection magnétique s'est aussi révélée importante dans le cas de réseaux de concentration induits par un éclairage non-homogène en présence d'un champ magnétique [31, 32]. Par ailleurs, les études des instabilités conduisant à des digitations suscitent toujours un grand intérêt, comme le montrent des publications récentes qui sont liées non seulement à la stabilité d'interfaces entre fluides non-miscibles [33, 34, 35], mais aussi à des situations entre fluides miscibles [36].

La micro-convection étant toujours mal comprise, elle est ici étudiée plus avant. Nous nous focalisons ici sur les aspects expérimentaux. Des investigations théoriques sont réalisées en parallèle, qui au départ ont utilisé le modèle de Darcy. Celui-ci est présenté ci-dessous en unités adimensionnées en introduisant les échelles de longueur  $h$ , de temps  $h^2/D$ , de vitesse  $D/h$ , de pression  $12\eta D/h^2$  et de potentiel magnétostatique  $M_0 h$ :

$$-\nabla p - \mathbf{u} - 2Ra_m c \nabla \psi_m = 0 \quad (2)$$

$$\nabla \cdot \mathbf{u} = 0 \quad (3)$$

$$\frac{\partial c}{\partial t} + (\mathbf{u} \cdot \nabla) c = \Delta c. \quad (4)$$

Ici  $Ra_m = M_0^2 h^2 / 12\eta D$  est le nombre de Rayleigh magnétique, déterminé par le rapport entre le temps caractéristique de diffusion  $\tau_D = h^2/D$  et le temps caractéristique du mouvement  $\tau_M = 12\eta/M_0^2$ , lié au champ magnétique auto-induit non-homogène du fluide.

Le modèle de Brinkman, pour sa part, diffère du modèle de Darcy, par l'introduction d'un terme visqueux additionnel  $\Delta \mathbf{u}/12$  dans le membre de droite de l'équation (2).

Un travail synchrone entre les mesures expérimentales et les modélisations, d'abord avec le modèle de Darcy, puis avec celui de Brinkman, a permis d'améliorer sensiblement la compréhension des phénomènes, conduisant à deux publications [37, 38] et plusieurs communications présentées à des conférences.

## 2.1 Observations expérimentales

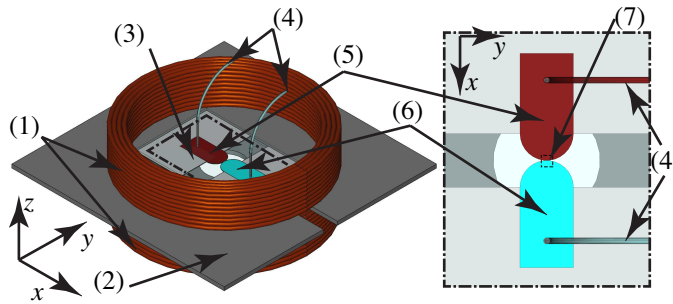


Figure 2: Le montage expérimental consiste en un système de bobines (1) ajusté pour être placé sur la platine d'un microscope (2). Une cellule de Hele-Shaw (3) avec ses tubes de connections pour l'introduction des fluides (4) est placée au centre. Une vue agrandie de la cellule montre comment les gouttes de fluide magnétique (5) et d'eau (6) sont amenées au contact l'une de l'autre au centre de la cellule de Hele-Shaw cell. Deux caméras filment la partie centrale de la cellule (7) où les gouttes se mélangent.

La microconvection magnétique à l'interface entre les deux fluides miscibles, est étudiée dans une cellule de Hele-Shaw, préparée avec deux lamelles de microscope séparées grâce à un espaceur fait de Parafilm M® de  $127 \mu\text{m}$  d'épaisseur. Le dispositif, qui est présenté sur la figure 2, permet d'amener une goutte d'eau distillée au contact du ferrofluide aqueux, d'observer les phénomènes sous microscope et de les filmer grâce à deux caméras, ayant une vitesse d'acquisition différente.

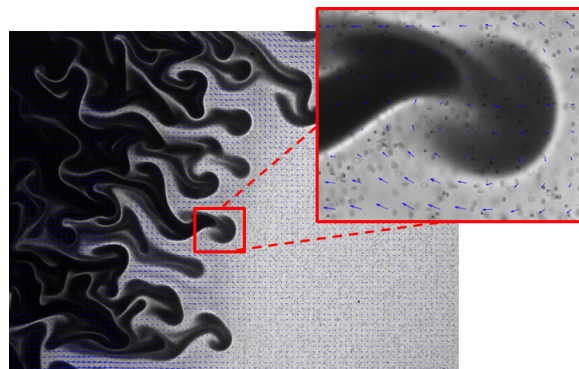


Figure 3: Carte du champ de vitesse lié à la micro-convection magnétique; l'agrandissement montre la fermeture des lignes du champ de vitesse autour de l'extrémité d'une digitation; observations à  $t = 6.5 \text{ s}$  et  $B = 18 \text{ G}$ , grâce à la méthode PIV.

Des expériences initiales ont été réalisées avec un dispositif légèrement plus simple, le ferrofluide *KTF09-13* et de l'eau additionnée de microparticules traceuses (0.1%vol). Elles

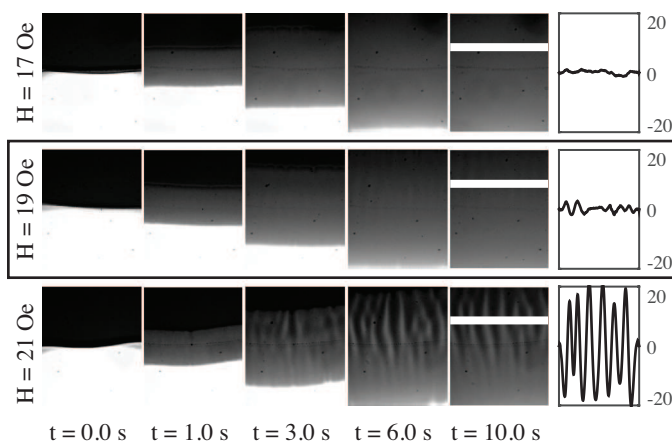


Figure 4: Détermination expérimentale du champ critique (marqué par un rectangle). Les dessins sur la droite montrent les valeurs de l'intensité le long des lignes blanches à  $t = 10.0$  s en u.a., après deux filtrages pour éliminer le bruit de fond et lisser les fluctuations. A  $H = 19$  Oe une digitation est visible (sur le dessin de droite), elle est petite mais notable par rapport aux fluctuations d'intensité autour du niveau de bruit à  $H = 17$  Oe. A  $H = 21$  Oe une digitation déjà bien développée est ici visible.

ont permis de suivre le phénomène avec des mesures de vélocimétrie par image de particules (PIV). La méthode PIV a permis pour la première fois d'obtenir le champ de vitesse dynamique pendant le développement de l'instabilité, un exemple est donné sur la figure 3. Des algorithmes spécialement développés [39], créés avec le dispositif *Dantec Dynamics* du constructeur permettent une comparaison quantitative avec les simulations numériques. Plus de détails sont donnés dans le mémoire et dans la référence [37].

Cependant, la formation de l'interface est apparue comme un point crucial pour la qualité de l'acquisition expérimentale. Le dispositif initial d'introduction des fluides a donc été amélioré en introduisant un contrôle microfluidique, comme cela est illustré par la figure 2 (4). Les expériences suivantes ont été réalisées pour différents champs magnétiques avec le ferrofluide *D107* et l'eau. Le champ critique auquel les digitations apparaissent est ici estimé à  $H_{crit} = 19 \pm 1$  Oe, (voir la figure 4). Une augmentation subsidiaire du champ (voir la figure 5) conduit d'abord à des digitations droites de plus en plus prononcées. Au-delà d'un second seuil moins net ( $H \approx 40$  Oe) on observe une courbure des digitations et une division ("splitting") de celles-ci. Lorsqu'on augmente encore le champ, l'instabilité se développe plus rapidement. A  $H = 138$  Oe, qui correspond au champ maximum de l'expérience, les digitations primaires se développent complètement en moins d'une seconde.

Par rapport à l'étude précédente, ici les expériences et leurs analyses sont principalement centrées sur la formation des digitations primaires. Les résultats sont comparés aux simulations numériques de micro-convection magnétique, obtenues dans le cadre du modèle de Brinkman, pour des conditions identiques. Ces résultats sont publiés dans la référence [38]. Le paramètre d'étalement de l'interface est ici estimé à  $t_0 \approx 0.05$  s à partir d'une étude expérimentale complémentaire, décrite dans la section 3.2. Il est, en effet, impossible d'extraire ce paramètre pour chacune des expériences.

Pour décrire quantitativement le processus, la dynamique et la dépendance en champ de plusieurs grandeurs sont déterminées par des méthodes "maison" d'analyse d'images. Elles sont basées sur des analyses de profils de concentration, obtenus en convertissant l'intensité

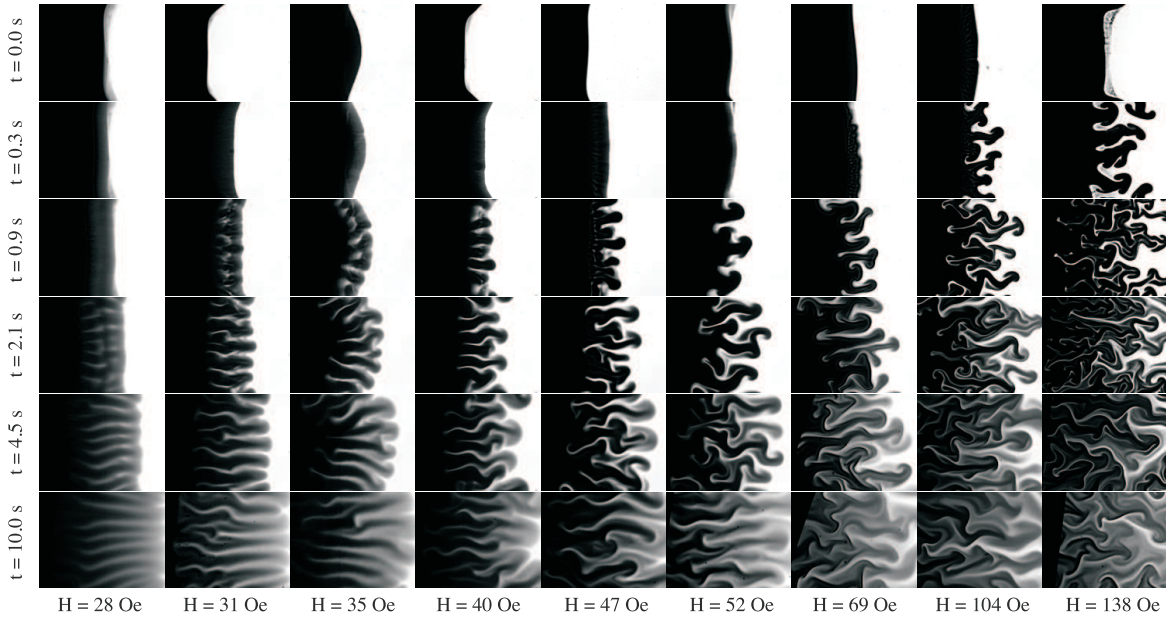


Figure 5: Images expérimentales du développement de la micro-convection magnétique pour différentes valeurs du champ magnétique. Chaque image correspond à une taille de  $0.7 \times 0.9$  mm.

des images via une loi de Beer-Lambert. Elles permettent de déterminer le vecteur d'onde caractéristique du profil par une analyse de Fourier et la vitesse de croissance initiale (voir le manuscrit pour plus de détails). La valeur du champ seuil nécessaire au développement de la micro-convection magnétique permet d'estimer un coefficient de diffusion "effectif" des nanoparticules  $D$ , qui, comme il est montré à la section 3.1, conduit à une valeur de  $D = 1.7 \cdot 10^{-5} \text{ cm}^2/\text{s}$  - une valeur du même ordre de grandeur que celle trouvée par les mesures de profil en champ nul décrites en section 3.2. Il est important de noter que ces valeurs sont beaucoup plus grandes que celles obtenues par la loi d'Einstein (5), conduisant à  $D \approx 6 \cdot 10^{-7} \text{ cm}^2/\text{s}$ , ce qui a amené au travail décrit dans la section 3.

La dépendance en champ est quantifiée en comparant les vitesses maximales moyennes d'avancée du profil de l'interface. La vitesse maximale  $v_{max}$  est trouvée pour chaque doigt et sa valeur moyenne  $\bar{v}_{max}$  ainsi que sa déviation standard sont calculées pour chaque champ magnétique. La vitesse maximale moyenne augmente comme le carré du champ, et donc comme le nombre de Rayleigh  $Ra_m$ , comme le montre la figure 6 (a). Après une conversion en unités adimensionnées, les données expérimentales présentent un très bon accord avec les données numériques obtenues dans le cadre du modèle de Brinkman, comme on peut le voir sur la figure 6 (b). La pente 0.27, qui est obtenue à partir de la dépendance expérimentale, linéaire de  $\max(|v|)$  en fonction de  $Ra_m$  est proche de la valeur 0.36 trouvée numériquement avec le modèle de Brinkman et assez loin de la valeur 1.39 trouvée numériquement dans le cadre du modèle de Darcy.

Proches aussi, sont les valeurs numériques de la vitesse des doigts, trouvées expérimentalement et numériquement avec le modèle de Brinkman. Par exemple, la valeur caractéristique de la vitesse d'un doigt à  $H = 104 \text{ Oe}$  est de  $0.64 \text{ mm/s}$ . En unités adimensionnées, cela correspond à 45 pour  $Ra_m = 181$ , ce qui est proche de la valeur 59 obtenue avec le modèle de Brinkman et est très différent de la valeur 180 obtenue avec le modèle de Darcy pour

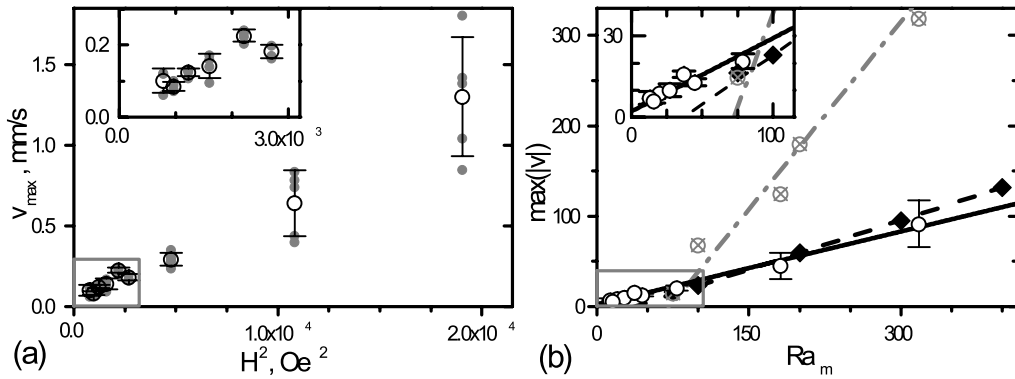


Figure 6: Vitesse maximale de digitation. (a) Données expérimentales de la vitesse maximale de digitation (points gris) et vitesse maximale moyenne (cercles vides avec barres d'erreur) en fonction du carré du champ magnétique. (b) Données numériques extraites de [38], et données expérimentales avec des ajustements linéaires : modèle de Brinkman (diamants noirs et ligne tiretée), modèle de Darcy (cercles ouverts avec une croix grise et ligne tiretée-pointillée) et données expérimentales en unités adimensionnées (cercles vides avec barres d'erreur et trait plein) en fonction de  $Ra_m$ . Les pentes ajustées et leur barre d'erreur sont  $0.36 \pm 0.01$ ,  $1.39 \pm 0.15$  and  $0.27 \pm 0.03$ . Les deux encarts montrent les agrandissements des portions de graphe marquées par des cases grises sur les figures principales.

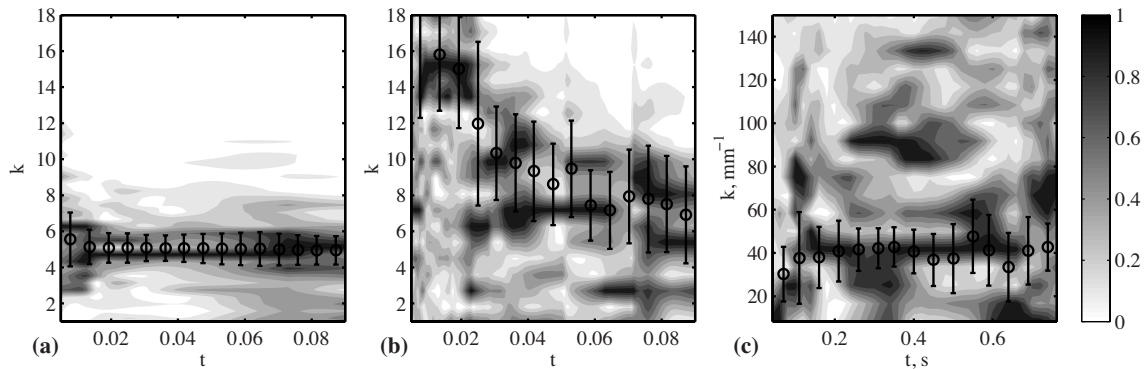


Figure 7: Analyse dynamique des digitations. Les graphes présentent des ajustements de contours, codés en échelles de gris, de l'évolution dynamique des spectres de Fourier. Sur ces graphes, on a superposé les nombres d'onde moyens. Ils sont indiqués par des cercles avec des barres d'erreur et sont déterminés par un algorithme de recherche de pics. Sur les figures (a) et (b), les résultats présentés sont des données de simulations numériques issues de la référence [38], obtenues à  $Ra_m = 318$  et  $t_0 = 0.005$  dans le cadre du modèle de Brinkman (a) et du modèle de Darcy (b) pour  $H = 138$  Oe. Sur la figure (c), les résultats présentés sont des données expérimentales obtenues à  $H = 138$  Oe. En unités adimensionnées, ces différents graphes ont les mêmes échelles et sont de "taille" équivalente.

$Ra_m = 200$  (voir la figure 6 (b)).

L'évolution dynamique des spectres de Fourier associés aux perturbations de concentrations est présentée sur la figure 7. Pour simplifier la comparaison entre expériences et simulations, les échelles des graphes sont choisies de façon à être identiques en termes d'unités

adimensionnées. Les données expérimentales de la figure 7(c) conduisent à un vecteur d'onde caractéristique  $k \simeq 40 \text{ mm}^{-1}$ . En multipliant celui-ci par l'épaisseur de la cellule de Hele-Shaw  $h = 120 \text{ }\mu\text{m}$ , on trouve  $kh \simeq 5$  en unités adimensionnées. Ceci est en bon accord avec les données de simulations numériques obtenues dans le cadre du modèle de Brinkman, comme le montre la figure 7 (a) et l'analyse linéaire. Au contraire, le modèle de Darcy prédit une digitation initiale à beaucoup plus petite échelle avec une dynamique plus rapide comme l'illustre la figure 7 (b).

Le bon accord qualitatif et quantitatif obtenu ici montre que le modèle de Brinkman, dans lequel un terme de friction est introduit, est tout à fait approprié pour décrire la micro-convection magnétique, au moins au cours du développement des premières digitations [38].

## 2.2 Possibilités de développement en microfluidique

Au cours des 15 dernières années, le domaine de la microfluidique a continuellement progressé, aussi bien pour des applications que pour des études scientifiques [1]. La microfluidique est basée sur la manipulation de très petits volumes de fluides dans des canaux de largeur typique quelques centaines de microns, ce qui est intéressant dans de larges domaines, en particulier pour les sciences de la vie. La microfluidique permet une réduction d'échelle, en réalisant des expériences avec une quantité de réactant extrêmement petite [40]. Dans de tels systèmes, le nombre de Reynolds est en général extrêmement petit, et beaucoup d'efforts ont donc été développés pour accélérer les mélanges, qui sont limités par la vitesse de diffusion [41]. Comme la diffusion est typiquement un processus lent, de très longs canaux sont nécessaires pour des mélanges corrects.

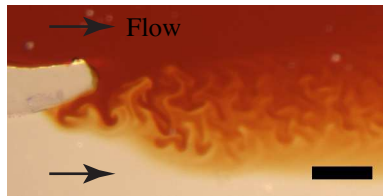


Figure 8: Test préliminaire de mélange par micro-convection magnétique dans un écoulement microfluidique simple. La barre d'échelle est égale à 0.5 mm.

Dans la référence [42], la micro-convection magnétique a été évaluée pour une application de mélange. Un test expérimental préliminaire, présenté sur la figure 8 et des évaluations numériques démontrent qu'il est possible d'accélérer le mélange de fluides via la micro-convection magnétique. Par ailleurs, de nouvelles expériences dédiées aux phénomènes de micro-convection pourront être réalisées à l'avenir grâce à la microfluidique.

## 3 Diffusion de particule dans les fluides magnétiques

La diffusion est un phénomène provoqué par le mouvement au hasard, des molécules à température finie. Ici les investigations concernent un système de particules magnétiques, de tailles nanométriques, dispersées dans un liquide porteur. Lorsque ce liquide est de l'eau, il peut être considéré comme un fluide Newtonien incompressible, sans visco-élasticité ni autre contribution complexe. Le mouvement diffusif d'une particule individuelle dans l'eau correspond à une marche au hasard. Son déplacement carré moyen  $\langle x^2 \rangle$  augmente linéairement avec le temps  $t$  et le coefficient de proportionnalité est le produit du nombre de

directions indépendantes de l'espace, où le mouvement a lieu, par le coefficient de diffusion  $D$  [43]. Dès lors la distance moyenne associée à un processus de diffusion est proportionnelle à  $\sqrt{t}$ . Le coefficient de diffusion  $D$  dépend de la taille des particules et des propriétés du solvant. Si il n'y a aucune interaction entre les particules, ces grandeurs sont reliées par l'équation de Stokes-Einstein [43] :

$$D = \frac{k_B T}{3\pi\eta d}, \quad (5)$$

où  $k_B$  est la constante de Boltzmann,  $T$  la température,  $\eta$  la viscosité du solvant et  $d$  le diamètre des particules sphériques. Il faut noter qu'ici les effets du champ magnétique [44] sur la diffusion ne sont pas tenus en compte, on suppose raisonnablement qu'ils sont faibles. La diffusion d'un ensemble de particules conduit à un changement de la position des particules. Si la concentration est initialement homogène, alors la diffusion ne provoque que des fluctuations locales de concentration. Au contraire, si la concentration est initialement inhomogène, son profil est étalé par le processus de diffusion. Quand l'étalement d'une interface est suffisamment large, celui-ci est visible macroscopiquement. Dans le cas d'un gradient de concentration, le processus de diffusion peut être décrit par la seconde loi de Fick [45] :

$$\frac{\partial c}{\partial t} = D\Delta c, \quad (6)$$

où  $\Delta$  est l'opérateur Laplacien,  $c$  et  $D$  sont la concentration et le coefficient de diffusion de l'espèce diffusante,  $t$  désigne le temps.

### 3.1 Estimation du champ critique de micro-convection magnétique

Les mesures expérimentales précises de la figure 4 indiquent que le champ critique vaut  $H_{crit} = 19 \pm 1$  Oe pour le ferrofluide *D107*. De façon alternative, la courbe neutre de l'analyse de stabilité linéaire dans le cadre du modèle de Brinkman (voir la figure 3 de la ref [38]) suggère que le champ critique correspond à  $Ra_m^{crit} \approx 6$ . Donc, compte tenu de la définition du nombre de Rayleigh  $Ra_m = M_0^2 h^2 / 12\eta D$ , où l'aimantation  $M_0 = \chi H$ , on peut estimer le coefficient de diffusion  $D$  de la façon suivante :

$$D = \frac{\chi^2 H_{crit}^2 h^2}{12\eta Ra_m^{crit}}. \quad (7)$$

Toutes ces quantités ont été soit mesurées dans les sections 1.2 et 2.1 (épaisseur de cellule  $h = 0.012$  cm, viscosité  $\eta = 1$  cP (water), susceptibilité  $\chi = 0.016$ ) , soit déterminées ici (nombre de Rayleigh  $Ra_m^{crit} = 6$  et champ critique  $H_{crit} = 19$  Oe). On trouve dès lors  $D = 1.7 \cdot 10^{-5}$  cm<sup>2</sup>/s. Cette valeur ainsi obtenue, bien que beaucoup plus grande que celle d'une nanoparticule individuelle dans l'eau, est du même ordre de grandeur que celle mesurée dans l'expérience suivante.

### 3.2 Evolution de l'interface d'un ferrofluide en réponse à une marche de concentration

En analysant la réponse à une marche de concentration, dans le cas à une dimension ( $c = c_0$  pour  $x \leq 0$  et  $c = 0$  pour  $x > 0$  à  $t = 0$ ) et en résolvant la seconde loi de Fick (6)

avec ces conditions initiales, on obtient une expression analytique de la concentration  $c$  en tout point  $x$  et à chaque instant  $t$  [45] :

$$c(x, t) = \frac{c_0}{2} \left[ 1 - \operatorname{erf} \left( \frac{x}{2\sqrt{Dt}} \right) \right], \quad (8)$$

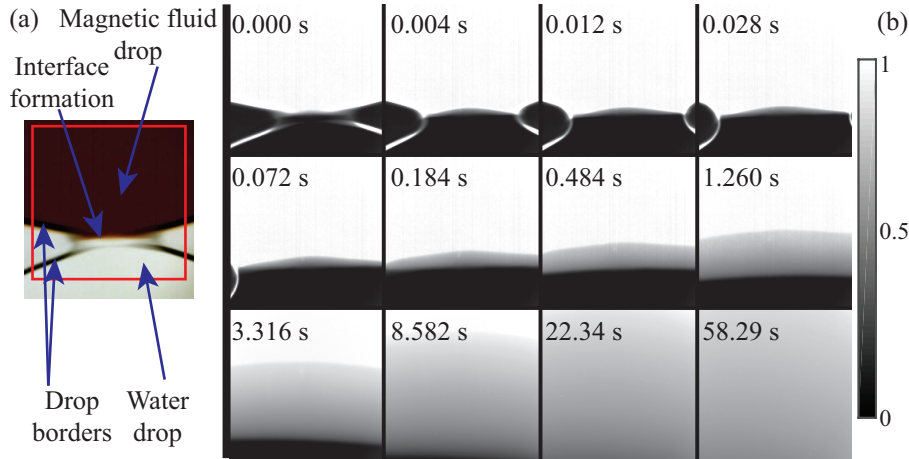


Figure 9: Mesures à  $H = 0$  avec le dispositif expérimental initial. (a) Image de la formation de l'interface à  $t = 0$  s. Les objets importants sont pointés par des flèches. Le rectangle rouge marque la zone analysée. (b) Evolution temporelle de la densité de concentration en nanoparticules magnétiques au cours du mélange à l'interface entre les deux fluides magnétique et non-magnétique. Le champ d'observation de chacune des images est de  $1.05 \times 1.08 \text{ mm}^2$ .

où  $D$  est le coefficient de diffusion et  $\operatorname{erf}$  est la fonction erreur. On peut de plus définir une longueur de diffusion  $\delta = 2\sqrt{Dt}$  mesurant l'extension du front de diffusion. La diffusion est un processus lent et pour des nanoparticules de diamètre de l'ordre de 10 nm,  $D$  devrait être de l'ordre de  $10^{-7} \text{ cm}^2/\text{s}$  et la longueur  $\delta \sim 0.3 \text{ nm}$  au bout d'une heure. Cependant les expériences ci-dessous réalisées en champ nul avec le dispositif de la section 2.1, montre que l'élargissement du front est beaucoup plus rapide.

Les données sont obtenues par des techniques de traitement d'images, en les convertissant en profils de concentration et en les analysant. Tout ceci conduit à une distance caractéristique évoluant comme  $\sqrt{t}$  mais donne un coefficient de diffusion  $D \sim 6.5 \cdot 10^{-5} \text{ cm}^2/\text{s}$ , plusieurs centaines de fois plus grand que celui des nanoparticules individuelles, associé un profil de concentration assez mal décrit par une fonction  $\operatorname{erf}$ . Pour expliquer ces différences, nous avons d'abord fait l'hypothèse d'une augmentation de la diffusion par diffusophorèse [46], reliée à la présence des ions citrate en solution dans le ferrofluide, d'une façon similaire à celle observée pour des sphères de silice de diamètre 200 nm, le long d'un gradient de sel [47, 48]. Différents essais ont été faits en mélangeant la goutte de ferrofluide avec des gouttes de solutions aqueuses de citrate, de différentes concentrations. L'hypothèse s'est révélée mauvaise comme l'a montré une expérience faite avec l'échantillon surfacté *DF105*.

### 3.3 Effet de la gravité

Jusqu'ici nous avons mené nos études expérimentales dans l'hypothèse d'un écoulement de Hele-Shaw [49], qui résume l'écoulement à un écoulement 2D. Cependant des effets de gravité

peuvent apparaître dans la troisième dimension (selon la force pointant verticalement dans la direction  $-\vec{z}$  sur la figure 2). La gravité a une influence sur l'interface entre deux fluides miscibles lorsque ceux-ci n'ont pas la même densité, comme cela a été montré dans [37]. L'effet résultant dans le plan  $x - z$  peut alors être décrit par le modèle de Stokes, avec une concentration  $c$  fonction de la force de gravité et une équation de diffusion écrite de façon adimensionnée avec le nombre de Rayleigh associé aux effets de gravité  $Ra = \Delta\rho gh^3/8D\eta$ , où  $h$  est l'épaisseur de la cellule,  $\Delta\rho$  est la différence de masse volumique entre les fluides,  $D$  est le coefficient de diffusion des nanoparticules concentrées et  $\eta$  est la viscosité du fluide, supposée la même partout.

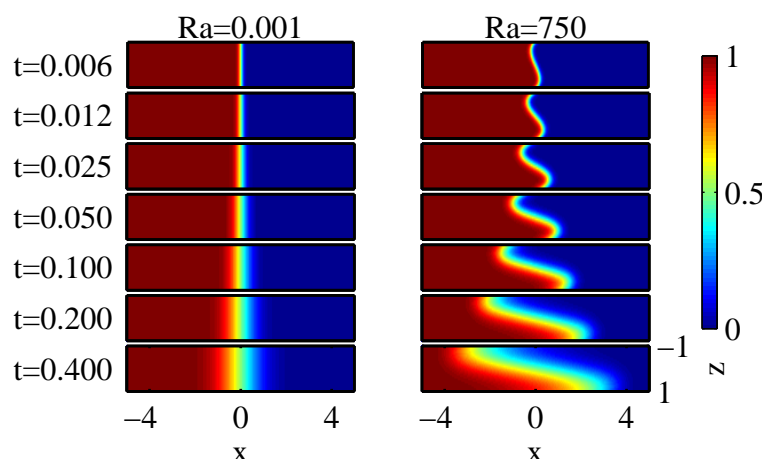


Figure 10: Simulations numériques, pour deux valeurs très différentes du nombre de Rayleigh  $Ra$ , de l'évolution temporelle du profil de concentration. La diffusion normale est visible pour  $Ra = 0.001$  (à gauche), tandis que pour  $Ra = 750$  (à droite) un mouvement initial rapide du fluide le plus lourd est superposé à l'effet de diffusion plus lent.

Les simulations numériques sont réalisées avec un programme COMSOL, déjà développé pour [37] avec une interface initiale très légèrement élargie et des conditions de non-glissement dans la géométrie adaptée. Les solutions sont recherchées à partir de  $t = 0$  pour des intervalles  $\Delta t = 0.001$  et pour différentes valeurs du nombre de Rayleigh gravitationnel  $Ra$ . Deux exemples de résultats sont présentés sur la figure 10 pour un très petit nombre de Rayleigh  $Ra = 0.001$  et pour une valeur assez moyenne  $Ra = 750$ . Déjà pour des valeurs de cet ordre, on observe une influence notable des effets de gravité par rapport au cas purement diffusif. Une comparaison quantitative est réalisée en calculant l'évolution dynamique de la concentration  $\bar{c}(x)$ , moyennée sur le profil en épaisseur. On peut alors trouver le coefficient de diffusion effectif  $D_{\text{eff}}$  en différenciant l'équation 8 autour de  $x = 0$  et en ajustant les données respectives. Le résultat est une augmentation linéaire de  $D_{\text{eff}}$  au-delà d'une valeur critique, comme le montre la figure 11 (a).

Une comparaison qualitative de la dynamique des profils de concentration moyenne, à ceux obtenus expérimentalement montre rapidement d'importantes similarités. Une comparaison quantitative est faite en calculant  $Ra$  dans chacune des expériences effectuées. Le coefficient de diffusion effectif obtenu (en forme adimensionnée  $D_{\text{eff}}/D_0$  avec  $D_0 = 2.5 \cdot 10^{-7} \text{ cm}^2/\text{s}$  déterminé par des expériences complémentaires) est présenté sur la figure 11 (b). Compte tenu des erreurs inhérentes aux traitements, l'accord est très raisonnable et confirme la présence d'effets gravitationnels dans les expériences de la section 2.1. Cependant pour une

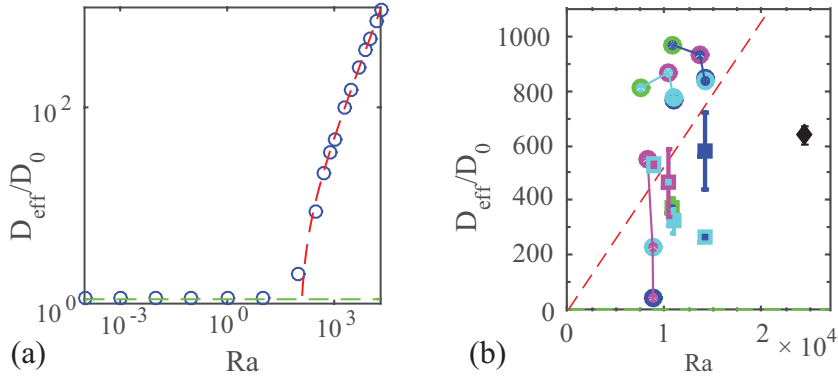


Figure 11: (a) Coefficient de diffusion effectif en fonction du nombre de Rayleigh gravitationnel dans une représentation log-log. Les cercles bleus indiquent les résultats des simulations numériques. Pour  $Ra < 10$  il n'y a pas de diffusion effective  $D_{\text{eff}} = D_0 = 1$  (ligne verte hachurée), mais pour  $Ra > 300$ ,  $D_{\text{eff}}/D_0$  augmente linéairement avec  $Ra$  comme  $D_{\text{eff}} = 0.053(Ra - Ra_c)$ , où  $Ra_c = 105$  (ligne rouge hachurée). (b) Coefficients de diffusion effectifs mesurés dans les diverses expériences sous forme adimensionnée  $D_{\text{eff}}/D_0$  en fonction de  $Ra$ . Pour plus d'informations se référer au mémoire.

justification plus complète une autre expérience a été réalisée et est présentée ci-dessous.

Pour obtenir des informations sur la distribution de concentration à 3 dimensions (ou au moins des coupes 2D de celle-ci), il aurait fallu par exemple disposer d'un microscope confocal [50, 48]. Malheureusement ce n'était pas notre cas pour cette étude, une solution beaucoup plus simple a été choisie : changer la direction de la force de gravité par rapport à la cellule, en tournant le microscope lui-même et en assurant le contrôle de l'arrivée des fluides dans la cellule microfluidique par des pousse-seringues.

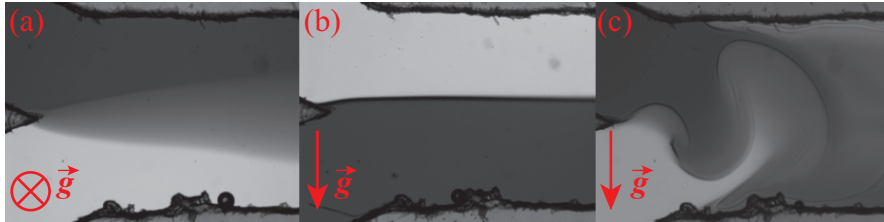


Figure 12: Mélange des fluides dans la cellule microfluidique en l'absence de champ magnétique, pour différentes directions de la gravité  $\vec{g}$ . Chaque image a une taille de  $2.2 \times 1.7 \text{ mm}^2$  et correspond à un écoulement de débit  $Q = 2.4 \mu\text{L}/\text{min}$ .

Différentes expériences de mélange du ferrofluide *D107* avec de l'eau distillée, dans une cellule microfluidique, ont été réalisées pour trois directions différentes de la gravité par rapport au sens de l'écoulement. La figure 12 montre une image caractéristique du processus dans chacune de ces configurations. Sur la figure 12 (a), la gravité  $\vec{g}$  est perpendiculaire à la cellule et donne les mêmes résultats que précédemment.

La figure 12 (b) par contre est obtenue avec la gravité  $\vec{g}$  dans le plan de la cellule et pointant vers le liquide le plus dense. Elle démontre que l'effet d'étalement de l'interface est bien sûr lié à un effet de gravité, puisqu'aucune diffusion n'est visible sur l'image. Si le liquide le plus dense est maintenant placé en haut, les conditions pour obtenir une instabilité de

Rayleigh-Taylor sont alors remplies et l'étude de cette instabilité est un sujet scientifique qui reste d'actualité [51, 52]. Cette instabilité est observée sur la figure 12 (c) et on peut noter que ses digitations sont de taille bien différente de celles observées dans la section 2.1. Il faut noter que, sans se placer en écoulement microfluidique, de telles expériences auraient été très difficiles à réaliser.

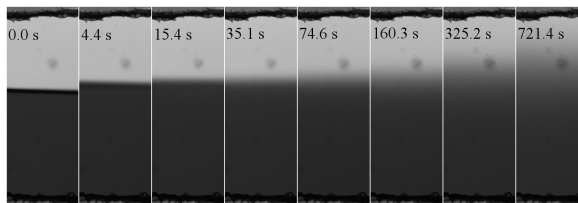


Figure 13: Clichés de la diffusion des nanoparticules magnétiques perpendiculairement au microcanal alors que l'écoulement est arrêté. Largeur du canal 1.4 mm.

Le coefficient de diffusion des nanoparticules magnétiques peut donc être déterminé dans cette expérience, en supprimant ainsi tout effet de gravité, si on place la cellule de Hele-Shaw verticalement avec le fluide le plus dense en bas de la cellule microfluidique. Pour réaliser la mesure, l'écoulement est arrêté brusquement, de façon à obtenir un système immobile avec une interface nette, qui s'étale pendant le mélange comme l'illustrent les clichés de la figure 13. Le processus observé est beaucoup plus lent et même après 12 minutes, l'étalement de l'interface est très faible. La diffusion des nanoparticules est analysée comme précédemment et le coefficient de diffusion ainsi déterminé  $D \approx 5.5 \cdot 10^{-7} \text{ cm}^2/\text{s}$ , est beaucoup plus proche de la valeur  $D_0$  obtenue, avec le même liquide magnétique mais par d'autres méthodes expérimentales, comme la diffusion dynamique de la lumière ou par diffusion Rayleigh forcée. Une autre méthode de mesure de  $D_0$  par photoblanchiment de nanoparticules fluorescentes est aussi proposée dans le mémoire.

## 4 Instabilités de ferrofluides démixés en deux phases liquides

Un phénomène intéressant associés aux ferrofluides est leur capacité à se séparer en deux phases liquides. Une suspension de nanoparticules, dispersées de façon homogène peut devenir biphasique sous l'action de différents paramètres. Les investigations sont ici limitées au cas où une démixion est induite par ajout de sel, provoquant l'apparition de gouttes de liquide magnétique concentré au sein d'une phase plus diluée. Dans certains cas, un champ magnétique fort est aussi appliqué.

Les premières observations d'une séparation de phase dans les fluides magnétiques datent des années 1970 [53]. Depuis un gros travail a été dédié à la caractérisation des différents paramètres influençant le processus de séparation de phase [54, 55, 56, 57] et sur les transitions magnéto-induites [58]. Mais de nombreuses questions restent en suspens au plan colloïdal.

Les gouttes de phase concentrée ont été étudiées à la fois au plan expérimental et au plan théorique [8], elles présentent des instabilités tout aussi spectaculaires en présence d'un champ magnétique statique et homogène [59, 60, 61], qu'en présence d'un champ magnétique tournant [4, 62]. De façon alternative des gouttes magnétiques modèles peuvent être obtenue avec des émulsions magnétiques, basées sur un fluide magnétique et un fluide non-magnétique et non-miscible [63, 64, 65, 64, 66].

Dans la littérature [4, 63], les gouttes magnétiques sont souvent caractérisées par un nombre de Bond magnétique sans dimension, défini comme  $Bm_H = H^2 R / \sigma$ , où  $\sigma$  est la tension de surface,  $R$  est le rayon initial et  $H$  est le champ magnétique. Quand une goutte magnétique et liquide est placée dans un champ magnétique homogène, elle s'allonge dans la direction du champ  $\vec{H}$ . Sa forme résulte d'un équilibre entre énergie de surface et énergie magnétique. En approximant la forme de la goutte sous champ par un ellipsoïde de révolution, on peut la décrire par la formule suivante [59, 67] :

$$\frac{H^2 R}{\sigma} = \left[ \frac{4\pi}{\mu - 1} + N \right]^2 \frac{1}{2\pi} \frac{\left( \frac{3-2e^2}{e^2} - \frac{(3-4e^2) \arcsin e}{e^3(1-e^2)^{\frac{1}{2}}} \right)}{(1-e^2)^{\frac{2}{3}} \left( \frac{(3-e^2)}{e^5} \ln \left( \frac{1+e}{1-e} \right) - \frac{6}{e^4} \right)}, \quad (9)$$

où  $e$  est l'excentricité de l'ellipsoïde, définie comme  $e = \sqrt{1 - \frac{b^2}{a^2}}$ ,  $\mu$  est la perméabilité magnétique, qui est connectée à la susceptibilité  $\mu = 1 + 4\pi\chi$ , et  $N$  est le facteur démagnétisant, qui dans le cas d'un ellipsoïde de révolution prolata s'exprime :  $N = \frac{4\pi(1-e^2)}{2e^3} \left( \ln \frac{1+e}{1-e} - 2e \right)$ . Quand le champ est coupé, la goutte magnétique relaxe vers sa forme sphérique initiale. Si la forme de la goutte est suffisamment proche d'une forme sphérique, ce processus peut être décrit par une relaxation exponentielle de temps caractéristique  $\tau$  [68], tel que :

$$\tau = \frac{R(16\eta_d + 19\eta_c)(3\eta_d + 2\eta_c)}{40\sigma(\eta_d + \eta_c)}. \quad (10)$$

Ces relations permettent de caractériser la phase magnétique concentrée qui coexiste avec la phase diluée, en réalisant sur une même goutte de phase concentrée une expérience d'élongation sous champ magnétique puis une relaxation sous champ nul, ce qui est réalisé dans la section 4.2.1.

#### 4.1 Système de bobines pour explorer sous microscope les propriétés des fluides magnétiques démixés, soumis à des champs dépendant du temps

Pour cette étude, un nouveau système de bobines a été développé avec une unité de contrôle associé. Ils peuvent être utilisés avec le microscope *ZEISS Axio Observer.D1* disponible au laboratoire PHENIX. En s'appuyant comme point de départ sur le système existant à Riga [69], le design et des changements technologiques ont été réalisés en répondant aux besoins expérimentaux. Une description du système, qui est reproduit sur la figure 14, peut être trouvée dans le mémoire. Le système comprend 4 bobines pour créer un champ tournant horizontal et 2 bobines pour créer un champ vertical, ce qui peut résulter en un champ précessant aisément contrôlable. Les bobines sont commandées par 3 alimentations pilotées par ordinateur et sont refroidies par un système à circulation d'eau. Au cours de l'expérience, les images sont enregistrées par une caméra synchronisée. Le système permet l'observation d'objets microscopiques sous champ précessant ou dans des configurations de champ plus simples jusqu'à 50 Oe et 500 Hz, tandis que l'expérience peut être filmée jusqu'à 60 Hz. Le tout est contrôlé par un programme écrit en Labview.

#### 4.2 Expériences réalisées avec des micro-gouttes issues de la séparation de phase d'un ferrofluide

Les gouttes sont observées avec le nouveau dispositif. Les solutions sont placées dans des cellules optiques de 100 à 200  $\mu\text{m}$  d'épaisseur. Les gouttes sont obtenues par augmentation

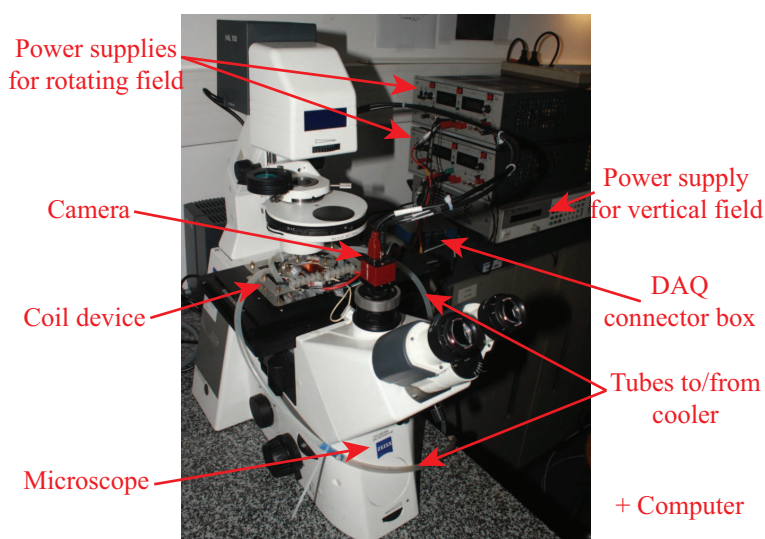


Figure 14: Le système de bobines et ses composants, développés pour l'exploration expérimentale des ferrofluides démixés en deux phases fluides.

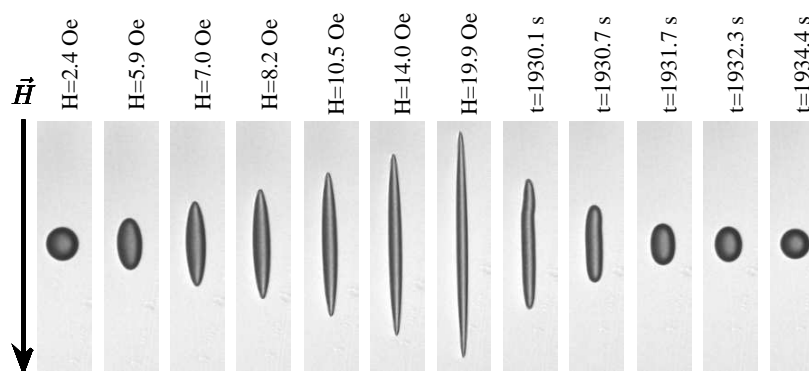


Figure 15: Clichés d'une série de mesures d'élongation-relaxation d'une goutte de phase concentrée. Les valeurs de champ appliqué pendant l'élongation et de temps pendant la relaxation en champ nul sont indiquées sur la figure. Chaque image a une taille de  $115 \times 25 \mu\text{m}^2$ .

de la force ionique d'un ferrofluide monophasique soit en ajoutant du EAN à l'échantillon p146, ou bien du citrate de sodium dans l'échantillon D107, ce dernier étant subsidiairement soumis à un fort champ magnétique pendant un temps court. Les informations sur les caractéristiques des gouttes sont extraites des films en utilisant un algorithme de traitement d'image, donnant le meilleur ajustement par une ellipse. On trouvera plus de détails dans le mémoire.

#### 4.2.1 Propriétés de la phase concentrée issue de la séparation de phase

Des expériences d'élongation sous champ et de relaxation en champ nul peuvent être menées sur des gouttes individuelles de phase concentrée. Elles permettent de déduire leur susceptibilité magnétique  $\chi$ , leur tension de surface  $\sigma$  et leur viscosité  $\eta$ . Une série de

clichés associés à une séquence de mesure d'élongation-relaxation d'une goutte de phase concentrée est présentée sur la figure 15. Durant la première partie de l'expérience, associée à l'élongation de la goutte une lente série de pas en champ est réalisée manuellement, permettant à la goutte d'atteindre un état stationnaire pour chacun des champs intermédiaires. Quand une élongation suffisante est atteinte, le champ est ramené brutalement à zéro, laissant la goutte relaxer vers une forme sphérique.

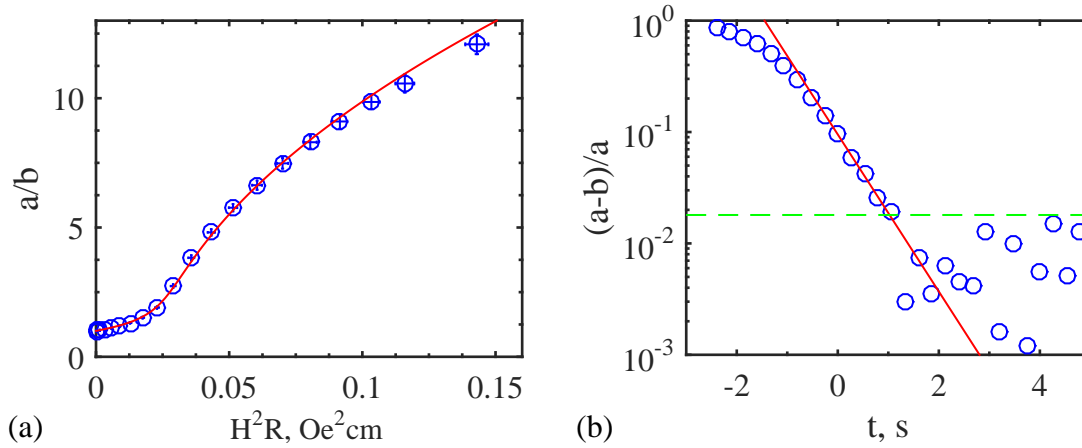


Figure 16: Ajustement des données expérimentales. Les cercles bleus indiquent les données et les courbes rouges les ajustements. (a) Données associées à l'élongation, rapport des demi-axes  $a/b$  en fonction de  $H^2R$ , ajusté avec l'équation (9). (b) Relaxation de forme décrite par l'évolution temporelle de  $(a - b)/a$ , en termes de différence entre les demi-axes, normalisée par  $a$ . Cette quantité relaxe vers zéro et peut être ajustée par l'expression  $A \cdot e^{-t/\tau}$ . La ligne verte hachurée indique le niveau de bruit en dessous duquel l'ajustement n'a plus de sens.

Un exemple d'analyse des données est présenté sur la figure 16. L'ajustement de la figure 16(a) par l'équation (9) permet de déduire la perméabilité magnétique  $\mu = 8.1$  et la tension de surface  $\sigma = 1.9 \cdot 10^{-3}$  dyn/cm. Pour sa part, l'ajustement (semi-automatisé) de la figure 16(b) par une relaxation de la forme  $A \cdot e^{-t/\tau}$  conduit à  $\tau = 0.6$  s. Si la viscosité du fluide magnétique est approximée par celle de l'eau  $\eta_d = 0.01$  P dans l'équation (10), et en prenant pour  $\sigma$  la valeur obtenue par la mesure d'élongation, on obtient  $\eta_c = 1.77$  P pour la viscosité de la phase concentrée. Ce sont des ordres de grandeur habituels pour ce type de gouttes.

Le ferrofluide *p146* avec 1.5 M de EAN ajouté, qui est utilisé plus loin, présente des gouttes plus magnétiques et plus visqueuses, de caractéristiques restant constantes au cours du temps durant l'expérience :  $\mu = 16.6 \pm 1.2$ ,  $\sigma = (4.4 \pm 0.3) \cdot 10^{-3}$  dyn/cm et  $\eta_c = 10.2 \pm 2.4$  P. Pour leur part, les gouttes du ferrofluide *D107*, induites par un champ magnétique fort, diminuent en taille avec le temps, tandis que leurs propriétés évoluent elles-aussi. Plus d'informations sur ce comportement qui n'a jamais été rapporté jusqu'ici peuvent être trouvées dans le mémoire.

#### 4.2.2 Micro-gouttes magnétiques en champ tournant et en champ précessant

Les gouttes magnétiques n'ont jamais été étudiées en champ précessant. L'ensemble des angles de précession  $\theta$  possibles n'a pas été exploré ici et cette étude est centrée sur la configuration à l'angle magique  $\theta_{\text{magic}} = 54.74^\circ$ , qui est particulièrement intéressante, puisque

dans ce cas la contribution à l'énergie magnétique est la même dans les trois directions de l'espace (les deux directions dans le plan du champ tournant et la direction du champ statique normal à ce plan). Ceci favorise la forme sphérique et peut inhiber certaines transitions de forme.

Les expériences en champ précessant sont réalisées parallèlement à des mesures de référence en champ tournant, qui ont déjà été explorées auparavant [4]. Chaque série de mesures est commencée avec une goutte (supposée) sphérique en 3D et le champ magnétique est lentement augmenté par pas progressifs. Quand le champ magnétique maximum désiré est atteint, la mesure est terminée soit par une relaxation en champ nul en coupant le champ brutalement, soit en le diminuant pas à pas.

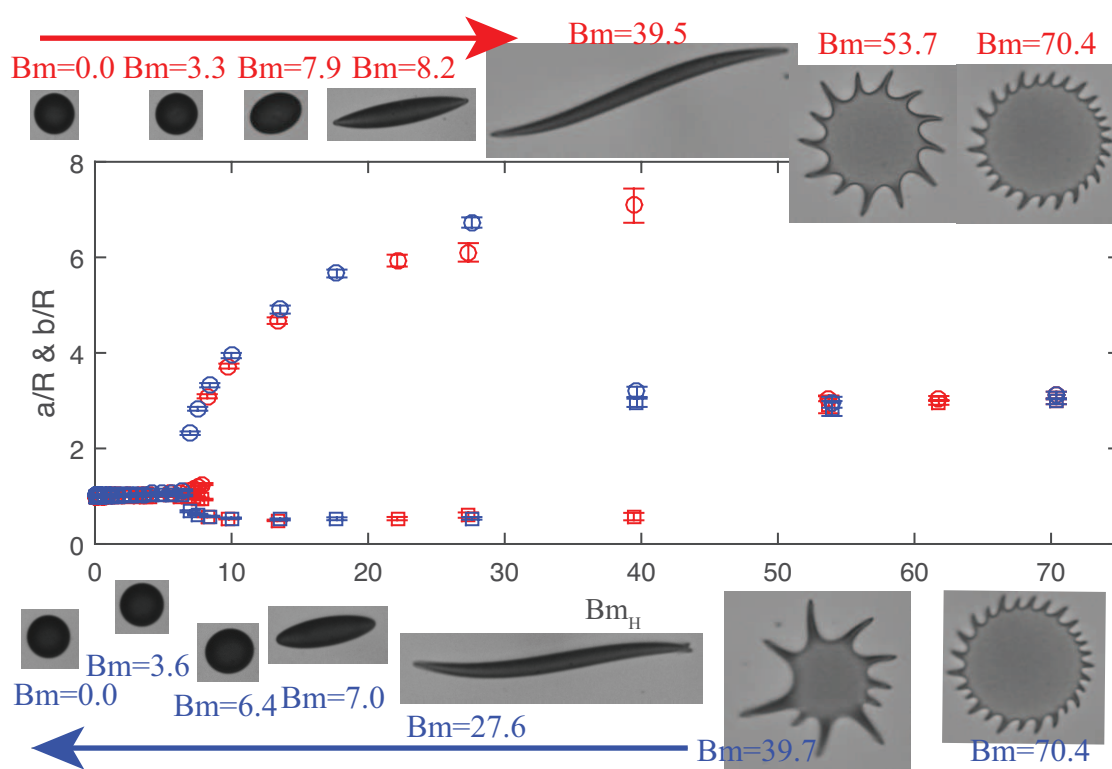


Figure 17: Déformation d'une goutte magnétique en champ précessant. Les demi-axes (normalisés) de l'ellipse  $a/R$  (cercles) et  $b/R$  (carrés) sont représentés en fonction du nombre de Bond. Cette évolution est illustrée par quelques images caractéristiques. La couleur rouge indique des mesures faites en augmentant le champ, la couleur bleue, les mesures faites en diminuant celui-ci.

Les gouttes de la phase concentrée du ferrofluide *p146* (with 1.5 M EAN) soumises à un champ précessant conduisent aux formes présentées sur la figure 17. On peut distinguer deux instabilités de forme, l'une pour  $Bm_H \approx 8$ , où la goutte s'allonge brusquement, ce qui conduit à une forme prolate, l'autre pour  $Bm_H \approx 40$  où la goutte, de forme très allongée (prolate), se transforme en un objet oblate, couronné des pics caractéristiques des ferrofluides. Ce comportement est très proche de celui qui a été observé sous champ tournant dans la référence [4] (voir le texte du mémoire).

La seule différence notable peut être pointée à faibles  $Bm_H$ , sur la figure 18, où la goutte en champ précessant préfère garder "plus longtemps" une forme proche de la sphère, ce à quoi

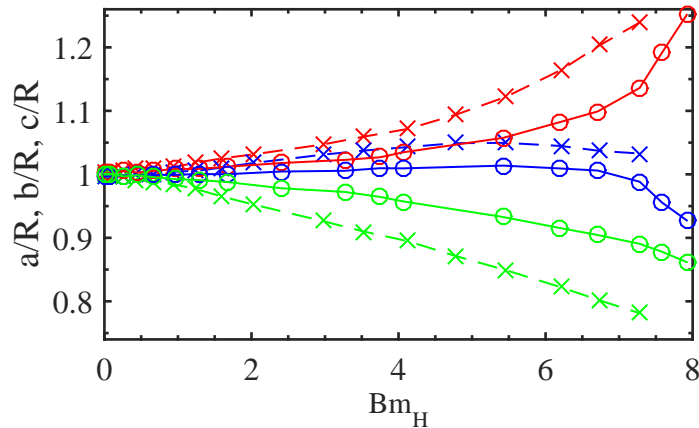


Figure 18: Evolution de la goutte à faible nombre de Bond en champ tournant (croix, lignes hachurées) et en champ précessant (cercles, ligne pleine). Les données associées au demi-axe long  $a$  sont en rouge, celles associées au demi-axe court  $b$  sont en bleu. En faisant l'hypothèse d'un volume de goutte constant au cours de l'expérience, on peut calculer le troisième demi-axe  $c$ , il est ici représenté en vert.

on peut s'attendre. La résolution limitée et d'autres effets, en particulier dûs à la gravité, rendent difficile une réponse formelle, et des travaux supplémentaires sont nécessaire pour conclure sur ce point.

Parallèlement à ces expériences, d'autres observations inattendues ont été faites au cours de cette étude, elles sont détaillées dans le mémoire.

## Conclusions

Des études expérimentales extensives sur des fluides magnétiques ont été confrontées tout au long de ce travail à des prédictions théoriques. Elles ont conduit à d'importantes conclusions regroupées ici selon chacune des sections du travail.

Une caractérisation soignée des fluides magnétiques utilisés a montré que les différentes techniques accessibles donnent des résultats comparables, même si ces comparaisons ne sont pas toujours simples en raison de la polydispersité en taille des nanoparticules, parce que les différentes mesures réalisent des moyennes différentes sur cette distribution en tailles.

L'étude expérimentale de microconvection magnétique entre fluides miscibles dans la cellule de Hele-Shaw a permis des déterminations qualitatives et quantitatives. La mesure du champ de vitesse, lorsque l'instabilité apparaît, a été pour la première fois réalisée en vélocimétrie par image de microparticules (PIV). Il a été ensuite montré, d'abord qualitativement, puis quantitativement après des améliorations du dispositif expérimental, que la micro-convection dépend d'un nombre magnétique sans dimension, le nombre de Rayleigh magnétique, qui est proportionnel au carré du champ. Plusieurs grandeurs mesurées expérimentalement, telles que le champ magnétique critique, la largeur caractéristique et la vitesse d'avancée des digitations, ont présenté un bon accord quantitatif avec le modèle de Brinkman, le modèle de Darcy, qui néglige un important terme lié à la viscosité, n'étant pas apte à re-

produire les données expérimentales quantitativement. Il a été par ailleurs montré qu'il est possible de mettre en oeuvre la micro-convection pour réaliser des mélanges en microfluidique.

Une très rapide "diffusion effective" des nanoparticules à l'interface entre les fluides miscibles a été observée au cours de cette étude, aussi bien via la détermination du champ seuil que par des observations en champ nul. Des expériences complémentaires ont démontré l'influence déterminante d'effets de gravité, liés à la différence de densité entre les deux fluides. Ce processus s'échelle selon un nombre sans dimension, le nombre de Rayleigh  $Ra$ . Des simulations numériques ont montré qu'un mouvement convectif apparaît, dès l'interface formée, forçant le fluide le plus dense à passer sous le fluide le moins dense. Si on moyenne la concentration en épaisseur, l'interface s'étale dans le temps en imitant un processus diffusif (avec un profil de forme toutefois différent) permettant de définir une "diffusion effective" comparable à celle déterminée dans l'expérience de micro-convection.

En tournant de dispositif expérimental, y compris le microscope, pour supprimer l'effet de la gravité en plaçant le fluide dense en bas et en réalisant l'expérience dans une cellule microfluidique, où l'écoulement est arrêté brutalement, on retrouve un élargissement de l'interface au cours du temps, associé la "vraie" diffusion des nanoparticules. Le coefficient de diffusion trouvé alors est tout à fait comparable à celui trouvé par des méthodes plus traditionnelles : par diffusion de lumière et par diffusion Rayleigh forcée. Si maintenant le fluide dense est placé en haut dans cette même géométrie expérimentale, une instabilité de Rayleigh-Taylor peut être observée.

Un dispositif expérimental, à base de bobines pilotables et refroidies, pour permettre l'observation sous microscope en présence d'un (faible) champ magnétique dépendant du temps, de gouttes de phase concentrée issues d'une démixion a été mis au point, et de premières mesures ont été réalisées. Les gouttes issues de démixion présentent des instabilités de forme spectaculaires qui permettent la détermination des propriétés physiques de la phase concentrée (susceptibilité magnétique, tension de surface et viscosité). Selon le système physico-chimique et la méthode adoptée pour induire la séparation de phase, ces propriétés restent stables au cours du temps ou bien évoluent progressivement, c'est un point qui reste à explorer. Le comportement de gouttes en champs précessant est étudié ici pour la première fois et comparé au comportement en champ tournant pour des gouttes aux propriétés stables pendant la durée de l'expérience. Ce comportement est piloté par un nombre de Bond magnétique et deux instabilités sont successivement observées. La goutte initialement sphérique adopte d'abord une forme prolate, puis se transforme en une forme oblate couronnée de pics, comme en champ tournant.

Finalement il est possible de conclure qu'une grande diversité de phénomènes complexes sont rencontrés avec des ferrofluides, la plupart étant connectés à des instabilités. Ces instabilités peuvent être caractérisées par des nombres réduits, s'échelant tous ici avec le carré du champ. Cependant, bien que les échelles typiques de ces phénomènes soient petites, les effets de gravité peuvent jouer un rôle important, parfois même dominant et doivent être évalués avec un très grand soin.

## Bibliographie

- [1] G. M. Whitesides, *Nature* **442**, 368 (2006).
- [2] J.-C. Bacri, R. Perzynski, and D. Salin, *Endeavour* **12**, 76 (1988).
- [3] M. M. Maiorov and A. Cēbers, *Magnetohydrodynamics* **19**, 376 (1983).
- [4] J.-C. Bacri, A. Cēbers, and R. Perzynski, *Physical Review Letters* **72**, 2705 (1994).
- [5] A. Wu, P. Ou, and L. Zeng, *Nano* **5**, 245 (2010).
- [6] A. H. Lu, E. L. Salabas, and F. Schüth, *Angewandte Chemie - International Edition* **46**, 1222 (2007).
- [7] N. Carron, ArXiv:physics.hist-ph/1506.01951 (2015).
- [8] E. Blūms, A. Cēbers, and M. Maiorov, *Magnetic Fluids*, Walter de Gruyter, 1997.
- [9] R. Rosensweig, *Ferrohydrodynamics*, Dover Books on Physics, Dover Publications, 2014.
- [10] S. Odenbach, *Colloidal Magnetic Fluids: Basics, Development and Application of Ferrofluids*, Lecture Notes in Physics, Springer, 2009.
- [11] Q. A. Pankhurst, J. Connolly, S. K. Jones, and J. Dobson, *Journal of Physics D: Applied Physics* **36**, R167 (2003).
- [12] P. Tartaj, M. D. P. Morales, S. Veintemillas-Verdaguer, T. Gonzalez-Carreno, and C. J. Serna, *Journal of Physics D: Applied Physics* **36**, R182 (2003).
- [13] K. Ērglis et al., *Biophysical journal* **93**, 1402 (2007).
- [14] R. Massart, *IEEE Transactions on Magnetics* **17**, 1247 (1981).
- [15] F. Cousin, E. Dubois, and V. Cabuil, *Physical Review E* **68**, 021405 (2003).
- [16] R. Massart, E. Dubois, V. Cabuil, and E. Hasmonay, *Journal of Magnetism and Magnetic Materials* **149**, 1 (1995).
- [17] V. Sints, E. Blūms, M. Maiorov, and G. Kronkalns, *The European Physical Journal E* **38**, 35 (2015).
- [18] A. Cēbers and M. M. Maiorov, *Magnetohydrodynamics* **16**, 21 (1980).
- [19] A. Cēbers, *Magnetohydrodynamics* **33**, 48 (1997).
- [20] A. Cēbers, *Magnetohydrodynamics* **17**, 113 (1981).
- [21] D. P. Jackson, R. E. Goldstein, and A. Cēbers, *Physical Review E* **50**, 298 (1994).
- [22] M. Igonin and A. Cēbers, *Journal of Magnetism and Magnetic Materials* **252**, 293 (2002), Proceedings of the 9th International Conference on Magnetic Fluids.
- [23] M. Igonin and A. Cēbers, *Physics of Fluids* **15**, 1734 (2003).
- [24] M. Igonin, *Hydrodynamic instabilities of miscible and immiscible magnetic fluids in a Hele-Shaw cell*, PhD dissertation, Université Paris 7 - Denis Diderot, 2004.
- [25] C.-Y. Chen and C.-Y. Wen, *Journal of Magnetism and Magnetic Materials* **252**, 296 (2002).
- [26] C.-Y. Chen, *Physics of Fluids* **15**, 1086 (2003).
- [27] C.-Y. Wen, C.-Y. Chen, D.-C. Kuan, and S.-Y. Wu, *Journal of Magnetism and Magnetic Materials* **310**, e1017 (2007), Proceedings of the 17th International Conference on Magnetism The International Conference on Magnetism.
- [28] C.-Y. Wen, C.-Y. Chen, and D. Kuan, *Physics of Fluids* **19**, 084101 (2007).
- [29] C.-Y. Chen, W. K. Tsai, and J. A. Miranda, *Physical Review E* **77**, 1 (2008).
- [30] C. Derec, P. Boltenhagen, S. Neveu, and J.-C. Bacri, *Magnetohydrodynamics* **44**, 135 (2008).
- [31] A. Mezulis and E. Blūms, *Magnetohydrodynamics* **41**, 341 (2005).
- [32] D. Zablotzky, *Microconvective effects in non-isothermal and inhomogeneous dispersions of magnetic nanoparticles*, PhD dissertation, University of Latvia, 2012.

- [33] T. T. Al-Housseiny, P. A. Tsai, and H. A. Stone, *Nature Physics* **8**, 747 (2012).
- [34] E. O. Dias and J. A. Miranda, *Physical Review E* **87**, 1 (2013).
- [35] I. Bischofberger, R. Ramachandran, and S. R. Nagel, *ArXiv:physics.flu-dyn/1410.7623* (2015).
- [36] I. Bischofberger, R. Ramachandran, and S. R. Nagel, *Nature Communications* **5**, 1 (2014).
- [37] K. Ērglis et al., *Journal of Fluid Mechanics* **714**, 612 (2013).
- [38] G. Kitenbergs et al., *Journal of Fluid Mechanics* **774**, 170 (2015).
- [39] F. G. Ergin, B. B. Watz, K. Ērglis, and A. Cēbers, *Proceedings of the ASME 10th Biennial Conference on Engineering Systems Design and Analysis*, 1 (2010).
- [40] T. M. Squires and S. R. Quake, *Reviews of Modern Physics* **77**, 977 (2005).
- [41] Y. K. Suh and S. Kang, *Micromachines* **1**, 82 (2010).
- [42] G. Kitenbergs, K. Ērglis, R. Perzynski, and A. Cēbers, *Journal of Magnetism and Magnetic Materials* **380**, 227 (2015).
- [43] A. Einstein, *Investigations on the Theory of the Brownian Movement*, Dover Books on Physics Series, Dover Publications, 1956.
- [44] J.-C. Bacri et al., *Physical Review E* **52**, 3936 (1995).
- [45] B. Bokstein, M. Mendeleev, and D. Srolovitz, *Thermodynamics and Kinetics in Materials Science : A Short Course: A Short Course*, Thermodynamics and Kinetics in Materials Science: A Short Course, Oxford University Press, 2005.
- [46] J. L. Anderson, *Annual Review of Fluid Mechanics* **21**, 61 (1989).
- [47] B. Abécassis, C. Cottin-Bizonne, C. Ybert, A. Ajdari, and L. Bocquet, *Nature materials* **7**, 785 (2008).
- [48] B. Abécassis, C. Cottin-Bizonne, C. Ybert, A. Ajdari, and L. Bocquet, *New Journal of Physics* **11**, 075022 (2009).
- [49] G. Batchelor, *An Introduction to Fluid Dynamics*, Cambridge Mathematical Library, Cambridge University Press, 2000.
- [50] R. H. Webb, *Reports on Progress in Physics* **59**, 427 (1996).
- [51] S. N. Yakovenko, T. G. Thomas, and I. P. Castro, *Journal of Fluid Mechanics* **760**, 466 (2014).
- [52] F. H. C. Heussler, R. M. Oliveira, M. O. John, and E. Meiburg, *Journal of Fluid Mechanics* **752**, 157 (2014).
- [53] E. A. Peterson and D. A. Krueger, *Journal of Colloid and Interface Science* **62**, 24 (1977).
- [54] J.-C. Bacri, R. Perzynski, D. Salin, V. Cabuil, and R. Massart, *Journal of Colloid and Interface Science* **132**, 43 (1989).
- [55] E. Dubois, V. Cabuil, F. Boue, and R. Perzynski, *The Journal of Chemical Physics* **111**, 7147 (1999).
- [56] E. Dubois, R. Perzynski, F. Boué, and V. Cabuil, *Langmuir* **16**, 5617 (2000).
- [57] B. Frka-Petesic et al., *Magnetohydrodynamics* **49**, 328 (2013).
- [58] A. Cēbers, *Magnetohydrodynamics* **18**, 137 (1982).
- [59] J.-C. Bacri and D. Salin, *Journal de Physique Lettres* **43**, 649 (1982).
- [60] J.-C. Bacri and D. Salin, *Journal of Magnetism and Magnetic Materials* **39**, 48 (1983).
- [61] J.-C. Bacri and D. Salin, *Journal de Physique Lettres* **43**, 771 (1982).
- [62] E. Janiaud, F. Elias, J.-C. Bacri, V. Cabuil, and R. Perzynski, *Magnetohydrodynamics* **36**, 300 (2000).
- [63] S. Afkhami et al., *Journal of Fluid Mechanics* **663**, 358 (2010).

- [64] G.-P. Zhu, N.-T. Nguyen, R. V. Ramanujan, and X.-Y. Huang, *Langmuir* **27**, 14834 (2011).
- [65] A. Zakinyan and Y. Dikansky, *Colloids and Surfaces A: Physicochemical and Engineering Aspects* **380**, 314 (2011).
- [66] Y. Dikansky and A. Zakinyan, *Technical Physics* **55**, 1082 (2010).
- [67] A. Cēbers, *Magnetohydrodynamics* **19-27**, 137 (1985).
- [68] Y. Dikansky, A. Cēbers, and V. P. Shatsky, *Magnetohydrodynamics* **26**, 25 (1990).
- [69] K. Ērglis, *Experimental study of properties and motion of flexible magnetic microfilaments*, PhD thesis, University of Latvia, 2010.

# Contents

<b>Introduction</b>	<b>1</b>
A comment on the system of units . . . . .	3
<b>1 Magnetic fluids</b>	<b>5</b>
1.1 Preparation . . . . .	5
1.1.1 Functionalization with fluorescent molecules . . . . .	7
1.1.2 Magnetic fluids based on organic solvent . . . . .	7
1.2 Properties . . . . .	7
1.2.1 Transmission Electron Microscopy . . . . .	9
1.2.2 Dynamic Light Scattering . . . . .	9
1.2.3 Magnetization measurements . . . . .	12
1.2.4 Static birefringence . . . . .	14
1.2.5 Magnetic fluids used in experiments . . . . .	16
<b>2 Magnetic micro-convection</b>	<b>17</b>
2.1 Experimental observation . . . . .	19
2.1.1 Particle Image Velocimetry . . . . .	22
2.1.2 Further characterization . . . . .	25
2.2 Improved experimental setup . . . . .	28
2.2.1 Experimental Image Analysis . . . . .	32
2.2.2 Comparison of experimental and theoretical results . . . . .	35
2.3 Possibilities in microfluidics . . . . .	39
2.3.1 Mixing with magnetic micro-convection . . . . .	39
2.4 Difficulties and study possibilities in future . . . . .	44
<b>3 Particle diffusion in magnetic fluids</b>	<b>47</b>
3.1 Estimation from the critical field . . . . .	49
3.2 Diffusion on an interface with a concentration step . . . . .	49
3.2.1 Initial measurements . . . . .	50
3.2.2 Hypothesis of the ionic strength influence . . . . .	53
3.2.3 Merging of two droplets . . . . .	54
3.2.4 Continuous microfluidics . . . . .	57
3.2.5 Effect of gravity . . . . .	64
3.3 Forced Rayleigh Scattering . . . . .	73
3.4 Dynamic Light Scattering . . . . .	74
3.5 Fluorescence Recovery After Photobleaching . . . . .	75
3.6 Summary of results . . . . .	79

<b>4</b>	<b>Instabilities in phase separated magnetic fluids</b>	<b>81</b>
4.1	Preparation of phase separated magnetic fluids . . . . .	83
4.2	Methods for experimental studies of phase separated magnetic fluids . . . . .	85
4.2.1	Development of a coil system . . . . .	85
4.2.2	Verification of the coil system . . . . .	89
4.3	Experiments with microdrops in phase separated magnetic fluids . . . . .	90
4.3.1	Image processing algorithm . . . . .	90
4.3.2	Properties of the phase separated magnetic fluid . . . . .	91
4.3.3	Magnetic microdrops in rotating and precessing fields . . . . .	94
4.4	Other experiments with phase separated magnetic fluids . . . . .	99
4.4.1	Patterns in slightly precessing magnetic field . . . . .	99
4.4.2	Solidification of drops . . . . .	99
4.5	Remarks and outlook . . . . .	100
	<b>Conclusions</b>	<b>101</b>
<b>A</b>	<b>Source code of useful functions in MATLAB®</b>	<b>103</b>
A.1	Fitting functions . . . . .	103
A.1.1	Magnetization . . . . .	103
A.1.2	Birefringence . . . . .	104
A.1.3	Elongation of a magnetic droplet . . . . .	104
<b>B</b>	<b>Essentials of the used experimental systems</b>	<b>105</b>
B.1	Essentials for using cameras in microscopy . . . . .	105
B.1.1	Testing the camera linearity . . . . .	105
B.1.2	Spatial calibration for two cameras . . . . .	106
B.1.3	Image acquisition using LabView . . . . .	106
B.2	LabView program for coil system control . . . . .	108
<b>C</b>	<b>Description of the used software</b>	<b>111</b>
C.1	FEMM - Finite Element Method Magnetics . . . . .	111
C.2	MATLAB® . . . . .	111
C.3	COMSOL Multiphysics® Modeling Software . . . . .	111
C.4	LabVIEW System Design Software . . . . .	111
<b>D</b>	<b>Additional figures</b>	<b>113</b>
<b>E</b>	<b>Authors' publications</b>	<b>117</b>
	<b>Bibliography</b>	<b>167</b>

# Introduction

The title of this dissertation includes a combination of powerful words - "hydrodynamic", "magnetic fluid", "instability" and "microfluidic". Each of them represents an important field of physics. The first three have been widely studied for many years, while the field of microfluidics is rather new and rapidly developing [1]. Meanwhile, the rapidly changing world continuously asks for better understanding and control of various complex phenomena in order to predict and exploit them. This is only possible by combining the different fields of physics as is done in the study presented here.

This work is primarily devoted to experimental studies of systems with magnetic fluids and their behavior under magnetic field. Magnetic fluids are formed of nanosized colloidal particles. Appearing magnetic and liquid simultaneously at room temperature, they are an intriguing material with interesting properties [2]. When exposed to magnetic fields, an interplay of the unusual properties produces somewhat unexpected instabilities, two of which are discussed here in detail. Magnetic micro-convection [3], which is studied on a miscible interface, and magnetic drop shape instabilities [4], realized in phase separated magnetic fluid, are field dependent phenomena, that are mainly interesting from the fundamental point of view. However, they have close connections to the important and developing fields of biomedicine [5], nanotechnology [6] and microfluidics. These links should certainly lead to contributions in future applications. In addition, some possible uses are already proposed in this work.

Advances in technological developments of experimental techniques and data analysis allow to perform the experimental studies in a much more quantitative manner. The obtained results provide valid critics for the existing models and promotes their improvement. The excellent case of a parallel development in theory and numerical simulations by colleagues and experimental observations described in this work, has lead to a much deeper understanding of the studied processes.

The following objective and tasks have been formulated for this study.

*Objective:* to perform an experimental study on instabilities in magnetic fluid systems and subsequently improve and develop the methods and systems necessary in order to understand the underlying physical principles and compare to appropriate theoretical predictions and numerical simulations.

*Tasks:*

1. Perform a throughout characterization of the used experimental system.
2. Study and characterize the magnetic micro-convection on a miscible fluid interface.
3. Find the physical reasons for the rapid effective diffusion encountered in the previous task.
4. Develop a system for studies in phase separated magnetic fluids.

5. Observe and describe shape instabilities of a magnetic drop in precessing and rotating fields.

These tasks were accomplished and are presented in this work within four separate chapters supplemented with complementary information in appendices. Hereafter a brief introduction of each of them is given.

Chapter 1 is presenting magnetic fluids. First, a brief description of the aspects important for magnetic fluid colloidal stability, preparation method and functionalization process are given in § 1.1. It is followed by listing the important physical properties in § 1.2, including ionic strength, volume fraction, particle size distribution, saturation magnetization and magnetic susceptibility, and their determination methods. These methods, namely transmission electron microscopy, dynamic light scattering, magnetization and static birefringence measurements, are presented and used for characterization of magnetic fluid samples. This chapter is concluded by summarizing the essential properties of the magnetic fluids later used in experiments and paying particular attention to an adequate comparison of the particle size distribution parameters obtained with the different methods.

In chapter 2 the magnetic micro-convection on a miscible fluid interface is extensively studied experimentally. A summary of the previous investigations and a brief introduction of the theoretical models introduces the topic. Initially, in § 2.1 the development of the peculiar finger-like structures of this instability is observed with a microscope in a simple Hele-Shaw cell on the interface of two merging magnetic fluid and water drops under magnetic field. For the first time velocity fields are registered using micro-particle image velocimetry system with tracer particle addition. Existence of a critical field is detected and together with the observed features show a qualitative agreement with the numerical simulation results of the Darcy model obtained by colleagues. The experimental system is then improved in § 2.2 to have a greater control of the crucial interface formation and quantitative measurements are made, including a precise determination of the critical field and characterization of the finger pattern size and growth velocity dynamics. These parameters show a good agreement with theoretical predictions and numerical simulation results of the Brinkman model, which are performed by colleagues. Finally, the possibility of using this phenomenon for mixing enhancement in microfluidics in § 2.3.1 and potential improvement of the experimental results using microfluidics in § 2.4 are discussed.

The rapid effective diffusion of magnetic particles on the miscible fluid interface, first encountered in chapter 2, is investigated in chapter 3. At the beginning, general concepts of diffusion of magnetic fluid particles are introduced. The enlarged effective diffusion coefficient is then showed to be encountered in both an estimation of the critical field from theoretical predictions in § 3.1 and the initial experiments of the previously used setup with no magnetic field present in § 3.2.1. Then a hypothesis is formed in § 3.2.2 trying to explain this effect by the influence of a high ionic strength promoting a diffusiophoresis process. Further measurements in the same system in § 3.2.3 do not give a definite answer, therefore experiments are transferred to a continuous microfluidics system, as described in § 3.2.4. The complete results do not explain the enlarged effective diffusion, rejecting the hypothesis. Instead, the effect of gravity is evaluated in § 3.2.5 using numerical simulations to determine the influence of the density difference between the both fluids on the miscible fluid interface. An important impact, which has not been previously reported in microfluidics conditions, is noticed and compared with the previous experiments, showing a rather good agreement. However, notable differences are registered, which are possibly linked to the ionic strength influence. The effect of gravity is finally confirmed by carrying out an experiment where the gravity force works perpendicular to the interface and the heavier fluid is below the lighter

one. These measurements give a much smaller diffusion coefficient. In § 3.3 and § 3.4 the accessible forced Rayleigh scattering and dynamic light scattering methods are introduced and used to independently determine the diffusion coefficient of particles in the investigated magnetic fluid. This is followed by introducing an adapted fluorescence recovery after photobleaching method in § 3.5 to measure the diffusion of particles of a magnetic fluid that are functionalized with fluorescent dyes. The chapter is finished with a summary of results in § 3.6, where comparability of diffusion coefficient measurements of polydispersed systems is discussed.

Chapter 4 is mainly focused on describing the development of an experimental system based on under-field microscopy for phase separated magnetic fluid research. It starts with a small introduction of the phase separated systems, focusing on individual drops formed by the concentrated magnetic fluid phase co-existing with a more dilute phase. A particular attention is given to the drop under-field behavior and the appropriate models, as these drops can be used to characterize the phase-separated system. In § 4.1 the preparation of samples is explained, where the phase-separation is induced by either increasing ionic strength or magnetic field. It is followed with a detailed description of a specially developed coil system in § 4.2.1, which can be fitted on an inverted microscope and can produce any configuration of a precessing magnetic field up to  $H \approx 45$  Oe and  $f \approx 500$  Hz with the rotating component in the plane of the sample, which can be controlled from a computer. It is then used to study under-field shape elongation and subsequent relaxation of individual drops, which, after extracting shape information with specially made image processing algorithms described in § 4.3.1 and comparing it to the existing theoretical models, leads to detection of the phase-separated magnetic fluid properties in § 4.3.2. Unforeseen dynamics of the concentrated phase properties during out-of-equilibrium relaxation is observed after removing the fluid sample from the strong magnetic field. The study is then continued by observing for the first time a magnetic drop deformations under precessing magnetic field fixed at a magic angle in § 4.3.3, which is compared with experiments in a rotating field and shows several shape instabilities. A brief description of perspective experiments in phase-separated magnetic fluid systems in § 4.4, including pattern formation in a slightly precessing magnetic field and creation of solid-like objects during the out-of-equilibrium relaxation under small field, and general remarks conclude this chapter.

Conclusions are located after the four chapters and condenses the main results, emphasizing the novelty of this work.

Appendices contain supplementary information in order to give additional explanations where necessary. That includes source codes of useful functions in MATLAB® in appendix A, description of additional methods and solutions used in experiments are given in appendix B, a brief annotation of computer software used in this work can be found in appendix C, while some supplementary figures are located in appendix D.

This work contains novel research on magnetic micro-convection, gravity induced flows in colloidal systems and shape instabilities of magnetic drops. Obtained results are published in 3 publications, which can be found in appendix E and have been communicated in 12 conferences.

## A comment on the system of units

This work mainly uses units in CGS unit system, as people working on theory and simulations of magnetism in the Riga lab prefer to have constants  $\epsilon_0$  and  $\mu_0$  equal to unity. In order to have as simple comparison as possible, also experimental results are described in

the same unit system. The single exception is § 2.3.1, where SI unit system is preferred in order to be easier received by the microfluidics.

It is important to note that the independence of physical laws on system of units used is one of the most important principles of science. Additionally, the conversion between systems of units is mostly straightforward. Only greater care should be taken when converting the units of magnetic quantities, because of different relations for magnetic field inductions, where in CGS unit system  $B^{\text{CGS}} = H^{\text{CGS}} + 4\pi M^{\text{CGS}}$  versus  $B^{\text{SI}} = \mu_0 (H^{\text{SI}} + M^{\text{SI}})$  in SI unit system. A way to orient oneself between the unit systems is possible by noticing the units. However, this is challenging when talking about dimensionless quantities - magnetic susceptibility  $\chi$  and permeability  $\mu$ . To allow a fast conversion, if needed, formulas are given in the table 0.

Table 0: Conversion formulas for converting magnetic units from CGS unit system to SI unit system.

Quantity	Conversion formula
<b>Magnetic field</b>	$H^{\text{SI}}[\text{A/m}] = \frac{10^3}{4\pi} H^{\text{CGS}}[\text{Oe}]$
<b>Magnetization</b>	$M^{\text{SI}}[\text{A/m}] = 10^3 M^{\text{CGS}}[\text{G}]$
<b>Magnetic induction</b>	$B^{\text{SI}}[\text{T}] = 10^{-4} B^{\text{CGS}}[\text{G}]$
<b>Susceptibility</b>	$\chi^{\text{SI}} = 4\pi \chi^{\text{CGS}}$
<b>Magnetic permeability</b>	$\frac{\mu^{\text{SI}}}{\mu_0} = \mu^{\text{CGS}}$

There is a large number of materials accessible if additional questions are still present, for example, see [7].

## Chapter 1

# Magnetic fluids

Magnetic fluid is a system that consists of solid magnetic particles that are dispersed in a liquid medium. These conditions are present in a colloid with nanosized magnetic particles, frequently also called ferrofluid, which is the fluid of interest in this work. Magnetic particles of magnetic colloid are mono-domain, describable with magnetic dipoles, and they are small enough to resist sedimentation at room temperature due to the Brownian motion. If the characteristic particle size is larger, reaching a few microns, one talks about magnetorheological fluids. These are interesting for various industrial applications due to a huge change of their apparent viscosity in the presence of magnetic field [8], but are not considered here.

Magnetic fluids in the form they are understood today were first created around 60 years ago in the United States. The early development offered oil or organic solvent, later also water based fluids with iron or cobalt ferrite particles. Magnetically sealed joints, loud-speaker coils and shock absorbers were the first successful applications. Several other uses, including printing inks were proposed [2]. The impressive development of the nanoscience and nanotechnology in the last 15 years has brought a new interest to magnetic fluids from a different perspective by looking at magnetic nanoparticles as individual elements. In the field of biomedicine alone magnetic nanoparticles have numerous applications. These particles work as good contrast agents for magnetic resonance imaging. Functionalization of their surface allows to use them for magnetic separation, drug delivery and magnetofection, while combination with a high frequency magnetic field can heat them up and produce magnetic hyperthermia [5, 9]. This has been possible due to the extensive work on preparation methods that allow the control of the particle material, size, shape, structure and surface modification [6, 10].

To facilitate these advancements, further study of magnetic fluid behavior in complex systems is necessary. In this work the focus is on the use of conventional magnetic fluids, because their preparation methods have been perfected to level where various essential parameters can be controlled with a high precision.

The studies on magnetic fluids over last 60 years has has given a large amount of information on their preparation methods and their differences, on the fascinating and diverse physics, which can be found in them and on the possible applications. At least a notable part of it can be found in several books [11, 12, 13].

## 1.1 Preparation

If magnetic nanoparticles can be found in magnetotactic bacteria [14], then magnetic fluids are not present in nature, therefore they have to be created artificially. To produce a good magnetic fluid, several stability requirements have to be taken into account.

Sedimentation is insignificant if the thermal energy  $k_B T$  is greater than the gravitational energy  $\Delta\rho\pi d^3 g L/6$ , where  $L \approx 2$  cm is a typical height of the fluid container and  $\Delta\rho \approx$

$4 \text{ g/cm}^3$  is a density difference between the magnetic material and liquid medium. This gives an estimate for the diameter  $d \leq 25 \text{ nm}$ .

Another important aspect is related to the interaction between particles. The presence of magnetic and van der Waals promotes attraction that can lead to agglomeration, therefore a repulsive interaction between the colloidal particles has to be created. This is typically done by introducing steric repulsion by adding a surfactant or electrostatic interaction by having charged particles. [12].

To be compatible with the field of biomedicine, colloid has to be aqueous and stable at a normal pH 7. Seeing good perspectives in this field, the fluids that are used in this work are chosen to comply with these conditions. This can be achieved by producing magnetic fluid of maghemite ( $\gamma\text{-Fe}_2\text{O}_3$ ) nanoparticles with Massart's method [15], which has become a field standard for electrically stabilized aqueous magnetic fluids. At first, iron salts are coprecipitated in an alkaline solution. The acidic properties of the particle surface allow them to have a positive charge at a low pH water solution, forming a stable colloid.

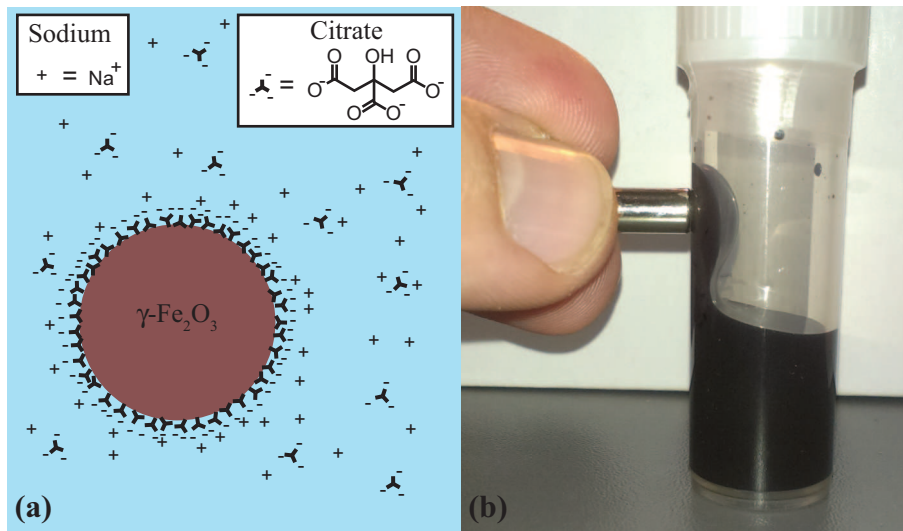


Figure 1.1: Magnetic fluid. (a) A scheme of a single magnetic nanoparticle in the magnetic fluid, stabilized with citrate ions. (b) Magnetic fluid is attracted by magnetic field gradient.

To obtain a stable colloid in pH 7, citrate ions ( $\text{C}_3\text{H}_5\text{O}(\text{COO})_3^{3-}$ ) from dissolved trisodium citrate salt ( $\text{Na}_3\text{C}_6\text{H}_5\text{O}_7$ ) are adsorbed on the particle surface. This leads to magnetic particles with a negative surface charge with a density 2 charges/ $\text{nm}^2$  (see figure 1.1 (a)), which is neutralized in the solution by the free sodium ions [16]. Particle interactions strongly depend on the properties of the solution, therefore a precise control of ionic strength and osmotic pressure is important. This is achieved by dialyzing colloid that is put in a bag of semipermeable membrane against a reservoir with known properties [17]. The described synthesis gives a rather polydispersed particle size distribution. It is possible to narrow it by performing size sorting, based on reversible phase separation after electrolyte addition [18]. Finally, the preparation process leads to a fluid that can be attracted with a magnet and appears in a dark color, which is actually reddish if viewed in a thinner layer (see figure 1.1 (b)). Magnetic fluids for experiments described further were made with this method in the MML lab in Riga and the PHENIX lab in Paris.

### 1.1.1 Functionalization with fluorescent molecules

Individual nanoparticles and even small clusters are too small to be seen in an optical microscope, but their visualization is important for the development of applications. This can be enhanced by using fluorescence microscopy [19, 20]. As already mentioned before, the surface of magnetic nanoparticles can be functionalized in various ways for multiple purposes. To benefit from fluorescence imaging, fluorescent molecules have to be added to the particle surface. For experiments in § 3.5 the particles of magnetic fluid were functionalized with a fluorescent molecule rhodamine B. The fluorescent magnetic fluid was made in the MMML lab in Riga, following the protocol described in the thesis of O. Petrichenko [21].

### 1.1.2 Magnetic fluids based on organic solvent

Alternatively to water based, it is possible to make magnetic fluids using organic solvents. In reality, these were the first magnetic fluids to be made, using surfactants for magnetic nanoparticle stabilization. They are typically allow industrial applications, because of greater stability [2].

In this study, § 3.2.4 in particular, a fluid of this type is used to make a comparable measurement because of the difference in stabilization mechanism. A magnetite based magnetic fluid *DF105*, which is stabilized with oleic acid in tetradecane solvent [22], was provided for this purpose by the Institute of Physics (Salaspils, Latvia). Its properties are given in table 1.1.

## 1.2 Properties

Quantitative experiments that are comparable to theoretical predictions are only possible if the properties of object of study are known. In this work four different magnetic fluids are used - *KTF09-13* and *KTF10-04* were synthesized in the MMML lab in Riga, while *D107* and *p146* were made in the PHENIX lab in Paris. Determination of the properties of magnetic fluids is illustrated with measurement data of these fluids and summarized at the end of this section.

Here is a list of the essential properties for magnetic fluids:

- Ionic strength  $I$ ;
- Osmotic pressure  $\Pi$ ;
- Volume fraction  $\Phi$ ;
- Size distribution with a mean diameter  $d_0$  and a polydispersity  $\sigma$ ;
- Saturation magnetization  $M_s$ ;
- Magnetic susceptibility  $\chi$ .

Ionic strength and osmotic pressure, as mentioned before, can be fixed during magnetic fluid preparation. Alternatively, ionic strength  $I$  can be estimated by conductivity measurements of the colloid and its comparison against a conductivity reference.

This was done for *D107*, as its ionic strength was not fixed during preparation. With an assumption that the conductivity and ionic strength arises only from the dissolved and fully dissociated [23] trisodium citrate molecules, a reference conductivity curve of citrate

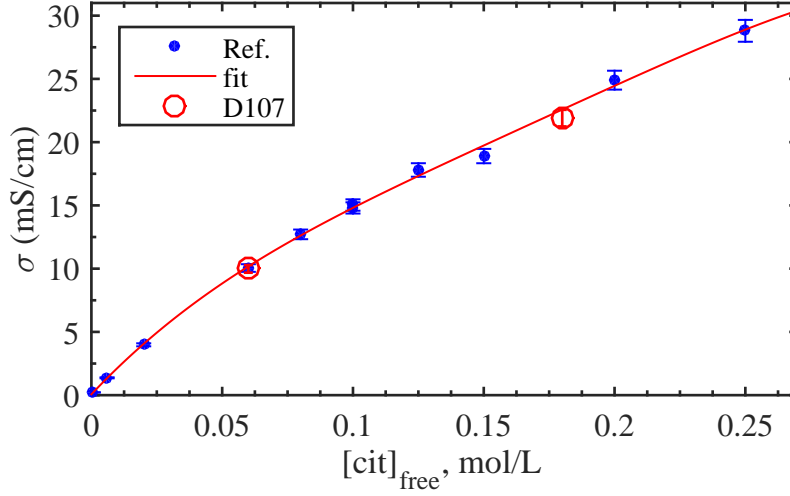


Figure 1.2: Ionic strength estimation of a magnetic fluid. Conductivity dependence on citrate concentration in a solution is marked with blue circles and its fit (4th order polynomial) with a red line. Red empty circles mark *D107* sample estimations.

solutions with various concentrations is made. Measurement points are fitted with a 4<sup>th</sup> order polynomial giving an empiric relation. The values of magnetic fluid conductivity at the original concentration and 1 : 3 dilution are simultaneously compared to the reference curve, finding that the free citrate concentrations are 0.18 mol/L and 0.06 mol/L respectively. This is illustrated in figure 1.2.

A precise measurement of the volume fraction is done by chemical titration of iron [17] in a small sample of a magnetic fluid. A complimentary method [21] uses analytical balance. The density of a magnetic fluid  $\rho_{mf}$  is calculated from a weight measurement  $m_{mf}$  of a known volume  $V_{mf}$ . As the densities of magnetic material  $\rho_{magn}$  and solvent  $\rho_{solv}$  are known, the volume fraction is calculated with the following expression

$$\Phi^w = \frac{\rho_{mf} - \rho_{solv}}{\rho_{magn} - \rho_{solv}}. \quad (1.1)$$

This method is particularly useful to quickly verify the volume fraction in a physics lab, as it can be changing due to the solvent evaporation.

For example, 1 ml *D107* weights 1.126 g, measured with analytical balance *KERN ALJ 120-4*. Water solution with 0.18 mol/L trisodium citrate has a density  $\rho_{solv} = 1.017$  g/mL, but maghemite  $\rho_{\gamma\text{-Fe}_2\text{O}_3} = 4.9$  g/mL, therefore  $\Phi_{D107}^w = \frac{1.126-1.017}{4.9-1.017} = 2.8\%$ .

For simplicity, magnetic fluid is assumed to consist of spherical magnetic particles. The diameters  $d$  of these particles can then be described with a log-normal distribution that's probability density is defined with a formula

$$P(d; d_0, \sigma) = \frac{1}{\sqrt{2\pi}\sigma d} e^{-\frac{(\ln \frac{d}{d_0})^2}{2\sigma^2}}, \quad (1.2)$$

which is characterized with two parameters - a characteristic diameter  $d_0$ , where  $\ln d_0$  is the mean value of  $\ln d$ , and polydispersity factor  $\sigma$ . These parameters can be found with multiple methods.

### 1.2.1 Transmission Electron Microscopy

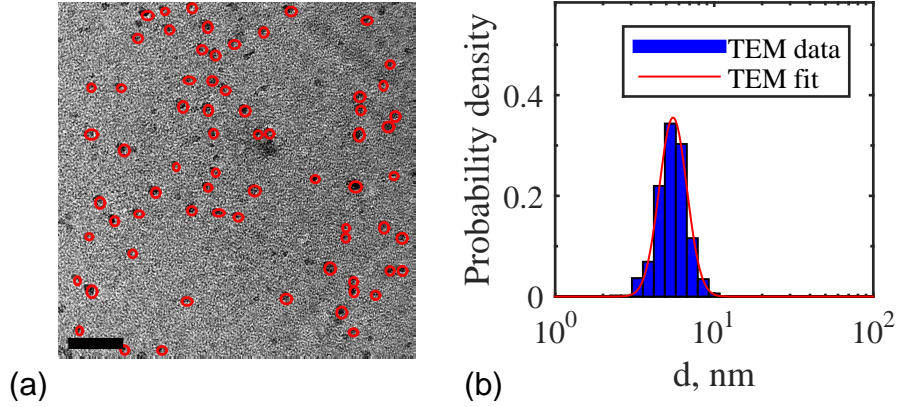


Figure 1.3: Particle size distribution determination with TEM. (a) A typical TEM image of magnetic fluid sample. Red circles mark recognized particles. Scale bar is 30 nm. (b) A histogram of particle diameter distribution. Bars show data measured from images, while the line corresponds to a log-normal distribution fit.

A direct measurement can be made with transmission electron microscopy (TEM) [24]. Images of nanoscaled objects are created by an accelerated electron beam crossing a thin sample. As magnetic material typically has a large atomic number, it provides sufficient contrast on its own.

This analysis was done for magnetic fluid *D107* in the Bio-Nano Electronics Research Center of the Toyo University (Kawagoe, Japan) on their JEOL JEM-2200FS. Because of a rather poor image quality, particle recognition was done manually by approximating each particle with an ellipse. A typical TEM image of magnetic fluid with recognized particles is showed in figure 1.3 (a). Taking the average diameters of several hundred particles in multiple images allows to form a particle size histogram, that is showed in figure 1.3 (b). As expected, the histogram resembles a log-normal distribution. Data are fitted with the equation 1.2 using the curve fitting toolbox in MATLAB® with nonlinear least squares method. Fit gives  $d_0 = 5.7$  nm and  $\sigma = 0.20$ . It is worth to remark that TEM analysis gives a number averaged result, because the particles are observed directly.

### 1.2.2 Dynamic Light Scattering

A rapid and convenient method for colloid characterization is dynamic light scattering (DLS). Using one of the many commercially available devices, credible information on particle sizes can be found in less than 10 minutes. The method is based on relating the scattering signal fluctuations with the Brownian motion of colloidal particles. This is typically accomplished with a laser beam which is shot in the sample. The scattering signal is measured in a position that is defined with a scattering vector  $q$ :

$$q = \frac{4\pi n}{\lambda} \sin \frac{\theta}{2}, \quad (1.3)$$

where  $\lambda$  is the laser wavelength,  $n$  is the refractive index of the medium and  $\theta$  is the angle between the direction of laser beam and scattering observation direction. The position is normally fixed in the backscattering mode, where  $\theta$  is close to 180°. This allows to minimize

the signal absorption in the sample and multiple scattering effect. The measured signal  $I(t)$  is autocorrelated with a delay time  $\tau$  and averaged over multiple measurements, which allows to calculate the normalized intensity  $g^2(\tau)$  and electric field  $g^1(\tau)$  autocorrelation functions:

$$g^2(\tau) = \frac{\langle I(t)I(t+\tau) \rangle}{\langle I(t) \rangle^2},$$

$$g^1(\tau) = \sqrt{g^2(\tau) - 1}.$$

An example of autocorrelated signal for *D107* sample can be seen in figure 1.4(a).

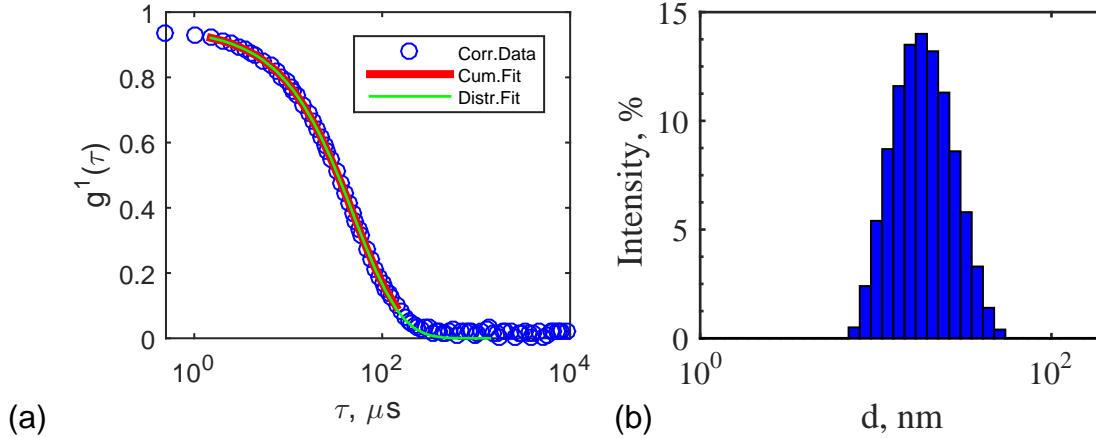


Figure 1.4: DLS data for a dilute sample of *D107* measured with Malvern Zetasizer NanoZS. (a) Autocorrelation - blue empty circles mark autocorrelation data, red curve is the cummulants fit and green curve corresponds to a *distribution fit*. (b) Intensity histogram of particle diameter as obtained from the *distribution fit*.

DLS experiments were done with two different devices - Malvern Zetasizer Nano ZS ( $\theta = 173^\circ$ ,  $\lambda = 633$  nm) and Cordouan Vasco<sup>γ</sup> ( $\theta = 135^\circ$ ,  $\lambda = 658$  nm) both in Riga and Paris. The first is convenient when small or moderate concentrations are used ( $\Phi$  less than few %), because the fluid is put in a disposable cuvette before inserting it in the apparatus. The second has a special sample chamber which allows to adjust even a very small fluid thickness, enabling to measure concentrated samples ( $\Phi$  up to 40%) more precisely. Devices are combined with an advanced software that guides the data collection and performs analysis to provide the information of particle sizes. Although the result is provided automatically, good understanding of the underlying physics is essential to do their interpretation correctly.

The autocorrelation function for a monodisperse suspension of spherical particles is an exponential decay due to the Brownian motion with a delay time  $\tau$  as

$$g^1(\tau) = A \cdot e^{-Dq^2\tau} + B, \quad (1.4)$$

where  $A$  is the amplitude,  $B$  is the baseline,  $q$  is the scattering vector, defined with equation 1.3, and  $D$  is the translational diffusion coefficient of the particles. Finally, the particle size can be determined, as the diffusion coefficient  $D$  is related to the hydrodynamic diameter of a particle  $d_H$  via the Stokes-Einstein relation (in the very dilute regime):

$$D = \frac{k_B T}{3\pi\eta d_H}, \quad (1.5)$$

where  $k_B$  is the Boltzmann's constant,  $T$  is the temperature and  $\eta$  is the solvent viscosity [25].

As a real colloid always is at least slightly polydispersed, description of autocorrelation data is more complicated. A very common simplification, which is valid for a narrow monomodal distribution, is called the method of cumulants. It expands the exponent in equation 1.4 around a mean value  $\bar{\Gamma} = \bar{D}q^2$ . After small transformations, a formula for cumulant analysis is obtained:

$$\ln(g^1(\tau)) = \ln B - \bar{\Gamma}\tau + \frac{\mu_2\tau^2}{2}, \quad (1.6)$$

where  $B$  is background and  $\mu_2$  is the variance. The mean diffusion coefficient  $\bar{D}$  via equation 1.5 gives the mean hydrodynamic diameter  $\bar{d}_H$ , which is also called the *z-average*. The size distribution is defined with a polydispersity index PDI [25]. It is also proportional to the square of the ratio of the standard deviation  $\sigma_H$  and the mean hydrodynamic diameter  $\bar{d}_H$ :

$$\text{PDI} = \frac{\mu_2}{\bar{\Gamma}^2} = \frac{\sigma_H^2}{\bar{d}_H^2}, \quad (1.7)$$

where  $\bar{d}_H$  and  $\sigma_H$  are related to the parameters of the log-normal distribution  $d_0$  and  $\sigma$  (equation 1.2) via

$$\sigma^{\text{dls}} = \sqrt{\ln(1 + (\sigma_H/\bar{d}_H)^2)} \quad (1.8)$$

$$\ln d_0^{\text{dls}} = \ln \bar{d}_H - \frac{(\sigma^{\text{dls}})^2}{2}. \quad (1.9)$$

Malvern software does the cumulant fit on *D107* sample autocorrelation data (figure 1.4(a)) and gives a mean value  $\bar{d}_H = 17.2$  nm and a polydispersity  $\text{PDI} = 0.13$ . The cumulant fit is usually valid until  $\text{PDI} < 0.1$  [25], therefore one can deduce that this fluid is around the limit of this approximation and has a rather narrow size distribution.

There are also other more advanced methods to analyze the autocorrelation data and many of them allow to detect a multimodal system. Depending on the manufacturer, varied amount of information on the data treatment is accessible about them. For example, Malvern software performs a *distribution fit* of the autocorrelation data (see figure 1.4(a)), that gives a particle size intensity histogram. Data of *D107* sample can be seen in figure 1.4(b). The device manual has no extra description about the analysis steps, while an informative leaflet names NNLS and CONTIN methods. More information about the methods can be found in the recent review [25].

After normalizing the *distribution fit* histogram to a total surface equal to 1 and calculating log-normal distribution parameters  $d_0^{\text{dls}} = 16.2$  nm and  $\sigma^{\text{dls}} = 0.35$  from cumulant fit results via equations (1.9) and (1.8) both methods are compared in figure 1.5(a). A small, but noticeable difference can be observed.

A special care has to be granted when comparing results to size distributions obtained with other methods. As DLS is based on the scattering intensity measurement, the direct results are intensity-weighted. Intensity is proportional to the 6th power of diameter, therefore the DLS results have to be converted to number-weighted size distribution before a proper comparison can be made. This can be done with expressions that link the mean hydrodynamic diameter  $\bar{d}_H$  and polydispersity index PDI of the DLS results with a mean

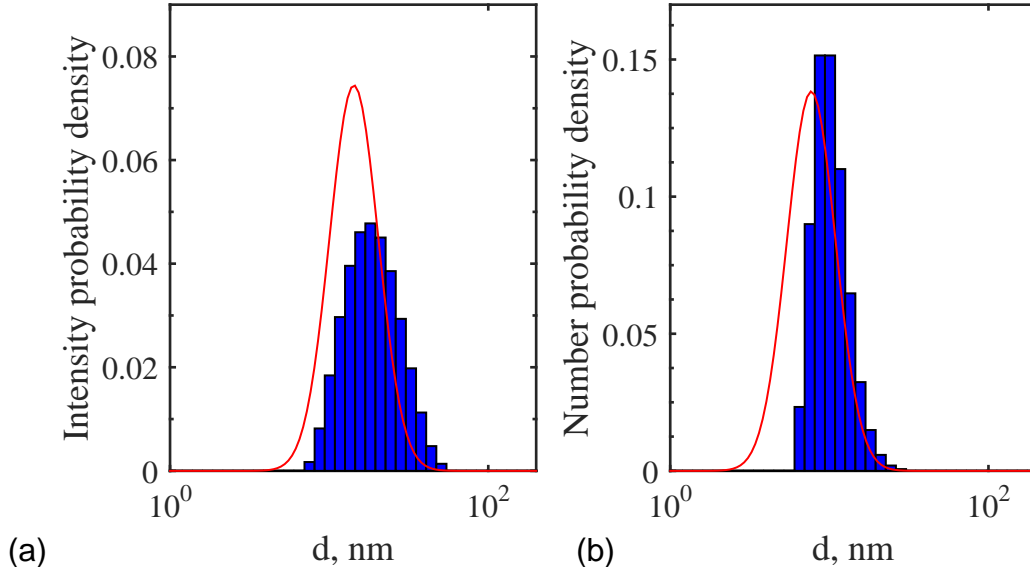


Figure 1.5: Magnetic fluid *D107* particle size distributions measured with Malvern Zetasizer NanoZS. Blue bars mark histogram from the *distribution fit*, red curve is the log-normal *distribution fit*. (a) Intensity-weighted distribution constructed from the parameters of the cumulants fit. (a) Intensity-weighted distribution. (b) Number-weighted distribution.

hydrodynamic diameter  $\bar{d}_H^N$  and its standard deviation  $\sigma^N$  of a number-weighted distribution [26]:

$$\bar{d}_H^N = \frac{\bar{d}_H}{(1 + \text{PDI})^5} \quad (1.10)$$

$$\sigma^N = \bar{d}_H^N \sqrt{\text{PDI}} \quad (1.11)$$

A comparison of the results of the two fitting methods in the number-weighted distributions is shown in figure 1.5(b). Malvern software offers to automatically recalculate the *distribution fit* results to the number-weighted distribution, while for cumulant fit results are converted to the number-weighted distribution parameters  $d_0 = \bar{d}_H^{\text{dls}} = 8.7$  nm and  $\sigma = \sigma^{\text{N}^{\text{dls}}} = 0.35$  via equations (1.8) to (1.11). Also here a slight difference is visible, but the reasons for that are out of the scope of this study.

The *distribution fit* results show a rather narrow monomodal size distribution that looks very similar to the cumulant fit results. This proves that the particles of the magnetic fluid indeed agree well with the log-normal distribution. For simplicity, only parameters from the cumulant fit results are used in further comparison.

### 1.2.3 Magnetization measurements

Magnetic fluid is primarily interesting because of its magnetic properties. These properties depend on the magnetic particles that form the magnetic colloid. Particles size is  $d \approx 10$  nm, therefore their magnetic properties are superparamagnetic, i.e. their ferromagnetic moments at zero magnetic field are randomly oriented due to the Brownian motion and hence the average magnetization  $\bar{\mu} = 0$ . With an increase of the magnetic field, the magnetic

moments on average tend to spend more time in the direction of the field, creating a non-zero average magnetization [12]. Each particle has a magnetic moment  $\mu$ , which depends on the saturation magnetization of the material  $m_s$  and the volume of particle  $V$ :

$$\mu = m_s V = \frac{m_s \pi d^3}{6}, \quad (1.12)$$

where  $d$  is the diameter, as the particles are assumed to be spherical. The field dependence of the average magnetization  $m_s$  follows a Langevin function:

$$\frac{\bar{\mu}}{\mu} = L(\xi) = \coth \xi - \frac{1}{\xi}, \quad (1.13)$$

where  $\xi$  is the Langevin parameter and defines the ratio between magnetic and thermal energy:

$$\xi = \frac{\mu H}{k_B T}, \quad (1.14)$$

where  $\mu$  is the magnetic moment from equation (1.12),  $H$  is the magnetic field,  $k_B$  is the Boltzmann's constant and  $T$  is the temperature [12].

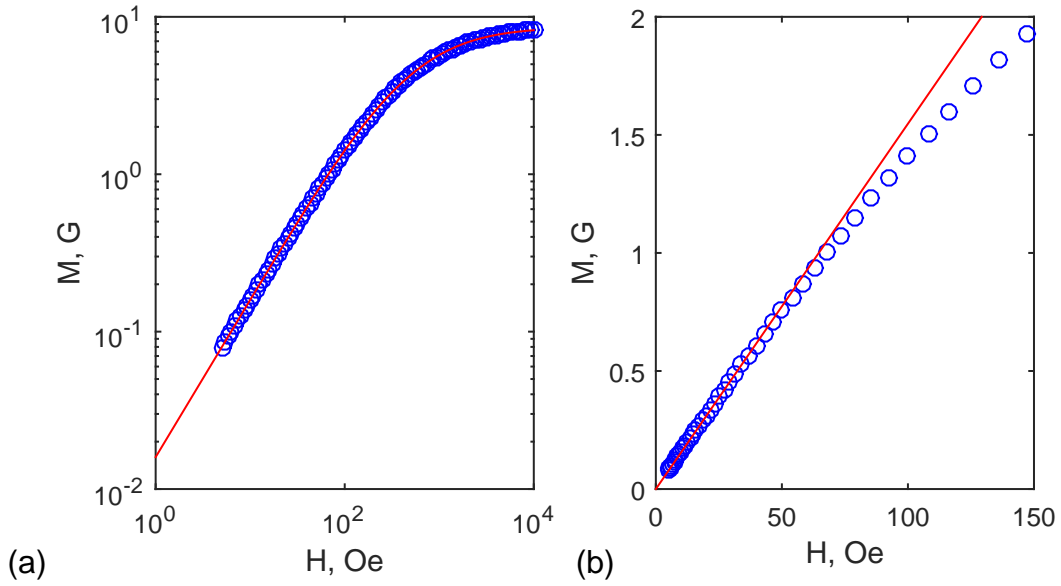


Figure 1.6: Magnetization curve of the magnetic fluid *D107*. Blue circles mark data measured with VSM, red curves - fits. (a) Complete magnetization curve. (b) Linear region of magnetization for susceptibility determination

Magnetic measurements are typically done with a Vibrating Sample Magnetometer (VSM), where a magnetic sample is vibrated between large coils producing homogeneous magnetic field. The magnetization of the sample induces a proportional voltage in detection coils, which is measured and converted to magnetization [24]. A typical magnetization curve, as measured for magnetic fluid *D107* can be seen in figure 1.6(a). Measurements were carried out with *Lake Shore 7400 VSM* by M.M.Maiorov at the Institute of Physics of the University of Latvia.

One important magnetic property of a magnetic fluid is its saturation magnetization  $M_s$ . If the measurements are made up to large fields, it can be approximately read from the

magnetization curve. In figure 1.6(a) the magnetization reaches  $M_s \approx 8.3$  G at  $H = 10$  kOe. Otherwise, it is typically assumed to depend on the saturation magnetization  $m_s$  of the magnetic material and its volume fraction  $\Phi$  via relation

$$M_s = \Phi m_s. \quad (1.15)$$

Using the previously obtained volume fraction  $\Phi = 2.8\%$ , a characteristic maghemite saturation magnetization  $m_s = 300$  G [24] and this formula, a very similar value  $M_s = 8.4$  G is obtained.

Alternatively, the saturation magnetization can be estimated with a fit of the magnetization curve. However, when fitting the magnetization curve, one has to remember that the magnetic fluid particles are polydispersed. For this reason magnetization curve is a composition of many magnetization curves of individual particles, thus information on particle size distribution can be extracted. A complete description of a polydispersed magnetic fluid magnetization is given with a formula [27]:

$$M(H) = \Phi m_s \frac{\int_0^\infty L(d, m_s, T, H) P(d; d_0, \sigma) d^3 dd}{\int_0^\infty P(d; d_0, \sigma) d^3 dd}, \quad (1.16)$$

where  $\Phi m_s$  correspond to the saturation magnetization,  $L(d, m_s, T, H)$  is the Langevin function defined in (1.13),  $P(d; d_0, \sigma)$  is the size probability density for a number-weighted distribution defined in (1.2) and  $d^3$  is needed for correct weighting, because magnetic properties are volume dependent. This relation is valid for the case when inter-particle interactions are negligible, e.g. magnetic fluids with a rather low concentration ( $\Phi \leq 1\%$ ).

Experimental data can be fitted with different approaches by changing the parameters that stay fixed. Typically a temperature  $T$  is measured during the experiment and saturation magnetization of the material  $m_s$  is known, leaving the characteristic diameter  $d_0$ , polydispersity  $\sigma$  and volume fraction  $\Phi$  for determination. Measurement data of *D107* were fitted using MATLAB® curve fitting toolbox (nonlinear least squares method, statistical weights) with a function (see Appendix A.1.1) constructed on the basis of equation (1.16), while fixing the saturation magnetization of the material  $m_s = 300$  G and the temperature  $T = 289.7$  K. The fit, visible in figure 1.6(a), gives the size information  $d_0 = 7.1$  nm and  $\sigma = 0.32$  and the volume fraction  $\Phi = 2.9\%$ .

An important magnetic property is the magnetic susceptibility  $\chi$ , because it relates magnetization  $M$  with magnetic field  $H$ :

$$M(H) = \chi H.$$

This relation applies only to the initial linear magnetization regime, which is also mostly used in the experiments carried out in this work. It can be found by a linear fit of the initial part of the magnetization data, as showed in figure 1.6(b). For magnetic fluid *D107* it is  $\chi = 0.016$  in CGS units.

#### 1.2.4 Static birefringence

Another technique to determine the polydispersity of the magnetic colloid is based on the optical properties of the magnetic media. The nanoparticles have an internal birefringence related to their shape and to their magnetic anisotropy [28] Magnetic moment inside a particle

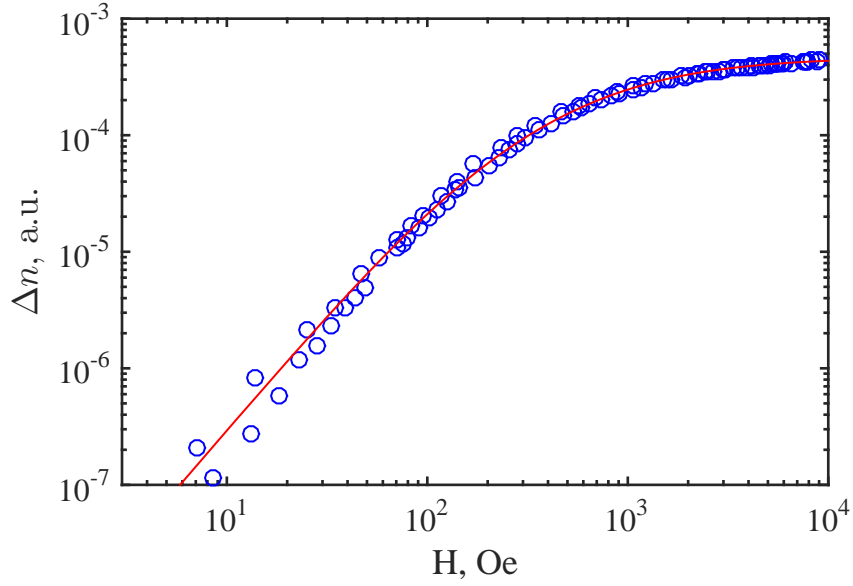


Figure 1.7: Static birefringence curve of the magnetic fluid *D107*. Blue circles mark experimental data, red curve - fit

has a preferred direction due to the magnetic anisotropy of the material. Hence, if in zero field the particles are oriented randomly, then at a strong magnetic field they are all aligned in the field direction. This can be measured by comparing a laser signal before and after a sample that is put between two large coils. Increasing of the field results in more oriented particles, which increases the birefringence signal. Similarly to magnetic measurements, also here it is advised to have a diluted enough sample. An example of the measured signal for the magnetic fluid *D107*, which is diluted three times, can be seen in figure 1.7. A formula has been developed to describe this process [27]:

$$\Delta n(H) = \Delta n_s \frac{\int_0^\infty N(d, m_s, T, H) P(d; d_0, \sigma) d^3 dd}{\int_0^\infty P(d; d_0, \sigma) d^3 dd}, \quad (1.17)$$

where  $\Delta n_s$  is the saturation birefringence when all particles have aligned,  $P(d; d_0, \sigma)$  is the size probability density for a number-weighted distribution defined in (1.2),  $d^3$  is needed for correct weighting.  $N$  is the birefringence factor and depends on the Langevin parameter  $\xi$ , which is defined with equation (1.13), as follows

$$N = \left( 1 - \frac{3}{\xi} \coth \xi + \frac{3}{\xi^2} \right).$$

Experimental data of of figure 1.7 were fitted with a function (see Appendix A.1.2) constructed on the basis of equation (1.17) using the MATLAB® curve fitting toolbox (nonlinear least squares method, statistical weights). As for magnetization, the measurement temperature  $T = 293$  K and saturation magnetization of the material  $m_s = 300$  G were fixed. The obtained curve is plotted above the data and corresponds to a size distribution data with the characteristic diameter  $d_0 = 9.2$  nm and the polydispersity  $\sigma = 0.25$ . The saturation birefringence is  $\Delta n_s = 4.7 \cdot 10^{-4}$ .

### 1.2.5 Magnetic fluids used in experiments

A summary of the essential properties of magnetic fluids used in the experiments can be found in table 1.1, where  $\Phi^W$  is volume fraction found by weighting,  $\Phi^M$ ,  $\chi$  and  $M_s$  are the volume fraction, magnetic susceptibility and saturation magnetization of the magnetic fluid found by fitting magnetization measurements,  $\bar{d}_H$  and PDI is the hydrodynamic diameter and polydispersity index measured with DLS. An extensive study of particle size distribution

Table 1.1 Essential properties of the magnetic fluids used in experiments

Name	$\Phi^W$ , %	$\Phi^M$ , %	$\chi$	$M_s$ , G	$d_0$ , nm	$\bar{d}_H$ , nm	PDI
<b>D107</b>	2.8	2.9	0.016	8.4	7.1	17.2	0.13
<b>KTF09-13</b>	2.0	3.3	0.064	10	14.0	79.1	-
<b>KTF10-04</b>	0.05	0.06	$9 \cdot 10^{-4}$	0.2	12.7	109	-
<b>DF105</b>	6.9	-	-	14.2	7.3	65.0	0.52
<b>p146</b>	$\approx 1$	-	-	-	10.0	-	-

in magnetic fluid *D107* was performed using multiple methods. Results of various methods are showed after conversion to two parameters - characteristic diameter  $d_0$  and polydispersity factor  $\sigma$  of a number-weighted monomodal polydispersed log-normal particle size distribution as defined in equation (1.2) - and are shown in table 1.2. Next to the name of the method, the volume fraction used in corresponding measurements is denoted in units of initial magnetic fluid concentration  $\Phi_0$ .

Table 1.2: Comparison of the magnetic fluid *D107* size distribution parameters measured with various methods

Method	$d_0$ , nm	$\sigma$
<b>TEM</b> , $0.001\Phi_0$	5.7	0.20
<b>DLS, Malvern</b> , $0.3\Phi_0$	8.7	0.35
<b>DLS, Malvern</b> , $\Phi_0$	9.3	0.43
<b>DLS, Vasco<math>^\gamma</math></b> , $\Phi_0$	9.6	0.40
<b>Magnetization</b> , $\Phi_0$	7.1	0.32
<b>Birefringence</b> $0.3\Phi_0$	9.2	0.25

The results show a rather good agreement. Slightly larger values are obtained with DLS at original concentration, which can be explained with higher concentration effects, as discussed earlier in § 1.2.2. Besides, DLS measures the hydrodynamic diameter, which is slightly larger than the real particle diameter because of the stabilizing citrate ions and interactions with the surrounding liquid. Birefringence measurement is giving a larger diameter value, because of the different relaxation mechanism as compared to magnetization measurements [24], which will not be discussed further. Rather small result is obtained with TEM microscopy, which might come from the poor quality images in combination with manual data analysis. Nevertheless, values from TEM measurements show that magnetic particles have a really small or almost non-existent outer non-magnetic layer.

## Chapter 2

# Magnetic micro-convection

Magnetic fluids possess both magnetic and hydrodynamic properties. Consequently these fluids can not only respond to an applied magnetic field, but also feed back by modifying the field via a change in the flow field. This modification typically happens abruptly at a critical point and leads to a different equilibrium state. The instability is usually observable due to an associated change in the flow field or shape. Magnetic fluids exhibit various different instabilities. The most common is the Rosensweig or normal-field instability, which makes the magnetic fluid drop look like a hedgehog (surface deforms into a series of regular spikes), when put in a strong vertical magnetic field, and is usually displayed when magnetic fluids are discussed [12].

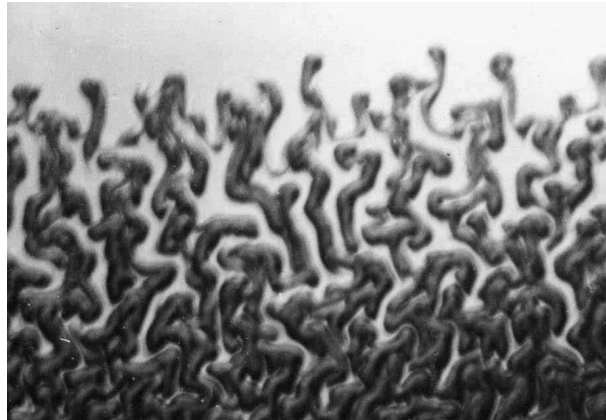


Figure 2.1: Magnetic micro-convection of a magnetic and miscible non-magnetic fluid interface in a Hele-Shaw cell as viewed from top. Image courtesy of M. M. Maiorov and A. Čēbers. More details in reference [3]

This chapter is devoted to a different instability which is called the magnetic micro-convection. Magnetic field driven micro-convection was found in the early 1980s by Maiorov and Čēbers [3], extending the concept of the self-magnetic field driven instabilities [29] for miscible fluids in a Hele-Shaw cell. The magnetic micro-convection is caused by a ponderomotive force acting on the magnetic fluid in a homogeneous applied field. This force is proportional to the concentration of the magnetic particles and the local gradient of the magnetic field, which arises from the self-magnetic field of the magnetic liquid. Moreover, it is potential only when the concentration gradient is collinear to the magnetic field gradient. A flow is therefore created by any concentration perturbation that destroys this collinearity. Induced flows form finger-like patterns that can be seen in figure 2.1.

In the last thirty years the phenomenon of the magnetic micro-convection has attracted attention of researchers from different points of view. Several theoretical studies have been devoted to this instability. The models used for the description of the phenomenon are based

on the Darcy equation, where ponderomotive magnetic force is taken into account, continuity equation and the convection-diffusion equation [30]:

$$-\nabla p - \frac{12\eta}{h^2} \mathbf{u} - \frac{2M(c)}{h} \nabla \psi_m = 0 \quad (2.1)$$

$$\nabla \cdot \mathbf{u} = 0 \quad (2.2)$$

$$\frac{\partial c}{\partial t} + (\mathbf{u} \cdot \nabla)c = D\Delta c, \quad (2.3)$$

where  $\Delta = \frac{\partial^2}{\partial x^2} + \frac{\partial^2}{\partial y^2}$ ,  $\nabla = (\frac{\partial}{\partial x}, \frac{\partial}{\partial y})$ ,  $p$  is the pressure,  $\mathbf{u} = (u_x(x, y), u_y(x, y))$  is the depth averaged velocity,  $\eta$  is the viscosity of the fluid,  $h$  is the thickness of the Hele-Shaw cell,  $D$  is the constant isotropic diffusion coefficient,  $M(c)$  is the magnetization,  $c$  is the concentration of the magnetic fluid normalized by its value far from the interface, while  $\psi_m$  is the magnetostatic potential and is given by [31, 32]

$$\psi_m(\mathbf{r}, t) = M_0 \int c(\mathbf{r}', t) K(\mathbf{r} - \mathbf{r}', h) dS', \quad (2.4)$$

where the integration is performed over the boundary of the Hele-Shaw cell:

$$K(\mathbf{r}, h) = 1/|\mathbf{r}| - 1/\sqrt{|\mathbf{r}|^2 + h^2}.$$

On this basis, several characteristics of the magnetic micro-convection were found by a linear stability analysis, also showing the importance of the initial smearing of the interface [33, 34, 35]. Numerical simulations using these models have been performed for a circular interface [36]. They were followed by adding a more complex model that included the Korteweg stress [37].

In comparison to the steadily ongoing theoretical development, the first detailed experimental study of the magnetic micro-convection was performed more than twenty years after the initial demonstration. A Taiwanese group investigated the instability on a circular interface formed by a magnetic fluid drop in a miscible non-magnetic fluid, finding a qualitative agreement with the numerical simulation results [38]. The study was extended with a more quantitative investigation, including variation of the cell thickness. It included the evaluation of the mixing length, as well as characterization of the larger secondary fingers, which were found to be connected with the third-dimension effects [39]. Later, the confined droplet was compared to an unconfined case where the normal-field instability is initially dominant [40]. In parallel a much more detailed study of magnetic micro-convection on a straight interface was conducted, giving a rich qualitative observation of the complicated dynamics. Additionally, it identified the presence of a critical magnetic field and characterized the primary finger width for various cell thicknesses, showing that they are approximately equal [41].

The research of magnetic micro-convection is also relevant for other studies. For example, a direct link is with the investigation of the concentration gratings induced by non-homogeneous illumination under the action of a magnetic field, where convective motion is present [42, 43]. Moreover, the studies of fingering instabilities still raise a general scientific interest. Recent publications show not only the more common interest on the stability for immiscible fluids [44, 45, 46], but also for situations with miscible fluids [47].

It is clearly visible that the topic of the magnetic micro-convection still lacks fundamental understanding. The experimental realization and characterization of this instability is the main goal of this chapter. Coextensive development of theory and numerical simulations by colleagues using the Darcy and Brinkman models has permitted to make direct comparisons. For Darcy model they use equations (2.1)-(2.3) put in dimensionless form by introducing

the following scales: length  $h$ , time  $h^2/D$ , velocity  $D/h$ , pressure  $12\eta D/h^2$ , magnetostatic potential  $M_0 h$ . As a result the set of dimensionless equations is

$$-\nabla p - \mathbf{u} - 2Ra_m c \nabla \psi_m = 0 \quad (2.5)$$

$$\nabla \cdot \mathbf{u} = 0 \quad (2.6)$$

$$\frac{\partial c}{\partial t} + (\mathbf{u} \cdot \nabla) c = \Delta c. \quad (2.7)$$

Here  $Ra_m = M_0^2 h^2 / 12\eta D$  is the magnetic Rayleigh number determined by the ratio of the characteristic time of diffusion  $\tau_D = h^2/D$  and the characteristic time of the motion due to a non-homogeneous self-magnetic field of the fluid  $\tau_M = 12\eta/M_0^2$ . The Brinkman model differs with an additional viscous term  $\frac{\Delta \mathbf{u}}{12}$  in the left side of (2.5). The synchronous work has allowed to improve the comprehension of the phenomenon, which has been communicated via several conference reports and two publications [48, 49]. The experimental aspects are discussed in a higher detail in § 2.1 and § 2.2 respectively. Therein comparisons with theory and numerical simulations are given via references to the corresponding places in the mentioned publications. Additionally, the possibility to use the magnetic micro-convection for mixing enhancement is discussed in § 2.3, as presented in a publication [50]. The chapter is finished with an outlook to the further development of the research on the magnetic micro-convection. For the relevant publications, see appendix E.

## 2.1 Experimental observation

Magnetic microconvection is studied on the interface between two miscible fluids. One is distilled water which contains 0.1 percent tracer microparticles for Particle Image Velocimetry (PIV) measurements, explained later in § 2.1.1. Second is water based magnetic fluid *KTF09-13* with properties summarized in § 1.2.5.

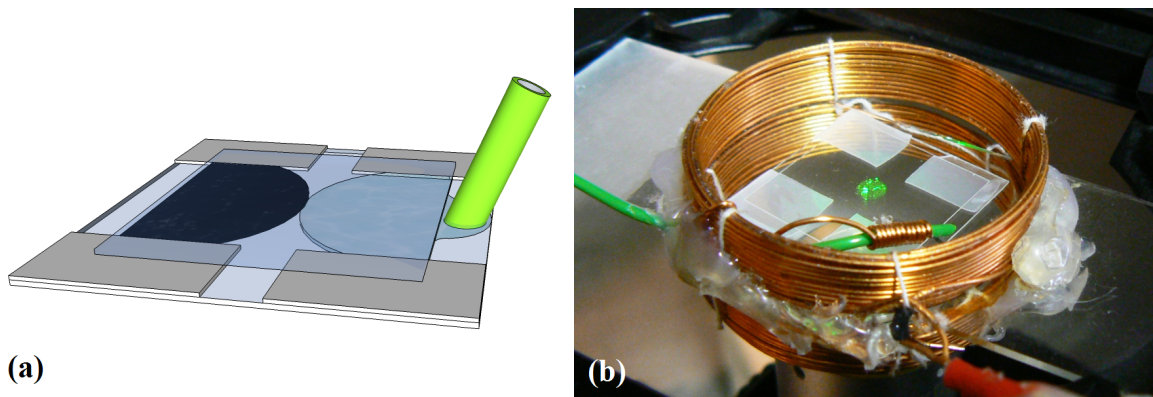


Figure 2.2: Experimental setup used for observation of the magnetic micro-convection. (a) A Hele-Shaw cell is made from two cover glasses with Parafilm M® spacers. Magnetic fluid (dark) and water (transparent) are brought to a contact in the middle of the cell. (b) The cell is placed inside a coil that is fixed on a microscope slide for fitting on a microscope. Water is introduced via the green tube. Images courtesy of K. Ērglis

The Hele-Shaw cell is prepared from two microscope cover glasses separated with  $127 \mu m$  thick Parafilm M®. It is cut to form channels for air and fluids, as can be seen in figure 2.2 (a). The horizontal dimensions of the resulting fluid channel are  $18 \text{ mm} \times 6 \text{ mm}$ .

After assembly the cell is heated on a hotplate to weld cover glasses. A few drops of magnetic fluid are placed on one side of cell until one half of cell is filled by magnetic fluid due to capillary forces. Thereafter the cell is put inside a coil and fixed on a microscope stage as showed in figure 2.2 (b). Coil is made around a microscope slide with 38 turns of 0.7 mm wire and produces a homogeneous magnetic field with strength  $H \in (0 - 30) Oe$  in its central part. Microscope slide allows an easy placement of the Hele-Shaw cell and fixation on a microscope stage. An inverted microscope *Leica DMILM* with a 10x (NA 0.25) objective and a micro-PIV system from *Dantec Dynamics* are used. The magnetic field is switched on after positioning the half-filled cell inside the coil. Then the small green tube (figure 2.2), which is connected to a syringe with the nonmagnetic fluid, is put to the opening of the other side of the cell. The fluid is slowly added using a microscrew that pushes the syringe until water comes in contact with the magnetic fluid. After droplet merging, the magnetic micro-convection can be observed. The process is recorded with the microscope camera from the micro-PIV system, described in more detail in § 2.1.1.

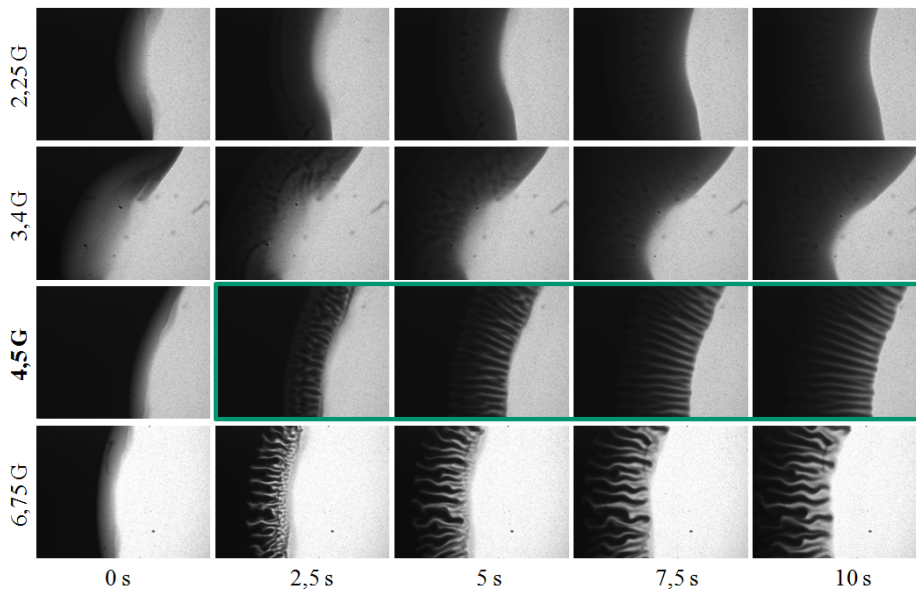


Figure 2.3: Determination of threshold value of magnetic field for finger-like pattern development.

The experimental data shown in figure 2.3 clearly confirm the existence of the critical value of the field strength below which the fingering due to the magnetic micro-convection is not observed. The critical field strength according to these data can be estimated as 3.4 G. Taking into account the physical properties of the magnetic fluid and experimental system, the magnetic Rayleigh number is  $Ra_m = 177$  - a value much larger than the critical value  $Ra_m \approx 5.5$  corresponding to  $t_0 = 0$  obtained analytically in [35]. Such a large value of the critical magnetic Rayleigh number corresponds to large values of the smearing parameter  $t_0$  (see figure 3 in [48], appendix E), which should not be expected if the particle diffusion is dominant. Hence, reasons for this discrepancy are searched.

An explanation might come from the gravitational force effects, as offered in [48]. In short, the gravitational Rayleigh number  $Ra = \Delta\rho gh^3/8D\eta$  for this system is quite large and exceeds  $3.5 \times 10^4$ . This difference creates counter flows in the lower and upper parts of the Hele-Shaw cell after the contact of liquids is formed, causing an additional smearing of

the interface. Numerical simulation results of the proposed model dynamics give a rather reasonable agreement with the experimental observation of the interface forming speed. It is assumed that the gravity effects causes a considerable smearing of the interface before the magnetic micro-convection starts, explaining the rather large values of magnetic Rayleigh number obtained previously. This topic is later discussed in § 3.2.5.

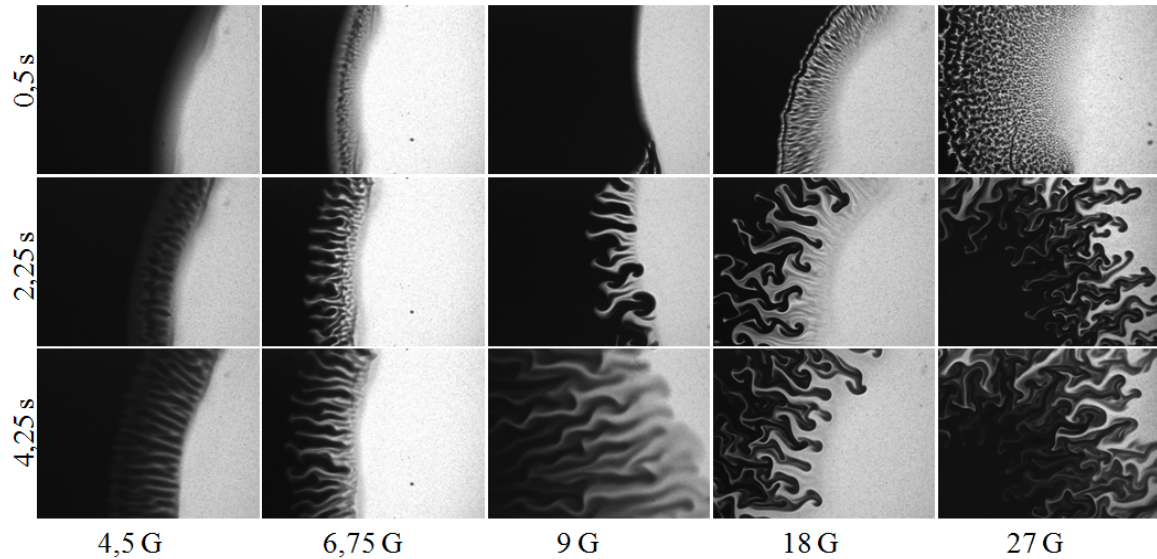


Figure 2.4: Fingering instability development in time for a few values of magnetic field strength.

The experimental results of the development of magnetic micro-convection for several values of the magnetic field strength are shown in figure 2.4. The patterns are close to the ones observed in numerical simulation results for moderate values of the magnetic Rayleigh number (see figure 4 in [48], appendix E). Particularly interesting is the grainy structure of the interface, which may be seen in figure 2.4 for larger values of the field (18  $G$  and 27  $G$ ). It is speculated that it is caused by the normal field instability [12] in the layer of magnetic fluid formed by the gravitational convection. To confirm this, an experiment of magnetic micro-convection for fluids with equalized densities was performed.

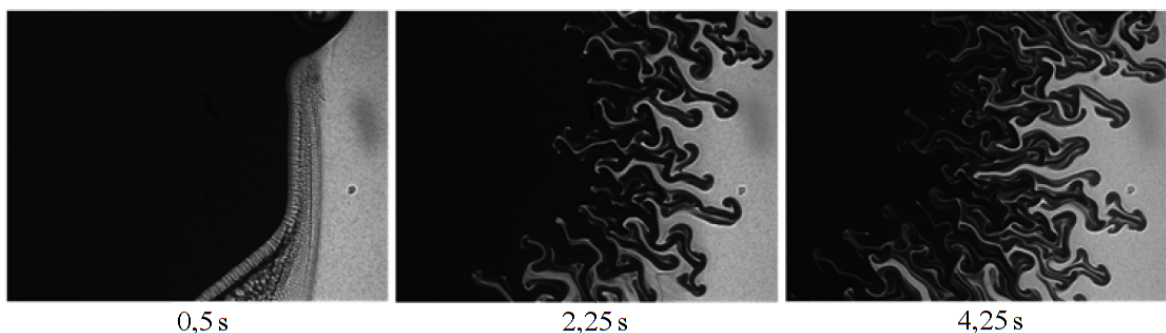


Figure 2.5: Fingering at the interface between the fluids with matched densities at  $B = 27 G$ .

Using water-glycerol mixture instead of pure distilled water allows to match the non-magnetic fluids density with that of the magnetic fluid *KTF09-13*. The fingering at the

interface for this experiment at  $B = 27$  G can be seen in figure 2.5. It is visible that the grainy structure has almost vanished, confirming the influence of gravitational flows in the previous experiments, while the dynamics of the micro-convection seem to be alike. However, it is worth to mention that matching the density of the magnetic fluid is a subtle issue since it is impossible to use salt solutions which would cause the coagulation of the electrostatically stabilized magnetic fluid. The use of water-glycerol solution creates another problem: the viscosity of the glycerol-water solution is higher than the viscosity of the magnetic fluid.

Thus the full model of the magnetic micro-convection might be much more complicated as considered here and should incorporate three dimensional equations for the magnetic field, concentration and flow.

Quantitative information about the velocity field of the micro-convection is obtained by PIV measurements, as explained further after the introduction of the method.

### 2.1.1 Particle Image Velocimetry

A useful method for liquid or gas flow visualization is Particle Image Velocimetry (PIV), which is based on the following principle. Small tracer particles are added to the fluids of interest and their movement in the flow of interest is captured with a camera. Consecutive image pairs of particle movement are analyzed during post-processing, typically based on image cross-correlation with algorithms using Fast Fourier Transformation. To obtain a two-dimensional information of the flows, images are split in regions, called interrogation windows, and the characteristic fluid displacements are found in each of them. Velocity plots are then calculated using the delay times between acquired images [51].

Experimental realization of such measurements and subsequent analysis has several challenges [51]:

- The particles have to be small and in low concentration not to change the flow of interest. However, their size has to be large enough to be recognizable in images and they have to be sufficiently many to be present in all the field of interest. This is achieved by selecting tracing particles individually for each experiment.
- A single camera can only image one plane of the three-dimensional flow, which has to be properly illuminated. A typical solution is to use a laser sheet illumination, which is obtained by expanding a laser beam. Alternatively, optical systems with a narrow depth of field, e.g. microscopes, can be used.
- The particle displacements between two consecutive images have to fall between certain limits. The minimum detectable displacement of tracer particles in two consecutive images should be at least a pixel, whereas the upper limit of the displacement is around a half of the interrogation window size or limited by the time the particle spends in the imaged plane. Tuning of particle displacements is easiest with adjusting the time between two consecutive images used in analysis.
- For precise displacement detection, the particle images should be clear and sharp. This requires very short image exposition times and powerful illumination. These specifications in combination with the previous point are difficult to meet for most of conventional cameras. Hence, a special kind of cameras have been created to acquire image pairs using a stroboscope principle, where images are formed by short light pulses.

- The highest possible precision is demanded, forcing to use the interrogation windows as small as possible. Additionally, the post-processing algorithms have to lead to a correct result. These demands are limited by the computation power accessible and the quality of the experimental images. However, advanced efficient algorithms with correction options allow to cope with these difficulties.

A successful solution for these challenges can be realized either by careful planning and development of a personalized system or by buying a commercially available system. The micro-PIV system from *Dantec Dynamics*[52] has been acquired by the Riga lab several years ago. It consists of the following elements:

- Inverted microscope *Leica DMILM* with a range of objectives and filter cubes for measurements using fluorescence;
- Camera HiSense MkII with a  $1344 \times 1024$  px 12-bit grayscale sensor and double frame acquisition function, recording at a maximum of 12 image pairs per second;
- *MicroStrobe* light source of a green diode;
- Computer with synchronization box for the coordination of light pulses and camera acquisition;
- *Dynamic Studio* software for experiment management and data analysis.

Latex microparticles from *Dantec Dynamics* with a  $1 \mu\text{m}$  diameter are added to water at 0.1% volume fraction as tracer particles. The light source is positioned above the sample, illuminating it as in a bright field mode. Acquisition settings are set to recording 4 Hz using two short light pulses, each  $300 \mu\text{s}$  long, that are  $\Delta t = 0.082$  ms apart. Tracer particles appear dark on a light background, as compared to largely preferred fluorescent particle detection in PIV applications [51] and magnetic fluid appears dark, as was visible in figure 2.4. The magnetic micro-convection instability is registered for several minutes, which creates data of several gigabytes.

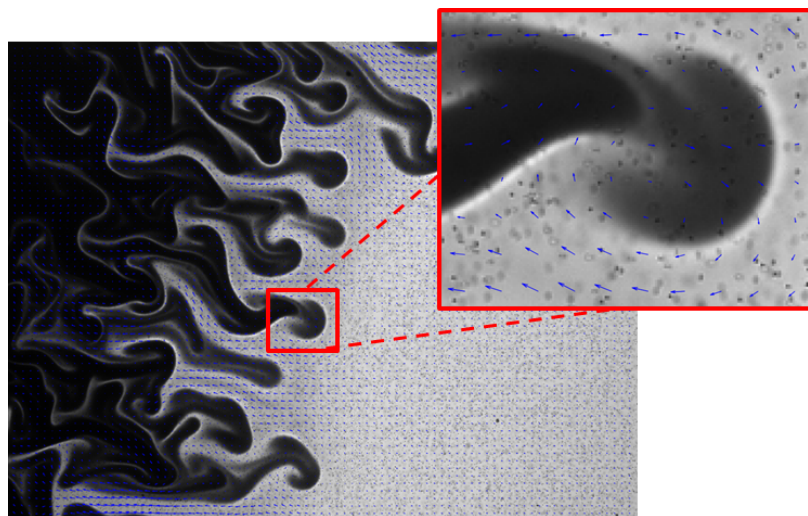


Figure 2.6: Velocity vector field of the magnetic micro-convection and its close-up around a finger tip at  $t = 6.5$  s and  $B = 18$  G found with the PIV method.

The poor image contrast in the darker regions of the magnetic micro-convection makes it impossible to use the conventional PIV algorithms for the visualization of flows in the whole sample. To solve this, a special image processing algorithm to improve the contrast has been developed in the collaboration between the Riga lab and the setup provider *Dantec Dynamics* [53]. This special algorithm includes image preprocessing for local image normalization and application of Difference of Gaussians filter in order to reduce noise. It allows to detect inhomogeneities inside the magnetic fluid that work as tracer particles.

Velocity vector field is obtained from the preprocessed image pairs by an adaptive correlation algorithm with 2 refined steps, 2 passes per step, 32-pixel wide interrogation windows with a 50 percent overlap. All image processing steps have been performed using *Dynamic Studio*. An example of the velocity field of the fingering pattern obtained at  $H = 180 Oe$  and  $t = 8.5 s$  is shown in figure 2.6. It reveals the formation of vortices that is similar to the observations in numerical simulation results (figure 5 in [48], appendix E).

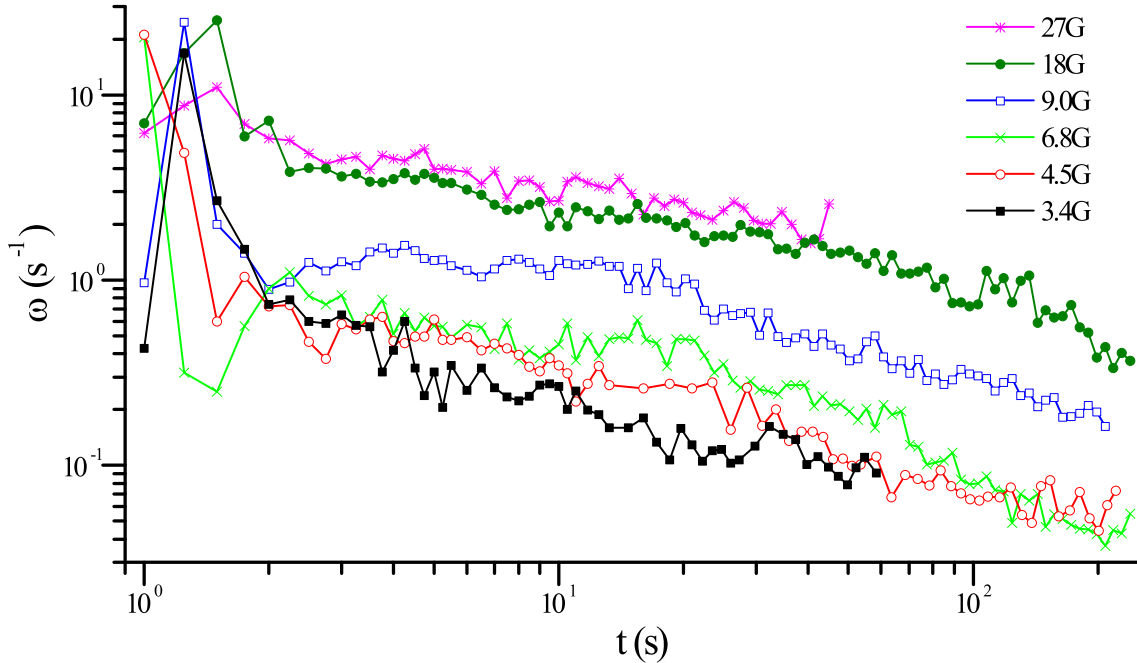


Figure 2.7: Maximal vorticity dependence on time for different magnetic field values as found with the PIV method.

Vorticities in each velocity plot are found for a qualitative comparison with the numerical simulation results *Dynamic Studio* software calculates the vorticity values from the velocity value differences in the neighboring interrogation windows. Afterwards the vorticity field values are exported. Data is further post-processed using MATLAB® to extract the necessary information, e.g., maximum absolute vorticity time dependence. Obtained results are shown in figure 2.7. Thus the developed algorithm allows us to obtain the evolution of the vorticity field during the development of the magnetic micro-convection and its decay due to the diffusion of the magnetic nanoparticles. This dependence may be characterized by a fast increase of the vorticity that is followed by its slow decay. Again a qualitative similarity between the experimental data and numerical simulation results (figure 6 in [48], appendix E) is observed.

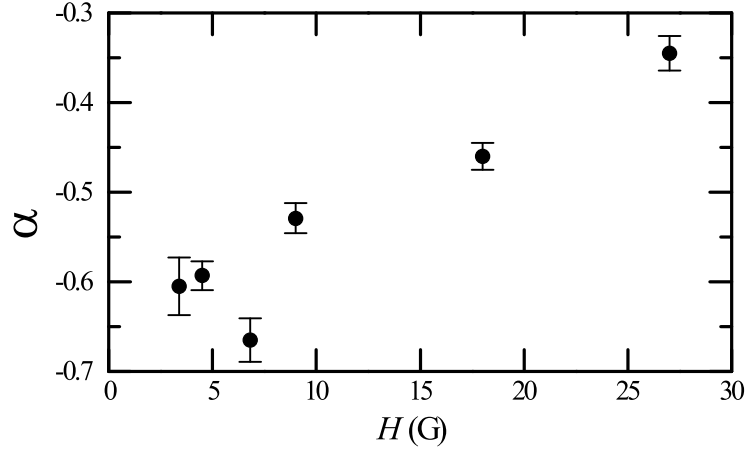


Figure 2.8 The exponent  $\alpha$  of the power law  $\omega_{max} \sim t^\alpha$  for different magnetic field values.

Experimental data for the vorticity decay can be fitted with a power law  $\omega_{max} \sim t^\alpha$ . The values of the exponent  $\alpha$  obtained from fitting data in figure 2.7 are shown in figure 2.8. This figure illustrates the increase of the exponent with the field strength, which corresponds to the slower decay of the fingering at larger fields. This trend correlates with the increase of the exponent obtained in the numerical simulations at several values of the magnetic field strength (figure 6 in [48], appendix E).

The experimental results and analysis up to this point have been summarized together with corresponding theoretical developments and numerical simulations in the framework of the Darcy model in a publication [48], which can be found in appendix E.

### 2.1.2 Further characterization

Numerical simulations and theory for the magnetic micro-convection are based on the magnetic particle concentration, while the microscope camera acquires an image which is an intensity plot  $I_t(i, j)$ , where  $i$  and  $j$  are spatial indexes and  $t$  is the time of the image acquisition. The experimental recording of the instability complies with the bright field microscopy and the magnetic fluid is absorbing light. Therefore the intensity data can be converted to a normalized concentration plot  $c_t(i, j)$  where the initial concentration is fixed at  $c_0 = 1$  via the Beer-Lambert law for a better comparison:

$$c_t(i, j) = \frac{\lg I_t(i, j) - \lg I_{\text{H}_2\text{O}}}{\lg I_{\text{FF}} - \lg I_{\text{H}_2\text{O}}}, \quad (2.8)$$

where  $I_{\text{H}_2\text{O}}$  and  $I_{\text{FF}}$  are the intensities of initial water and magnetic fluid concentrations, found in images at  $t = 0$ . If the real concentration is searched, it can be calculated by multiplying the real initial concentration with the normalized concentration, e.g. knowing the initial volume fraction of the magnetic fluid  $\Phi_0$ , the volume fraction concentration fields can be easily obtained by simple multiplication  $\Phi_t(i, j) = \Phi_0 \cdot c_t(i, j)$ .

To do the data conversion correctly, special care has to be taken to use the camera in the linear regime, where the recorded intensity is proportional to the number of photons and does not saturate the photosensitive matrix [54]. This can be easily tested, as described in appendix B.1.1. Additionally, a homogeneous illumination over the whole field of view is necessary.

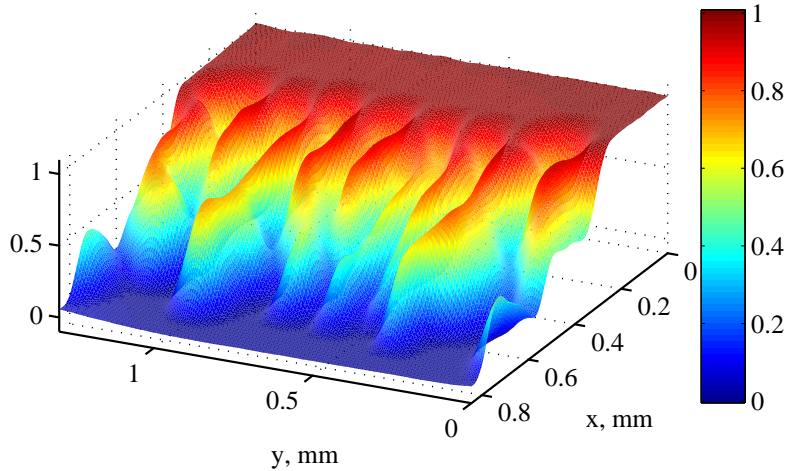


Figure 2.9: A 3D representation of the normalized concentration plot of the magnetic micro-convection at  $t = 2.2$  s and  $B = 42$  G

Images from *Dynamic Studio* can be extracted and further processed with "in-house" algorithms written in MATLAB®. Using the mean intensities of magnetic fluid and water measured in the first image of each recording allows to use (2.8) to convert image series to concentration plot series. An example of a concentration plot is showed in figure 2.9.

Images or corresponding concentration plots of the magnetic micro-convection record a large amount of information that can be further characterized. An apparent characteristic of the instability is its spacial periodicity. The characteristic wavelength  $\lambda$  of the magnetic micro-convection is defined as the mean distance between fingers. Some characterization has been done in Derec *et al.* [41], where wavelength in the linear (right after the formation of fingers) and the stationary (after a longer time) regimes were measured. As can be understood from the publication, the analysis was done manually by measuring the distance between multiple fingers in images by hand which is then divided by their number. The magnetic micro-convection is a dynamic process, therefore it would be of high interest to access the characteristic width time dependence. This can be achieved by developing image processing algorithms that extract this information, as manual processing of the large amount of data is too time consuming. However, it is not a straight-forward task, because of the variation in the interface formation and the complexity of the analyzable pattern.

The developed image processing algorithms for the determination of the characteristic wavelength are based on analysis of a concentration profile on a specific line, defined in the concentration plot coordinates. Various criteria for defining this line are tried. A simple approach is to define a line manually on a certain image and then use it also for other images. Alternatively, an automatic method can be developed. An example can be seen in figure 2.10. It works by defining the line of interest on a constant concentration level in the average concentration plot (b), which is obtained after a large Gaussian filter [55], where  $\sigma$  is typically three times larger than the expected wavelength. Along this the concentration profile (c) is extracted from the concentration plot (a). The benefit of using automatic methods is reducing the analysis time and removing human error. In addition, it allows to determine the line of interest in each image separately. This, in principle, could remove the effect of the interface modification during experiment due to microscopic flows and other effects, which are clearly present in the experimental system as seen in the images (figure 2.4).

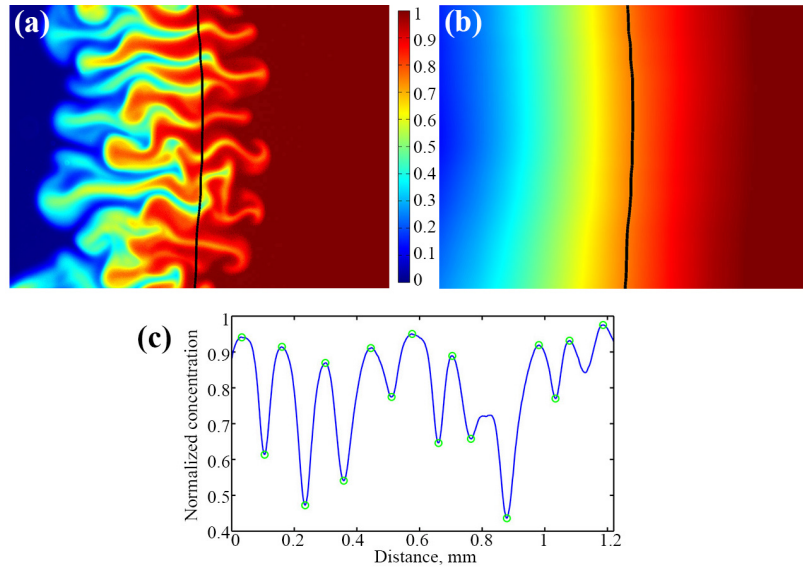


Figure 2.10: An example for retrieving a concentration profile for instability pattern characterization ( $t = 6.6$  s,  $B = 42$  G). (a) Concentration plot. (b) An average concentration plot. A line of a constant concentration (here  $c = 0.75$ ) is found (black) and used for finding concentration profile. (c) The concentration profile as found along the line in the concentration plot. Green circles mark concentration peaks, that are used for wavelength calculation.

Characteristic wavelength is calculated from the measurements of finger widths in the retrieved concentration profiles. These widths can also be found in various ways. For instance, from the length of each successive high and low state, obtained after thresholding the concentration profile with the mean concentration value. Alternatively, from the distance between consecutive peaks of the concentration profile, visible in figure 2.10 (c), that are found using peak finding algorithms in MATLAB®.

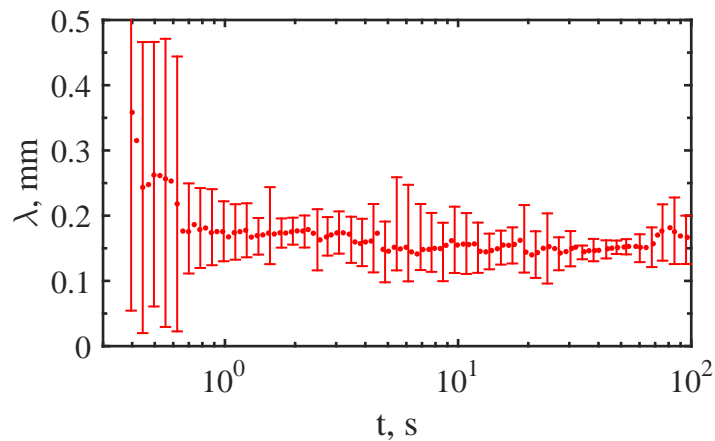


Figure 2.11: Dynamics of the characteristic wavelength of the the magnetic micro-convection at  $B = 42$  G.

A sample result of the characteristic wavelength dynamics at  $B = 42$  G is showed in figure 2.11. Image processing, as showed in figure 2.10, gives a set of distances between

fingers for each image. Characteristic wavelength and its error for each image are taken as the mean and standard deviation of this set. Data show that after the finger formation, the characteristic wavelength stays constant around a value  $\lambda \approx 0.15$  mm, which is close to the Hele-Shaw thickness ( $h = 0.12$  mm), which agrees with the previous observations [41].

The various methods give similar results and therefore are not showed here. However, results with such uniformity are only obtained in image series with rather straight fingers. Once the fingers exhibit splitting and merging, the mean value and errors of the characteristic wavelength become so large that the comparison is impossible. This could be improved by gathering large amount of statistics, which is not an option because of the difficulty and time needed for successful realization of experiments in the current setup.

Further experiments with the magnetic micro-convection have showed that the grainy structure of the interface appearing at short times and large fields (figure 2.4) is visible only if the interface is formed by a quickly approaching water droplet, when the microscrew of the water providing syringe has been turned too quickly or too far. In such a case, the extra pressure that pushes the water droplet forward forces water against the magnetic fluid. Due to the different densities, the less dense water slips above the magnetic fluid. As this pressure is typically small, the slipping stops quickly, leaving the interface of horizontal layers of both fluids in the field of view of the microscope. If magnetic field is applied, a normal-field instability is observed, as noted previously in this section.

At the same time experiments in the same setup without an applied field were carried out and are discussed in the next chapter in § 3.2.1. It was showed that the interface grows with a dependency on time as a function  $\sqrt{t}$ , which is a typical characteristic of a diffusive process from the concepts of the Brownian motion [56]. The effective diffusion coefficient of the process was found to be more that hundred times larger than measured with dynamic light scattering.

The arguments expressed in the previous two paragraphs motivated to continue the investigation of the magnetic micro-convection in two directions. First, improve the setup to have a better control of the initial interface formation and perform more quantitative measurements of the magnetic micro-convection, which is described in the next section. And two, investigate the reasons behind the large difference between the magnetic fluid particle diffusion coefficient and the effective diffusion coefficient of this particular system, for what the next chapter is devoted.

## 2.2 Improved experimental setup

The experimental setup is improved and adapted in several ways before further experiments and an illustration of it can be seen in figure 2.12. First of all, an attempt to improve the essential interface formation is made by having a more sensitive control over droplets. This is achieved by changing the way of fluid introduction in combination with redesigning the cell. The cell (figure 2.12 (3)) is now made of two Parafilm M® spacers that are cut in 'U' shapes. They are put opposite each other between two glass slides to form a rectangular cell leaving two outlets for air on the sides. Liquids are introduced through two metal tubes, glued in drilled holes in the upper glass slide. After assembly, the glass slides with spacers are welded together on a hot plate (75°C, 5 min), creating a cell with a  $5 \times 20 \times 0.12$  mm<sup>3</sup> size. Plastic tubing (figure 2.12 (4)) connects the metal tubes to syringes containing both fluids that are fitted on a syringe pump (*Harvard Apparatus* PHD Ultra). As compared to previous experiments, the cell is now initially half filled with water, which is then followed by magnetic fluid introduction. It is empirically observed that the magnetic fluid droplet

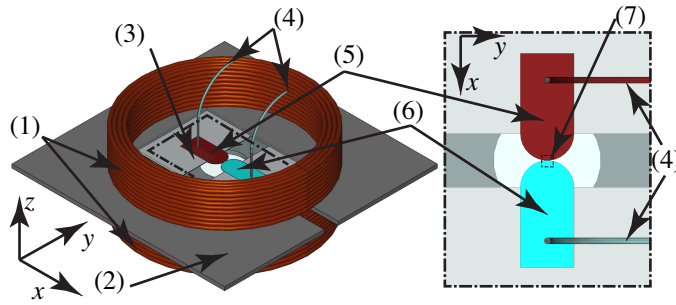


Figure 2.12: Experimental setup consists of a coil system (1) fitted on a microscope stage insert (2). A Hele-Shaw cell (3) with tubing connections for fluid introduction (4) is placed in the center. A closer view of the cell displays how magnetic fluid (5) and water (6) droplets are brought to a contact in the center of the Hele-Shaw cell. Cameras are recording only the central part of the cell (7) where droplets merge.

typically has a larger radius of curvature in this system, probably because of different properties, hence it is easier to be controlled. Microsteps of the syringe pump allow to bring magnetic fluid to a contact with a very high precision, as showed in figure 2.13. This allows to keep the important parameter  $t_0$ , which denotes the initial smearing, as small as possible.

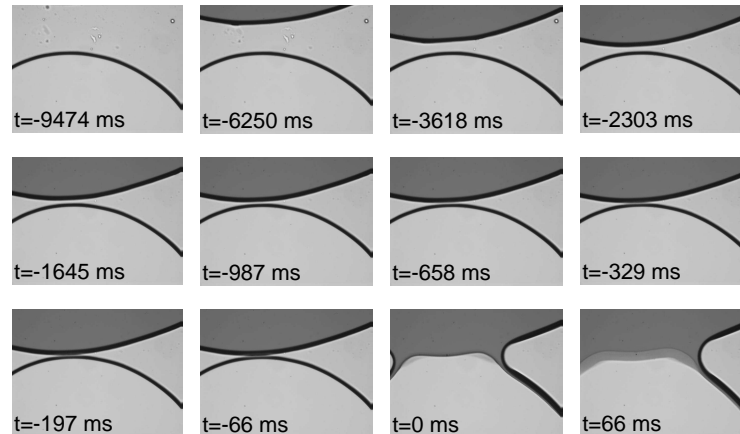


Figure 2.13: Magnetic fluid drop is brought to a contact with the water drop with a high precision, as possible with the improved experimental setup.

Also a new coil system that gives an access to higher magnetic fields is designed and produced to improve the setup, sketched in figure 2.12 (1). It is required that the coils system fits on the motorized stage *ASI MS-2000* of the *Leica DMI 3000B* microscope and produces a homogeneous magnetic field up to  $H = 150$  Oe in  $z$  direction in at least a few milliliter range in the center of the sample at room temperature without extra cooling. Microscope objectives give a limitation of the inner diameter of the coils  $d_{in} \geq 45$  mm, while the stage insert has a 1 mm thickness. An appropriate system is designed with the *FEMM* software, which is a useful tool for magnetic field calculations and is described in appendix C.1. A combination of two identical coils made with 200 turns of copper wire with a diameter  $d = 0.7$  mm and are 19 mm high and have inner and outer diameters of  $d_{in} = 45$  mm and  $d_{out} = 57$  mm respectively fulfill the demands.

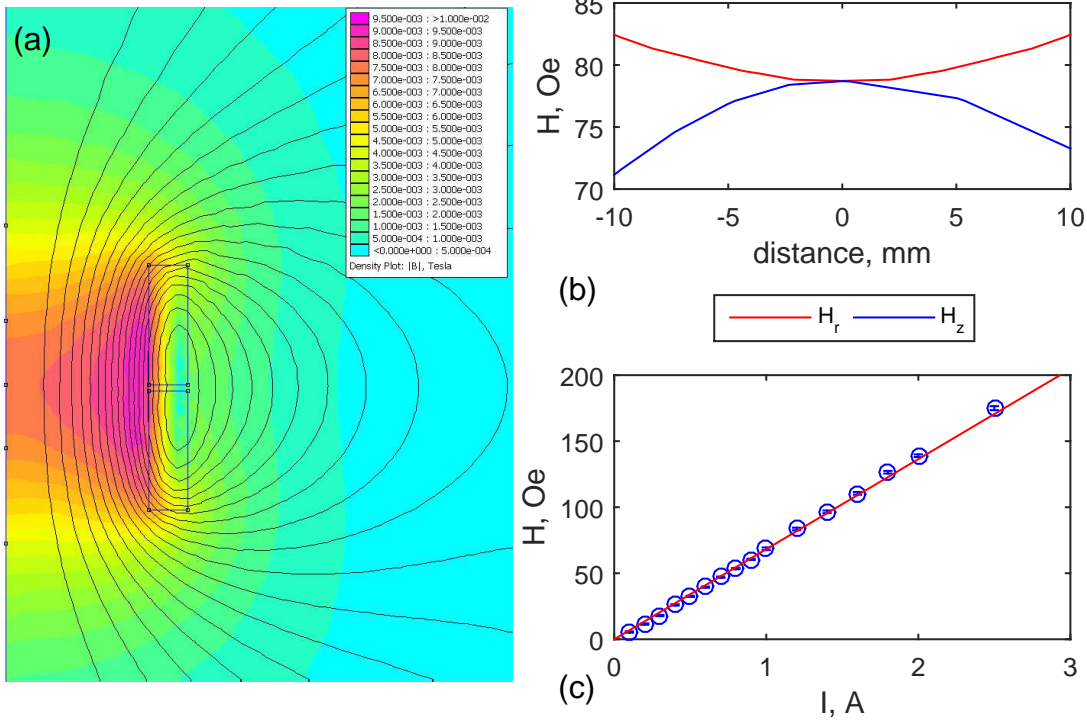


Figure 2.14: Coils of the improved experimental setup. *FEMM* model for a current  $I = 1$  A gives information on magnetic field (in mT) (a) and its homogeneity around the center of the sample position (b). Magnetic field experimental calibration measurements are showed in (c). Linear fit gives  $H(\text{Oe}) = 68 \cdot I(\text{A})$ .

A model of the coil system in *FEMM* using cylindrical symmetry is visible in figure 2.14 (a). Its solution for a constant current  $I = 1$  A shows that coils should create a homogeneous magnetic field  $H = 79 \pm 1$  Oe in an area with a diameter 5 mm around the center of the sample position (see figure 2.14 (b)). Coils are made 'in-house'. Each layer of wires is fixed with a *Formvar* tape, while the final protective layer is made with electric tape. Magnetic field calibration for various currents is done with a *SENIS* Hall probe 03G. Results are showed in figure 2.14 (c) and their linear fit give a proportionality  $H(\text{Oe}) = 68 \cdot I(\text{A})$ , which is slightly smaller than expected from numerical simulations. The total resistance of the coil system  $R_{tot} = 2.9\Omega$  allows to use it for currents up to 3 A, limiting the obtainable field by  $H < 200$  Oe.

To access the dynamics of the magnetic micro-convection in a wider timescale, it is chosen to record the process with a conventional bright field microscope instead of focusing on flow measurements with a PIV setup as done previously. This is achieved with an inverted microscope *Leica* DMI 3000B with a 10x objective and a halogen lamp for bright field. It is equipped with two cameras that record simultaneously. The fast camera *Mikrotron* MC1363 records with 50 Hz, while the regular camera *Lumenera* Lu165c films with 15 Hz.

Cameras are calibrated for a simultaneous use. The temporal calibration is done manually by fixing  $t = 0$  for the frame of each camera where droplet merging has been recorded. This gives an error, but it does not exceed the delay-time between two recorded images, which is less than 70 ms and is negligible. Spatial calibration, on the other hand, is done semi-

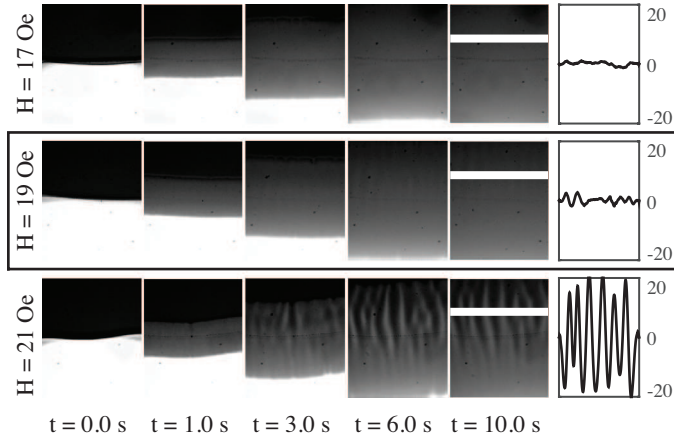


Figure 2.15: Experimental determination of the critical field (marked with a rectangle). Plots on the right side show intensity values along the while lines at  $t = 10.0$  s in a.u., after two moving average filters for removing background and noise. At  $H = 19$  Oe small, but notable fingering pattern is visible, as compared to intensity fluctuations around the noise level at  $H = 17$  Oe. At  $H = 21$  Oe already a well-developed fingering pattern is visible.

automatically by cross-correlating initially acquired images of a fixed stage micrometer, as described in appendix B.1.2. This links the coordinate systems of both cameras, which is essential for image processing.

Magnetic micro-convection experiments in the improved experimental setup are performed with a distilled water and a magnetic fluid *D107* with characteristics summarized in § 1.2.5 as described earlier.. As compared to the previous study, here the experiments and subsequent analysis are mainly focused to the primary finger formation, which are compared to the results of numerical simulations of the magnetic micro-convection for the same conditions in the framework of the Brinkman model. These are carried out by colleagues in the Riga lab Simulation results, as well as these experimental results and their comparison are summarized and published in [49], which can be found in appendix E. The important smearing time parameter is estimated to be  $t_0 \approx 0.05$  s from an additional study, described in § 3.2 as it is impossible to extract it directly for each experiment. Therein it is showed that this experimental system (with a concentration jump) has an effective diffusion coefficient  $D = 5.4 \cdot 10^{-5} \text{ cm}^2 \cdot \text{s}^{-1}$  at zero-field.

Experiments are performed for various magnetic field values. The critical field at which the fingering pattern appears is here estimated to be  $H_{crit} = 19 \pm 1$  Oe, as justified by the experimental images in figure 2.15. Further increase of the field, as can be seen in figure 2.16, at first leads to straight fingers becoming more pronounced. Above a less obvious second threshold ( $H \approx 40$  Oe), finger bending and splitting is observed. A further increase of the magnetic field causes the instability to develop faster. At  $H = 138$  Oe, which is the largest magnetic field used in experiments, the primary fingers develop completely in less than a second.

To describe the process quantitatively several characteristics are retrieved with image analysis methods and are explained below.

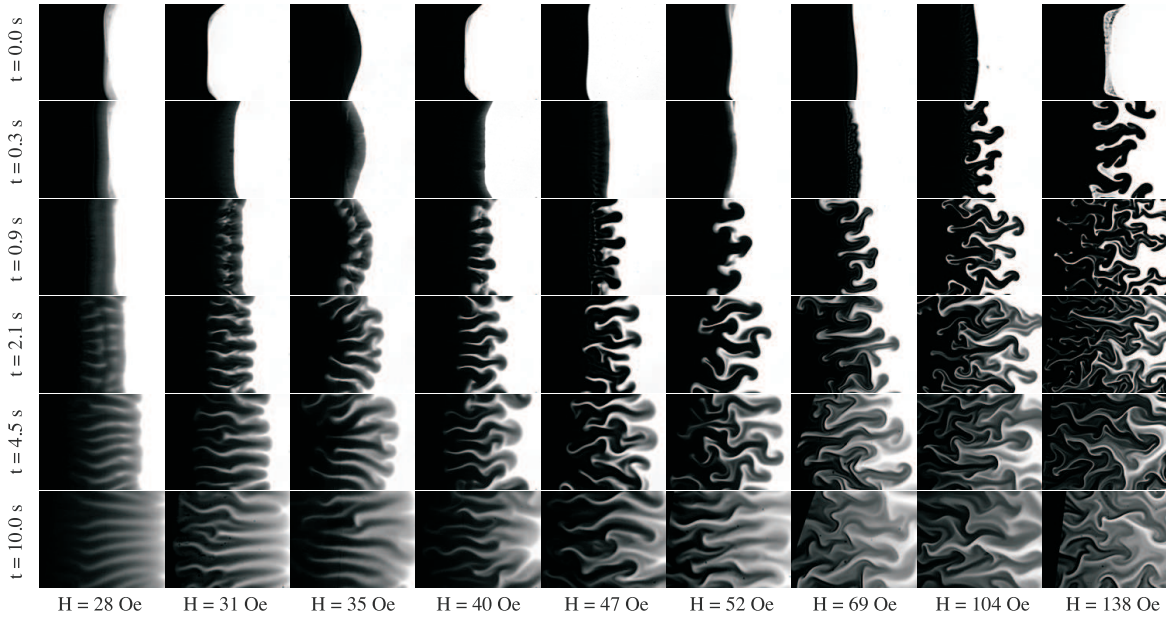


Figure 2.16: Experimental images of the magnetic micro-convection development for various magnetic field values. Each image has a  $0.7 \times 0.9$  mm size.

### 2.2.1 Experimental Image Analysis

The experimental snapshots in figure 2.16 clearly indicate a field dependence. The analysis of the experimental data is performed to retrieve the characteristic Fourier coefficients and wave-number of the instability pattern and also the primary finger velocities. This is done with 'in-house' image processing algorithms written in MATLAB®.

Both cameras record color images that are first converted to 8-bit grayscale images ( $I_{\text{GRAY}} = 0.2989 \times I_{\text{R}} + 0.5870 \times I_{\text{G}} + 0.1140 \times I_{\text{B}}$ ) and then converted to concentration plots using (2.8) as described earlier.

#### Analysis of fingering pattern dynamics

The spatial periodicity is characterized by finding the dynamics of the characteristic Fourier coefficients of the concentration profile along the initial fluid interface, using an algorithm that is explained graphically in figure 2.17. At first, a fixed line  $l$  is defined. It is manually defined for each experiment, marking the initial fluid interface (a). If necessary, a segmented line is used, allowing to remove the interface formation effects. Then the concentration information is retrieved from concentration plot on this line  $l$  at each time moment  $t_i$  ((b)- an example at  $t = 3.0$  s,  $H = 52$  Oe). This gives a concentration profile  $c(l)$  for each  $t_i$ .

Fourier coefficients  $|\hat{c}(k)|$  of the concentration profile are found with a fast Fourier transform. They are normalized with respect to the maximal value  $\max(|\hat{c}(k)|)$  at each  $t_i$ . Only Fourier coefficients in the  $k$  range  $[0; 150] \text{ mm}^{-1}$  are used (d), as they correspond to realistic finger wavenumber values. Repeating this for each time  $t_i$  gives an array of Fourier coefficients  $|\hat{c}(k, t)|$ . Result can be displayed with a color coded grayscale contour-plot as in figure 2.18 for several magnetic fields. For  $H = 138$  Oe it is shown next to numerical simulation data in figure 2.22 (c).

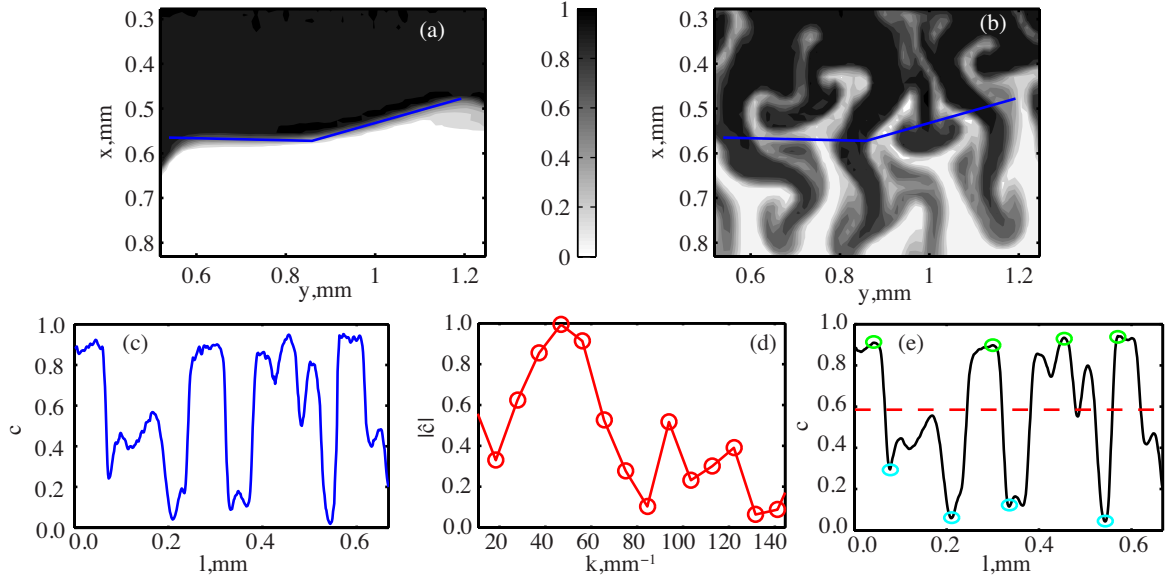


Figure 2.17: Steps for finding the characteristic Fourier coefficients: (a) define a fixed line  $l$  (blue), (b) find  $l$  (blue) for each  $t$ , (c) retrieve concentration profile  $c(l)$ , (d) calculate normalized Fourier coefficients  $|\hat{c}(k)|$ . In (e) the characteristic width estimation by the peak finding algorithm is showed. The concentration profile (from (c)) for experimental data is first smoothed (black line). Peaks (maxima - green circles, minima - light blue) are found using two criteria, described in text. Mean concentration value is represented with a red dashed line.

To verify the Fourier coefficient accuracy, an additional algorithm finds the average wave number dynamics in the same concentration profiles. It is based on peak finding and is explained in (e) of figure 2.17. For experimental data, the concentration profile is first smoothed to reduce noise. Then a MATLAB® built-in function *findpeaks* is used to find peaks. Two peak selection criteria are used. First defines minimum peak height  $H_p$ . It must be greater than the difference between mean ( $\bar{c}$ ) and minimum ( $\min(c)$ ) concentration and greater than the average concentration noise  $\Delta(c_n)$  estimated from the image noise levels. This allows to stop peak finding in low contrast data, where huge errors otherwise appear. Second, the minimum distance between two consecutive peaks  $\Delta H_p$  is greater than an arbitrary fixed value. For experimental data it is  $60 \mu\text{m}$ , which is half of the expected width.

By applying these criteria, one finds the maximum and minimum peak positions  $l_i^{pmax}$  and  $l_j^{pmin}$ . The characteristic wavelength is calculated as the average value of the differences between consecutive maximum and minimum peaks

$$\lambda^p = \overline{(l_{i+1}^{pmax} - l_i^{pmax}), (l_{j+1}^{pmin} - l_j^{pmin})}$$

and its error  $\Delta\lambda$  is taken as the standard deviation of these differences. Afterwards, wavenumber is calculated with  $k^p = \frac{2\pi}{\lambda^p}$ . Repeating this step for each time  $t_i$  gives a vector of the average wavenumbers  $k^p(t)$ . The average wave numbers are plotted as circles with error-bars on top of the Fourier coefficient contour plots in figure 2.18. Values for  $H = 138 \text{ Oe}$  are

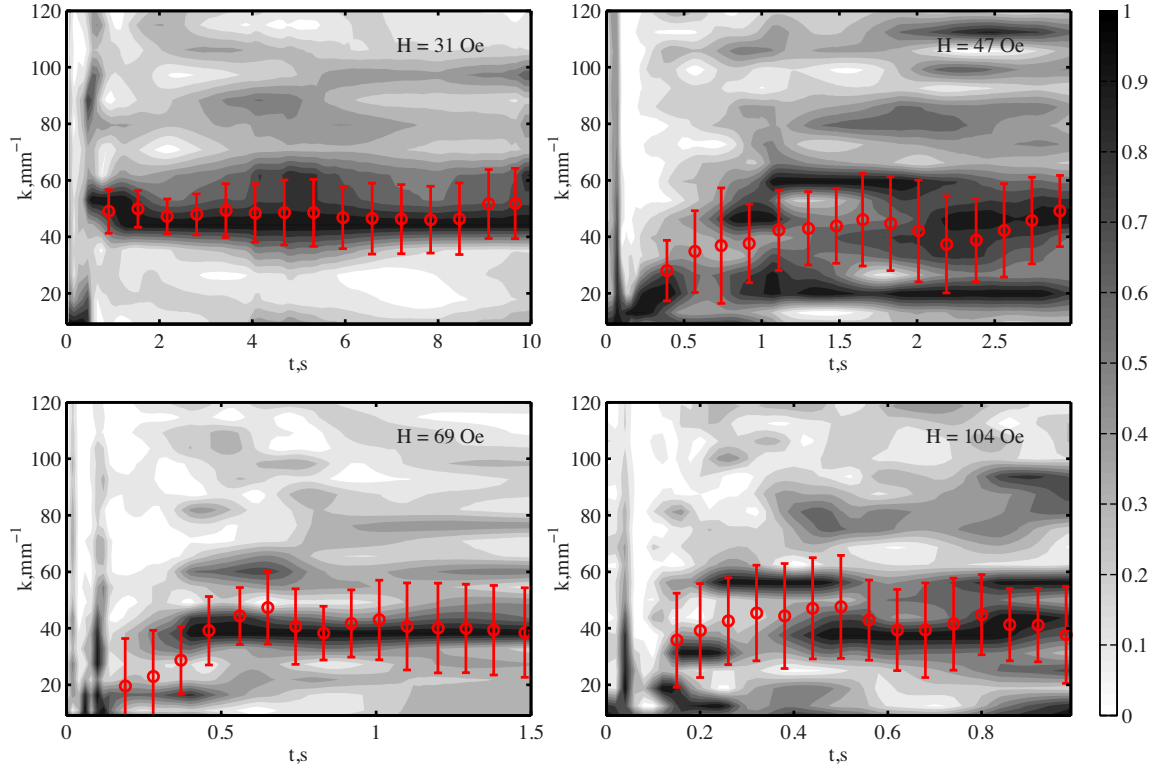


Figure 2.18: Primary finger pattern dynamics for  $H = 31, 47, 69$  and  $104$  Oe. Grayscale contourplot shows dynamics of normalized Fourier coefficients (colorbar on the right). Red circles and error-bars mark the wavenumber values found with the peak finding algorithm.

showed in figure 2.22 (c) in § 2.2.2 together with comparable numerical simulation results from [49].

Three points are worth to be noticed. First, the dominant Fourier coefficients and average wave numbers match well, confirming that the two algorithms are working accurately. Second, the characteristic wave number stays constant during the development of the primary fingers. Deviations from this constant value are visible only at the very beginning of each experiment, due to the time needed for the formation of the fluid interface and the first notable finger tips. And most importantly, the characteristic wave numbers are close to the same value  $k \simeq 40 - 50 \text{ mm}^{-1}$  for a wide range of magnetic fields ( $H = 19 - 138$  Oe).

This wave number  $k$  corresponds to a characteristic wavelength  $\lambda \simeq 125 - 160 \text{ }\mu\text{m}$ . It is close to the cell thickness  $h$  and therefore consistent with the earlier observations in [41].

### Analysis of the finger velocities

To characterize the instability dynamics across the initial interface we choose to find the primary finger velocity dynamics. Velocities are found by locating the displacement of the maximal concentration gradient on the primary finger trajectories. The algorithm works as follows (see figure 2.19 for graphic explanation)

At first, a line  $j$  is manually chosen by a visual inspection of the image series, so that it approximates the finger peak trajectory with line segments. For each time moment  $t_i$ , the concentration profile along this line  $j$  is extracted. Then the concentration gradient is

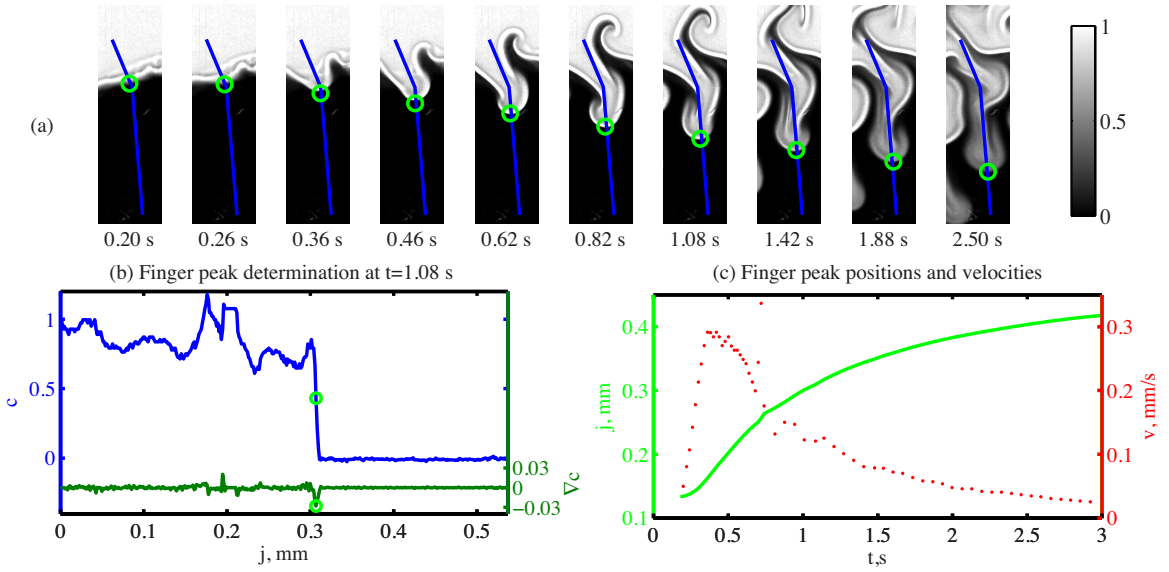


Figure 2.19: Explanation of the algorithm used for finding finger velocity (an example for  $H = 69$  Oe.) (a) Concentration plots show finger growth on the manually chosen fixed  $j$  line (blue) and the finger peak locations (green circle) over time. (b) The concentration profile (blue) at a time  $t$  (here  $t = 1.08$  s) is used to calculate the concentration gradient (dark green). The location of its negative maximum marks the finger peak position (green circles). (c) Velocities (red dots) are calculated from the peak positions (green line).

calculated from the concentration profile with the central finite difference method. The finger peak position is set at the the negative maximum of the concentration gradient. Performing this step for each image gives a finger peak position on the line  $j$  for each time  $t_i$ . As a result, the finger peak position time series  $j(t_i)$  is obtained. After a smoothing step that reduces noise, the velocities  $v(t)$  are calculated from the position data with  $v(t_i) = \frac{j(t_{i+1}) - j(t_{i-1}))}{t_{i+1} - t_{i-1}}$ .

In each experiment the velocity dynamics is retrieved for several fingers. Averaging over these fingers and logarithmic time spans gives the average velocity dynamics and its standard deviation as the error for each magnetic field. Several of them are shown in figure 2.20. Data indicate that for fields larger than  $H = 40$  Oe (corresponding to the second magnetic micro-convection threshold) the velocity first increases reaching a maximum value  $v_{max}$  which is followed by a slower decay. For lower fields (data shown only for  $H = 28$  Oe) the primary finger velocity first remains roughly constant without any well pronounced maximum and later slowly decreases.

The field dependence is quantified by comparing the average maximal velocities. The maximal velocity  $v_{max}$  is found for each finger and the average value  $\bar{v}_{max}$  and its standard deviation are calculated for all magnetic fields. The average maximal velocity increases as a function of the magnetic field. It scales as  $H^2$ , thus as Rayleigh number  $Ra_m$ . Data are shown in figure 2.21 (a) as a function of the square of the magnetic field strength.

## 2.2.2 Comparison of experimental and theoretical results

The experimental results showed above and the theoretical results using Brinkman and Darcy models, published in [49], which can be found in appendix E, are compared here.

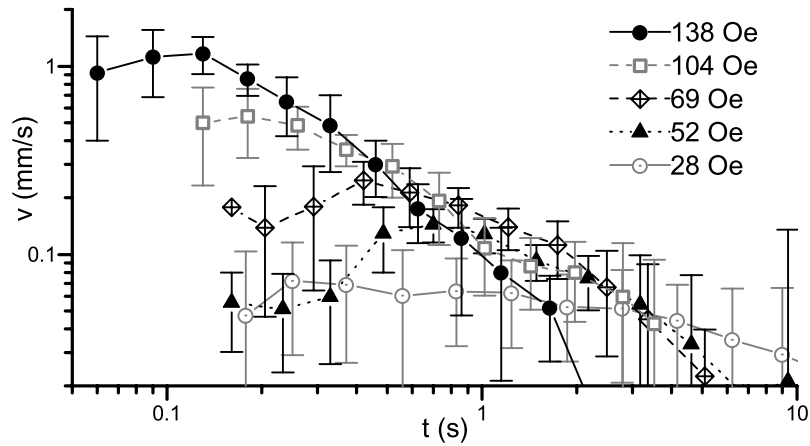


Figure 2.20: Experimentally measured average finger velocity dynamics for several magnetic field values.

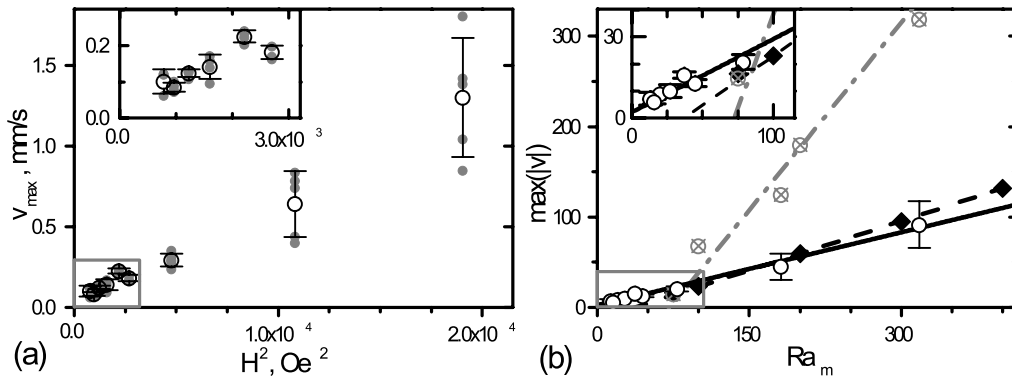


Figure 2.21: Maximal finger velocity. (a) Experimental data of the maximal finger velocity (gray dots) and average maximal velocity (empty circles with error-bars) as a function of the square of the magnetic field strength. (b) Numerical simulation data from [49], given in appendix E, and experimental data with linear fits: the Brinkman model (black diamonds and a dashed line), the Darcy model (gray crossed open circles and a dash-dot line) and experimental data in dimensionless units (empty circles with error-bars and a straight line) as a function of  $Ra_m$ . Fitted slopes and their uncertainties are  $0.36 \pm 0.01$ ,  $1.39 \pm 0.15$  and  $0.27 \pm 0.03$ . The two insets show the parts of graphs marked with gray boxes in the main figures.

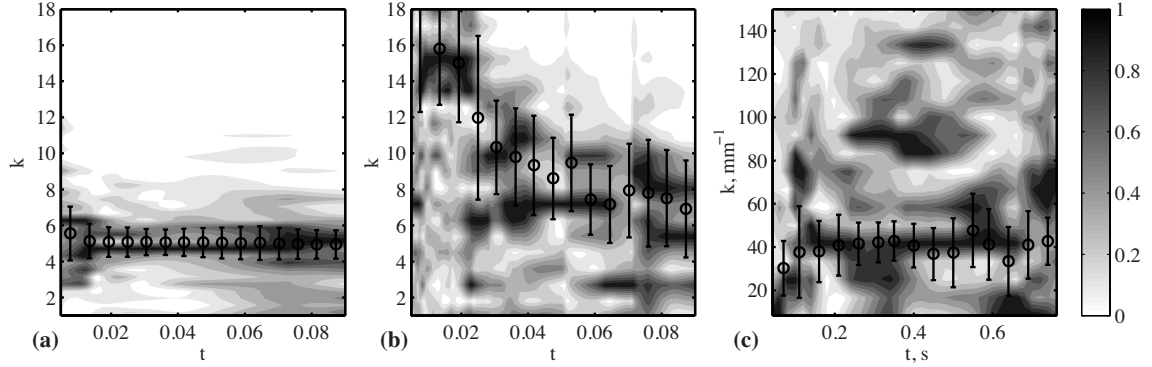


Figure 2.22: Analysis of the fingering pattern dynamics. Graphs have color-coded grayscale contourplots of the Fourier coefficient dynamics. On top of these graphs the average wavenumbers found by peak finding algorithm are marked as circles with error-bars. Results are shown for numerical simulation data from [49], given in appendix E, at  $Ra_m = 318$  and  $t_0 = 0.005$  of (a) the Brinkman model, (b) the Darcy model and (c) the experimental data at  $H = 138$  Oe. The sizes of graphs are equal with respect to dimensionless quantities.

The development of the micro-convection depends on the magnetic Rayleigh number  $Ra_m = M_0^2 h^2 / 12 \eta D$ . The threshold value of the field strength necessary for the development of the magnetic micro-convection allows to estimate the diffusion coefficient of the particles. It is done in § 3.1 and gives a diffusion coefficient for the particles to be  $D = 1.7 \cdot 10^{-5} \text{ cm}^2/\text{s}$  - a value of the same order of magnitude as the one found in the measurements of the diffusion profile in zero field described in § 3.2.1. It is worth noting that is much larger than the value calculated according to Einstein formula (1.5), which gives  $D \approx 6 \cdot 10^{-7} \text{ cm}^2/\text{s}$ . In the next chapter and § 3.2.5 in particular it is showed that this effect arises mostly from the density difference between fluids.

The Fourier spectra dynamics of the concentration perturbations are shown in figure 2.22. To simplify the comparison, the plot sizes are equalized with respect to the dimensionless quantities. For the experimental data figure 2.22(c), the characteristic pattern wave number gives  $k \simeq 40 \text{ mm}^{-1}$ . Multiplying it with the thickness of the Hele-Shaw cell  $h = 120 \mu\text{m}$ , one finds  $kh \simeq 5$  in dimensionless units. This is in good agreement with the numerical simulation data in the frame of the Brinkman model, visible in figure 2.22 (a) and its linear analysis. On the contrary, the Darcy model in figure 2.22 (b), which was used for qualitative comparison in § 2.1, predicts an initial pattern with a much smaller scale and faster dynamics.

The experimental data of finger velocity dynamics after conversion to non-dimensional quantities can be seen in figure 2.23. They show a non-monotonous time dependence, which agrees well with the numerical simulation results in the framework of the Brinkman model as compared to the Darcy model, which predicts faster growth and decay of the finger velocity.

A quantitative comparison of the magnetic micro-convection field-dependence is done by comparing the maximal primary finger velocity as a function of the magnetic Rayleigh number. The experimental data from figure 2.21 (a) after conversion to non-dimensional units show a good agreement with the numerical data obtained in the framework of the Brinkman model as can be seen in figure 2.21 (b). The slope 0.27, which is obtained for the linear dependence of  $\max(|v|)$  as a function of  $Ra_m$  for the experimental data, is close to the value 0.36 for the Brinkman model and quite far from the value 1.39 for results in the frame of the Darcy model. Close are also the numerical values of the finger velocities

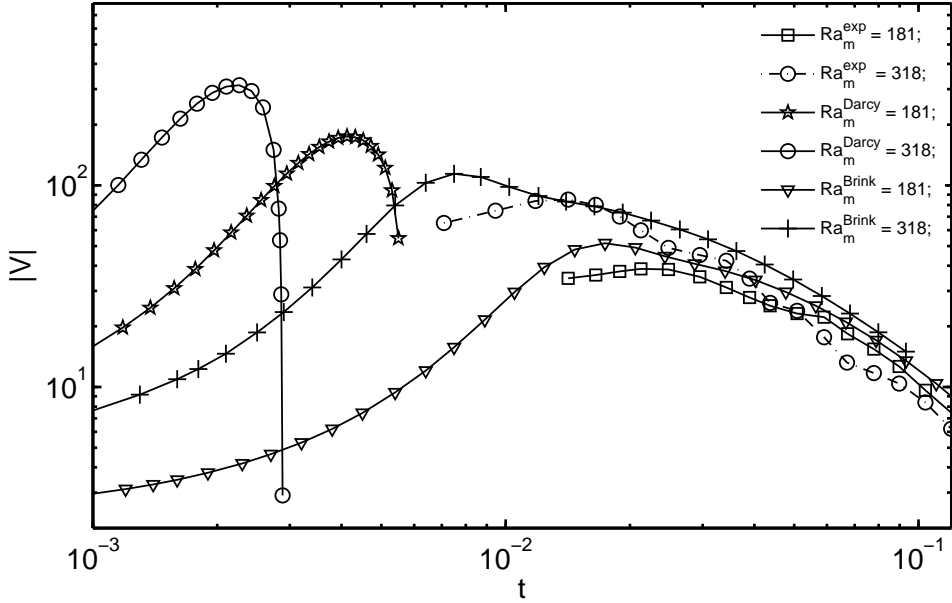


Figure 2.23: Finger velocity  $|V|$  as a function of time for two values of the magnetic Rayleigh number  $Ra_m$ . Data according to the Brinkman model: triangles  $Ra_m = 181$ , cross  $Ra_m = 318$ ; the Darcy model: stars  $Ra_m = 181$ , open circles  $Ra_m = 318$ . Simulation data are from [49], given in appendix E. The experimental data: squares  $Ra_m = 181$ , open circles on dot-dashed line  $Ra_m = 318$ .

between experimental results and the Brinkman model. For example, the characteristic value of the finger velocity at  $H = 104$  Oe is 0.64 mm/s. In dimensionless units, it corresponds to 45 at  $Ra_m = 181$ , which is close to the value 59 obtained with the Brinkman model and very different from the value 180 obtained with the Darcy model for  $Ra_m = 200$  (see figure 2.21 (b)).

It is interesting to remark that both in experiments and numerical simulations (not shown), if the magnetic Rayleigh number is large enough, the relation  $v_{max}t_{max} = \text{const}$  holds with a good accuracy, where  $t_{max}$  is the time at which the maximal finger velocity  $v_{max}$  is reached. This corresponds to the following scaling  $v_{max} = h\tau_D^{-1}Ra_m$  and  $t_{max} = \tau_D/Ra_m$ , leading to  $v_{max}t_{max} = h$ . Experimental data in figure 2.24 clearly agree with this observation.

The development of the micro-convection as can be observed in the experiments (figure 2.16  $35 \text{ Oe} < H < 40 \text{ Oe}$ ) has the same features as the results of numerical simulations. Both in numerical simulations and experiments the formation of mushrooms is observed, which as it is shown by numerical calculations, are connected with the dynamics of vortices at the development of the micro-convection (figure 9 in [49], given in appendix E).

The qualitative and quantitative agreement shown here indicates that the Brinkman model, as introduced in [49] (given in appendix E), is appropriate for the description of the magnetic micro-convection at least during the primary finger formation.

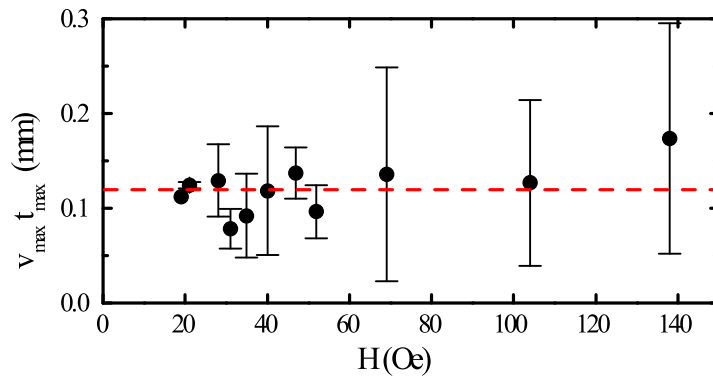


Figure 2.24: Factor  $v_{max}t_{max}$  is approximately constant for all measurements and agrees with the thickness of the cell, which is marked with a red dashed line.

## 2.3 Possibilities in microfluidics

Over the last 15 years the field of microfluidics has continuously advanced, providing an interesting framework for various applications and scientific studies [1]. It is based on the manipulation of small volumes of fluids through microscopic channel structures, which is interesting in a wide range of subjects, especially in life sciences. Microfluidics allows to perform the same experiments, but using a very small amounts of reagents [57].

These approaches are very attractive for the a lab on a chip (LOC) concept - putting a chemistry lab on a single chip. A large variety of production methods [58] has allowed to create many different LOC devices. The vast majority of them are made for medical purposes and diagnostics in particular [59]. Nevertheless, many challenges are still present in the way for development of more sophisticated devices.

Microfluidic systems typically have a small Reynolds number. Therefore, a lot of effort has been devoted to enhance mixing, which is otherwise limited by diffusion speed [60]. As diffusion is typically a slow process, long channels are needed.

Mixers in microfluidics can be divided into passive and active, where the latter need an external energy supply [61]. A convenient energy source for active mixing systems is an external magnetic field, as the energy can be transmitted to the microfluidics chip or cell without direct connectors. It is particularly interesting for systems with magnetic particles. Magnetic fluid, being a colloidal dispersion of magnetic particles, can be used as a model system for future applications. Several examples of magnetic and non-magnetic fluid mixing have already been demonstrated [62, 63].

Using the knowledge obtained in the previous sections, an evaluation of the possible use of the magnetic micro-convection phenomenon for mixing applications is performed and described further. This is also summarized in a publication [50], given in appendix E.

### 2.3.1 Mixing with magnetic micro-convection

Mixing effect estimation is done with a part of the experimental measurement data acquired in the previous section. Data are limited to short times (acquired with the faster camera) and higher magnetic field values, as quick mixing is preferred. For easier reception in the microfluidics community and comparison with previously presented methods, SI system units are used here (Conversion to CGS units is explained in the introduction). Hence, the magnetic fluid *D107* is characterized with a diameter  $d = 7.0$  nm, polydispersity  $PDI = 0.33$ ,

saturation magnetization  $M_{sat} = 8.4$  kA/m at  $B_{sat} = 1$  T, susceptibility  $\chi_0 = 0.20$  in the range up to  $B = 20$  mT and volume fraction  $\phi = 2.9$  % as obtained from magnetization measurements.

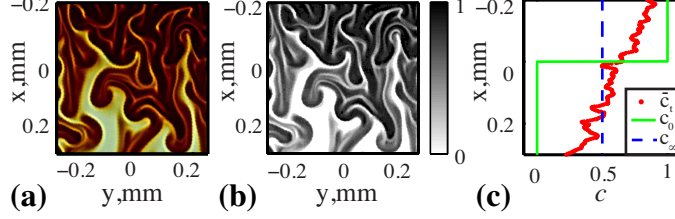


Figure 2.25: Example of image analysis sequence for finding concentration distribution. (a) Original image  $I$ . (b) Concentration plot  $c$ , found via Beer-Lambert law. (c) Spatially averaged concentration  $\bar{c}$  calculated with Eq. 2.9 is marked with dots, while theoretical initial state  $c_0$  and final mixed state  $c_\infty$  are marked with solid and dashed lines.

Data are analyzed in a  $0.5 \times 0.5$  mm<sup>2</sup> area around the miscible interface. To characterize a mixing system quantitatively, information on concentration distribution is necessary. Accordingly, the original image  $I_t(i, j)$ , where  $t$  is time, and  $i$  and  $j$  denote spatial indexes with the total length  $N = 360$  px for both  $x$  and  $y$  axes (see figure 2.25 (a)) is first converted to a concentration field  $c_t(i, j)$  (see figure 2.25 (b)) as previously via (2.8). A spatially averaged concentration  $\bar{c}_t(i)$  is then calculated from the concentration data, to characterize concentration in the mixing direction along  $x$  axis (see figure 2.25 (c)):

$$\bar{c}_t(i) = \frac{1}{N} \sum_{j=1}^N c_t(i, j). \quad (2.9)$$

To quantify mixing dynamics, mixing efficiency  $M_{\text{eff}}(t)$  is defined as follows:

$$M_{\text{eff}}(t) = 1 - \frac{\sqrt{\frac{1}{N} \sum_{i=1}^N (\bar{c}_t(i) - c_\infty(i))^2}}{\sqrt{\frac{1}{N} \sum_{i=1}^N (c_0(i) - c_\infty(i))^2}}, \quad (2.10)$$

where  $c_0$  and  $c_\infty$  are theoretical concentration distributions before mixing starts ( $t = 0$ ) and when mixing has finished ( $t \rightarrow \infty$ ) (see figure 2.25 (c)). Definition of  $M_{\text{eff}}$  is a slight variation of other measurements from literature, e.g. mixing ratio [62] and percentage mixed [64], adjusted for better representation of the experimental data.

The experiment involves an interface formation, which creates a slightly mixed state that differs from one time to another, due to the experimental limitations instead of a theoretical step like concentration distribution  $c_0$ , as already discussed in the previous section, when estimating  $t_0$ . We remove this influence by introducing a relative mixing efficiency  $M_r(t)$  for  $t > t_0$ , which subtracts the mixing efficiency that has been made due to the interface formation. This value  $M_{\text{eff}}(t_0)$  is taken at a manually chosen time  $t_0$ , when it can be seen that the interface formation is finished (typically  $t_0 = 0.04$  s):

$$M_r(t) = M_{\text{eff}}(t) - M_{\text{eff}}(t_0). \quad (2.11)$$

Snapshots of magnetic micro-convection development at several time moments used for mixing evaluation can be seen in figure 2.26 (a). As seen already before, larger field provokes

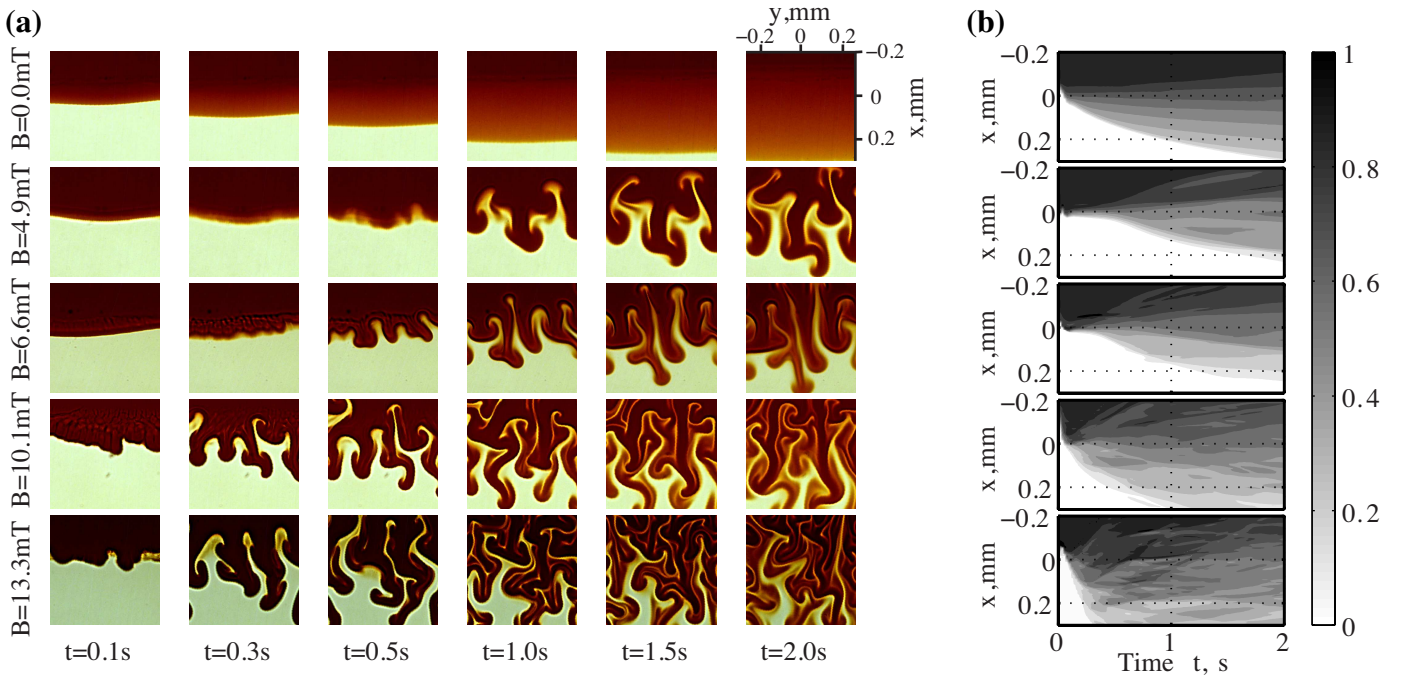


Figure 2.26: (a) Snapshots of the magnetic micro-convection development at several times for various applied magnetic fields  $B$ . The field of view is  $0.5 \times 0.5 \text{ mm}^2$ . (b) Spatially averaged concentration time dependence for the same magnetic fields as in (a) qualitatively revealing mixing enhancement and dynamics.

a faster evolution of the instability, hence, it enhances mixing. It becomes more apparent, when one observes the spatially averaged concentration  $\bar{c}_t$  dynamics, shown in figure 2.26 (b) contour plots. In the case of diffusion ( $B = 0$ ), more than 2 seconds are needed for mixing to change the initial concentrations  $c_0$  near the edges of the  $x$ -axis  $0.5 \text{ mm}$  field of view, whereas for the largest field  $B = 13.3 \text{ mT}$  it happens in less than  $0.5 \text{ s}$ . Clearly, an increase in the field strength increases the mixing development, although, interface formation influence makes it less notable.

A more quantitative result of the magnetic micro-convection influence can be seen in figure 2.27 (a), where relative mixing efficiency  $M_r(t)$  is showed for a range of magnetic field values. Achieved  $M_r$  values might seem small, but it is important to remember its definition (equations 2.10&2.11) and the experimental cell, which is much larger than the considered field of view ( $0.5 \times 0.5 \text{ mm}^2$ ) and accordingly has two large basins of the original concentrations, making it very long to reach completely mixed state. Overall, small fields ( $B < 7 \text{ mT}$ ) seem to enhance mixing over diffusion only slightly, while further increase of magnetic field boosts mixing. This can be explained by Fig.2.27 (b), where relative mixing efficiency is plotted as a function of magnetic field squared for several time values. Data points in graph agree well with the fitted lines, implying mixing efficiency to be square dependent on the field. This result is consistent with the findings of the field dependence of magnetic micro-convection characteristics in the previous section.

Magnetic field influence on mixing can be analyzed by observing the change in slopes of the fitted lines in figure 2.27 (b). The slopes are  $0.7$ ,  $2.0$ ,  $2.0$ ,  $1.7$  and  $1.5 \times 10^{-3} \text{ mT}^{-2}$  for  $0.1$ ,  $0.3$ ,  $0.5$ ,  $1.0$  and  $2.0 \text{ s}$  time values respectively. The variation in slopes for different times arises from the phenomenon and diffusion interplay. At small, but finite times ( $t = 0.1 \text{ s}$ ,

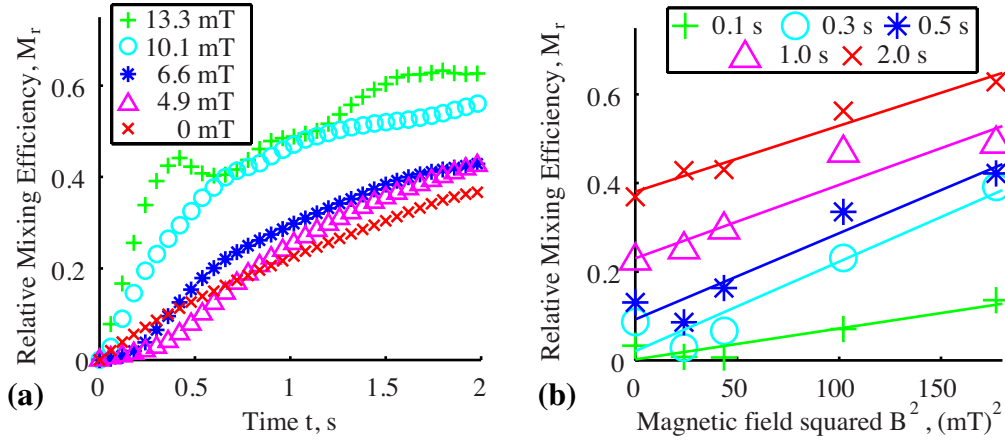


Figure 2.27: (a) Relative mixing efficiency as a function of time for various magnetic fields. A clear mixing enhancement is visible. (b) Relative mixing efficiency as a function of magnetic field squared for various time moments.

$t = 0.3$  s), the instability forms and enhances mixing, increasing the slope until a maximum. Afterwards ( $t > 0.5$  s), a slow decrease of the slope can be seen, as the concentrations tend to equate. In addition, these fits offer an estimate of the relative mixing efficiency after a selected time as a function of magnetic field. For example, after  $t = 0.5$  s (linear fit for data marked with asterisk in figure 2.27 (b)):

$$M_r(t = 0.5 \text{ s}) = 0.002 \times (B[\text{mT}])^2 + 0.092, \quad (2.12)$$

which is valid for this particular system with  $B < 20$  mT.

A direct comparison between the magnetic micro-convection and other active mixing methods for magnetic/non-magnetic fluid systems is difficult due to the different geometries and fluids used. Wen et. al [62], where mixing in a microchannel is achieved with an AC magnetic field, has mentioned that the characteristic fingers reach both channel walls, which are  $\Delta x = 0.15$  mm apart, after  $t = 0.5$  s at  $B = 14.6$  mT. In comparison, after the same time and a similar field strength, we have observed that fingers created by micro-convection are  $\Delta x = 0.5$  mm long, which is 3 times more, although the particle concentration and the initial susceptibility for our magnetic fluid is smaller. Partly this comes from the differences in thicknesses. In Zhu et al. [63] mixing with an in-plane DC field is achieved in a reservoir with a 0.5 mm radius. The mixing efficiency in this paper is insufficiently explained, allowing us only to surmise that magnetic micro-convection creates instabilities in similar length and time scales for alike magnetic fields.

The results showed above clearly indicate the advantages of using magnetic micro-convection for mixing. It is very simple to realize it in an already existing microfluidics setup, by adding small coils in the desired place of mixing, as proposed in figure 2.28.

To test this concept, a preliminary experiment has been made in a simple continuous flow microfluidics setup as similar as possible to the proposed concept. The flow cell is made of a 'Y' shape cut in a single Parafilm M® layer ( $20 \times 50 \text{ mm}^2$ ) with two inlet channels ( $\approx 5 \times 20 \text{ mm}^2$ ) having a  $\approx 15^\circ$  angle between them that join in a common outlet channel ( $\approx 10 \times 20 \text{ mm}^2$ ). Two glass slides are welded together with this layer using the same method as described as described previously, making a flow cell with a 0.12 mm thickness. The upper glass slide has glued metal tubing connections for inlets (magnetic fluid and water)

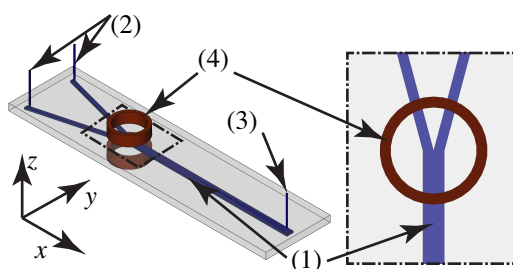


Figure 2.28: A proposed test setup with microfluidics channel (1), inlets (2), outlet (3) and small coils (4)

and outlet. Syringe pump produces a  $v = 0.15$  mm/s flow in  $x$  direction over the field of view, as determined with a micro PIV method and setup, described in § 2.1.1.

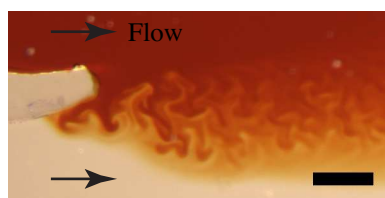


Figure 2.29: A preliminary test of mixing with magnetic micro-convection in a simple microfluidics flow cell. Scale bar is 0.5 mm.

Magnetic micro-convection in the flow cell test (see figure 2.29) creates a similar pattern as seen above, most likely inducing a comparable mixing enhancement. A more detailed study in specially designed microfluidics channels should be performed to characterize the applicability of the phenomenon in specific systems, but the concept and its benefit has been showed.

In these experiments the magnetic field is created with a coil system, because it can be easily installed on a microscope stage, without blocking the observation ability of the microscope. Besides, the field strength is adjustable with a power supply and does not involve any moving parts on the microscope stage. However, a homogeneous magnetic field needed for evoking magnetic micro-convection can also be obtained differently. For example, permanent magnets can be advantageous in applications where a connection to a power supply is impossible and a flexible adjustment of the used field is not needed. In addition, they can provide high fields while having a small size. Another apparent method is micro-fabrication, where micro-coil or permanent magnet systems can be implemented in the microfluidics chip during its production. In fact, the magnetic field source should be selected after considering the requirements of the desired application and the critical field, discussed in the previous section, needed for the magnetic micro-convection.

A limitation of boosting mixing by increasing the magnetic field strength comes from the saturation of magnetic fluid particle magnetization. It is efficient to increase the field only during the linear regime, which can be found from the magnetic fluid magnetization curve (§ 1.2.3) and is  $B_{\text{sat}} \approx 20$  mT for this particular magnetic fluid.

Magnetic nanoparticles are well known in many scientific and clinical applications [65]. As magnetic fluid is a colloid that consists of magnetic nanoparticles, it should be possible

to realize magnetic micro-convection with any magnetic particle ensemble, if colloidal, magnetic and setup properties are properly combined. For example, we can consider a colloidal dispersion of magnetic particles that is functionalized with antibodies. Mixing it with an analyte in a microfluidics flow cell by using the magnetic micro-convection should decrease the time needed for cell or biomolecule magnetic labeling. Together with a consecutive magnetic sorting and subsequent analysis, an accelerated immunoassay test in a lab on a chip system can be achieved. Other possible applications are in speeding up sorting mechanisms based on ferrohydrodynamics [66] or increasing the mixing speed of selected tracers that are suspended in the magnetic fluid.

## 2.4 Difficulties and study possibilities in future

An extensive experimental investigation of the magnetic micro-convection has been described in this chapter. It has allowed to characterize this instability quantitatively and show that the Brinkman model is valid at least at small times. Additionally, the possibility to use this phenomenon for mixing enhancement has been showed.

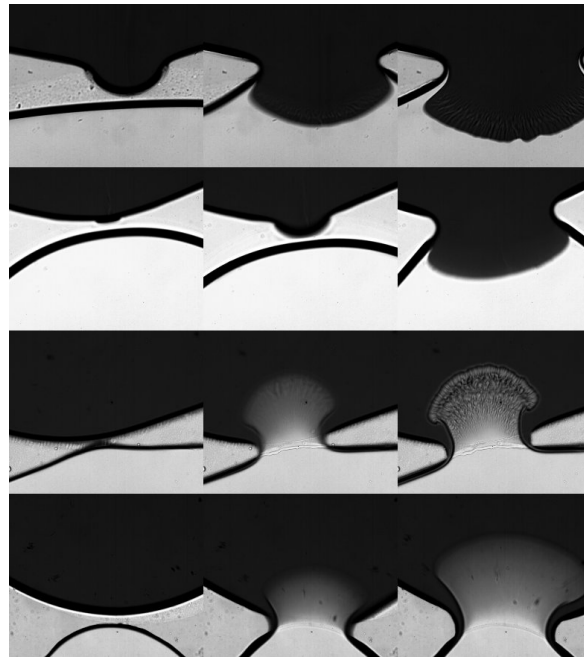


Figure 2.30: Mishaps during interface formation. Each row contains an image sequence with 0.04 s between two consecutive images.

The improved experimental system, described in § 2.2, allowed to obtain good experimental results. However it has an evident drawback - the interface formation during droplet merging depends on a large number of various factors, therefore it is very difficult to control. Only about one of every three experiments leads to a nicely formed interface. Some examples of such mishaps are showed in figure 2.30.

A possible solution for the interface formation problem is to realize this experiment in a continuous microfluidics setup which would provide a continuous interface. However, the speed of flow and its parabolic profile complicate may be needed to add to the theoretical description. The first successful tests of magnetic micro-convection in microfluidics were

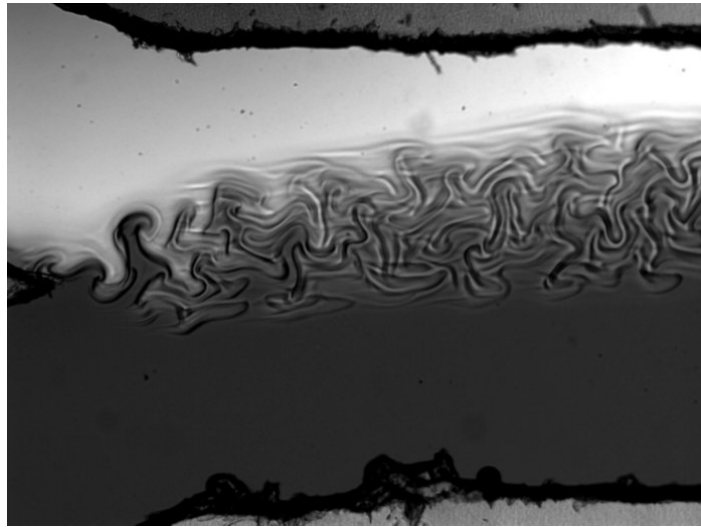


Figure 2.31: Magnetic micro-convection is realized in a microfluidics flow cell. The field of view is  $2.2 \times 1.7$  mm.

realized only at the very end of this dissertation (see an example in figure 2.31), hence it was not possible to do quantitative measurements.

Nevertheless, this offers multiple directions where this study can be continued. For example, a continuous experiment with certain periodicity will allow to collect statistics on the instability characteristics. Ability to look at the growth of a single micro-convection finger should give access to the microscopic flow, if tracer particles are added and PIV method is used.

Research could be continued also in the direction of possible applications. It would be of high interest to see if magnetic micro-convection can be realized with larger magnetic particles which are used for magnetic separation [67]. Accordingly, lab on a chip devices for rapid mixing and subsequent separation of magnetic particles might be useful to improve the speed of analysis.



## Chapter 3

# Particle diffusion in magnetic fluids

Diffusion is a phenomenon caused by random motion of molecules. All molecules for temperatures higher than absolute zero molecules exhibit thermal motion of a random character, however this process is more dependent on the physical state of the molecules than the temperature. Thermal motion for molecules in liquid state is notable, while it is much more pronounced in gas phase and very limited in solids [68].

Here the investigation concerns a system of nano-sized magnetic particles dispersed in a carrier liquid, as introduced in chapter 1. Carrier liquid, being water, and the resulting system is considered as an incompressible Newtonian fluid. Having no viscoelastic or other complex contributions to take into account, a simpler theoretical description can be used and is described here further. Thermal motion of water molecules forces each magnetic particle to continuously change its orientation and position in time, which are accordingly called rotational and translational diffusion [68]. In this study only the latter is considered, as it is the limiting factors of the magnetic micro-convection, studied extensively in chapter 2.

Although the effect of diffusion can be observed even in macroscopic scale, its nature arises from the microscopic level. Accordingly, the description of diffusion can be done for both macroscopic and microscopic scales, and only their combination allows a sufficient comprehension of the processes.

The diffusive movement of a single magnetic particle in water corresponds to a random walk. Its mean square displacement  $\langle x^2 \rangle$  increases linearly with time  $t$  and the coefficient of proportionality is a multiplication of the number of directions of motion and the diffusion coefficient  $D$  [56]. For a one dimensional case it is

$$\langle x^2 \rangle = 2Dt, \quad (3.1)$$

where 2 corresponds to the possible back and forward direction of motion in one dimension. The diffusion coefficient represents the ability of a particle to explore the area around it. Accordingly, a larger coefficient indicates that the particle on average will explore a larger area in a given time. Besides, it is worth to remark that an average distance for diffusion process is hence proportional to  $\sqrt{t}$ .

The diffusion coefficient  $D$  depends on the particle size and the solvent properties. If there is no interparticle interaction, they are linked with the Stokes-Einstein equation [56]

$$D = \frac{k_B T}{3\pi\eta d}, \quad (3.2)$$

where  $k_B$  is the Boltzmann's constant,  $T$  is the temperature,  $\eta$  is the solvent viscosity and  $d$  is the diameter of the spherical particle. This relation is utilized in numerous applications, including particle characterization when the solvent properties are known, as shown for

the Dynamic Light Scattering method in § 1.2.2, or together with (3.1) in investigation of the properties of complex fluids with viscoelastic properties[69], using the framework of microrheology [70]. However, here the interest is limited to the diffusion of magnetic particles in magnetic fluid.

Additionally, it should be emphasized that here magnetic field effects on diffusion are not taken into account. In reality, the diffusion coefficient of magnetic fluid particles is field dependent [71]. However, this dependence is moderate, usually being up to two times larger or smaller depending on the direction of motion with respect to the field, and can be observed for larger fields. Measurements in this chapter are performed with no applied field. Largest magnetic fields that are used in the study of magnetic micro-convection in chapter 2, where the investigation of diffusion coefficient is also important, are less than 150 Oe, causing a difference in diffusion coefficient less than 10%. Hence, neglecting these effects is a reasonable simplification.

A diffusion of an ensemble of particles leads to a change of the particle positions, hence their concentration. If this concentration is initially homogeneous, then diffusion only results in local concentration fluctuations. But if the initial particle concentration has a certain pattern, then diffusion smears it out. When initial pattern is sufficiently large, the resulting change is visible macroscopically. The process of particle diffusion in a case of concentration gradient can be described with the second Fick's law [72]

$$\frac{\partial c}{\partial t} = D\Delta c, \quad (3.3)$$

where  $\Delta$  is the Laplacian operator,  $c$  and  $D$  are the concentration and diffusion coefficient of the diffusing species and  $t$  denotes time.

This chapter summarizes the efforts put to understand the reasons behind the large effective diffusion coefficient encountered in the magnetic micro-convection experiments in chapter 2 and § 2.2 in particular. Here below is the line that is followed in this chapter.

The deduction of the enhanced diffusion coefficient from the critical field of the magnetic micro-convection threshold is described in § 3.1. It is followed by the investigation of the magnetic fluid diffusion on a step-like interface in § 3.2, relevant for the magnetic micro-convection. First, corresponding experiments in the experimental setup of the magnetic micro-convection with no field applied, described in § 3.2.1, approved the existence of the increased effective diffusion. The reasons behind this are searched and a hypothesis based on the diffusio-phoresis phenomenon, described in § 3.2.2, is made.

To verify this, special magnetic fluid samples with varied ionic strength are made and new measurements with these samples and water and citrate solutions in water as the miscible fluids are performed, as described in § 3.2.3. These experiments do not give a definite answer to the hypothesis and are repeated in a microfluidics flow cell, to remove the influence of the interface formation effects. Results from the experiments in microfluidics, summarized in § 3.2.4 disprove the hypothesis, as the effective diffusion does not disappear, although slight differences for the different samples are observed.

Thus, the influence of gravity by inducing a convective flow because of the difference in fluid densities, as proposed in [48], is revisited. A quick estimation of the theoretical values using the better defined experimental system shows a good agreement with the characteristics of the observed phenomena. Consequently, a careful investigation on this effect is carried out in § 3.2.5. Numerical simulations and experimental demonstration prove that the small density difference between magnetic fluid and the miscible non-magnetic fluid creates a convective flow. This flow makes the average concentration profile with a particular shape,

while its dynamics resembles a diffusive process with a large diffusion coefficient as compared to that of single magnetic particles.

In parallel, the diffusion coefficient of particles in magnetic fluid is determined with other methods available in both labs to provide a justified comparison for the main experiments. Magnetic fluid is investigated with a forced Rayleigh scattering setup, as described in § 3.3. A careful estimation of the single particle diffusion coefficient is carried out in § 3.4. Even an adapted version of fluorescence recovery after photobleaching method was tried with the available magnetic fluid functionalized with fluorescent dyes and is presented in § 3.5.

### 3.1 Estimation from the critical field of the magnetic micro-convection

The magnetic micro-convection, as explained in chapter 2, develops on the miscible interface of magnetic and non-magnetic fluids if the magnetic field is larger than the critical. Precise experimental measurements in § 2.2 and figure 2.15 in particular indicate that the critical field for magnetic fluid *D107* for the particular conditions is  $H_{crit} = 19 \pm 1$  Oe. Alternatively, the neutral curve of the linear stability analysis of the magnetic micro-convection in the framework of the Brinkman model, as visible in figure 3 in [49], given in appendix E, suggests that the critical field for no initial smearing corresponds to the  $1/Ra_m \approx 0.16$ . That is,  $Ra_m^{crit} \approx 6$ . The experimentally estimated smearing time of the diffusion front  $t_0 \approx 0.05$  s, when converted to dimensionless units is approximately  $5.7 \cdot 10^{-3}$ . This value is close to zero, and thus in agreement with  $t_0 = 0$  used for critical  $Ra_m$  determination.

Hence, as the magnetic Rayleigh number is defined as  $Ra_m = M_0^2 h^2 / 12\eta D$ , where magnetization  $M_0 = \chi H$  it is possible to estimate the diffusion coefficient

$$D = \frac{\chi^2 H_{crit}^2 h^2}{12\eta Ra_m^{crit}}. \quad (3.4)$$

Knowing all quantities from § 1.2.5 and § 2.2, i.e. cell thickness  $h = 0.012$  cm, viscosity  $\eta = 1$  cP, susceptibility  $\chi = 0.016$  and previously mentioned  $Ra_m^{crit} = 6$  and  $H_{crit} = 19$  Oe one finds  $D = 1.7 \cdot 10^{-5}$  cm<sup>2</sup>/s. The obtained value, while much larger than that of an individual particle in water, is of the same order of magnitude as the one found in the measurements described in the initial measurements of the next section and lead to the study summarized in this chapter. This diffusion coefficient is also used in comparing the experimental and numerical simulation results in § 2.2.2 and discussion of [49], which can be found in appendix E.

### 3.2 Magnetic fluid diffusion on an interface with a concentration step

If an experiment with a magnetic fluid and a non-magnetic fluid is performed in the experimental setup of the magnetic micro-convection described in § 2.2 with no magnetic field applied, one would expect to observe magnetic particle diffusion until the magnetic particle concentration in the whole fluid equalizes.

This experimental situation corresponds to a one-dimensional case of a step-like initial concentration pattern ( $c = c_0$  for  $x \leq 0$  and  $c = 0$  for  $x > 0$  at  $t = 0$ ). Solving the second Fick's law (3.3) with the mentioned initial conditions and boundary conditions ( $\frac{\partial c}{\partial x}|_{x=-\infty, t=}$

0 and  $\frac{\partial c}{\partial x}|_{x=+\infty, t} = 0$  gives an analytical expression for concentration value  $c$  at any position  $x$  and time  $t$  [72]

$$c(x, t) = \frac{c_0}{2} \left[ 1 - \operatorname{erf} \left( \frac{x}{2\sqrt{Dt}} \right) \right], \quad (3.5)$$

where  $D$  is the diffusion coefficient and  $\operatorname{erf}$  is the error-function, defined as

$$\operatorname{erf}(x) = \frac{2}{\sqrt{\pi}} \int_0^x e^{-t^2} dt.$$

Additionally, the quantity named diffusion length  $\delta$  that gives a measure for the propagation of the diffusion can be defined

$$\delta = 2\sqrt{Dt}. \quad (3.6)$$

The diffusion should be a slow process, as the characteristic diffusion coefficient for particles of a size around  $\approx 10$  nm is of the order  $\approx 10^{-11}$  m<sup>2</sup>/s, giving a characteristic diffusion length  $\delta \approx 0.3$  mm for one hour. However, the experiments below indicate that this happens much faster.

### 3.2.1 Initial measurements

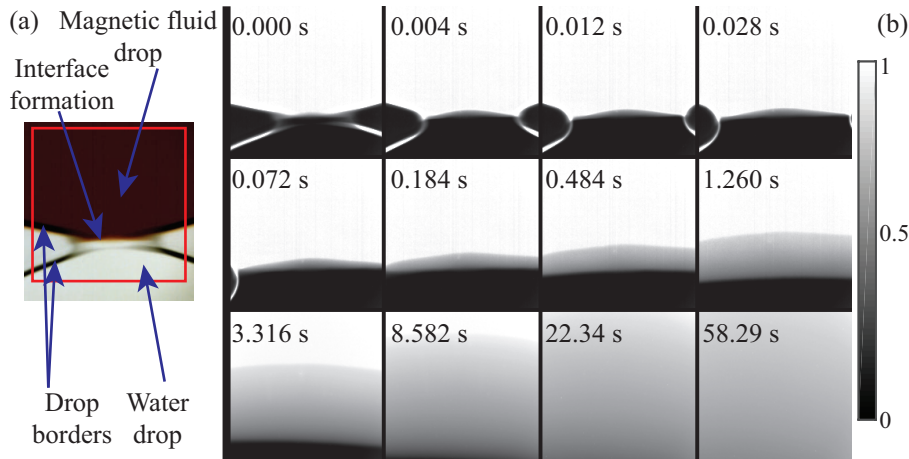


Figure 3.1: Initial measurements. (a) Single image of interface formation at  $t = 0$  s. Important objects are pointed with arrows. Red rectangle marks the analyzed area. (b) Time-series of magnetic particle concentration density plots of the mixing on the interface of magnetic and nonmagnetic fluids. The field of view for each image is  $1.05 \times 1.08$  mm<sup>2</sup>. Droplet borders appear white until the interface has become larger than the field of view.

Experiment of the mixing of magnetic and non-magnetic fluids in a Hele-Shaw cell with no magnetic field is performed in the experimental setup described in § 2.2 and figure 2.12. Similarly to experiments of the magnetic micro-convection, the cell is initially half filled with distilled water. Then the magnetic fluid *D107* is slowly introduced with a microfluidics pump until both fluid drops merge and form an interface, over which the magnetic particles start to mix. Also here the mixing of fluids is observed with two cameras simultaneously. For easier comparison images are converted to concentration plots via (2.8). A time-series of normalized concentration plots of the initial measurement can be seen in figure 3.1.

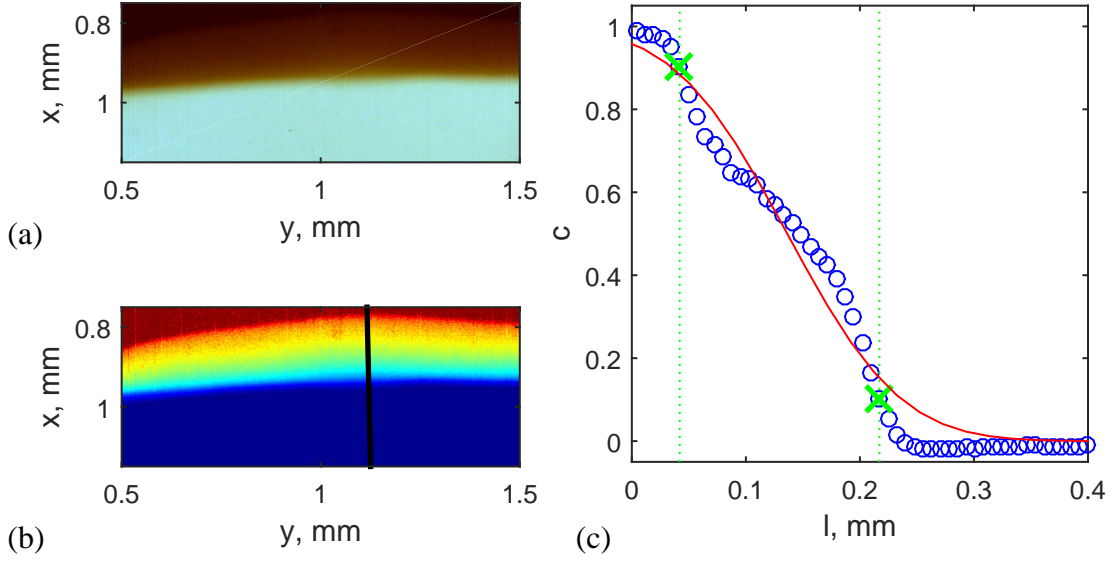


Figure 3.2: Analysis example of the mixing process on the interface of magnetic and nonmagnetic fluids at  $t = 1$  s. The acquired image (a) is converted to the normalized concentration density plot (b), in which a characteristic line (black) is drawn. The normalized concentration profile (blue circles) along the interface is extracted on this line. It can be further analyzed by fitting with a solution for diffusion (red line) or finding the double diffusion length  $2\delta$  (distance between the green crosses).

The obtained data are analyzed to access the information of the mixing process. Analysis process is characterized in figure 3.2. After converting the initial image (a) to the normalized concentration plot (b), a characteristic line is defined along the mixing interface. Selection of this line can be easily automated by defining it along a radius of an arc fitted on a constant concentration level. The concentration profile is the extracted along this line (c).

The information from the concentration profile can then be further processed to characterize the mixing process. One option is to fit it with the solution of the diffusion equation (3.5) finding the diffusion length  $\delta$ . However, the fit (red line in figure 3.2 (c)) does not seem to resemble the shape of the experimentally measured concentration profile. Therefore it is proposed to quantify the mixing with a quantity named double diffusion length  $2\delta$  which is defined as the distance between the points on the concentration profile as defined by

$$2\delta(t) = x(t)|_{c=0.5(1-\text{erf}(+1))} - x(t)|_{c=0.5(1-\text{erf}(-1))}. \quad (3.7)$$

It is worth to remark that these definitions should be complementary when the shape of concentration profile agrees well with the solution for normal diffusion in (3.5).

In both cases the relation of the diffusion length and time in (3.6) allows to access the diffusion coefficient  $D$ . As the diffusion length is proportional to  $\sqrt{t}$ , it is particularly convenient if the data are transformed to  $\delta^2/4 = D_\delta \cdot t$  and  $(2\delta)^2/16 = D_{2\delta} \cdot t$  respectively, as then the a linear relationship for the case of a diffusive regime is obtained and the coefficient of proportionality is the diffusion coefficient.

Experimental data in the previously introduced form are shown in figure 3.3. A linear dependence on time is clearly visible for both analyzed quantities. The coefficients of pro-

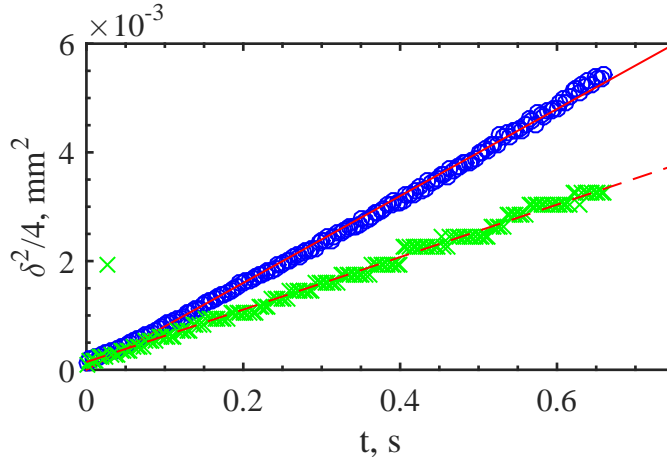


Figure 3.3: Experimental results on the mixing of magnetic and non-magnetic fluid interface indicates a diffusive behavior. Fit (red line) of the diffusion length  $\delta$  data (blue circles) gives a diffusion coefficient, which is slightly larger than the diffusion coefficient obtained with fitting (red dashed line) the data of the double diffusion length  $2\delta$  (green crosses).

portionality are  $D_\delta = 8.0 \cdot 10^{-5} \text{ cm}^2/\text{s}$  for diffusion length  $\delta$  and  $D_{2\delta} = 4.8 \cdot 10^{-5} \text{ cm}^2/\text{s}$  for double diffusion length  $2\delta$ .

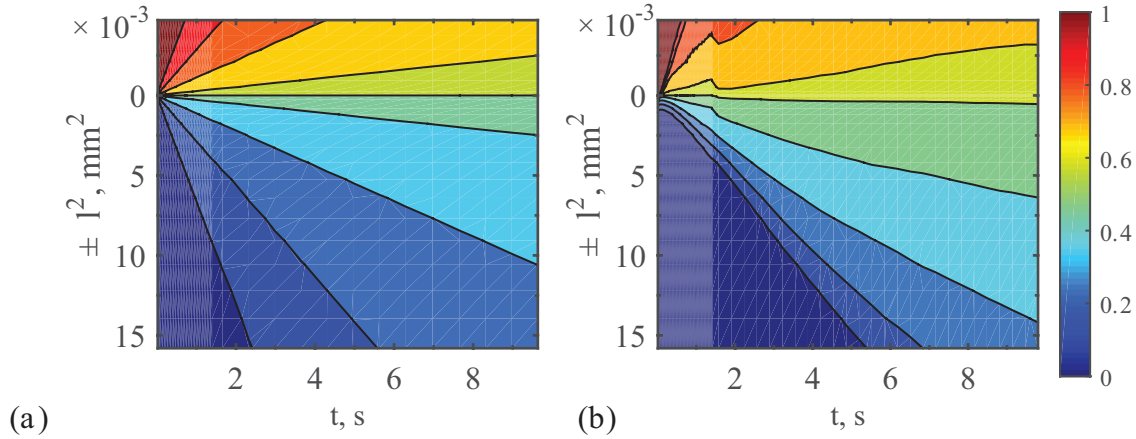


Figure 3.4: Concentration profile dynamics contour plot as  $c(\pm l^2, t)$ , where  $\pm l^2$  is defined in (3.8). (a) Theoretical result as calculated with (3.5) for  $D = 8.0 \cdot 10^{-5} \text{ cm}^2/\text{s}$ . (b) Data from an experiment with magnetic fluid *D107* and water.

An alternative way to represent the data on concentration profile dynamics  $c(x, t)$  is by displaying it with a two dimensional colored contour plot. Also here it is useful to transform the  $x$  coordinates to  $\pm l^2$  using

$$\pm l^2 = \frac{(x - x_0)^2}{4} \cdot \frac{(x - x_0)}{|x - x_0|}, \quad (3.8)$$

where  $x_0$  is the coordinate of the interface. This value has to be detected precisely, which is not always simple, because the merging of the two droplets is impossible to control precisely. Hence, a semi-automatic approach has been developed to remove the possible artifacts and is described in figure D.1.

Plotting concentration profile dynamics as  $c(\pm l^2, t)$  is effective to visually verify if the mixing process is proportional to  $\sqrt{t}$ , as then the lines corresponding to equal concentrations appear linear. It is clearly visible in figure 3.4 (a) where the theoretical concentration profile dynamics is displayed using the solution of the step-like concentration profile diffusion formula in (3.5) with a diffusion coefficient  $D = 8.0 \cdot 10^{-5} \text{ cm}^2/\text{s}$ . Next to it, in figure 3.4 (b), the experimentally measured concentration profile dynamics is showed. It also indicates a linear change of positions of equal concentrations. Small disparities can be seen at small times  $t < 1.5 \text{ s}$ , due to the impossibility to perfectly calibrate both cameras used in recordings.

A rather good qualitative agreement between the two graphs in figure 3.4 can be seen. However, at least two differences can be noted. First, the linear slopes for fixed concentrations are different in both cases, as the shapes of concentration profiles are also different, showed before in figure 3.2. Second, the propagation of magnetic particle concentration seems not to be symmetric in both directions, as compared to the solution in the ideal case.

Concerning the values of diffusion coefficients as obtained fitting the data in figure 3.3, they are much larger than could be expected. The Stokes-Einstein relation (3.2) for magnetic particles with a characteristic size  $d \approx 9 \text{ nm}$  (as found in § 1.2) gives  $D \approx 5 \cdot 10^{-7} \text{ cm}^2/\text{s}$ . Alternative measurements for the same magnetic fluid *D107* in § 3.3 and § 3.4 give the diffusion coefficient values  $2.3 \cdot 10^{-7} \text{ cm}^2/\text{s}$  and  $\approx 2.5 \cdot 10^{-7} \text{ cm}^2/\text{s}$ , which agree quite well with the value calculated by the Stokes-Einstein relation.

### 3.2.2 Hypothesis of the ionic strength influence

A conclusion from the observations, measurements and calculations above is that there is an additional effect present in this particular system that enhances mixing in a way that resembles diffusion. This enhanced diffusion can be described with an effective diffusion coefficient  $D_{\text{eff}}$ , which is measured to be  $\approx 200$  times larger than the diffusion coefficient of the individual magnetic particles.

The possible explanations of this effect were searched. The rapid smearing of the initial interface because of the gravitational effects as proposed in [48] was initially dismissed, as the control of the interface formation was substantially improved in the updated setup. Additionally, the observed effect was showing a diffusive time dependence ( $\sqrt{t}$ ) for times of few tens of seconds that correspond to the concentration propagation across the whole field of view.

Instead, a hypothesis was formed, proposing to attribute the diffusion enhancement to diffusiophoresis [73]. The magnetic fluids used here are stabilized with citrate ions, as described in § 1.1. To keep the citrate ions present on the surface of particles, an excess free citrate has to be present in the surrounding liquid. The free citrate is added by dissolving an additional trisodium citrate, which dissociates into ions. For the magnetic fluid *D107* the ionic strength and free citrate concentration is particularly large, as revealed by measurements in § 1.2. As a result, when the magnetic fluid is put in contact to a miscible fluid, the free citrate ions should diffuse towards the miscible non-magnetic liquid. This citrate diffusion might create an effect similar to recent findings in diffusiophoresis, where an enhanced movement of silica spheres of 200 nm size was observed along a salt gradient [74, 75].

To verify this, special magnetic fluid samples with varied ionic strength were made from the initial magnetic fluid *D107* in the Paris lab. It is possible by using osmotic compression [17]. Sample information on the free citrate concentrations and magnetic particle volume fractions deduced by titration method are summarized in table 3.1. Description of additional mixing experiments with these magnetic fluid samples and water or citrate solutions in water

Table 3.1: Magnetic fluid samples with varied ionic strength as the free citrate concentration  $[cit]_{free}$  made from the magnetic fluid *D107* given with their volume fraction  $\Phi$  and density  $\rho$ .

Nr.	$[cit]_{free}$ , M	$\Phi$ , %	$\rho$ , g/mL
1	0.18	2.8	1.13
2	0.03	2.4	1.10
3	0.0024	2.9	1.08

and their results are showed further.]

### 3.2.3 Merging of two droplets

The experimental measurements were continued in the same system as was described in § 3.2.1. Differently, here pairs of miscible fluids with ionic strengths of different magnitudes were used. Magnetic fluid samples were already described in table 3.1. The other fluid was either water or three different trisodium citrate solutions in water. They are different with free citrate concentrations  $[cit]_{free}$  which are fixed at 0.00 M for distilled water and 0.0024 M, 0.03 M and 0.18 M. As before, the non-magnetic fluid here being citrate solution in water is brought to the middle of the Hele-shaw cell. Then the magnetic fluid is slowly introduced until both droplets merge and an interface is formed. The mixing process happening on an interface is here recorded only with the slower *Lumenera 165c* camera, as framerate 15 Hz is sufficient for the investigated process. A special program using LabView programming language is made to precisely control the continuous recording (see Appendix B.1.3). It addresses a special care to saving the images and their acquisition times, as the computer recording speed can produce lost frames from time to time.

As already mentioned before in § 2.4, even after the improvements of the experimental setup, the interface formation is difficult to control. Also here on average only every third experiment results in a nicely formed interface that is worth to record and use in later analysis. Besides, the interface is not always formed in the place where it is expected and it is necessary to move the microscope stage to change the field of view during experiment. Nevertheless, several image series for some pairs of fluids were recorded. They look similar to images in figure 3.1, but have different curvatures of the initial interface, making it difficult to compare without image analysis.

Here the analysis process is improved by using a larger area to obtaining the concentration profile information. An arc of interest is specified around the single line, which is defined as in figure 3.2 (b). Instead of retrieving the concentration profile on the single line, it is obtained from this arch by averaging the concentrations for equal radii. Resulting concentration profiles do not differ much for both processing methods, but a reduction of image noise and minimization of dirty spot influence is achieved with the latter one. This allows to increase the image analysis automation, which is essential here because of the large amount of data.

The obtained concentration profile dynamics for several fluid pairs in the form of  $c(\pm l^2, t)$  (for  $\pm l^2$  see (3.8)) is shown in figure 3.5. The title for each plot indicates the free citrate concentration in the fluids, where the first value is for magnetic fluid, but the second for citrate solution in water. In the cases when the microscope stage was moved during process recording, the data during stage motion are not considered (white areas in the plots), but the important interface coordinate  $x_0$  for the next position is found by locating the coordinate in the first concentration profile after movement at which the concentration is equal to the

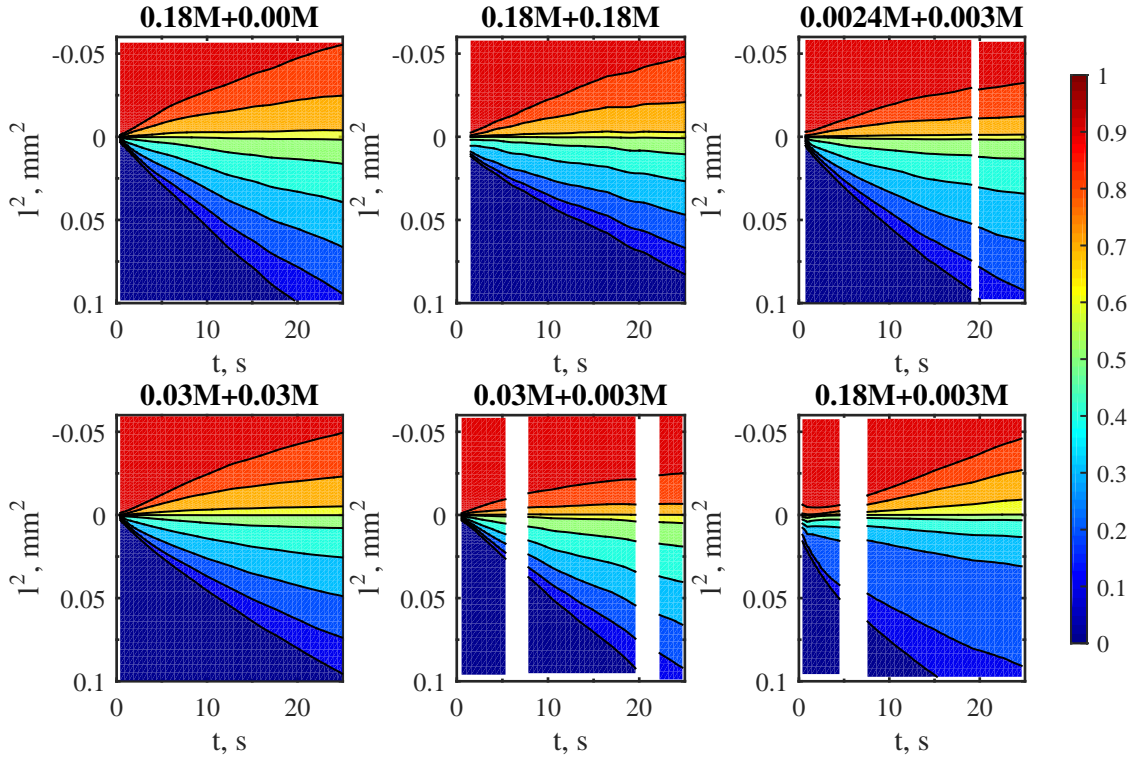


Figure 3.5: Contour plots of concentration profile dynamics during mixing of several pairs of magnetic fluids and citrate solutions in water. The title of each plot denotes the free citrate concentration in magnetic fluid and the citrate solution.

concentration at the interface coordinate in the last concentration profile before movement. This method seems to work well, as the resulting plots of concentration profile dynamics seem continuous.

Results in figure 3.5 show a similar behavior as was seen in the initial measurements. Lines of equal concentrations seem parallel in most cases, with tiny exceptions at times larger than  $t > 15$  s. The free citrate concentration seems to have an influence as the different pairs of fluids have different results. However, these differences are rather small and seem to strongly depend on the quality of the interface formation. Even the results of several measurements of the same fluid pair (not shown) show only a moderate agreement, most probably because of the influences from the interface formation.

Concentration profiles of the same pairs of fluids at several time moments are shown in figure 3.6. These profiles look very similar for most experiments and seem to preserve the shape with time, but, as noticed earlier, are very different from the error function shape, which is the expected solution for normal diffusion. Additionally, it can be seen, that normalized concentration value at the interface coordinate is  $c \approx 0.6$ , which indicates that the process indeed is not symmetrical.

These results imply that the effect of interface formation has to be removed, as it is impossible to control the local wetting, surface tension, pressure and other parameters in the area where droplets are merging in such a simple experimental setup. An alternative is to put this experiment in microfluidics system, which is tried further in § 3.2.4.

It is interesting to remark that during these experiments conditions at which the magnetic colloid becomes unstable and starts to coagulate were found. An image of this process during

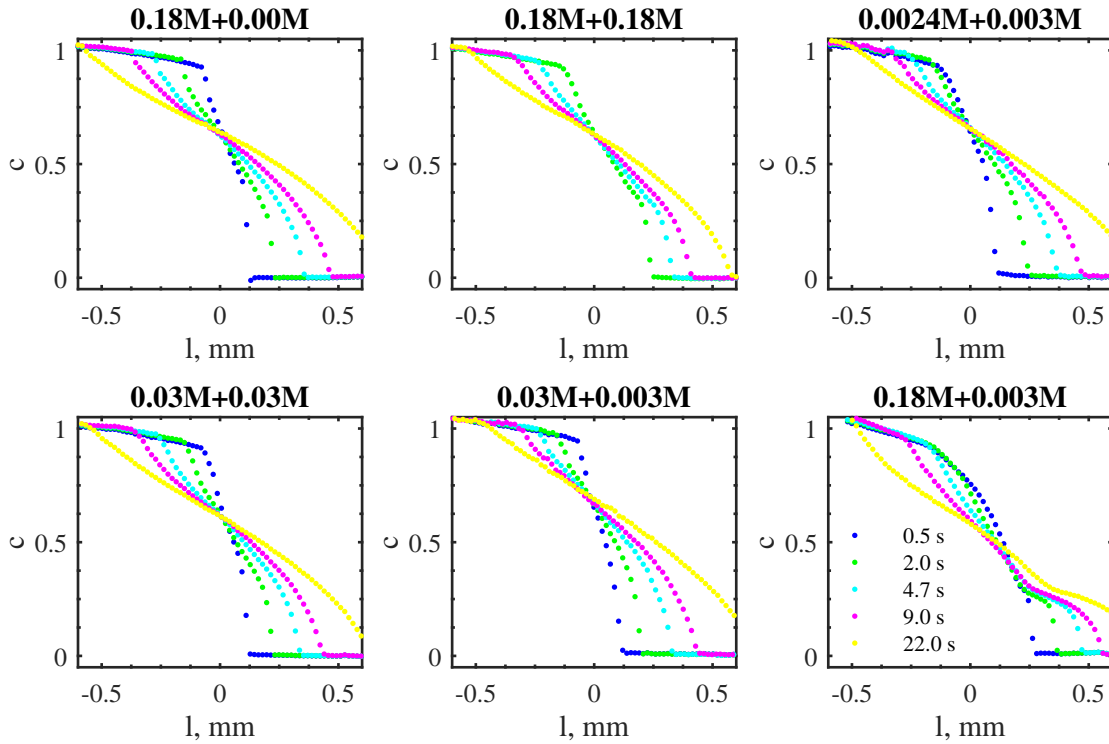


Figure 3.6: Concentration profiles at several time moments for several pairs of magnetic fluids and citrate solutions in water. The title of each plot denotes the free citrate concentration in magnetic fluid and the citrate solution. White areas correspond to invalid measurements during the stage motions.

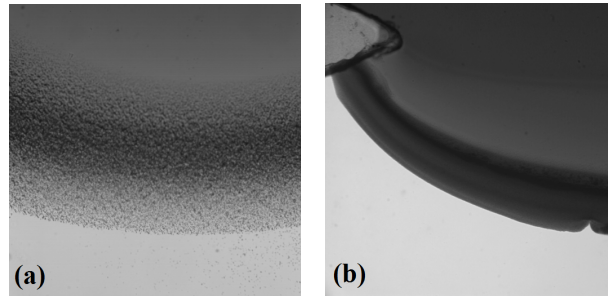


Figure 3.7: Coagulation of particles of magnetic fluid when mixing happens between a magnetic fluid of an extremely low free citrate concentration 0.0024 M and a very concentrated citrate solution in water with the free citrate 0.18 M as seen (a) during droplet merging and (b) experiments in microfluidics flow cell. Both images correspond to  $1.2 \times 1.2 \text{ mm}^2$

drop merging experiment can be seen in figure 3.7 (a). It happened for a magnetic fluid of a very low free citrate concentration 0.0024 M mixing with a citrate solution in water with a very high concentration 0.18 M. This is most probably related to the fact that the Debye length of colloidal particles, which characterizes the electrostatic interaction range, strongly depends on the ionic strength of the system [76]. A large number of free ions from the citrate solution in water can quickly penetrate the volume around magnetic particles in the magnetic fluid with low free citrate concentration, compensating their charge. This might result in

partial disappearance of repulsive forces, that lead to opportunity of magnetic particles to meet and coagulate. Nevertheless, this process should be addressed in a separate study.

### 3.2.4 Continuous microfluidics

To remove the interface formation effects during mixing of fluids in a Hele-Shaw cell, a transfer of the experiment to a microfluidics system is considered. The concepts of microfluidics were already introduced in § 2.3. Also a suitable system of Y channel system for this demand was already proposed in § 2.3.1 figure 2.28. The two inlets should be connected to syringes that contain magnetic fluid and citrate solution in water in the same way as for merging the droplets experiments. If the syringe pump is now run continuously, both fluids flow first in the separate channels which later merge and form a continuous interface where the investigated phenomenon should be observable.

Although the microfluidics system has a clear advantage in forming a continuous interface, two apparent drawbacks can be expected, as a pressure driven system is planned to be used. First, it is impossible to characterize the very beginning of the process, as the tip of the two channels connection point is not infinitely small. Second, a continuous fluid flow will have a friction on the walls, leading to a parabolic velocity profile along the channels and notable velocity distortion around the tip mentioned in the previous sentence. Nevertheless, these effects can be neglected using a wide microchannel at slow flow speeds and analyzing only the data that are obtained slightly away from the tip.

Many possible ways of producing microfluidics systems are described in literature. Convenient methods utilize a poly(dimethylsiloxane) (PDMS) material, as it allows to use soft lithography methods [77]. Combining it with the rapid prototyping [78, 79] gives a fast and reproducible way to produce any desired two dimensional microfluidics system in a reasonable period of time. However, it requires access to cleanroom facility that is equipped with lithography tools in order to produce a mold that is later used in replicating the pattern of channels. Unfortunately, the groups in Riga and Paris had no experience in this field, making it expensive and time consuming to obtain a microfluidics system using these methods.

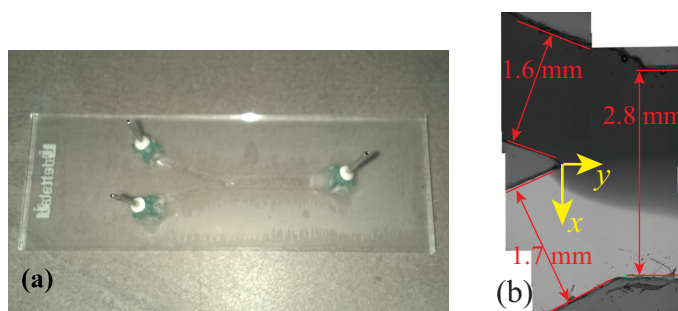


Figure 3.8: Microfluidics flow cell with a Y channel system, fabricated by welding two microscope slides with a patterned Parafilm M® spacer. (a) Image of the actual setup. Microscope slide is 75 mm long. (b) A collage of microscope images of the channel connection point with channel width measures. Yellow arrows mark the definition of coordinate axis with an origin fixed at the tip.

An alternative was found by expanding the limits of use of the Parafilm M® spacers using the same fabrication steps as for production of the Hele-Shaw cell as described in § 2.2. First, three holes were carefully drilled in a microscope slide. To provide tubing

connections, syringe needles are cut from both ends. The sharp end is cut to a preferred length, depending on the tubing, and straighten with pliers, while the plastic needle hub is cut until the metallic tube tip is shorter than 1 mm. This allows to fix the cut syringe tips in the holes of the microscope slide. For stable fixation they are glued with a *Super Glue* adhesive. The microfluidics channels are cut very carefully in a layer of Parafilm M®, using a knife for paper and magnifying goggles. This layer is placed between the glass slide with tubing connectors and another glass slide so that the inlets and outlet agree with the channel structure and heated on a hot plate. Keeping it at 75°C for at least 5 minutes, welds the two glass slides together, producing a microfluidics channel pattern as was cut previously with a thickness  $h \approx 0.13$  mm, which is confirmed by measurements on a microscope with a calibrated focus ring. An example of a resulting cell is visible in figure 3.8.

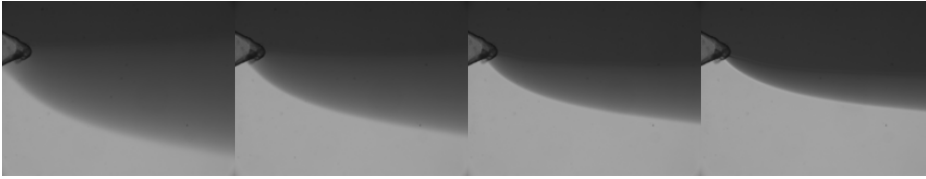


Figure 3.9: Mixing of magnetic fluid D107 with a 0.18 M free citrate concentration and a distilled water is observed in a microfluidics flow cell at various flow speeds, which are 2.4, 4.8, 9.5 and 23.9  $\mu\text{l}/\text{min}$  for each fluid. The actual size of each image is  $1.6 \times 1.2$  mm<sup>2</sup>

The experiments are continued with the same experimental system with a single change of using the new microfluidics cell. The cell is initially characterized by measuring channel widths, as showed in figure 3.8 (b). Later, the magnetic fluid and a citrate solution in water are filled in syringes and placed in the syringe pump. Turning it on to run in a continuous mode makes the fluids travel through the cell. As expected, mixing on the interface is observed, as shown in figure 3.9. The process is recorded with the *Lumenera* camera as done previously. Typically 200 images are recorded in every measurement and averaged to remove image noise or dirt.

Before further analysis, it is important to determine the flow speed in the microfluidics channel. An average velocity in the channel can be estimated via

$$\bar{v} = \frac{2Q}{h \cdot w}, \quad (3.9)$$

where  $Q$  is the flow rate of fluids, which are controlled by the syringe pump,  $h$  is the channel thickness and  $w$  is its width. As  $h$  and  $w$  are previously measured, the average velocity estimation gives  $\bar{v} = 92$   $\mu\text{m}/\text{s}$  assuming a steady flow of each fluid at  $Q = 1$   $\mu\text{L}/\text{min}$

Precise experimental measurements can be made with a Particle Image Velocimetry, introduced in § 2.1.1, but it take a long preparation and acquisition. Alternatively, a numerical 2D simulation of the actual geometry can be performed in COMSOL multiphysics software. Putting a no-slip condition for the boundaries, using a Hele-Shaw cell approximation and fixing the flow rate at  $Q = 1$   $\mu\text{L}/\text{min}$  for each fluid gives a stable solution. The corresponding velocity distribution is showed in figure 3.10. They indicate that a characteristic velocity around the region of interest is in agreement with the previous estimation and is therefore fixed at  $v = 90$   $\mu\text{m}/\text{s}$  for flow rate  $Q = 1$   $\mu\text{L}/\text{min}$ . Additionally it clearly indicates that the velocity around the tip is smaller, thus this area should not be used for data analysis. The size of this region is  $\approx 100$   $\mu\text{m}$ . Channel flow velocity then can be calculated by simply using

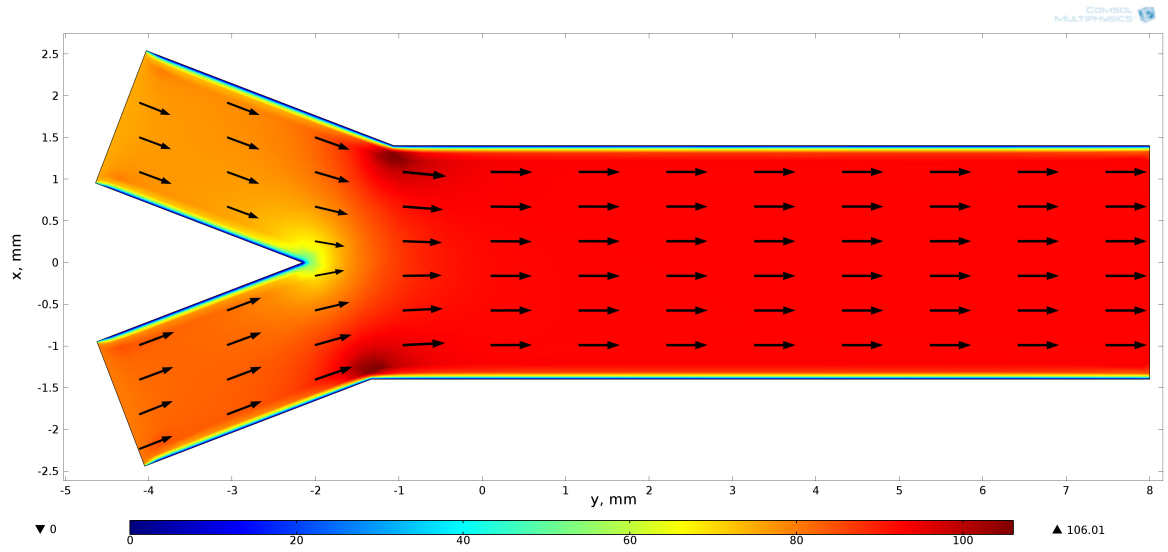


Figure 3.10: Numerical simulation solution for theoretical fluid Hele-Shaw flow in the specified geometry that was found with the COMSOL software and gives the velocity plot. A typical velocity along the channel is  $\approx 90 \mu\text{m/s}$  when each fluid has a fixed flow-rate  $Q = 1 \mu\text{L/min}$ .

this formula

$$v_Q = Q \cdot \left( \frac{v}{Q} \right)_0, \quad (3.10)$$

where  $Q$  is the flow rate for each fluid and  $\left( \frac{v}{Q} \right)_0 = 90 \frac{\mu\text{m}}{\text{s}} \cdot \frac{\text{min}}{\mu\text{L}}$ .

The coordinate system is defined as shown in figure 3.8 (b) with an origin at the tip of the channel connection. As was visible in images in figure 3.9, the mixing interface does not stay at a constant  $x$ , but rather forms a curve. For analysis purposes, this effect should be compensated and the interface coordinate  $x_0$  for each  $y$  along the channel must be found.

This curvature appears, because the fluids first come to a contact next to the tip ( $x = 0$ ) of the channel junction, but flowing further along the channel each fluid takes a certain width, placing the interface at the coordinate  $x'$ , which is not necessarily equal to 0. Hence, the fluid interface relaxes from an initial to a final stable state, which unfortunately is not clearly visible because of the concentration smearing on it. This stable state at coordinate  $x'$  depends on the proportion of the viscosities of both fluids [80]. In a hypothetical case when two immiscible fluids with viscosities  $\eta_1$  and  $\eta_2$  flow in this system, they should form a sharp interface, with fluid widths  $w_1$  and  $w_2$ , where their proportion is

$$\frac{w_1}{w_2} = \frac{\eta_1}{\eta_2}. \quad (3.11)$$

The difference between  $x = 0$  and  $x'$  also depends on the position of the tip of Y channel system. Current fabrication method does not let to control its position precisely, which, in a perfectly symmetric system, should be equally displaced from the walls of the common channel. In this particular cell, as measurable in figure 3.8 (b), these distances are 1.29 mm and 1.51 mm, being largely responsible for the notable curvature of the interface.

The shape of the interface curve seems to remain constant when fluid flow rates are changed, which is consistent with what is expected for incompressible fluid flow at low

Reynolds numbers [80]. Hence, it is reasonable to assume that smearing of the interface, when the flow rate is changed, is mostly coming from the additional effect of diffusive behavior. An algorithm to determine coordinates of this interface curve using images of fluid mixing at different flow rates can therefore be proposed.

The images are first transformed to concentration plots, as already done previously using (2.8). Concentration profiles  $c(y, Q)$  are then retrieved from the concentration profiles at each  $y$  for the different flow rates  $Q$ . The change in concentration profiles at  $y = \text{const}$  for different flow rates can be explained with the diffusive behavior already seen in experiments during droplet merging. A time  $t = y/v_Q$  can be calculated for each flow rate, where  $v_Q$  is defined in (3.10), to quantify the time necessary for the fluid to travel from the tip of the junction to the  $y$  position. Then, the propagation of constant concentration levels  $c_x$  at a fixed  $y$  can be described with

$$x(t)|_{c=c_x} = x_0 + C|_{c=c_x} \sqrt{t}, \quad (3.12)$$

where  $C$  is a characteristic coefficient for every concentration level. This relation is further used in analysis of the experimental data.

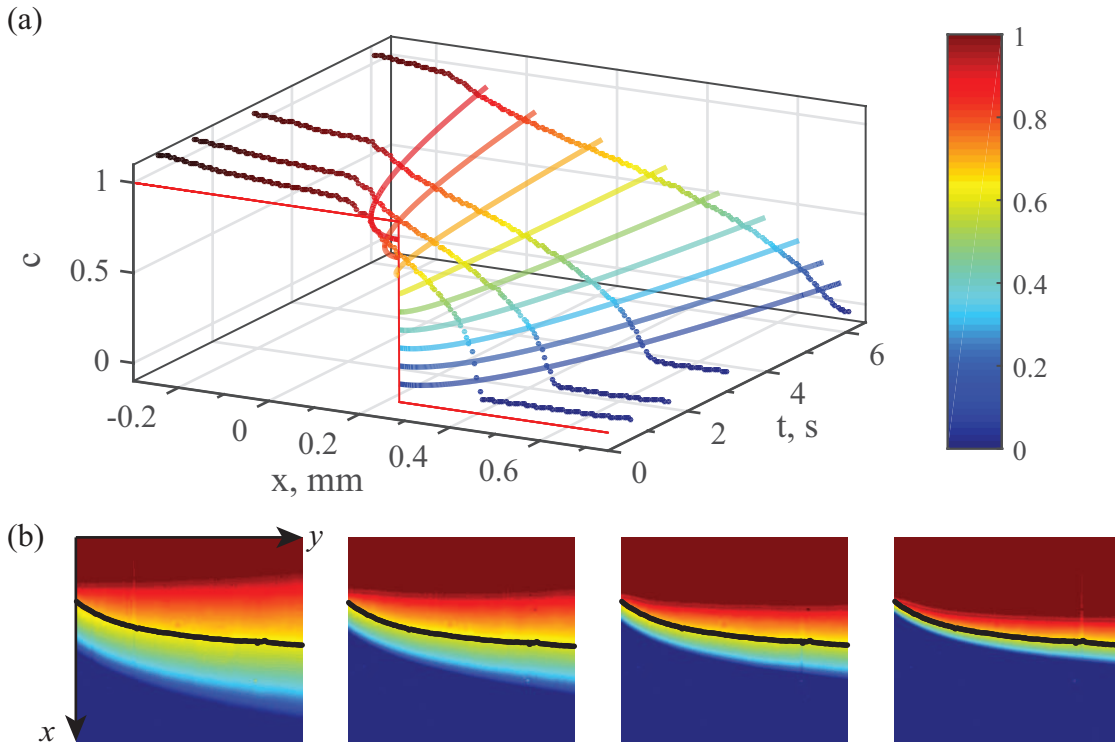


Figure 3.11: Determination of the interface coordinates  $x_0(y)$ . (a) Simultaneous fit of several concentration levels of concentration profiles from various flow rates at  $y = 1.34$  mm with (3.12) gives  $x_0$ . (b) The determined interface coordinates  $x_0(y)$  plotted with black dots on top of the concentration density plots of various flow rates that were used in fitting.

Data fitting is done with the fitting toolbox of MATLAB® implying (3.12) simultaneously for nine concentration levels (0.1, 0.2, ..., 0.9) of the concentration profiles obtained for different flow rates (or times) at a fixed  $y$ . The fitting parameter  $C$  (coefficient) is forced to be the same only for the four points of the same concentration level, while  $x_0$  is kept the

same for all particular data points. An illustration of this process is showed in figure 3.11 (a), where the several concentration levels of the four concentration profiles (at different  $t$  in  $x-c$  plane) are successfully fitted (at different  $c$  in  $t-x$  plane), resulting in finding a common initial interface position  $x_0$  (red line). Repeating this process for every  $y$ , the interface coordinates  $x_0(y)$  are found. The resulting curve  $x_0(y)$  is showed with a black line on the corresponding concentration plots in figure 3.11 (b). Alternatively, this line might be obtained using a very high flow rate. However, this approach was not used in order to save the magnetic fluid and skip the possibly nonlinear effects.

When the interface coordinates  $x_0(y)$  are known, the results may be analyzed in the same way as for droplet merging. There are only two minor differences. The first is that concentration profile dynamics for each fluid pair measurement is visible in a single image, where  $y$  coordinate can be transformed to time  $t$  as was already demonstrated before. Secondly, the interface coordinate  $x_0$  depends on  $y$  (and accordingly on  $t$ ) and it has to be taken into account when calculating  $l^2$ , as defined in (3.8).

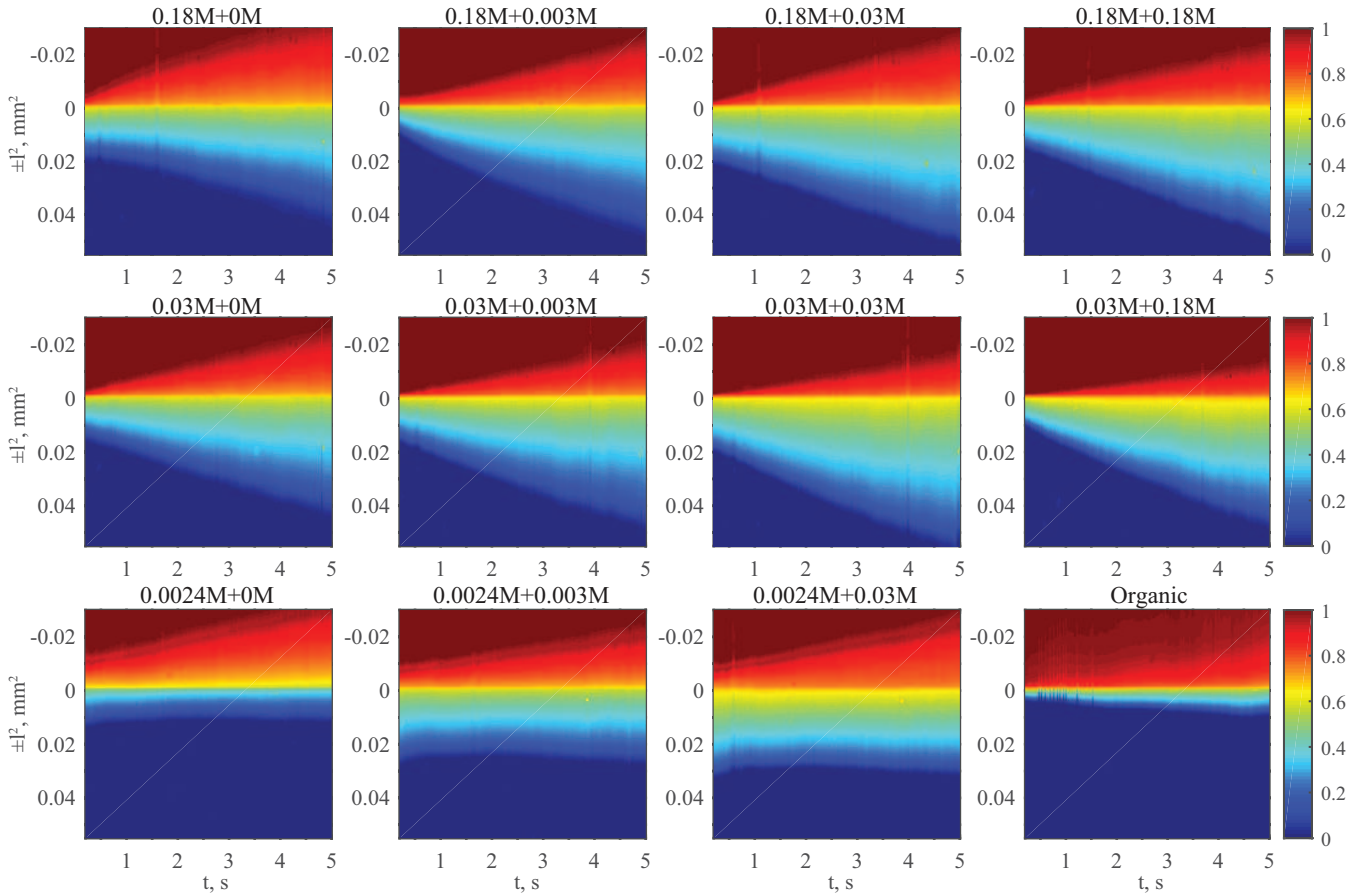


Figure 3.12: Density plots of concentration profile dynamics during mixing in microfluidics of all miscible pairs of magnetic fluids and citrate solutions in water. The title of each plot denotes the free citrate concentration in magnetic fluid and the citrate solution. The lower left plot shows these dynamics during mixing of a magnetic fluid based on an organic solvent.

Also here experiments were indicated that the magnetic fluid with an extremely low free citrate concentration  $[cit]_{free} = 0.0024$  M coagulates when mixing with a concentrated citrate solution in water  $[cit]_{free} = 0.18$  M. This is showed next to the example observed during

droplet merging in figure 3.7 (b). The concentration profile dynamics in the form  $c(\pm l^2, t)$  for all other possible pairs of magnetic fluids and citrate solutions in water are displayed in figure 3.12, while figure 3.13 shows the concentration profiles at several times for the same pairs. Results are obtained from recordings at the smallest flow rate  $Q = 2.4 \mu\text{L}/\text{min}$  in order to probe longer times of the phenomenon. The field of view in  $y$  direction from the tip is  $\approx 1.2 \text{ mm}$ , which limits the accessible times to  $t_{max} = y_{max}/v_Q \approx 5 \text{ s}$ .

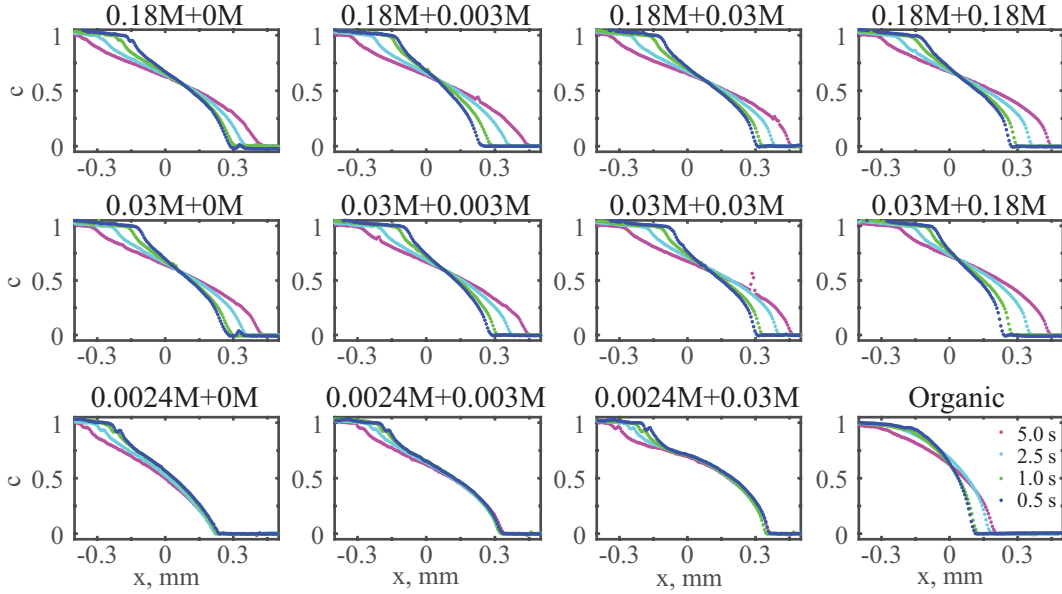


Figure 3.13: Concentration profiles at several time moments for all miscible pairs of magnetic fluids and citrate solutions in water. The title of each plot denotes the free citrate concentration in magnetic fluid and the citrate solution. The lower left plot shows these profiles during mixing of a magnetic fluid based on an organic solvent.

These results are comparable with the process dynamics in mixing after successful merging of drops (in § 3.2.3) for the similar regions and the obtained values mostly appear similar. Nevertheless, microfluidics results are more consistent, without large variations in observations of similar quantities. Also they can be obtained much faster and with less of fluids consumed, allowing measurements for all possible pairs of magnetic fluids and citrate solutions.

Results indicate that in most cases the concentration propagation is slower when magnetic fluids are mixed with citrate solution of a higher free citrate concentration, but this effect reduces the effective diffusion coefficient only two to three times. Additionally, the shapes of concentration profiles change only slightly, in most cases being the change in concentration at the interface coordinate. The only clear visual differences can be seen for the mixing of magnetic fluid with the very low 0.0024 M free citrate concentration. For it, in microfluidics experiments a large concentration smearing that goes up the stream, is created as soon as the fluids have formed an interface. These results significantly differ from the observations in droplet merging. This might have appeared because of the insufficient stability of this particular magnetic fluid. Its properties were not rechecked during experiments and after some more time it had either gelified or dried out and it was not possible to perform the dynamic light scattering experiments in § 3.4.

However, the results indicate that our hypothesis may be wrong. To have another ver-

ification, the same experiment was performed with magnetic fluid based on organic solvent mixing with this solvent, which is discussed further.

### Experiment with magnetic fluid on the base of organic solvent

If the hypothesis of diffusiophoresis is true then this effect should have no visible influence if the same experiment is repeated with magnetic fluid on the base of organic solvent, as introduced in § 1.1.2, because its stabilization mechanism is steric and not electrostatic.

Experiments are performed with the magnetic fluid *DF105*, which consists of magnetic particles stabilized with oleic acid in tetradecane  $C_{14}H_{30}$  and has properties as stated summarized in § 1.2.5. The solvent itself is chosen as the miscible non-magnetic fluid. Tetradecane at room temperature has a density  $\rho_{C_{14}H_{30}} = 0.763$  g/mL and a viscosity  $\eta_{C_{14}H_{30}} = 2.3$  cP [81].

Results for experiments on mixing of these fluids in the same microfluidics flow cell are shown in lower right corner of figures 3.12 & 3.13. Although the process appears to be slower, as compared to the mixing of water based magnetic fluids, it is inappropriate to compare them directly because of the difference in viscosity. It is more that two times larger for the organic solvent system.

An effective diffusion coefficient estimation using  $2\delta$  characteristic gives  $D_{eff} \approx 1 \cdot 10^{-5}$  cm<sup>2</sup>/s, which is also almost 200 times more than the diffusion coefficient measured with DLS. However, the precision of this measurement is lower than for others, as the microfluidics cell turned out not to be resistant to tetradecane, which slowly degraded the cell during experiment.

### Conclusions on the hypothesis about diffusiophoresis

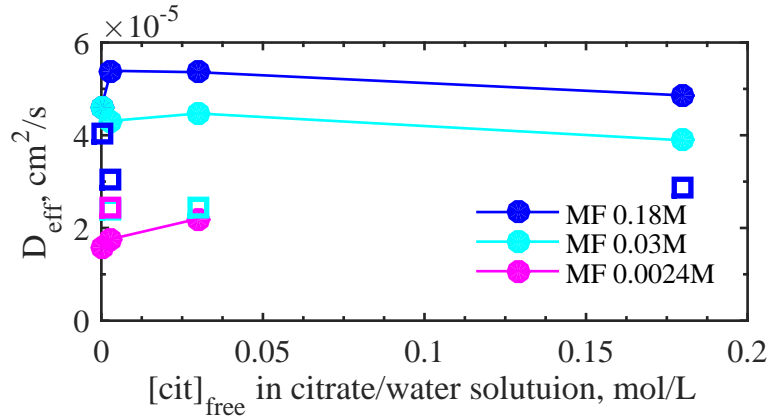


Figure 3.14: Effective diffusion coefficients for the various magnetic fluid and citrate solution in water pairs. Full circles with lines, as denoted in legend, show microfluidics results for each of the magnetic fluid samples for various citrate solution concentrations, while empty squares mark data from the individual measurements of droplet merging with the same color coding.

A summary of effective diffusion coefficient measurements for magnetic fluid and citrate water solution pairs is given in figure 3.14. Overall, this graph shows that there are differences between different systems. Similarities can be seen in the measurements for magnetic fluids with 0.03 M and 0.18 M free citrate concentrations, however, no clear trend is present.

Moreover, the differences between measured pairs are much smaller than the magnitude of the effective diffusion coefficient. These observations together with the result for experiments with magnetic fluid on the base of organic solvent, clearly indicate that our hypothesis has been wrong and diffusiophoresis is not the main reason for the large increase of the mixing speed.

Thereafter, a different explanation for this phenomenon was searched. On the way, the factor of gravity was revisited, as proposed in [48]. Recalculation of the characteristic gravitational Rayleigh number for this system gave a huge value  $Ra \approx 10^4$ , which was consistent with the earlier estimation. A surprise came when the characteristic time was found to be  $\tau \approx 100$  s, which meant that the effect should be present not only at the smearing of the initial interface, but also during the whole experiment. Adapting and solving the appropriate numerical simulation model in COMSOL [48], gave values which, when put to dimensional units, were comparable with the experimental observations. Therefore, a more careful study of the gravity influence on this system was carried out further.

### 3.2.5 Effect of gravity

So far the investigation of the enhanced effective diffusion, as well as the magnetic micro-convection in chapter 2, were studied in the framework of the Hele-Shaw flows [80]. This approximation allows to consider flows to be present only in two dimensions, neglecting the effects in the third dimension. It is a preferred approximation both for numerical simulations and experimental observation, because simulations in two dimensions are much less time consuming and conventional microscopy tools, including bright field microscopy which is used here, allow observation only in two dimensions. Gravitational force in the present experimental, showed in figure 2.12, points in the negative direction of  $z$ -axis and therefore has been so far neglected in this Hele-Shaw model.

The gravity influence on a miscible fluid interface arises when there is a density difference between the fluids. Resulting effect in  $x - z$  plane can be illustrated by the Stokes model with the concentration  $c$  dependent gravity force and the diffusion equation, as is done in [48]. The corresponding set of partial differential equations (PDEs) in dimensionless form is

$$-\nabla p + \Delta \vec{v} - c \vec{e}_z = 0, \quad (3.13)$$

$$\frac{\partial c}{\partial t} + Ra(\vec{v} \cdot \nabla)c = \Delta c, \quad (3.14)$$

where  $Ra = \Delta \rho g h^3 / 8 D \eta$  is gravitational Rayleigh number. It is obtained by scaling time by  $h^2 / 4D$ , length by  $h/2$  and the velocity by  $\Delta \rho g h^2 / 4 \eta$ , where  $h$  is the cell thickness,  $\Delta \rho$  is the density difference between fluids,  $D$  is the diffusion coefficient of the concentrated particles and  $\eta$  is the fluid viscosity, assumed to be equal across the fluid.

Numerical simulations are performed in a program made in COMSOL that was developed already for [48]. The simulation is defined with PDEs of (3.13), (3.14) for a two dimensional side view of a cell in  $x - z$  plane with the initial conditions (a slightly smeared normalized step-like concentration interface as defined in (3.5) with  $t = 0.05s/\tau = 4 \cdot 10^{-4}$  in dimensionless units) and no-slip boundary conditions. The cell is defined with a thickness 2 and the width is 30 for  $Ra > 1000$  and 10 for smaller gravitational Rayleigh numbers. Solutions are searched from times  $t = 0..1$  with a  $\Delta t = 0.001$  interval for many gravitational Rayleigh number  $Ra$  values.

Numerical simulation results in the form of a time-series of concentration density plots are shown in figure 3.15 for a large  $Ra = 10000$  value and in figure 3.16 for small  $Ra = 0.001$

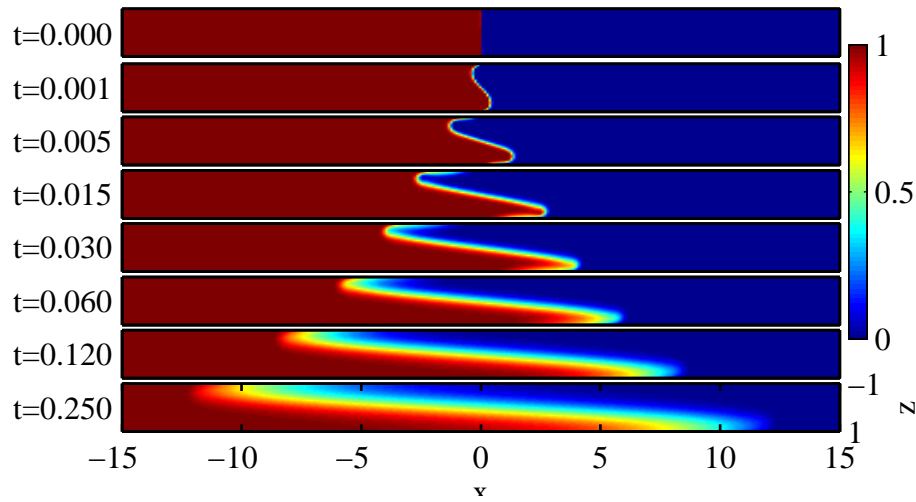


Figure 3.15: Numerical simulation results for  $Ra = 10000$  as a time-series of concentration density plot development. A rapid movement of the heavier liquid under the lighter can be seen.

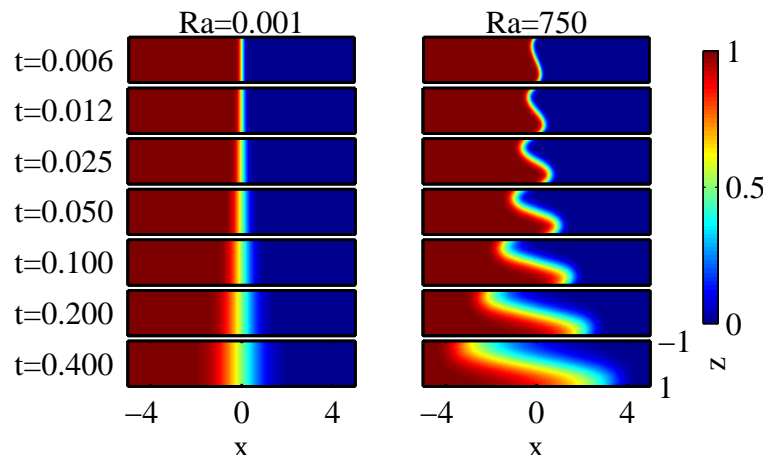


Figure 3.16: Numerical simulation results for two different  $Ra$  values as a time-series of concentration density plot development. Normal diffusion is visible for  $Ra = 0.001$ , while for  $Ra = 750$  an initially rapid movement of the heavier liquid is later surpassed by diffusion.

and medium  $Ra = 750$  values. Results for a small  $Ra = 0.001$  show that there is no notable difference along the  $z$  axis, what could be expected, while dynamics at a large  $Ra = 10000$  appear to be very different. Concentration plot dynamics indicate a convective motion, that pushes the concentrated fluid to flow under the lighter. The speed of this flow appears to decay with time until the diffusion starts to dominate. If the gravitational Rayleigh number is increased, the convective motion as compared to diffusion becomes faster. Similarly, the displacement of fluids for the same time  $t$  also is larger for a higher  $Ra$ . This is taken into account in simulations by choosing a larger width of the cell in  $x$  direction for larger  $Ra$  values and using only those results, where concentrations close to the left and right boundaries have not changed from the initial conditions.

To be able to quantify numerical simulation results and compare them with experimental

observations, it is useful to calculate the average concentration profile  $\bar{c}(x)$  along  $x$  axis

$$\bar{c}(x) = \frac{1}{2} \int_{-1}^1 c(x, z) dz, \quad (3.15)$$

where factor  $1/2$  comes from the cell thickness which is 2. This step can be directly implemented in COMSOL, using *linproj1* operator.

Concentration profiles for a few  $Ra$  values at several times  $t$  are shown in figure 3.17 (a). The shape of profiles for larger  $Ra$  values substantially differs from the smooth error function shape expected for diffusion. It can be described with a region of linear concentration smearing around  $c = 0.5$ , which stays fixed at  $x = 0$ , and faster concentration jumps close to  $c = 1$  and  $c = 0$ . This shape resembles the concentration profiles observed in experimental measurements in figures 3.2, 3.6 & 3.13.

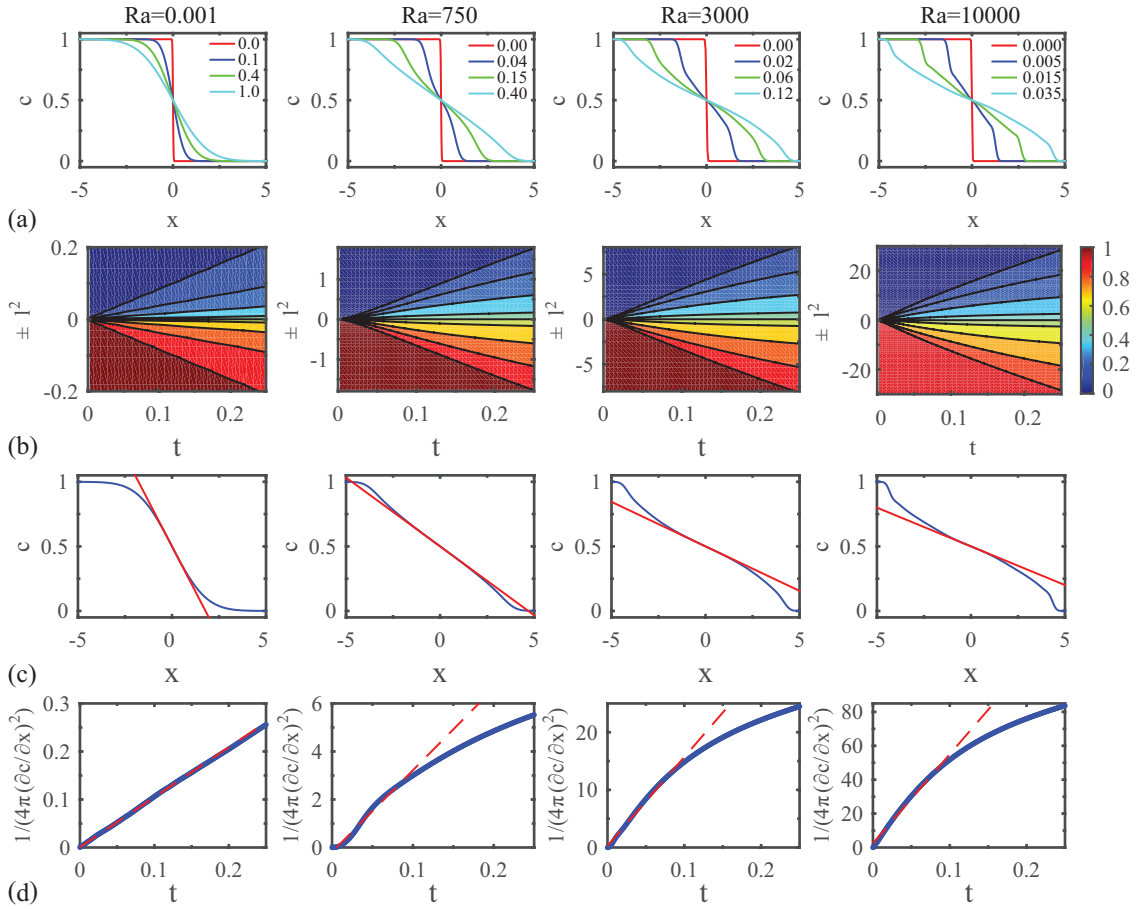


Figure 3.17: Analysis of the numerical simulation results using average concentration  $\bar{c}$  for several  $Ra$  values. (a) Concentration profiles  $\bar{c}(x)$  at several times  $t$ . (b) Contour plots of concentration profile dynamics shown as  $\bar{c}(\pm l^2, t)$ . (c) Finding  $\partial c / \partial x|_{x=0}$  at  $t = 1$  for  $Ra = 0.001$ , at  $t = 0.4$  for  $Ra = 750$ , at  $t = 0.12$  for  $Ra = 3000$  and at  $t = 0.035$  for  $Ra = 1000$ . (d) Determination of the effective  $D_{\text{eff}}$  for  $t < 0.1$ . Blue curves in (c) and (d) are numerical simulation data, but red lines mark their fits.

In (b) of figure 3.17 concentration profile dynamics in the form  $c(\pm l^2, t)$  are shown for four different  $Ra$  values, where  $\pm l^2$  is defined in (3.8). For  $Ra = 0.001$  lines of equal concentrations

are perfectly straight and are distributed very unevenly for the different concentration levels. This is typical for normal diffusion process, as concentration smearing is very pronounced at the borders of the interface and can also be seen for the analytical solution of diffusion in figure 3.4 (a). For larger  $Ra$  values lines of equal concentrations also appear to be linear, which indicates a behavior similar to diffusion, as distances are proportional to  $\sqrt{t}$ , as was observed at experiments. However, some deviation from this starts to appear at longer times  $t > 0.1$  and are more pronounced for concentration levels around  $c = 0.5$ .

The shapes of concentration profiles at small and large  $Ra$  significantly differ, making it difficult to compare them directly using  $\delta$  and  $2\delta$  methods introduced previously in § 3.2.1. A meaningful alternative is to compare the concentration gradients  $\partial c/\partial x$  at the initial interface  $x = 0$ . It is easy to find it in data by fitting the concentration profile around  $x = 0$  with a straight line, as is showed in figure 3.17 (c). The partial derivative of the analytical solution for diffusion (3.5) against  $x$  at  $x = 0$  allows to link it to define an effective diffusion coefficient

$$\left. \frac{\partial c}{\partial x} \right|_{x=0} = \frac{1}{2} \cdot \frac{1}{\sqrt{\pi D_{\text{eff}} t}} \quad (3.16)$$

This equation can be transformed to obtain a linear relationship that is suitable for fitting

$$\frac{1}{4\pi \left( \frac{\partial c}{\partial x} \right)^2} = D_{\text{eff}} t \quad (3.17)$$

Results on concentration gradients for the four different  $Ra$  are displayed in figure 3.17 (d) in the form proposed in equation 3.17. A straight line with a slope equal to unity is obtained for  $Ra = 0.001$ , which is exactly what is expected for normal diffusion, as the value of diffusion coefficient is dimensionless. Differently, data for larger  $Ra$  values shows a more complex behavior. Nevertheless, a linear region at  $t < 0.1$  can be discriminated. Fitting it with a linear slope gives values of the effective diffusion, which are  $D_{\text{eff}} = 34$  for  $Ra = 750$ ,  $D_{\text{eff}} = 154$  for  $Ra = 3000$  and  $D_{\text{eff}} = 525$  for  $Ra = 10000$ .

Performing such analysis for multiple  $Ra$  values allows to find the effective diffusion  $D_{\text{eff}}$  dependence on the gravitational Rayleigh number. Results that are shown in figure 3.18 indicate that the effective diffusion coefficient is equal to the actual diffusion coefficient up to a critical value  $Ra_c$ , which is found to be  $\approx 105$ . Above it,  $D_{\text{eff}}$  increases linearly with  $Ra$  with a slope 0.053. The transition between the two regimes appears to be smooth, which is because  $D_{\text{eff}}$  is determined with a linear fit, which blurs some non-linear effects happening at  $t < 0.1$ , as could be seen in figure 3.17 (d) for  $Ra = 750$  and other results that are not shown here.

Effective diffusion coefficients in experimental data are found in the same way as for numerical simulations at the initial interface coordinate  $x_0$ . Experimental data and fits can be found in Annex D. Figure D.2 summarizes data for all experiments in droplet merging, which are of good or reasonable quality in terms of the initial interface formation. For fluid pairs with several measurements, the mean value of the effective diffusion coefficient is calculated. Data for all miscible fluid pairs including magnetic fluid based on organic solvent and corresponding fits can be seen in figure D.3.

To calculate the gravitational Rayleigh number for each fluid pair, their densities are needed. If values for magnetic fluid samples have been measured and can be found in tables 1.1&3.1, then densities for trisodium citrate solutions in water at room temperature can be calculated from data in [82]. For the range up to 0.50 M they have a linear dependence

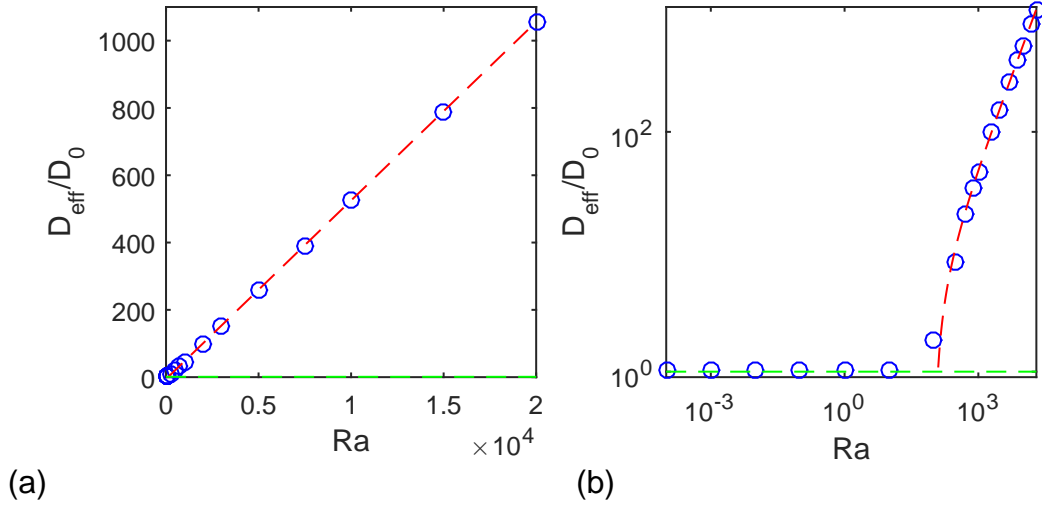


Figure 3.18: Effective diffusion coefficient dependence on the gravitational Rayleigh number in (a) linear plot and (b) log-log plot. Blue circles mark numerical simulation results. For  $Ra < 10$  there is no effective diffusion  $D_{\text{eff}} = D_0 = 1$  (green dashed line), but for  $Ra > 300$  it grows linearly with  $Ra$  as  $D_{\text{eff}} = 0.053(Ra - Ra_c)$ , where  $Ra_c = 105$  (red dashed line).

on the dissolved citrate concentration

$$\rho_{\text{citr.sol.}} = 0.176 \cdot [\text{cit}]_{\text{free}} + 0.998. \quad (3.18)$$

A test measurement of the citrate solution density verified this. For the viscosity, an approximate value  $\eta_w = 0.01$  P is taken for water based systems, while for magnetic fluid based on organic solvent it is taken as the measured viscosity  $\eta_o = 0.07$  P. Finally, to compare the experimental values to numerical simulation results, effective diffusion coefficients  $D_{\text{eff}}$  are converted to dimensionless quantities by dividing them with the appropriate magnetic particle diffusion coefficient  $D_0$ , which are taken  $D_{0,w} = 2.5 \cdot 10^{-7}$  cm<sup>2</sup>/s for water based fluid pairs (characteristic value based on measurements in § 3.4) and  $D_{0,o} = 7.0 \cdot 10^{-8}$  cm<sup>2</sup>/s for organic solvent based system.

The values of effective diffusion coefficient in a dimensionless form  $D_{\text{eff}}/D_0$  as a function of gravitational Rayleigh number for experimental measurements can be seen in figure 3.19. Data points with error-bars from fits are showed in shape and color coded manner. The definitions are given in the figure caption.

Majority of data points show a reasonable agreement with the theoretical prediction. Some exceptions can be seen, but these differences are most probably present because of the experimental limitations, change of fluid parameters over time or additional effects, including the previously discussed diffusiophoresis. For example, effective diffusion coefficient values from the well controlled experiments in microfluidics with a precisely characterized magnetic fluid *D107* and citrate solutions do not decrease linearly with the decrease of the density difference, which is smaller when citrate solution is more concentrated. Instead, as can be better seen in (b) of figure 3.19, it rather increases. It is worth to mention that the calculated  $Ra$  might have a considerable error, because it very sensitive to the determination of  $h$ , as  $Ra \propto h^3$  and  $h$  in this system is determined with an  $\approx 5\%$  error.

Nevertheless, these results indicate that the major contribution to the effective diffusion increase comes from the gravitational influence. Yet, for a complete justification, an

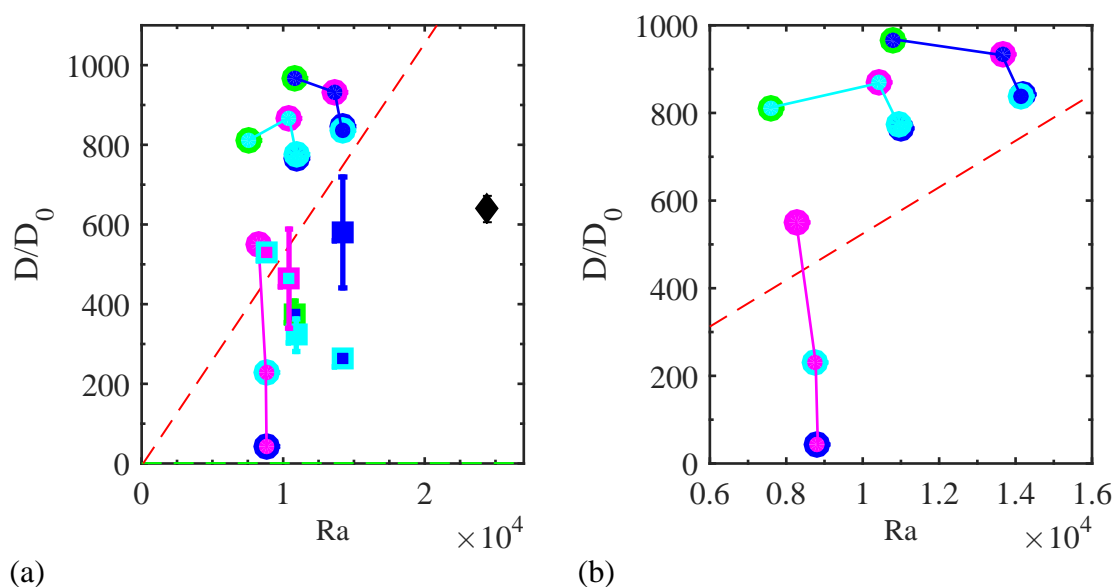


Figure 3.19: Experimentally measured effective diffusion coefficient in the dimensionless form  $D_{\text{eff}}/D_0$  as a function of  $Ra$ . Shape defines measurement method - circles - microfluidics, squares - drop merging. Color pairs mark fluid pairs. Face color defines magnetic fluid sample: blue - 0.18 M, cyan - 0.03 M and magenta - 0.0024 M. Edge color marks citrate solution: blue - distilled water with 0 M, cyan - 0.003 M, magenta - 0.03 M and green - 0.18 M. Black diamond shows result of organic solvent based magnetic fluid. In (a) all data are shown. In (b) only results from microfluidics can be seen.

experimental demonstration is wanted and is showed further.

### Experimental proof

Information of the 3D concentration distribution or at least on a 2D cross-section are impossible to register with a conventional bright field microscope that is used in these experiments. However, it should be achievable with a confocal microscope [83, 75], especially because the concentration smearing across the interface in a continuous microfluidics cell is stable. Unfortunately, during this study, it was not possible to do such measurements.

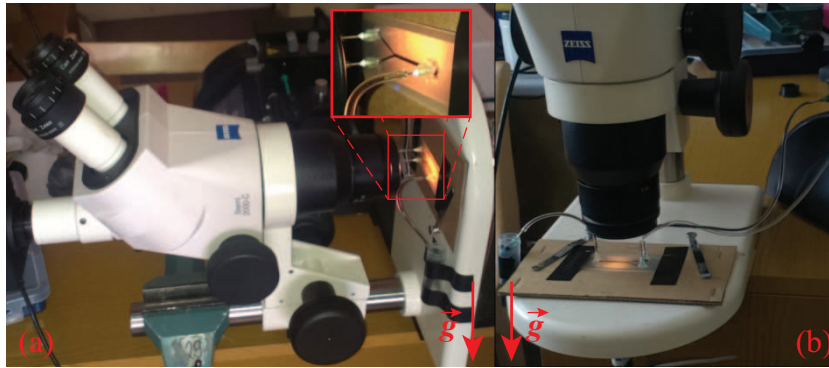


Figure 3.20: Experimental setup for observing gravitational effects in microfluidics flow cell placed horizontally with  $\vec{g}$  in the plane of the cell in (a) and vertically with  $\vec{g}$  perpendicular to the pane of the cell (b).

Instead a much simpler solution was chosen. Rather than obtaining the concentration distribution in the third dimension of the Hele-Shaw cell, the direction of the gravitational force was changed in the system by turning the position of the cell. As it is rather difficult to turn an inverted microscope, a *Zeiss* stereoscope Stemi 2000-C was used instead, as is visible in figure 3.20. Illumination was provided as in the bright field mode with a Dolan-Jenner MI-150 Fiber Optic Illuminator from *Edmund Optics*. Process was recorded with *Lumenera* camera which has been introduced earlier. A new microfluidics cell was made for these experiments following the same fabrication steps as described in § 3.2.4 and a more symmetric Y channel system was obtained with a width of the common channel  $w = 1.4$  mm. Microfluidics flow cell was placed in a cardboard holder, which was fixed to the stereoscope base. Fluid control was done as previously, using the microfluidics pump PHD Ultra from *Harvard Apparatus*.

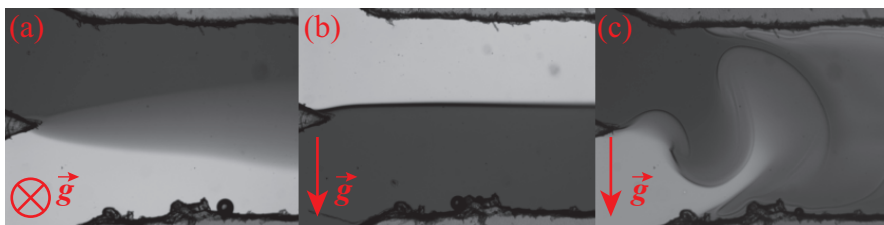


Figure 3.21: Fluid mixing in microfluidic flow cell with no magnetic field present, but with different directions of  $\vec{g}$ . Each image is  $2.2 \times 1.7$  mm<sup>2</sup> large and the flow rate is  $Q = 2.4$   $\mu$ L/min for each fluid.

Measurements of mixing of magnetic fluid *D107* with the free citrate concentration 0.18 M and distilled water in a microfluidics flow cell was observed at three different relative directions of the gravitational force. Characteristic images of the process for each configuration are shown in figure 3.21. Image (a), where  $\vec{g}$  is perpendicular to the cell, corresponds to the configuration studied so far and, as expectable, resembles these previous observations. Image (b), where  $\vec{g}$  is in the plane, pointing from the less dense distilled water to the more dense magnetic fluid, proves that the concentration smearing on the interface indeed comes from the gravitational contribution, as almost no diffusion is visible in the field of view. If this is inverted and  $\vec{g}$  points from the heavier fluid to the lighter fluid, conditions for the common Rayleigh-Taylor instability, which is still a subject of interest [84, 85], are obtained and a different fingering is observable instability, as visible in (c). It is worth noting that such experiments would be extremely difficult if they would not have been transferred to microfluidics.

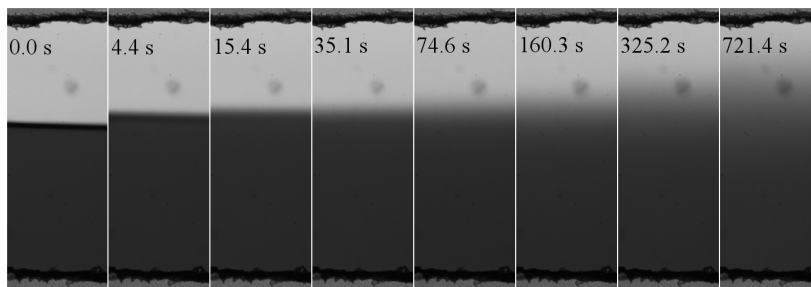


Figure 3.22: Snapshots of magnetic particle diffusion across the microchannel with a stopped flow. Channel width 1.4 mm.

It is now easy to find the magnetic particle diffusion coefficient using the experimental configuration from (b) in figure 3.21, where the Hele-Shaw cell is placed vertically and the denser liquid is in the lower part of the cell, thus excluding the gravitational effects. For this, the flow is suddenly stopped, obtaining a still system with a sharp initial interface. The mixing process can be seen in the snapshots displayed in figure 3.22. A much slower process is visible and even after 12 minutes the interface smearing is small.

Recorded image series of the magnetic particle diffusion is analyzed as described previously in § 3.2.1 for a manually selected area of the channel, converting images to concentration plots, which are averaged for each image to access the average concentration profile, and finding the initial interface coordinate  $x_0$ . Analysis results are summarized in figure 3.23. Concentration profiles in (a) and the concentration profile dynamics  $c(\pm l^2, t)$  in (b) look much more similar to what is expected for the analytical solution of diffusion in (3.5). However, there are some differences. For example, the concentration level at the initial interface coordinate  $x_0$  seems to increase with time and the concentration profile dynamics shows an asymmetry with respect to the initial interface coordinate  $x_0$ . Some of these effects might come from the poor illumination control as compared to an inverted microscope. Nevertheless, further study possibilities can be defined here, for instance, on the possible effect of difussiophoresis.

A quantitative determination of the magnetic particle diffusion coefficient is done using all the methods proposed in this work and their results are summarized in figure 3.24 (a). The diffusion length  $\delta$  dynamics, which is obtained by fitting the average concentration profile from each image with the analytical solution (3.5) is showed with blue circles. Fitting  $\delta^2/4$  as a function of  $t$  with a linear slope gives the diffusion coefficient  $D_\delta = 5.5 \cdot 10^{-7} \text{ cm}^2/\text{s}$ . The

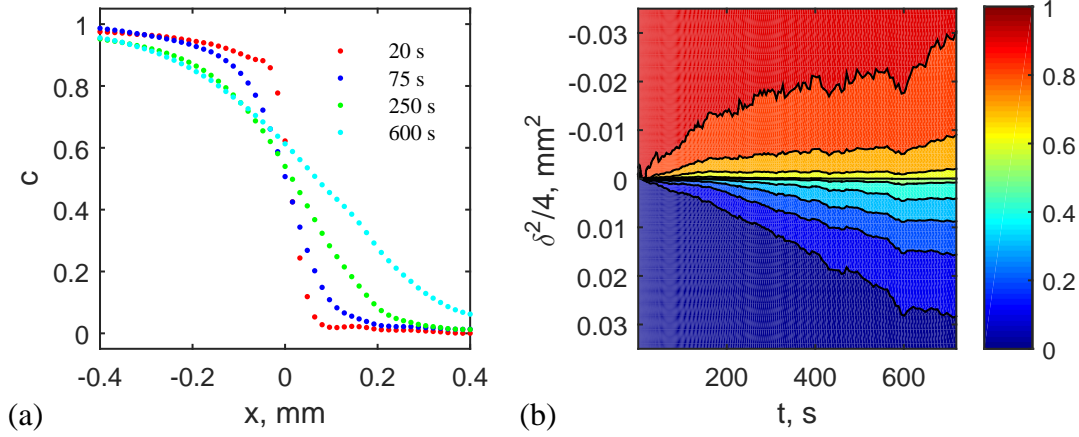


Figure 3.23: Analysis of the magnetic particle diffusion in a Hele-Shaw cell with negligible influence of gravity. Concentration profiles at several time moments are shown in (a), while contour plot of concentration profile dynamics in the form of  $c(\pm l^2, t)$  is shown in (b).

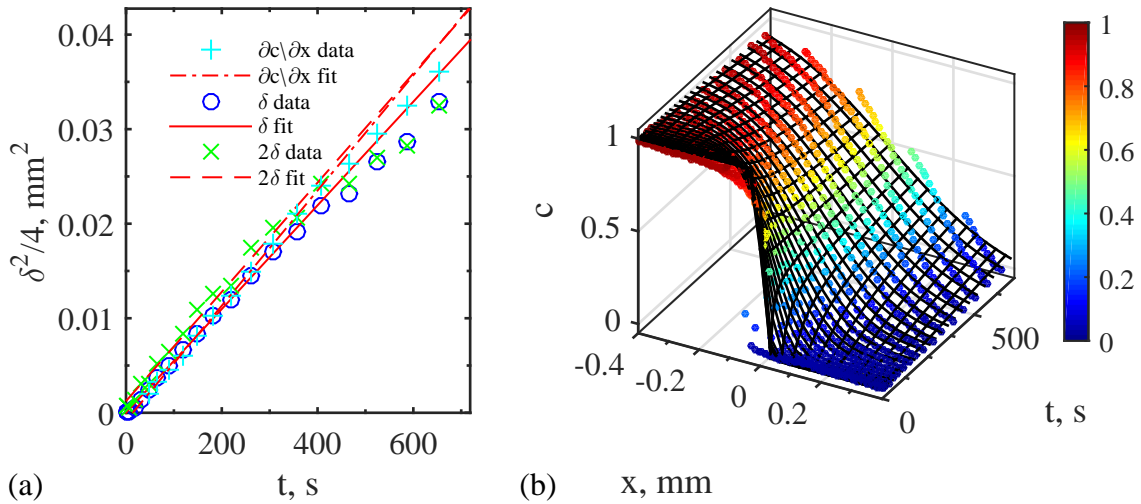


Figure 3.24: Determination of the magnetic particle diffusion coefficient  $D$ . (a) Results of  $\delta$ ,  $2\delta$  and  $\partial c/\partial x$  methods show a good agreement around a  $D \approx 5.7 \cdot 10^{-7}$  cm<sup>2</sup>/s. (b) 2D fit of the concentration profile dynamics. Colored dots are experimental data, while the black grid shows the fitted surface.

double diffusion length measure  $2\delta$ , defined with (3.7) is marked with green crosses. The appropriate linear fit for  $(2\delta)^2/16$  as a function of  $t$  gives  $D_{2\delta} = 5.8 \cdot 10^{-7}$  cm<sup>2</sup>/s. Finally, the concentration gradient at the initial interface  $\partial c/\partial x$  dynamics data are marked with cyan plus signs and the corresponding fit of  $1/(4\pi(\partial c/\partial x)^2)$ , as developed in (3.17), gives  $D_{\partial c/\partial x} = 6.1 \cdot 10^{-7}$  cm<sup>2</sup>/s. All of them show good linear time dependence for  $15 < t < 380$  s, which is used for fitting, to remove the initial interface stabilization and later confinement effects. Also the fitted values agree well.

Alternatively, a direct 2D fit using (3.5) can be performed on the concentration profile dynamics data  $c(x, t)$ , as shown in (b) of figure 3.24. Using data only for  $t > 15$  s to remove

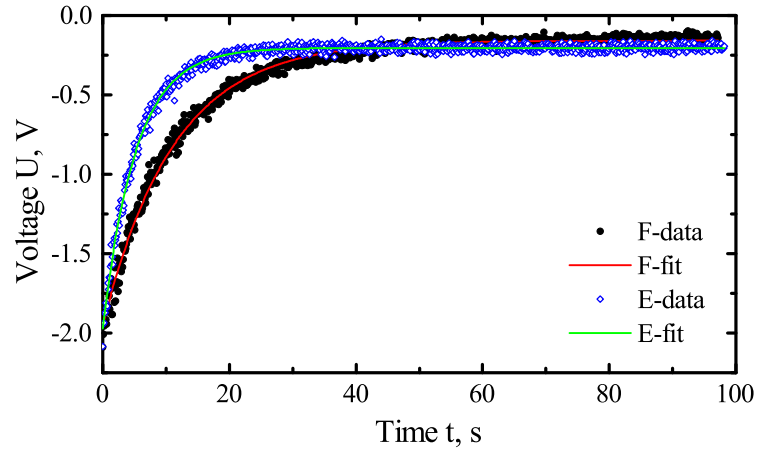


Figure 3.25: Examples of the FRS intensity decay data and their fits for  $F$  and  $E$  line patterns.

the interface stabilization after stopping the flow, the fitted surface shows a rather good agreement with the data and gives  $D_{2D} = 5.5 \cdot 10^{-7} \text{ cm}^2/\text{s}$ .

Overall, the obtained diffusion coefficient value  $D \approx 5.5 \cdot 10^{-7} \text{ cm}^2/\text{s}$  is in reasonable agreement with the values measured with the FRS method in § 3.3 and DLS method in § 3.4, which concludes this investigation.

### 3.3 Forced Rayleigh Scattering

Forced Rayleigh scattering (FRS) [86] is a technique that allows to determine the diffusion coefficient in magnetic fluids even for large volume fractions. The working principle is based on measuring the relaxation of an induced concentration grating in a thin magnetic fluid layer. The characteristic decay time  $\tau$  depends on the diffusion coefficient  $D$  and the wavenumber of the induced grating  $q$  as follows

$$\frac{1}{\tau} = 2D \cdot q^2 \quad (3.19)$$

The experiments are done on the experimental setup located in the PHENIX lab in Paris as explained. A small amount of magnetic fluid *D107* is filled in a  $100 \mu\text{m}$  thick quartz cuvette. This cuvette is placed in the sample holder of the FRS setup. An optical system with a mercury lamp illumination focuses an image of a regular line pattern on the sample. After some time a regular concentration grating is formed according to the illuminated pattern because of the thermophoresis of absorbing magnetic particles. A laser with  $\lambda = 632.8 \text{ nm}$  is pointed towards sample at a  $45^\circ$  angle and forms a diffraction pattern after crossing the induced grating. A photodiode is then placed at the first diffraction maximum to record the intensity measurement. At a certain time the illumination of the mercury lamp is blocked and the induced concentration grating smears out. This is registered as an intensity decay on the photodiode.

Experiments are performed with four different line patterns, that have defined  $q^2$  values  $1.22 \cdot 10^9 \text{ m}^{-2}$  for G pattern,  $1.99 \cdot 10^9 \text{ m}^{-2}$  for F pattern and  $4.26 \cdot 10^9 \text{ m}^{-2}$  for E pattern. Examples of the registered intensity decay curves can be seen in figure 3.25. To find the characteristic decay time  $\tau$ , each curve is fitted with an exponential  $A \cdot e^{-t/\tau} + C$ , where  $C$

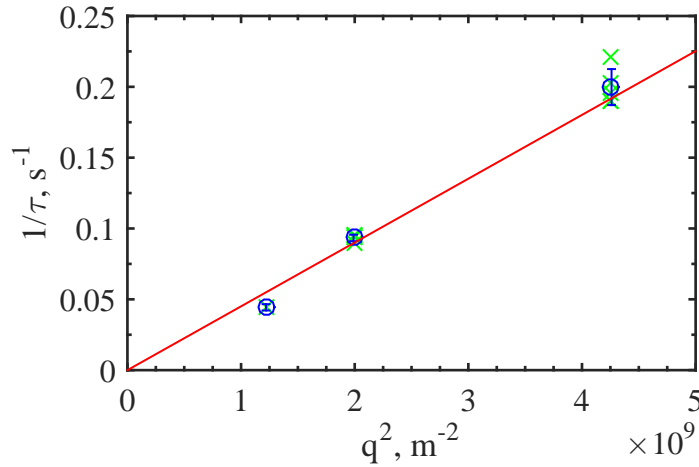


Figure 3.26: Determination of the magnetic particle diffusion coefficient with the FRS method. Green crosses mark individual measurement, blue circles show the mean values for each line pattern with standard deviation as error and red line is the linear fit of (3.19), which gives  $D = 2.3 \cdot 10^{-7} \text{ cm}^2/\text{s}$ .

is the baseline. Several measurements for each line pattern are made and an average decay time  $\tau$  is calculated

The diffusion coefficient is found by fitting the measured data with (3.19). For experimental data of magnetic fluid *D107* this gives  $D = 2.3 \cdot 10^{-7} \text{ cm}^2/\text{s}$ , as can be seen in figure 3.26. This result is consistent with the DLS results in the following section.

### 3.4 Dynamic Light Scattering

The method of dynamic light scattering (DLS) was introduced already in § 1.2.2 as a tool for colloid size distribution determination. There it was explained how the cummulant method allows to extract the diffusion coefficient from the autocorrelation data. However, it does include interparticle interaction contribution. Performing multiple measurements of  $D$  at various concentrations allows to estimate the diffusion coefficient of single magnetic particle at an infinite dilution  $D_0$  from a formula [25]

$$D = D_0(1 + k_D \cdot \Phi), \quad (3.20)$$

where  $\Phi$  is the volume fraction and  $k_D$  is the diffusion virial coefficient.

Measurements are performed with Malvern NanoZS Zetasizer device, which is introduced in § 1.2.2, for two samples of magnetic fluid *D107* with the free citrate concentrations of 0.18 M and 0.03 M, diluting them with the corresponding citrate solutions in water. It was not possible to perform the measurements for the third sample as it had dried out.

Results are summarized in figure 3.27. Diffusion coefficients  $D_0$  are obtained by fitting data of diluted samples for concentrations higher than the lower limit defined in the device's user manual. The values are  $D_0^{0.18 \text{ M}} = 2.81 \cdot 10^{-7} \text{ cm}^2/\text{s}$  and  $D_0^{0.03 \text{ M}} = 2.45 \cdot 10^{-7} \text{ cm}^2/\text{s}$  respectively.

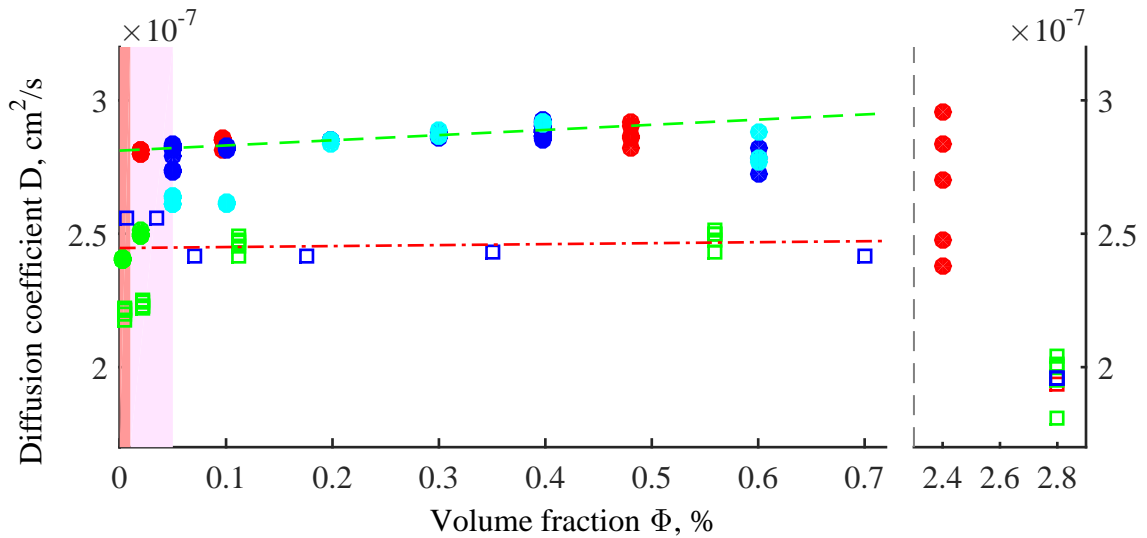


Figure 3.27: Determination of diffusion coefficients of magnetic particles at infinite dilution  $D_0$  for the magnetic fluid *D107* at different free citrate concentrations. Filled circles correspond to the free citrate concentration 0.03 M, while empty squares to 0.18 M. Different colors mark separate measurement series. Red and green lines show the linear fits according to (3.20). The shaded areas with a lighter and darker red colors show accordingly the apparent concentration detection limit and above limit zones, as explained at the device's manual.

The values are close and comparable with other methods. However, there is a notable difference for the two samples, which should be connected to the difference in Debye lengths [76] for different ionic strengths, but is out of the scope of this study.

### 3.5 Fluorescence Recovery After Photobleaching

Fluorescence recovery after photobleaching (FRAP) is a method that is mostly used in the characterization of dynamics of microscopic biological processes, as fluorescence labeling has become a standard method in visualization of biological processes. It is based on the photobleaching effect, which reversibly or irreversibly destroys the fluorescence ability of the fluorescent material when exposed to high power illumination. If a quick pulse of powerful illumination is applied to a region of interest, then this area becomes dark in as compared to the surroundings in terms of fluorescence signal. However, because of thermal fluctuations, directed transport or other effects, the new fluorescent material appears in this area and fluorescence signal regenerates. Measuring dynamics of this process allows to characterize the process of interest [19].

FRAP principle can be applied to colloid dynamics studies in the same way. Unfortunately, neither of the labs this study was performed in, is equipped with a conventional FRAP setup. Instead a modified version of fluorescence photobleaching system is proposed and studied.

The inverted *Leica* microscope DMI 3000B is equipped with a metal halide lamp EL6000, which, together with a filter cube *N2.1* provides a system that can excite rhodamine-B fluorescent dyes that are attached to magnetic fluid *KTF10-04*. If the maximum power of the lamp is used, a gradual photobleaching is observed in the exposed area. This area can

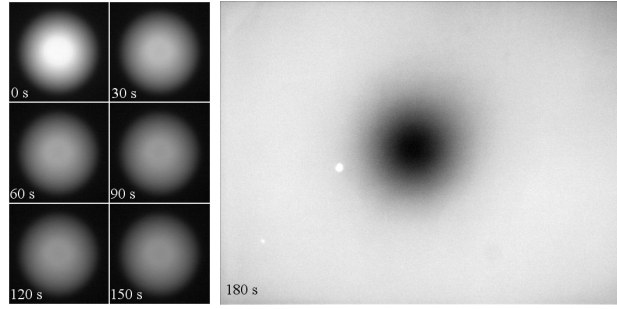


Figure 3.28: Continuous photobleaching of a circular area (left) in magnetic fluid *KTF10-04* for  $t_p = 180$  s results in a darker spot as compared to the surrounding fluid when the whole field of view is imaged (right).

be limited to a circular spot with a diaphragm, which can be controlled with a switch on a microscope. If, after some time  $t_p$  of photobleaching, the whole field of view is suddenly exposed, an image of fluorescence intensity distribution is obtained.

Such measurements are performed using a diaphragm with a radius  $R = 84 \mu\text{m}$  for various photobleaching times  $t_p$ . Images are recorded with a sensitive fluorescence camera DFC310 FX from *Leica*. An example of measurement images for  $t_p = 180$  s can be seen in figure 3.28.

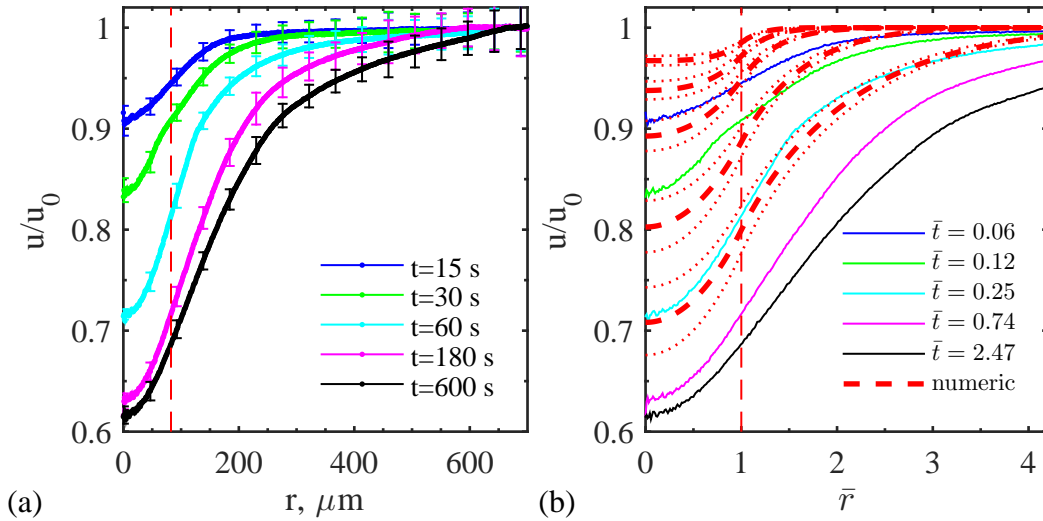


Figure 3.29: Measurements of the fluorescence intensity distribution after continuous photobleaching. (a) Experimental results for several  $t_p$  values normalized with respect to initial fluorescence intensity. (b) Experimental results in dimensionless units and their comparison with the numerical calculations using  $\varkappa$  and its error as determined in figure 3.30. Red dashed and dotted lines mark the calculated values and their confidence intervals.

The experimental results are then averaged with respect to the circular symmetry and then normalized against the initial intensity. Correction by adjusting the maximal intensity levels where necessary is also performed. The results for five different photobleaching times  $t_p$  are shown in figure 3.29 (a).

A model and its solution to describe this intensity distribution after the whole field of

view is illuminated after photobleaching time  $t_p$  has been developed by prof. A. Cēbers and prof. M. Belovs at the University of Latvia, which is introduced further. In the simplest approximation this process depends only on two factors - photobleaching speed, which is estimated to be an exponential decay with a characteristic decay time  $\tau$ , and diffusive transport with a diffusion coefficient  $D$ . An appropriate 2D model of circular symmetry is then defined with equations

$$\begin{cases} \frac{\partial u}{\partial t} = D \cdot \frac{1}{r} \frac{\partial}{\partial r} \left( r \frac{\partial u}{\partial r} \right) - \frac{1}{\tau} u & 0 < r \leq R \\ \frac{\partial u}{\partial t} = D \cdot \frac{1}{r} \frac{\partial}{\partial r} \left( r \frac{\partial u}{\partial r} \right) & r > R \end{cases}, \quad (3.21)$$

where  $R$  is the radius of the illuminated circle and  $\tau$  the decay rate of photobleaching and  $u$  is the fluorescence intensity. At  $t = 0$ , the fluorescence intensity is  $u = 1$  for all  $r$ .

This system of equations is transformed to a dimensionless form by defining  $\bar{r} = r/R$  and  $\bar{t} = t/\tau$  and introducing a dimensionless parameter

$$\varkappa = \frac{R^2}{D\tau}, \quad (3.22)$$

Equations in (3.21) can be solved for  $\bar{t} \rightarrow \infty$ , and the solution gives

$$u = \begin{cases} \frac{2u_0 I_0(\sqrt{\varkappa} \cdot \bar{r})}{\sqrt{\varkappa} \cdot I_1(\sqrt{\varkappa})} \cdot \frac{1}{\ln \bar{t}} & 0 < \bar{r} \leq 1 \\ \frac{2u_0}{\ln \bar{t}} \left( \frac{1}{\sqrt{\varkappa}} \frac{I_0(\sqrt{\varkappa})}{I_1(\sqrt{\varkappa})} + \ln \bar{r} \right) & 1 < \bar{r} < 3.4\bar{r} \end{cases}, \quad (3.23)$$

where  $I_0$  and  $I_1$  are the modified Bessel functions of the first kind.

It is interesting to notice that for large  $t$  the following relationship for intensity proportion is valid

$$\frac{u|_{r=1}}{u|_{r=0}} = I_0(\varkappa), \quad (3.24)$$

where  $u|_{r=1}$  and  $u|_{r=0}$  are respectively the intensities at the center and at the border of the illuminated radius. This relationship can be exploited to find the dimensionless parameter  $\varkappa$ .

This proportion is calculated for the different photobleaching times  $t_p$  and can be seen in figure 3.30 (a). Results indicate that this proportion seems to saturate around a value  $\frac{u|_{r=1}}{u|_{r=0}} = 1.14 \pm 0.02$ . Using this value and (3.24), the dimensionless parameter is found and is  $\varkappa = 0.54 \pm 0.08$ . However, to find the diffusion coefficient, the unknown photobleaching decay rate is needed.

The photobleaching decay rate  $\tau$  can be tentatively estimated from an experiment. Instead of observing magnetic particles in a liquid sample where they are free to move, it is possible to dry them on a microscope glass. Then, continuously photobleaching this region should allow us to find the decay rate, as the particles are not allowed to move, so no new particles are arriving. This is realized in an experiment, which is summarized in figure 3.31. Calculating the average intensity dynamics during photobleaching and fitting them with a decaying exponent gives an estimation for the characteristic decay rate  $\tau = 243$  s.

Using (3.22) and the measured and calculated values, one finds  $D = (5.3 \pm 1.0) \cdot 10^{-7}$  cm<sup>2</sup>/s. This value is around ten times larger than the one measured with the dynamic light scattering, but not as much as in § 3.2. To verify the model at least in some

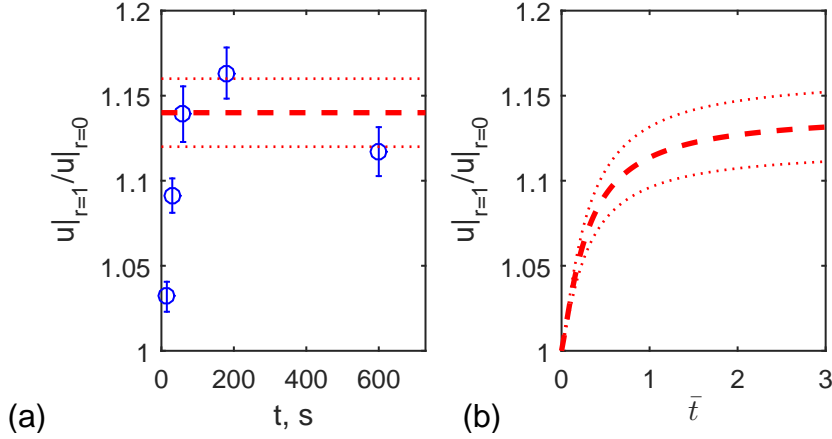


Figure 3.30: Determination of the dimensionless parameter  $\varkappa$  from (3.24). The obtained value is  $\varkappa = 0.54 \pm 0.08$ . Experimental results are shown in (a) and the numerical simulation results in dimensionless units with a comparable plot-size is shown in (b).

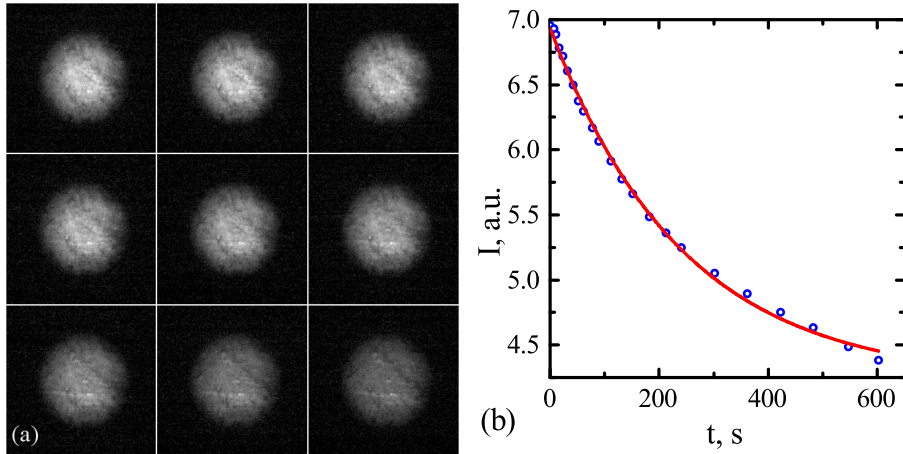


Figure 3.31: Experimental determination of the photobleaching decay rate  $\tau$  by photobleaching a dried sample of magnetic fluid *KTF10-04*. (a) Image snapshots during photobleaching. (b) Fitting average intensity decay with an exponent  $I = A \cdot e^{-t/\tau} + C$  and obtaining  $\tau = 243$  s

way, numerical calculations are performed with a program developed by prof. A. Cēbers. First, the intensity distributions for the various photobleaching times are calculated. Their comparison with the experimental results, transformed to dimensionless units, can be seen in figure 3.29 (b). It is visible that both results have qualitative resemblance, however it seems that the decay rate  $\tau$  has been overestimated. A similar conclusion can be found when looking at (b) of figure 3.30, where the proportion  $\frac{|u|_{r=1}}{|u|_{r=0}}$  is showed. Having the same limits of plot scales with respect to dimensional quantities at (a), the dynamics in experiments seem to happen faster, meaning once again that the decay rate  $\tau$  has been overestimated. However, if  $\tau$  is decreased, the diffusion coefficient  $D$  should increase, meaning that the difference against the DLS measurement would become larger and would raise further questions.

The photobleaching effect in reality is much more complex and, first of all, is very dependent on the environment around it [19]. Hence, decay rate estimation is not necessarily

correct. Additionally, the model is two-dimensional and is photobleaching a sharp circle. In reality, it is a volume with obscure boundaries being exposed to three-dimensional effects.

All these effects should be taken into account to improve the method, which should be particularly interesting as a simple reference method, as it does not ask for investment in expensive improvements for the experimental system as compared to conventional FRAP or similar systems.

### 3.6 Summary of results

The aim of this chapter was to determine the reasons behind the unusually large effective diffusion coefficient encountered in the study of the magnetic micro-convection in chapter 2. In § 3.2 it was proved that gravity effects can not be neglected even in thin cells, if miscible fluids have slightly different densities. Starting from moderate gravitational Rayleigh number values ( $Ra > 100$ ), which, as shown in § 3.2.5 govern this process, a convective motion inside the cell appears and pushes the denser fluid under the other. When observing from above, the depth averaged concentration smearing around the interface develops proportionally to  $\sqrt{t}$ , resembling a diffusive behavior with a larger diffusion coefficient which depends on  $Ra$ . Afterwards, eliminating the gravitational influence by turning the cell with the denser fluid below with respect to the gravitational field, it was possible to determine the diffusion coefficient from the interface smearing process via direct microscopy observation.

Table 3.2: Comparison of diffusion coefficient values for magnetic fluid *D107* obtained with various methods.

Method	$D, \cdot 10^{-7} \text{ cm}^2/\text{s}$	Sensing mech.
<b>FRS § 3.3</b>	2.3	Intensity
<b>DLS § 3.4</b>	2.45	Intensity
<b>Microscopy</b>	5.5	Volume

In table 3.2 results from diffusion coefficient measurements of magnetic particles in magnetic fluid *D107* using different methods available are compared. It can be seen that the values from the conventional forced Rayleigh scattering (FRS) and dynamic light scattering (DLS) techniques agree within error limits, while there is a notable (two times) difference between these values and the measurement of the concentration smearing using a microscope. However, in authors' opinion, it is incorrect to compare them directly because of the polydispersity of the magnetic fluid. These reasons were already discussed while comparing parameters of magnetic particle size distributions obtained with various methods and described in § 1.2. To remind, the difference lies in different dependencies between the measured physical quantities and particle size. In other words, if a single parameter is deduced from measurement, then it describes the mean value of the system. But the corresponding size depends on the physical connection between this measured value and size.

In this case, FRS and DLS methods measure the intensity changes of light scattered by the sample, while in microscopy light absorption by particles is detected and it depends on the volume concentration. As already mentioned in § 1.2, intensity is proportional to  $d^6$ , while volume concentration only to  $d^3$ , meaning that the actual difference between diffusion coefficients is smaller. To see if this explains the difference, it is convenient to convert the diffusion coefficients to the corresponding hydrodynamic diameters.

Takings average  $D^{\text{int}} = 2.4 \cdot 10^{-7}$  cm<sup>2</sup>/s for intensity weighted measurements and  $D^{\text{vol}} = 5.5 \cdot 10^{-7}$  cm<sup>2</sup>/s for volume weighted, one finds hydrodynamic diameters  $d_H^{\text{int}} = 17.8$  nm and  $d_H^{\text{vol}} = 7.9$  nm using equation (3.2) with  $k_B T = 4.1 \cdot 10^{-14}$  erg and  $\eta = 0.01$  P. From calculations in § 1.2.2 it can be deduced that for  $d_H^{\text{int}} \approx 17$  nm the characteristic diameter of the log-normal distribution (defined in (1.2))  $d_0 \approx 9$  nm, which is still larger than volume weighted diameter  $d_H^{\text{vol}} = 7.9$  nm. Hence, additional effects must be adding up for this difference. One of the possible causes can be effects of free citrate ions present in the magnetic fluid, as the determination of diffusion coefficient with microscopy in § 3.2.5 was done for magnetic fluid and distilled water pair with free citrate concentrations 0.18 M and 0 M, respectively. Unfortunately, further measurements were not performed during this study, leaving determination of influence of this effect an open question.

## *Chapter 4*

# Instabilities in phase separated magnetic fluids

An interesting phenomenon associated with magnetic fluids is their ability to undergo a phase separation process. That is, a colloidal suspension of homogeneously dispersed magnetic particles becomes a biphasic system. This can be induced by applying an external magnetic field, increasing the ionic strength, decreasing the temperature or increasing the particle concentration. The investigations here are primarily limited to the cases where liquid drops of a much higher concentration in magnetic particles form along the initial magnetic fluid. This is achieved with an increase of the ionic strength with or without applying a strong magnetic field for some time.

The first observations of phase separation in magnetic fluids were done in the late 1970s [87]. Since then a notable work has been devoted to characterize the different parameter influence on the phase separation process. The here relevant experimental studies on ionic concentration induced phase separation included determination of process phase diagrams [88] and the threshold values for phase separation [16], which were later reevaluated by including concepts of Liquid-Gas transitions [89] and gels [90]. Induced phase separation turned out to be a useful tool in creating monodispersed magnetic fluids [18]. However, even today a full understanding and control of phase separation using ionic concentration increase is missing.

In parallel, after first theoretical models in early 1980s [91], even a larger interest was attributed to magnetic field induced phase separation, because it corresponds to a peculiar type of phase transition that includes long range interactions. However, these effects have a limited importance for this study, because it happens at large fields, while here only the obtained droplets are important.

In this chapter the main focus is on the study of individual drops of the concentrated phase of the magnetic fluid in different magnetic field configurations. Such drops correspond to a concept of a magnetic drop in a non-magnetic medium or non-magnetic drop in magnetic medium. These systems have been studied both experimentally and theoretically and their fundamental concepts can be found in [11].

Several experiments have been performed with drops in phase separated magnetic fluids. The initial studies revealed a shape instability of the drop while increasing a homogeneous magnetic field [92], which has hysteresis if magnetic properties are strong enough [93]. Simultaneously, it was showed how a group of such drops can create hexagonal patterns that can be detected with light scattering [94]. Later, magnetic drops were exposed to rotating magnetic fields, where another shape anisotropy with characteristic spikes similar to peak instability was detected [4]. It was followed by a study where a phase diagram of shapes in a rotating field was marked for the first time [95].

Alternatively, magnetic drop model can be realized using magnetic emulsion, which con-

sists of a magnetic and an immiscible non-magnetic fluids and has recently drawn a wider attention. Single drop experimental and numerical studies for uniform fields show discrepancies from previous models at large fields [96] or include gravitational effects [97], while multi-drop systems investigate the effects of drop volume ratio [98]. Also experiments in rotating field have been performed. Experiments on drop arrays reveal back and forth motion and offer mixing applications [97], while single droplet observation in different conditions show direct visual similarities with experiments in phase separated magnetic fluids [99]. However, all these systems have a notable difference as the obtainable surface tension is at least several orders of magnitude larger than in phase separated systems.

Effects in magnetic drops can be characterized with a dimensionless magnetic Bond number  $Bm$ , which compares magnetic and surface forces and is defined [11]

$$Bm = \frac{M^2 \left(\frac{3V}{4\pi}\right)^{1/3}}{\sigma}, \quad (4.1)$$

where  $V$  is the volume of the drop,  $M$  is the magnetization and  $\sigma$  - surface or interface tension. It is usually assumed that the drop volume is constant, which means that  $\left(\frac{3V}{4\pi}\right)^{1/3}$  can be substituted with magnetic drop initial radius  $R_0$ . In low field, magnetization  $M$  for a drop can be found by

$$M = \frac{\chi H}{1 + \chi N}, \quad (4.2)$$

where  $H$  is the magnetic field,  $\chi$  is the susceptibility and  $N$  is the coefficient of the demagnetizing field, which is shape dependent.

Except for ellipsoids, an analytic description of  $N$  is usually hard, which makes it difficult to calculate  $Bm$ . Instead, typically a simpler dimensionless quantity, which is commonly also called Bond number in literature [4, 96], is defined using measurable or estimable quantities  $Bm_H = \frac{H^2 R}{\sigma}$ . In this work it is made distinguishable by adding a subscript index  $H$ . For a more quantitative comparison a value that characterizes magnetic properties (susceptibility  $\chi$  or permeability  $\mu$ ) should be given along the characteristics as a function of  $Bm_H$ .

The literature analysis shows that so far no experiments in precessing magnetic fields have been performed with phase separated magnetic fluids and drops of the concentrated phase in particular. Hence, a field for novel studies is clearly visible. To observe these phenomena, a new magnetic coil system based on a microscope is developed in § 4.2.1. A special attention is given to a precessing field, fixed at the magic angle  $\theta_m = 54.7^\circ$ , because this configuration can provide equal magnetic interaction energy for each axial component, if demagnetizing factors for them are equal. Investigation of magnetic fluid drop deformations at this magnetic field configuration is performed in § 4.3.3

Observing the behavior of a magnetic drop in a homogeneous magnetic field provides a tool to measure several important quantities, therefore hereafter some relevant theoretical considerations are noted.

### Magnetic drop in a homogeneous magnetic field

When a magnetic drop is placed in a homogeneous magnetic field  $H$ , it elongates in the direction of the field. A theoretical model for this situation is developed in [11]. The shape of this drop can be described with an ellipse with  $a$  and  $b$  being the longer and shorter semi-axes, but its behavior depends on a dimensionless magnetic Bond number  $Bm$ , which is defined

The shape of a magnetizable fluid drop in a homogeneous magnetic field results from a minimization of total energy (both from magnetic and surface origin). Assuming an ellipsoidal shape for the drop and keeping its volume constant, the under field shape can be described with the following formula [92, 100]

$$\frac{H^2 R}{\sigma} = \left[ \frac{4\pi}{\mu - 1} + N \right]^2 \frac{1}{2\pi} \frac{\left( \frac{3-2e^2}{e^2} - \frac{(3-4e^2) \arcsin e}{e^3(1-e^2)^{\frac{1}{2}}} \right)}{(1-e^2)^{\frac{2}{3}} \left( \frac{(3-e^2)}{e^5} \ln \left( \frac{1+e}{1-e} \right) - \frac{6}{e^4} \right)}, \quad (4.3)$$

where  $e$  is the eccentricity of an ellipse, defined as  $e = \sqrt{1 - \frac{b^2}{a^2}}$ ,  $\mu$  is the magnetic permeability, which is connected to the susceptibility  $\mu = 1 + 4\pi\chi$ , and  $N$  is the demagnetizing coefficient, which can be expressed for a prolate ellipsoid of revolution in the following way

$$N = \frac{4\pi(1-e^2)}{2e^3} \left( \ln \frac{1+e}{1-e} - 2e \right). \quad (4.4)$$

This model is valid for weak fields, when magnetization of the magnetic fluid grows linearly with the applied field. When the field is turned off, magnetic drop relaxes to its initial spherical shape. Relaxation speed depends on the viscosities of the dilute magnetic fluid  $\eta_d$  and of the concentrated phase  $\eta_c$  and their interface tension  $\sigma$ . This process, if the shape of a drop is sufficiently close to a sphere, can be described with an exponential decay with a decay time  $\tau$  [101], which can be found by

$$\tau = \frac{R(16\eta_d + 19\eta_c)(3\eta_d + 2\eta_c)}{40\sigma(\eta_d + \eta_c)}. \quad (4.5)$$

These relationships allow one to characterize the phase separated magnetic fluid by performing an elongation and subsequent relaxation experiment with a drop of the concentrated phase, which is done in this study in § 4.3.2.

## 4.1 Preparation of phase separated magnetic fluids

In this study two of the methods mentioned earlier in the chapter introduction are used for inducing phase separation in magnetic fluids. Those are increase of the ionic strength and an eventual application of an external magnetic field. Both of them are carried out in order to obtain suitable drops for experiments in § 4.3, where a single drop with a diameter of a few tens of microns per field of view is desired.

As the process of phase separation is still poorly understood, the appropriate sample preparation is a typical trial and error process. Samples are either prepared by the experienced chemists of Paris lab or following their advices. Two magnetic fluids are used here. First is magnetic fluid *D107*, which was initially prepared for this purpose, as it has a very high initial ionic strength, but it was also used for various experiments throughout this work. Here its salt concentration is largely increased by adding sodium chloride. The second is magnetic fluid *p146*, which is prepared with the same size-sorting method [18], but is size-sorted to have larger magnetic particles and the nature of the added salt is different.

At first, it is tried to induce the phase separation in both samples by increasing the ionic strength. For *D107*, following a recipe advised by chemists it is done by adding 25  $\mu\text{L}$  of 4 M NaCl solution to a 2 mL sample, which corresponds to a 0.05 M addition. The quantity of concentrated phase obtained by phase separation is too small to allow experiments. It is

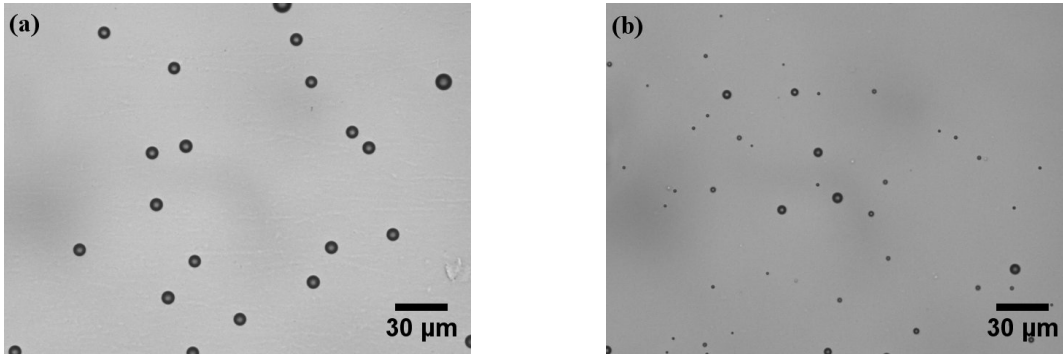


Figure 4.1: Phase separated magnetic fluid - darker droplets of the concentrated phase are surrounded with dilute coexisting magnetic fluid. (a) *D107*. (b) *p146*.

then tried to apply a magnetic field by putting samples on one of the two different permanent magnets for some time. Magnet 1 is small and strong, having  $H_{1l} \approx 2000$  Oe near its surface, while the magnet 2 is larger and creates a weaker but more homogeneous field  $H_2 \approx 650$  Oe. This allows to induce phase separation and to produce concentrated droplets in appropriate quantity. For example, after leaving a cuvette of the sample for 36 hours on magnet 2, many drops of the concentrated phase with an average diameter  $d \approx 7 \mu\text{m}$  are formed, as can be seen in figure 4.1 (a). However, it turns out that these droplets are metastable and shrink over time. This effect and the property change during it is studied in § 4.3.2.

Phase separated magnetic fluid *p146* samples are made by simply adding an ionic liquid ethylammonium nitrate (EAN). Ionic liquids can be defined as liquid salts. They have interesting properties that have recently drawn an increasing attention for their possible use in chemical industry [102]. In Paris lab the interest lies in using ionic liquids instead of usual solvents in magnetic fluids [103]. Nevertheless, here EAN is used because it is formed of larger monovalent ions as compared to NaCl. Of three different EAN concentrations tried, namely 0.58 M, 1.0 M and 1.5 M, only the last one produces observable phase separation without an external field. An example of obtained droplets is visible in figure 4.1 (b). Average diameter varies from 1 – 7  $\mu\text{m}$ . As compared to *D107*, the droplets of this magnetic fluid do not decrease in size with time. On the contrary, their size is slowly increasing when exposed to magnetic fields during experiments. However, this effect is small, if the droplets are not kept under field too long

For experimental observation magnetic fluid samples are placed in two part quartz cuvettes of 100 or 200  $\mu\text{m}$  thicknesses from *Hellma Analytix*. Cuvettes are filled using plastic pipettes, which allow to extract specific part of the magnetic fluids in order to maximize the amount of the concentrated phase resulting in the cuvette. After filling they are sealed with *Apiezon N* vacuum grease in order to eliminate evaporation and microflows.

The concentrated phase has a larger particle volume fraction than the surrounding magnetic liquid, thus it is denser, therefore drops sediment towards the bottom wall of the cuvette. In a case of a dirt or a scratch present on this wall, the drop tends to get stuck, making it difficult to continue the experiments. Yet, in most cases drops in the phase separated *D107* only rest close to this wall. It is different with *p146*. In the first experiments after obtaining the mixed sample from chemists it seemed that the drops are a bit "stickier". Nevertheless, experiments could be performed taking a special care to verify if the drops have not adhered. However, after a few days the situation turned bad and it became impossible to find a single drop which was not stuck, as can be seen in figure 4.2. No solution was found, although

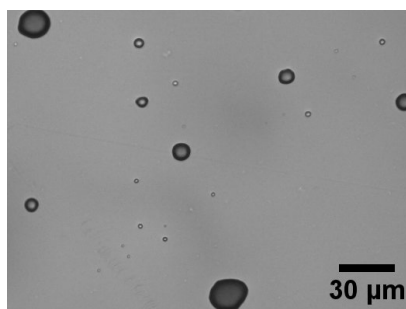


Figure 4.2: Drops of phase separated magnetic fluid *p146* get adhered to the cuvette wall, forcing to stop experiments.

careful cleaning of cells with hydrochloric acid to remove adhesion centers and using a UV filter for illumination to exclude photo-degradation effects were tried, suggesting that these effects might be connected to some slow transformation or aging effect. These problems in combination with a limited amount of time, resulted in smaller amount of experimental data.

## 4.2 Methods for experimental studies of phase separated magnetic fluids

This chapter, as introduced earlier, is focusing on experimental studies of phase separated magnetic fluids. General studies can be performed using scattering techniques, including small angle neutron or x-ray scattering experiments [17] or magnetic resonance method [104]. However, here, as mentioned in the introduction of the chapter, it is desired to study the individual drops of the concentrated phase. For that a suitable experimental system, based on microscopy methods, is necessary.

The Riga lab is equipped with a custom made magnetic coil system which can be fitted on a motorized stage of an inverted microscope [105]. Four water cooled coils are located on the microscope stage. With a computer control they can create various alternating field configurations in the plane of observation. Additionally, a small pair of coils is present in the system to create static fields in the direction perpendicular to the sample cell. This system is a powerful tool that is used mainly for magnetic microrheology studies. However, it has several drawbacks. First and the major drawback is that the magnetic field in the direction perpendicular to the cell can be controlled only manually, hence no automatic field adjustment with precessing fields is possible. Second, the coil setup is positioned on the microscope stage, forcing to use an objective extender to lift it to the plane of sample. This prohibits or influences the use of several advanced microscopy methods, namely differential interference contrast (DIC) [54] and fluorescence microscopies. Besides, there was no suitable equipment for such studies in the Paris lab, but an available microscope with a computer that could be adapted for experiments.

### 4.2.1 Development of a coil system

Considering previously mentioned factors, it was decided to develop a new coil system together with an associated control unit that can be used with the available *ZEISS* Axio Observer.D1 microscope in Paris lab. Taking the system in Riga [105] as the starting point,

design and technological changes in preparation are made to suit the experimental needs, while trying to entirely use the already available parts, devices and solutions.

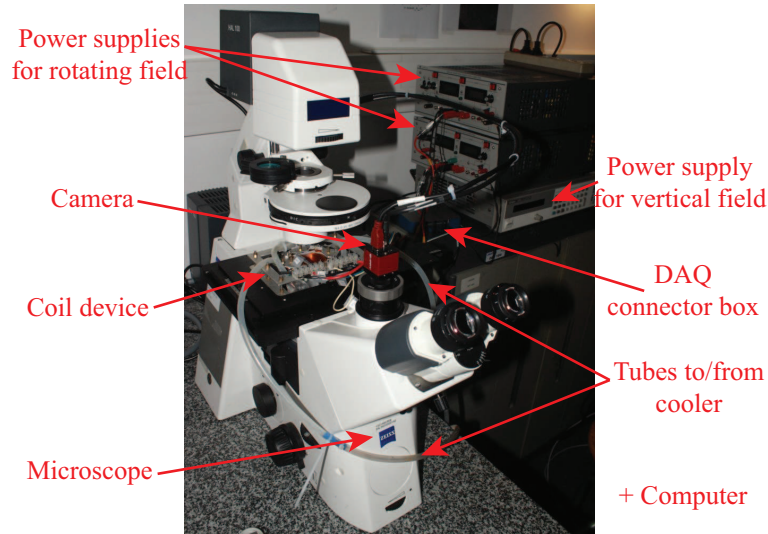


Figure 4.3: The coil system and its components, developed for experimental investigation of phase separated magnetic fluids.

A description of the produced system, which can be seen in figure 4.3, is given hereafter. It is divided in separate sections for coil device, magnetic field generation, visualization & recording and synchronization & control.

### Coil device

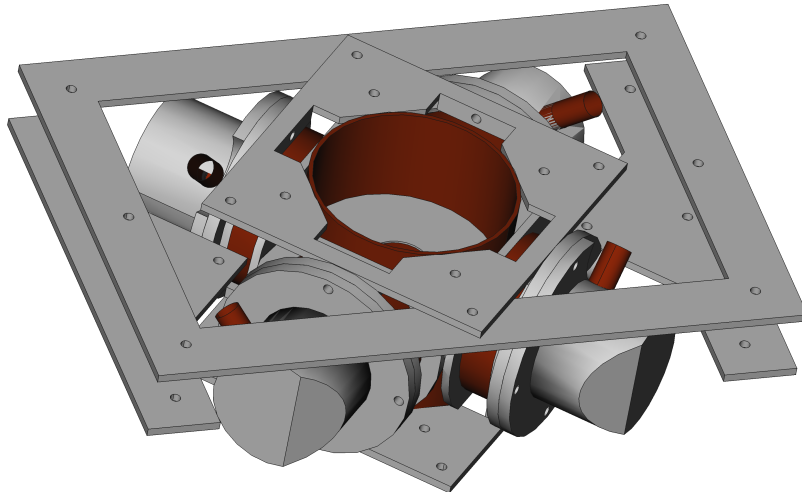


Figure 4.4: A 3D model of the coil device, including device frame, sample holder, coil holders with cooling units and coils.

The coil device design has to take into account the following concepts and limitations. First, the device is designed to fit in the insert's place of a microscope stage *Leica* 432016 – 0000 – 000 in a way that the level of the sample stays the same as with an original insert.

Second, the space of the sample holder is adapted to fit samples of a size up to 50 mm, basing on the commonly used Quartz cuvettes from *Hellma Analytics* (height is 45 mm). Additionally, the inner diameter of the coils for the vertical field is limited by the outer diameters of the objectives and the field of view necessary. Mostly a 40x objective with a 38 mm outer diameter is expected to be used. Desired magnetic field root mean squared value  $H_{\text{rms}}$  should be at least few tens of oersteds in all directions, while frequencies up to  $\approx 500$  Hz should be possible. To facilitate this, water cooling can be implemented.

A suitable 3D model of coils that takes into account these demands is made with *FreeCAD* software and can be seen in figure 4.4. The model is developed in parallel with magnetic field simulations using *FEMM* (see appendix C.1) to reconcile the coil parameters, while getting a homogeneous magnetic field in a volume of few millimeters around the center of the sample.

After model is confirmed, it is produced. The individual parts are made by José Carlos Gomes in the workshop of the PHENIX lab in Paris following the drawings from the model. Coils are wound manually with a copper wire (diameter  $d = 0.54$  mm), fixing each layer with a *Formvar* tape. Each cooling unit is fixed to a corresponding coil with screws and sealed with silicone sealant. Outlets of cooling units are interconnected with a silicone tubing making a circuit to be connected to a cooler. Assembling all parts according to the model leads to a coil device which can be seen in figure 4.5.

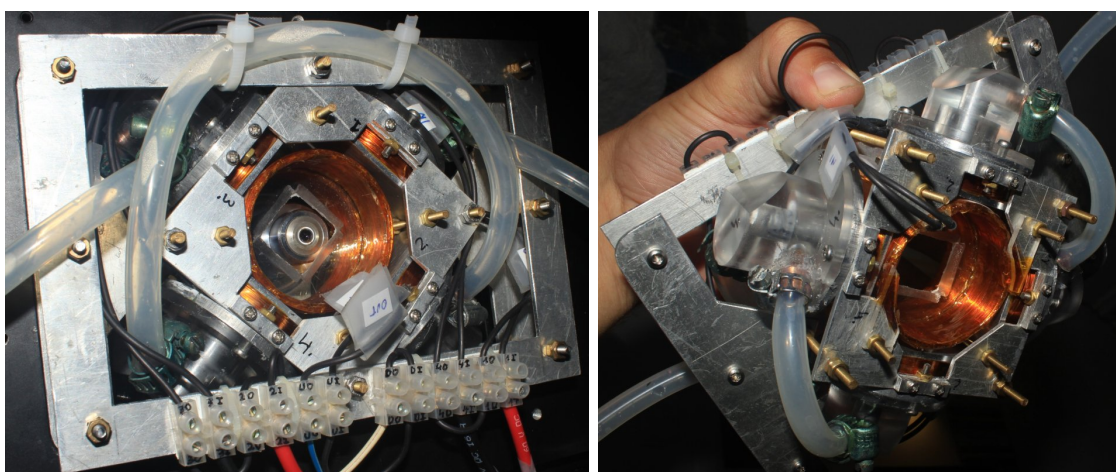


Figure 4.5: Coil device as viewed from top (left) when fixed on a microscope and from bottom (right), when held in hand.

Coils are then calibrated with a *Walker* MG-4D gauss-meter. Each pair of rotating field coils creates a  $H = 16.5$  Oe magnetic field for each ampere of current flowing in them and, with cooling on, they can be used up to  $I_{\text{max}} = 3.5$  A, which gives up to almost 60 Oe. Coils for the vertical field produce  $H = 42.5$  Oe for  $I = 1$  A current, which is also the maximal current, as they have no water cooling.

The cooler is made from an electric circulator pump and a water container, which can be connected to the coil cooling circuit with plastic tubes.

### Magnetic field generation

Controllable power supplies are used to control the current flow in the coils. For rotating field it is done in a very similar manner as in the Riga setup [105]. That is, each of two *KEPCO* BOP 20-10ML power supplies is connected to a pair of coils for rotating field. The

current is controlled by a voltage on a programming input. The voltage signal is created by a *National Instruments* data acquisition (DAQ) system consisting of PCIe-5323 card and SCB-68a connector block, which allows up to four analog outputs and can be controlled from computer. A rotating field can then be simply produced by applying a sinusoidal signal in both pairs of coils with a  $\pi/2$  phase difference.

The current in the coils of the vertical field is generated by a *Agilent* 6632B power supply. It has a RS-232 connection, which allows a command based control from computer.

An additional current measurement is done on fixed resistances that are inserted in series with each pair of coils. Respective voltage drops are registered on computer using differential connections on the same DAQ system.

### Visualizing & recording

A camera is necessary to record the dynamics of interest. It is chosen to have a maximum functionality without large financial investment following these considerations This camera should use a FireWire data connection, which is the fastest of those already present in the computer and it matches the hard disk drive writing speed, allowing a continuous recording. The maximal frame rate should be around 50 Hz to allow recording of slow dynamics with higher precision, while a lower frame rate is suitable for time-averaged processes. This limits the image size to around 0.3 mega pixels, what is suitable, as different objectives can be used to achieve a greater resolution. Finally, the camera has to be mounted on a C-mount and have an external trigger for synchronization.

An appropriate choice is *AVT* Guppy F-046B, which fulfills all these criteria. It is an 8-bit grayscale camera with maximal resolution  $780 \times 582$  px at 49 Hz, which can be increased by selecting a smaller region of interest. Camera is fixed on the microscope with a 0.5x C-mount and can be control from computer using *National Instruments* Vision Acquisition Software IMAQdx drivers.

### Synchronization and control

The experimental system is managed from a computer with a program written in Lab-View. It allows a synchronous control and data acquisition of magnetic coils and the camera, as the components have been chosen to be compatible with this programming language.

The front panel and the main view of the block-scheme of this program are shown in appendix B.2. It is developed to permit a continuous experiment. Camera parameters can be chosen before each recording, while magnetic fields can be changed in real time. When recording is started, the camera and magnetic field data recording triggers are synchronized with the start of the voltage signal generated for the magnetic field creation. Several automatic options of magnetic field configurations are possible, including rotating field and precessing field at the magic angle. If magnetic field value is changed in the program, the actual signal change happens with a delay. For the coils of rotating field it happens because the corresponding signals are generated in predefined lengths. This becomes essential also when very low frequencies are used. In comparison, for the third pair of coils the delay corresponds to the time needed by the *Agilent* power supply to process the command sent via RS-232 cable. Nevertheless, these delays are not important in the measurements of interest. Recorded images and data together with an info file are written in an initially specified directory.

## 4.2.2 Verification of the coil system

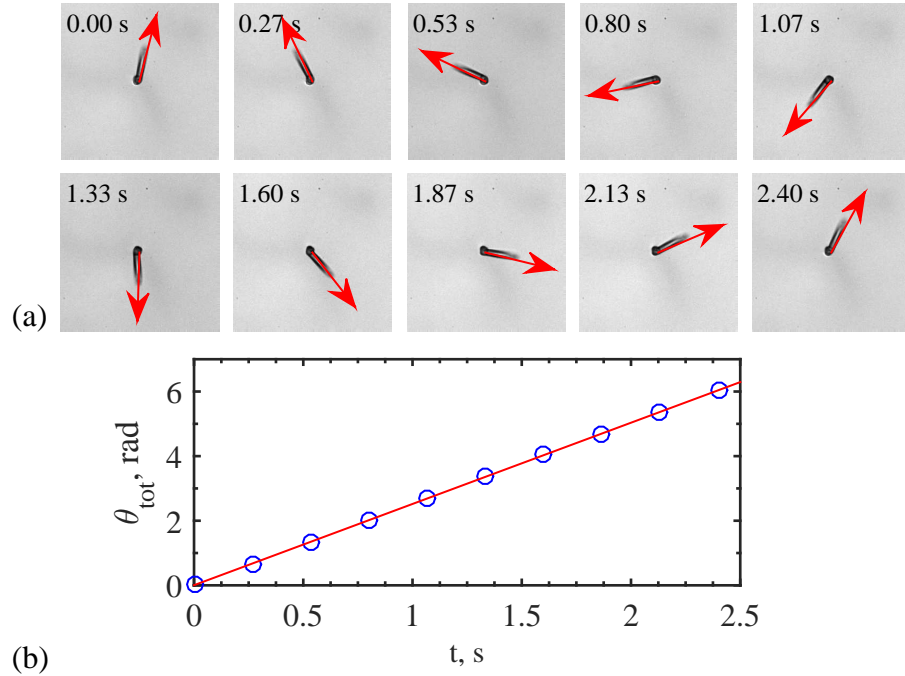


Figure 4.6: Verification of the experimental system with a partially stuck droplet under a slow precessing magnetic field at  $f = 0.4$  Hz. (a) Series of images with acquisition times. Red arrows mark the direction of the rotating component of the magnetic field as calculated from the measurement data. (b) Accumulated angle  $\theta_{\text{tot}}$  as a function of time. Blue circles are calculated data, while red line is a linear fit.

To verify the developed system, some test measurements are necessary. This is done using a sample of phase separated magnetic fluid, where a droplet is partially stuck to the lower surface of the cell. Then a slowly precessing  $f_H = 0.4$  Hz magnetic field fixed at the magic angle with a value  $H_m = 18$  Oe is applied. The droplet elongates and follows the magnetic field, while staying fixed with one end on the surface. The process is recorded with a camera at  $f_{\text{cam}} = 3.75$  Hz. An image series of the process can be seen in figure 4.6 (a). Corresponding magnetic field direction is calculated from the measurement data and plotted above the images using red arrows that start in the center of the stuck part of the droplet. A very good agreement between the direction of the elongated droplet and direction of the field can be seen.

Additionally, the accumulated angle  $\theta_{\text{tot}}$  for each image is calculated and its dependence on time can be seen in figure 4.6 (b). During a slow rotation  $\theta_{\text{tot}}$  should linearly increase, what can be observed. Fitting data with a linear function gives a slope which, when described with  $2\pi f$ , gives  $f = 0.400$  Hz, confirming that the droplet rotates synchronously with the field.

A more careful magnetic field calibration could be done with a 3D magnetic gauss-meter, which, unfortunately, was not accessible in the Paris lab during this study.

### 4.3 Experiments with microdrops in phase separated magnetic fluids

This section presents the experimental investigation of the phase separated magnetic fluids by microscopic observation of deformations of drops of the concentrated phase. Microdrops are deformed with external magnetic field in several configurations using the previously developed coil system (in § 4.2.1).

The coil system was made fully functional only in November 2014, due to long part production and delivery times and limited mobility opportunities. Hence, it was decided to limit the quantitative experiments during this study to the investigation of drop deformations under precessing field fixed at a magic angle, as a continuation to the work on deformations under rotating field [4]. These measurements are discussed in § 4.3.3. During this study, it was observed that depending on the method used for inducing phase separation in magnetic fluids, the drop stability is different and, surprisingly, the properties of the concentrated phase may change over time. It was attempted to characterize it by observing elongation of drops in a static field and their subsequent relaxation and this investigation is summarized in § 4.3.2.

Phase separated magnetic fluid samples in cuvettes are obtained as explained in § 4.1. Cuvette is placed on the sample holder plate inside the coil device of the coil system. Experimental measurements are controlled with the LabView program, described in § 4.2.1. As a result, image series of drop deformations and the corresponding magnetic field configuration data are obtained. Information drop parameters is extracted using image processing algorithm as described below.

#### 4.3.1 Image processing algorithm

Quantitative analysis of drops requires to characterize drop size during different stages of each experiment. This can be done manually, but it is much more efficient to use image processing techniques, as they allow to obtain more data, while automating analysis. A typical image processing algorithm that allows to access drop size information is described here below and its steps are visualized in figure 4.7. This algorithm is implemented in MATLAB® and is later used in the analysis of experiments in § 4.3.2 & § 4.3.3.

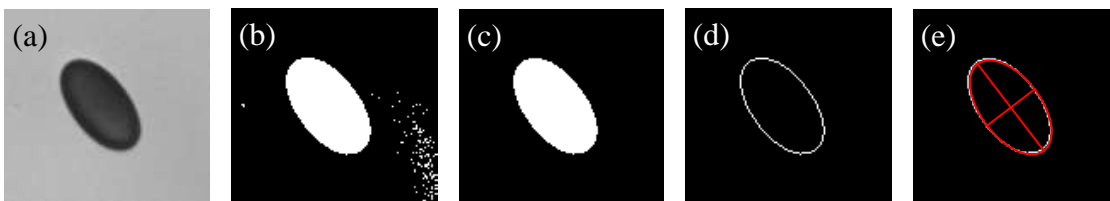


Figure 4.7: Visual representation of the image processing steps. (a) Original image. (b) Thresholded image. (c) Keeping the largest object. (d) Finding perimeter. (e) Fitting an ellipse (red).

The original image, shown in figure 4.7 (a), is undergoing the following image processing steps (letters correspond to images in figure 4.7), with appropriate MATLAB® functions in brackets

(b) It is thresholded to obtain a binary image (*im2bw*). The threshold value can be defined

automatically or chosen manually from image histograms by checking if the desired object has been recognized in all images. This value is the same for each recording.

- (c) As images usually have noise, dirt or small drops around the drop of interest, next step selects the largest object (*bwlabel*). If necessary, the holes in the largest object are filled to remove image noise or ease further analysis (*imfill*).
- (d) The perimeter of the drop is found for size characterization (*bwperim*).
- (e) The perimeter data points are approximated with an ellipse by fitting data with a least squares criterion (*fit\_ellipse* from [106]), giving ellipse parameters, their semi-axes in particular.

Using this method, drop shape characteristics can be extracted from every image.

### 4.3.2 Properties of the phase separated magnetic fluid

In order to better understand the phase separation of magnetic fluids, it is important to characterize them. The parameters of interest include volume fractions  $\Phi$ , susceptibilities  $\chi$ , interface surface tension  $\sigma$  and viscosities  $\eta$ . Finding these values is mostly important for the concentrated phase, as it can be assumed that the surrounding magnetic fluid does not change its properties, at the first order, during phase separation and its properties remains almost the same as initially.

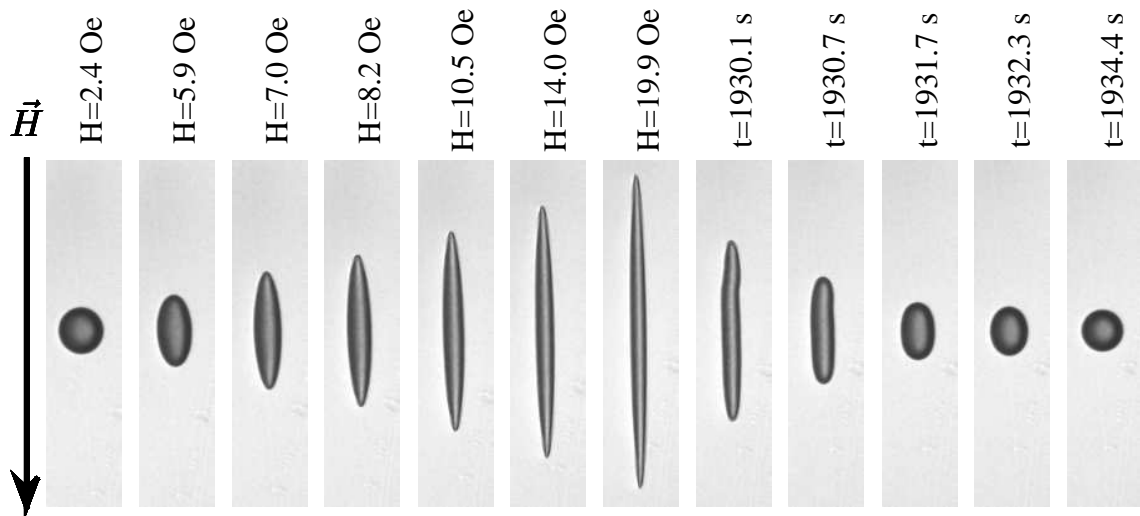


Figure 4.8: Images series of a drop elongation-relaxation measurement. Appropriate magnetic field or time values are shown. Each image is  $115 \times 25 \mu\text{m}^2$  large.

Relationships described with (4.3) & (4.5) allow to access all the searched parameters. To obtain these values, a single drop elongation-relaxation experiment has to be carried out. A sample image series can be seen in figure 4.8, where left part corresponds to elongation, while right part to relaxation process, as denoted by appropriate field or time values. During first part, a slow, stepwise increase of magnetic field is manually performed, allowing the drop to reach a steady state after each advance. After a sufficient elongation is achieved, the magnetic field is cut to zero and the droplet is allowed to relax to a spherical shape.

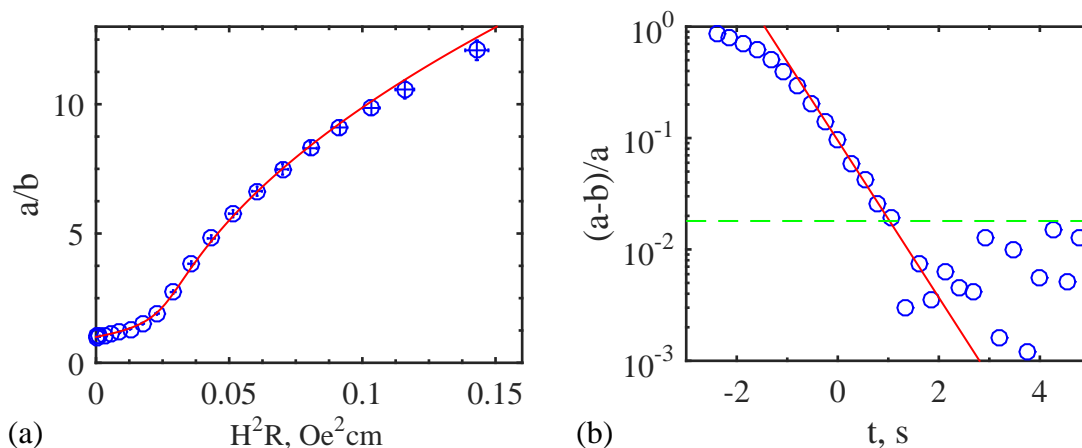


Figure 4.9: Fitting of experimental data. Blue circles mark data, red curves are fits. (a) Elongation data showed as semi-axes proportion  $a/b$  as a function of  $H^2R$ , fitted using (4.3). (b) Shape relaxation is described with normalized semi-axes difference  $(a-b)/a$  as a function of time  $t$ , which is decaying towards zero and can be fitted with  $A \cdot e^{-t/\tau}$ . Green dashed line marks the noise level below which fitting is not meaningful.

The image processing algorithm described in § 4.3.1 allows to obtain ellipse parameters, which are further used to find the searched parameters. Elongation data is plotted as semi-axes proportion  $a/b$  dependence on  $H^2R$  and can be seen in figure 4.9 (a). This is fitted with MATLAB® fitting toolbox using a custom function (see appendix A.1.3) on the basis of (4.3). The fitted curve shows a good agreement with data. Small differences can be observed for large semi-axes proportions, which is typical, because the elongated droplet starts to differ from an ellipsoid. For this example the following values for magnetic permeability  $\mu = 8.1$  and surface tension  $\sigma = 1.9 \cdot 10^{-3}$  dyn/cm are obtained.

Relaxation data are displayed with normalized semi-axes difference  $(a-b)/a$  as a function of time  $t$  and an example can be seen in figure 4.9 (b). Fitting is semi-automatized by selecting only data that are greater than noise level (marked with green dashed curve and correspond to 1/3 of a pixel), but still correspond to an exponential decay (accordingly shifting  $t$ ) and fitting them with  $A \cdot e^{-t/\tau}$ . In this example  $\tau = 0.6$  s and, if surrounding magnetic fluid viscosity is approximated with water  $\eta_d = 0.01$  P, then concentrated phase viscosity  $\eta_c = 1.77$  P, as calculated with (4.5), taking  $\sigma$  as measured from elongation data. In principle, the shape relaxation can be described also using other parameters, for example, eccentricity  $e$  or difference of semi-axes  $a - b$ , but, as the process is exponential, the decay time is the same for all of them.

Magnetic fluid *p146* with 1.5 M of EAN, as introduced in § 4.1, induces the only stable phase separation obtained in this study. Performing multiple elongation-relaxation measurements on various drops of the concentrated phase leads to rather constant values for the three parameters, which are:

- $\mu = 16.6 \pm 1.2$ ;
- $\sigma = (4.4 \pm 0.3) \cdot 10^{-3}$  dyn/cm;
- $\eta_c = 10.2 \pm 2.4$  P.

Contrary, drops from all other phase separated magnetic fluids derived from D107 were

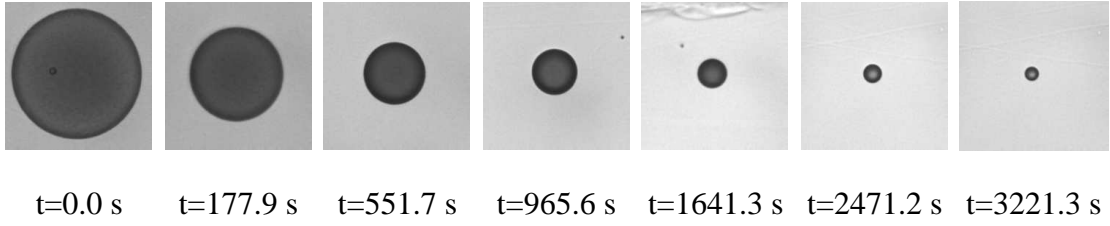


Figure 4.10: Drop of the phase separated *D017* concentrated phase is notably shrinking over time. Side of each image is  $83 \mu\text{m}$  long.

notably shrinking with time, as can be seen in figure 4.10. The obvious difference between the two cases is the method of inducing the phase separation. For all these samples it is induced with magnetic field, which apparently is creating a meta-stable state. This behavior is unexpected and was therefore additionally studied using magnetic fluid *D107* with added salt and phase separation induced with a large field by performing continuous elongation-relaxation experiments under low fields during shrinking. It was repeated for several droplets up to the resolution limit of a few image pixels.

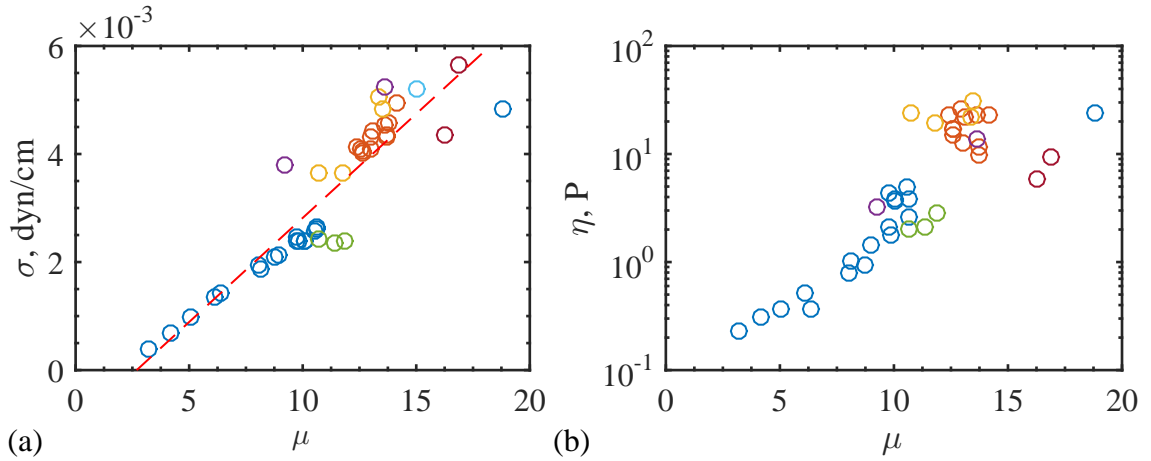


Figure 4.11: Connections between parameters of the concentrated phase. Different colors of circles denote different drops analyzed. (a) Interface surface tension  $\sigma$  as a function of magnetic permeability  $\mu$ . Red dashed line is a linear fit of all data. (b) Viscosity  $\eta_c$  as a function of magnetic permeability  $\mu$ .

Recordings were processed using the previously described image analysis and data fitting steps, which gave information on the parameter dynamics of the concentrated phase. It was observed that these parameters - magnetic permeability  $\mu$ , surface tension  $\sigma$  and viscosity  $\eta_c$  are changing in time, typically increasing while magnetic drop is decreasing. Drop size dynamics, which is not shown here, appeared to be slightly different for the several experiments, possibly because of the different initial conditions. For this reason the parameters of interest are compared against each other, namely, against magnetic permeability. These results are summarized in figure 4.11. In plot (a) the interface surface tension is shown as a function of magnetic permeability. These quantities appear to be linearly proportional. Meanwhile, the viscosity of the concentrated phase appears to grow exponentially with an increasing magnetic permeability, as can be seen in plot (b) of the same figure.

These results seem to indicate a physical pathway through which magnetic fluid returns to its initial state in zero field and might be representing a part of a phase diagram. Also a possible explanation can be added. Putting the sample in a large magnetic field induces a phase separation by lowering the osmotic pressure until an equilibrium is reached if one waits sufficiently long [91]. Then, when sample is taken away from the strong magnet and put for observation on the microscope, the system becomes out of equilibrium. If surrounding magnetic liquid returns to the equilibrium state with a high osmotic pressure faster than the concentrated phase, a pressure difference appears and the solvent starts to flow from the concentrated phase towards the surrounding liquid. This results in compression of magnetic particles, which would explain the observed increase in magnetic permeability, viscosity and surface tension. The compression continues until the pressure is balanced with particle-particle repulsion forces. Nevertheless, this should be evaluated and compared with results from further studies.

It is worth to mention that additional parameters can be obtained from the measured ones. For example, the volume fraction  $\Phi$  can be estimated from the magnetic properties using models for concentrated systems in [107, 108].

### 4.3.3 Magnetic microdrops in rotating and precessing fields

As mentioned earlier, magnetic drops have never been studied in a precessing field. Instead of tackling the wide range of possible angles, the study here is limited to the particularly interesting magic angle configuration.

To remind, magic angle is defined as the angle at which magnetic interaction energy for all axis agree. This agrees with a magnetic field configuration where the root mean squared values of magnetic field  $H_{\text{rms}}$  in all direction are the same. Precessing field is constructed of a rotating field in the plane and a static field perpendicular to it. This implies that the amplitude of the rotating field is  $H_r = H_{\text{rms}} \cdot \sqrt{2}$ , while the perpendicular field  $H_z = H_{\text{rms}}$ . The angle between them is

$$\theta_{\text{magic}} = \arctan \frac{H_r}{H_z} = \arctan \sqrt{2} = 54.74^\circ.$$

Experiments in precessing field are done in parallel with reference experiments in rotating field, which have been studied before [4]. Each measurement is started with a circular drop of the concentrated phase that is supposed to be a sphere in 3D. Magnetic field is slowly increased in a stepwise manner and the process is recorded. After reaching a desired magnetic field, the measurement is either finished with a sudden cut of the field or with a stepwise decrease. It is tried to take the time between steps sufficiently long for the drop to reach a stable state, which is particularly important when being close to critical values. However, it is difficult to realize, because of limitations in experiment time, connected to droplet size change and sticking to the walls.

Experiments are performed with drops of concentrated phase in phase separated magnetic fluids *p146* (with 1.5 M EAN) and *D107* (with added NaCl and applied field). Drops in *p146* are preferred because their properties can be considered constant during experiments, as measured in § 4.3.2. Results of a measurement series on a single drop (*p146*) in precessing and rotating field ( $f = 100$  Hz,  $\mu \approx 17$ ) is shown in figure 4.12. Plots display the lengths of semi-axes ( $a$  denotes longer,  $b$  - shorter) of an ellipse best fit as a function of magnetic Bond number  $Bm_H$  together with representative images of the drop shape. The  $H_{\text{rms}}$  is used for calculation of the Bond number, which is defined in (4.1). Measurements during increasing

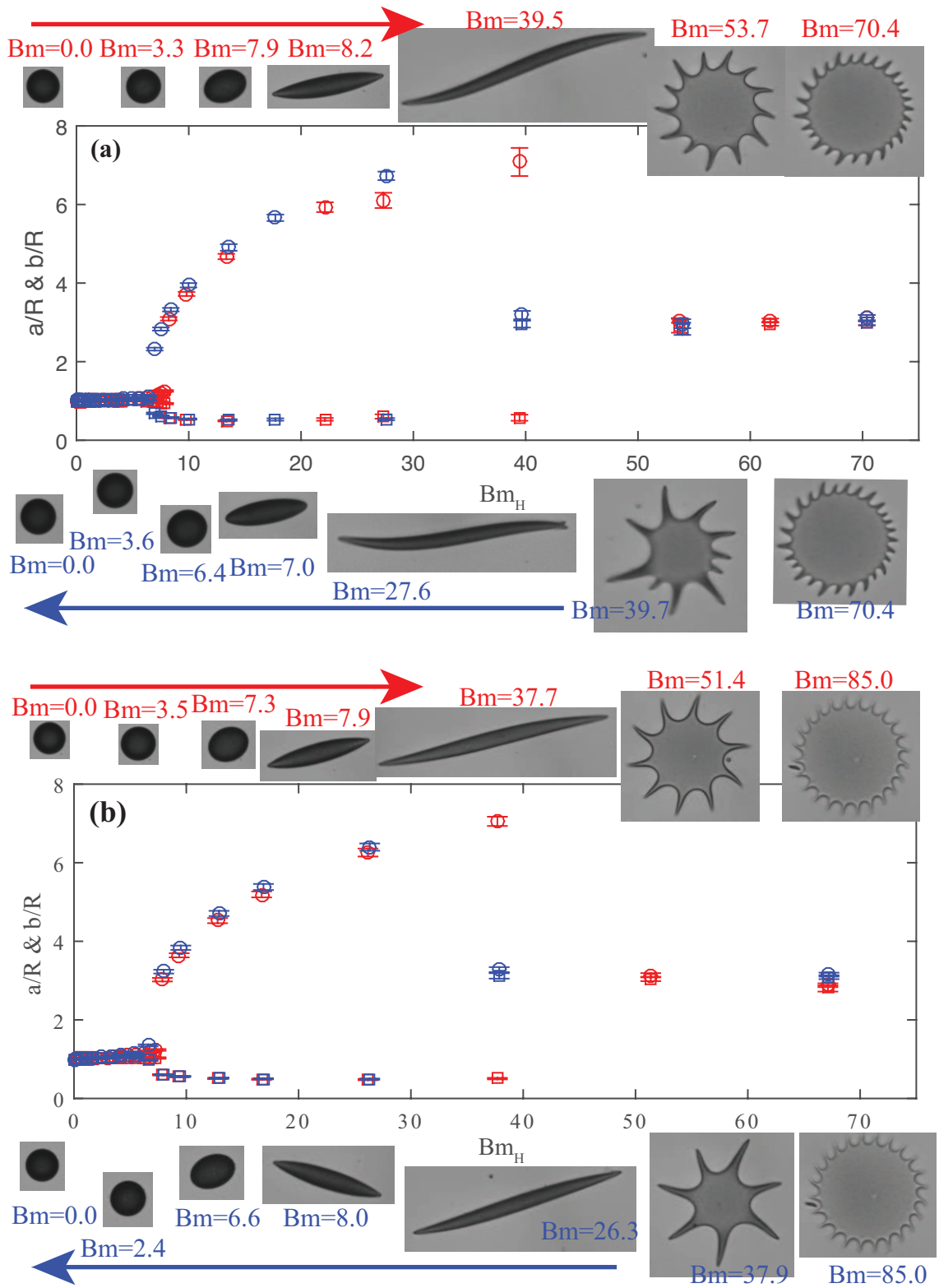


Figure 4.12: Deformation of a magnetic drop in precessing (a) and rotating (b) fields by showing normalized ellipse semi-axes as a function of Bond number together with characteristic images. Red data and labels indicate measurements during field increase, while blue - field decrease. Circles denote longer semi-axis  $a$ , while squares - shorter  $b$ .

field are indicated with red color, while during decrease - with blue. The slight increase of the drop size at zero magnetic field during experiment is taken into account in data analysis by assuming a linear change of the drop radius  $R$  over time. Here the radius has increased by 5% in a 50 minute long experiment.

Overall, results indicate no substantial differences between rotating and precessing field configurations. A drop with initial radius  $R = 8.3 \mu\text{m}$  in both cases undergoes two apparent shape instabilities. First happens at  $Bm_H \approx 8$ , when drop quickly elongates, going to a prolate shape.

The second is at  $Bm_H \approx 40$  and the very elongated prolate shaped droplet transforms to an oblate with characteristic spikes. It might seem that a hysteresis can be observed when comparing the results during increase and decrease of the field, however, the  $Bm_H$  step in measurements and the necessity to perform measurements rather quickly in order not to change the size and properties of the drops are serious constrains that disallow such a strong argument at the moment. More precise measurements for this are necessary.

These results are mostly consistent with observations and calculations in [4, 95], including the axial ratio 14 above which the second threshold happens. A greater interest is now turned to the shape deformations at small  $Bm_H$ , because it is expected to see differences between precessing and rotating field configurations. If a rotating field should steadily flatten a spherical droplet in an oblate ellipsoid, then in precessing field the droplet should keep its spherical shape constant, before the critical field is reached.

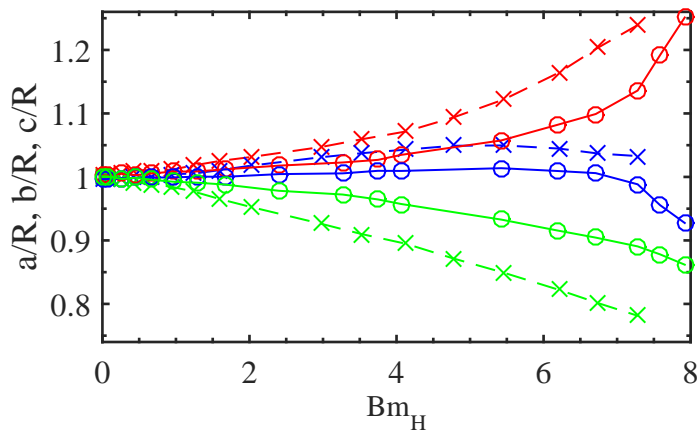


Figure 4.13: Drop size dynamics at small Bond numbers for rotating (crosses, dashed line) and precessing (circles, solid line) fields. Longer  $a$  semi-axis data are colored red, shorter  $b$  - blue. Assuming constant volume allows to calculate third semi-axis  $c$  - green.

This is inspected in figure 4.13, where the region of plot in figure 4.12 is limited to  $Bm_H < 8$  just before the first shape instability. Assuming that the drop initially has a spherical shape which is later deformed to an ellipsoid allows to calculate the third semi-axis  $c = \frac{R^3}{ab}$ , which is also shown in the graph in green. Results indicate that semi-axes  $a$  and  $b$  are equal within error limits up to  $Bm_H \approx 4$ , but they appear to slowly increase. This tendency is better notable when observing decrease in the calculated values of semi-axis  $c$ . At  $Bm_H = 4$ , in rotating field, drop semi axes  $a$  and  $b$  have increased by 6% as compared to the initial size, while in precessing field this change is only 2%, which is around the level of experimental error. This numbers are very small, but are confirmed by several measurements. For Bond number  $4 < Bm_H < 8$  the drop seems to gradually transform into a 3D ellipsoid

in both magnetic field configurations, which was not observed in [4]. There instead a critical axial ratio  $a/c = 1.5$  for transformation from oblate to prolate ellipsoid was noted. Here this transition happens from a 3D ellipsoid and can be characterized with critical semi-axes proportions in initial  $R$  units, which are  $a : b : c \approx 1.25 : 1.00 : 0.80$  for rotating field and  $a : b : c \approx 1.25 : 0.95 : 0.85$  for precessing field. In principle, this transformation from oblate/spherical shape to a 3D ellipsoid ( $4 < Bm_H < 8$ ) could be named an instability, but it is not distinguished here because of the small effect that should be confirmed with higher resolution experiments or numerical simulations.

Yet, it was expected to see a larger difference between the two magnetic field configurations. The concentrated phase is heavier than the dilute magnetic liquid in coexistence and it sediments, which is useful during size sorting step in magnetic fluid preparation [18]. In experiments described here, drops sediment on the lower wall of the cell. As they are liquid, a question appears - how true is the estimation that drops keep a spherical shape. This can be characterized using capillary length [80] estimate

$$\lambda_c = \sqrt{\frac{\sigma}{\rho_{\text{diff}}g}} = \sqrt{\frac{\sigma}{\Delta\rho\Phi g}} \quad (4.6)$$

where  $\sigma$  is the surface tension,  $\Phi$  is the magnetic particle volume fraction in the concentrated phase and  $\Delta\rho$  is the density difference between the material of magnetic particles and the surrounding liquid. Estimating  $\Phi \approx 0.25$  from literature [4, 18] and taking other values as previously gives  $\lambda_c = 21 \mu\text{m}$  which is slightly larger than the drop studied here. Hence, gravity is not completely negligible here, but its effect should be low.

A more precise comparison can be done by comparing surface and potential energies. Surface energy is given by  $E_s = \sigma A$ , where  $A = 4\pi R^2$  is the area. Potential energy adapted for this case is  $E_p = \Delta\rho V\Phi gh$ , where  $h = R$  is the height of the center of mass and  $\Delta\rho V\Phi$  is the mass of the drop with  $V = \frac{4}{3}\pi R^3$ . Comparing these, one finds the characteristic radius at which surface energy becomes equal to potential  $R_c = \sqrt{3} \cdot \lambda_c$ . This gives  $R_c \approx 36 \mu\text{m}$ , which is even larger as compared to a typical initial drop size  $R \approx 15 \mu\text{m}$ , meaning that the surface energy is larger than the potential and should resist the deformation of the initial spherical shape. Furthermore, the analysis can be extended by finding the minimum energy configuration. In microscope only a circular 2D projection can be observed and it does not give the information on the drop shape in the third dimension, which is necessary to calculate both the center of mass and the surface area, important in the energy calculations. A simple approximation of this probably complex drop shape can be made using an oblate ellipsoid, for which the shorter axis is perpendicular to the surface. This is helpful as the surface area for an oblate ellipsoid can be calculated from its semi-axes ( $a$  marks the two longer and equal, while  $c$  indicates the shorter) [109]:

$$A_{\text{ob}}(a, c) = \frac{\pi}{\sqrt{a^2 - c^2}} \left[ 2a^2\sqrt{a^2 - c^2} + ac^2 \ln \left( \frac{a + \sqrt{a^2 - c^2}}{a - \sqrt{a^2 - c^2}} \right) \right]. \quad (4.7)$$

Surface energy is then  $E_s = \sigma A_{\text{ob}}(a, c)$ , while potential energy is  $E_p = \Delta\rho \frac{4}{3}\pi R^3\Phi gc$ , as the volume of the drop is assumed to stay constant. The minimum energy configuration  $\min(E_s + E_p)$  is found for each initial radius  $R$  by changing the shorter semi-axis  $c$  length, as the longer  $a$  can be calculated with an expression using the constant volume  $a = \sqrt{R^3/c}$ . The semi-axes lengths corresponding to the minimum energy configuration are noted. The relevant case is retrieved by locating the configuration at which longer semi axis is equal to the observed one, in this case  $a = 83 \mu\text{m}$ . The initial radius is found to be  $R = 81 \mu\text{m}$  and the

shorter semi-axis  $c = 76 \mu\text{m}$ . Differences are in the order of the experimental error approving that the influence is very small and therefore concludes the discussion on gravitational effects in this particular case. Additional confirmation can be obtained when calculating the third semi-axis length  $c$  for the prolate state, which should be  $c = b$  (following the semi-axes definitions used here). Here, for Bond number  $Bm_H = 10$ , where prolate shaped droplet is already formed, the calculated  $c \approx (0.45 \pm 0.02)R$ , while  $b \approx (0.5 \pm 0.02)R$  and for both rotating and precessing fields, agreeing with the conclusions made earlier.

It should be added that gravity effects, even if not very important in these particular results, affect possible experiment improvements. This concerns the further studies of the shape dynamics. To see the small changes in the droplet shape, a higher resolution is necessary, but a limitation is put on an apparent way of improving measurement resolution via observing larger droplets. Instead a larger objective should be used or a camera with a higher resolution. Additionally, finer calibration of the generated magnetic fields might be influencing these differences at small Bond numbers. A good prerequisite for further setup improvement would be computer simulations on the initial deformations of magnetic drops at precessing and rotating fields.

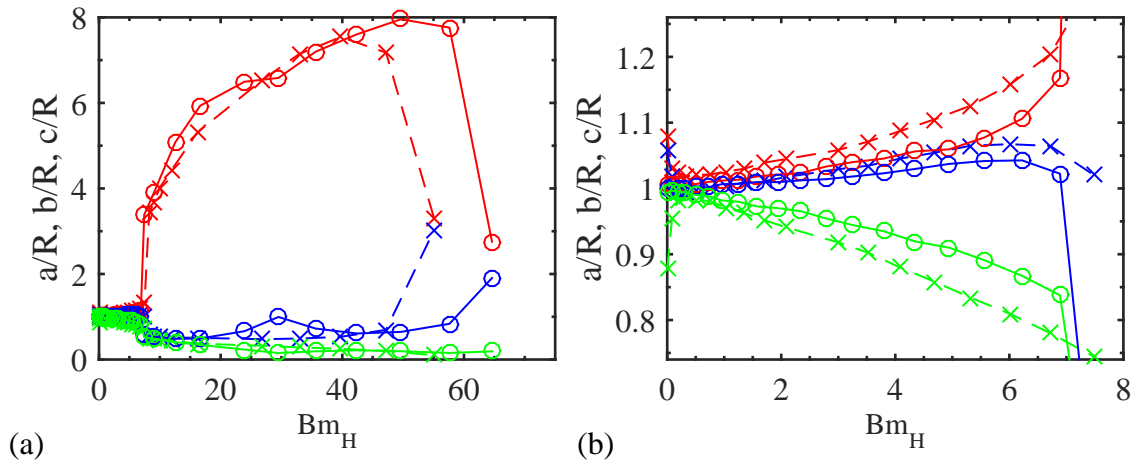


Figure 4.14: Drop size dynamics for rotating (crosses, dashed line) and precessing (circles, solid line) fields. Longer  $a$  semi-axis data are colored red, shorter  $b$  - blue and calculated third semi-axis  $c$  - green for phase separated magnetic fluid *D107* sample. (a) Whole view shows the two apparent shape instabilities. (b) View at small  $Bm_H$  shows transition to a 3D ellipsoid before having the shape instability to become a prolate.

Results with magnetic fluid sample *D107* with added NaCl and after application of a field, as shown in figure 4.14, are very similar. Measurements have to be done rather quickly in order to be able to assume constant parameters  $\sigma$ ,  $\mu$  and  $R$ . As a result, data quality is poorer, mostly because the state of a stable shape is not reached. Nevertheless, the two shape instabilities are observed and they happen at comparable  $Bm_H$ . That is reasonable, because the measured magnetic properties  $\mu = 17.2$  are close to those of *p146* sample with added EAN. In addition, also characteristics at small Bond number, shown in figure 4.14 (b), are comparable with observations in figure 4.13, including a slower size increase of  $a$  and  $b$  in precessing field as compared to rotating field and the transition to a 3D ellipsoid before the first shape instability for both field configurations.

## 4.4 Other experiments with phase separated magnetic fluids

Magnetic drop dynamics in precessing and rotating fields is only a tiny part of experiments that can be done in phase separated magnetic fluids. This framework allows one to obtain objects that are highly magnetic (high  $\chi$ ) and have a low surface tension (low  $\sigma$ ). Hence, high Bond numbers, which works as a process characteristic, can be achieved even with reasonable magnetic fields.

The designed and developed coil system allows to perform also many other experiments. Two examples that have been already tried are introduced hereafter.

### 4.4.1 Patterns in slightly precessing magnetic field

A magnetic drop confined between two glass slides under a homogeneous magnetic field that is perpendicular to the cell forms a so called labyrinthine structure [29], creating thin walls that are evenly spaced. If a large drop of the concentrated phase is put in a thin cell, it can take all the space from bottom to top in such a way agreeing with the previous condition.

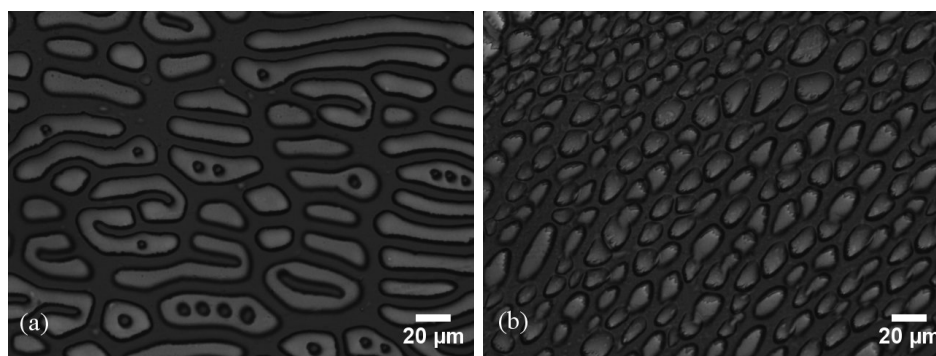


Figure 4.15: Patterns in a phase separated magnetic fluid under slightly precessing field. (a) Interconnection of labyrinth walls after adding a small rotating field component. (b) After a sudden application of a slightly precessing field.

An interesting change happens when a small rotating field component is added, as can be seen in figure 4.15. The obtained slightly precessing magnetic field allows the walls of the labyrinth to interconnect. This changes the pattern towards a honeycomb form. Similar structures under comparable conditions have been previously observed in [110, 111].

### 4.4.2 Solidification of drops

An interesting question can be asked about the field induced phase separation - what does happen to the droplets at the end of the shrinking process? A definite answer during this study was not obtained, as in most cases the drops had some dirt in them, which made it impossible to differentiate the concentrated phase from the dirt itself. However, an interesting change was observed when shrinking was happening under field, when a particular shape is imposed on the drop. Surprisingly, if specific conditions, which are not yet clear, were achieved, this shape remained unchanged after the field was turned of, suggesting that they have become solid. Also this could be explained by the current approximate understanding of the process, which included the osmotic pressure difference induced solvent flow. It could be that the additional field, which is present, could create an attractive force between particles that exceeds the particle-particle repulsion and forms an agglomerate of the fixed shape.

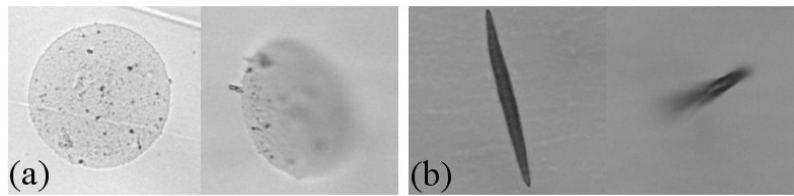


Figure 4.16: Solid-like objects formed from the concentrated phase in phase separated magnetic fluids, namely a pancake (a) and a rod (b).

Two examples are shown in figure 4.16, namely a solid pancake and rod. Several magnetic field configurations were further applied and the obtained objects followed them. These observations allows one to wonder about magnetically controlled micro-fabrication possibilities.

## 4.5 Remarks and outlook

In this chapter the development of a powerful experimental setup for phase separated magnetic fluid investigation was described. It was further tested with respect to known droplet shape dynamics in rotating magnetic fields [4], which were extended to precessing magnetic fields fixed at the magic angle. These dynamics appear alike, with slight differences at small fields.

On the way, this setup proved its capabilities on studying phase separated magnetic fluid properties, which is essential for improving their synthesis. In addition, other magnetic field configurations and related effects were noticed.

The contents of this chapter should be used as a starting point for multiple other studies that will deal with the rich diversity of phenomena observable in phase separated magnetic fluids.

# Conclusions

The extensive experimental studies in combination with appropriate theoretical predictions throughout the work have led to important conclusions that are grouped according to the four chapters.

A careful characterization of magnetic fluids has shown that the numerous techniques accessible for characterization provide comparable results. However, the comparison is not always obvious, as there are different relations between characteristic parameters and the measurable quantities. It is particularly important when comparing the size distribution of magnetic fluid particles, as different techniques provide different kinds of size averages.

The experimental study of magnetic micro-convection in a Hele-Shaw cell allowed to perform qualitative and quantitative measurements. The presence of a critical magnetic field needed for appearing of the instability was detected and the observed instability showed a qualitative agreement with theoretical predictions of the Darcy model, indicating that the micro-convective process depends on a dimensionless magnetic Rayleigh number  $Ra_m$  which scales with the square of applied magnetic field. In these experiments the flow fields during the instability development have been determined for the first time using a micro particle image velocimetry system. After improvements on the experimental setup, the characterization of important quantities is performed. A specially developed image processing algorithms allow to determine these quantities, including critical magnetic field, characteristic size and finger velocity dynamics, in a more precise manner. The measured parameters show a good and even quantitative agreement with the theoretical predictions of the more complete Brinkman model, which also indicates the dependence on the  $Ra_m$ . Conditions for the magnetic micro-convection realization correspond to a microfluidics subject and, as has been evaluated, have a potential in mixing, which is otherwise limited to diffusion as flows in microchannels are typically laminar. Additionally, realization of magnetic micro-convection experiments in continuous microfluidics should offer new possibilities in further quantitative measurements of the peculiarities of this process.

The rapid effective diffusion of magnetic fluid particles at the miscible fluid interface, which was first encountered in the studies on the magnetic micro-convection via the critical field estimation and later confirmed with additional measurements in zero-field conditions, has been shown to be connected to gravitational effects. Contrary to the initial hypothesis of high ionic strength induced diffusiophoresis, the main reason for this effect is the small density difference between magnetic fluid and miscible fluid. It can be described with an earlier introduced theoretical model, which depends on a dimensionless Rayleigh number  $Ra$ . Numerical simulations indicate that a convective motion appears immediately after the interface formation, forcing the denser fluid to flow under the lighter one. The concentration profile across the cell, averaged over the depth of the cell, smears in time and resembles a diffusive behavior with the difference in shape of the profile. Sharp jumps at the propagation limits of the concentration smearing instead of a smooth line described with an error

function can be seen and is consistent with the experimental measurements, which detect only the depth-averaged concentration. This concentration smearing can be described with a concentration gradient at the initial interface and allows to define an effective diffusion coefficient. Numerical simulations indicate that the effective diffusion coefficient increases linearly with the density difference above a small critical  $Ra$  and has a cubic dependence on the thickness of the system. Comparing the simulation results with the experimental measurements a reasonable agreement is visible, where the small disparities might be connected to the ionic strength effects. Nevertheless, it approves the large influence of the small density difference. In combination with the slowly diffusing magnetic particles, this effect causes important limitations for handling fluids in microfluidics, which, to author's knowledge, has not been discussed before. When gravity effects are minimized, as was obtained by turning a microscope and performing experiments in a microfluidics cell so that the gravitational force works in the direction perpendicular to the fluid interface and the heavier fluid is below the lighter one, the smearing dynamics is much slower and the measurements give a much smaller diffusion coefficient. If the fluids are placed the other way around, a Rayleigh-Taylor instability can be observed. The smaller diffusion coefficient value is in a reasonable agreement with the true diffusion coefficient for magnetic particles in magnetic fluid, which is measured with conventional diffusion measurement methods, including forced Rayleigh scattering and dynamic light scattering. Additionally, a novel simplified method for fluorescence recovery after photobleaching method is proposed for magnetic particle diffusion measurements.

The development of a coil system, its subsequent testing and use in measurements showed its capabilities and benefits in studies of phase-separated magnetic fluids. Measurements on individual magnetic drops, formed by the concentrated phase in a phase-separated magnetic fluid, offer an effective tool to study the properties of such systems. It was first shown here that, when phase separation is induced with a large magnetic field, the resulting out-of-equilibrium system relaxes in a peculiar way, which increases the magnetic permeability, viscosity and surface tension in time. However, magnetic drops are an interesting subject on their own. During this study, for the first time drop behavior under a precessing field fixed at the magic angle was inspected. The results indicated that its behavior, which depends on dimensionless magnetic Bond number, is very similar as in the case of a rotating field by undergoing two distinct shape instabilities. With an increase of Bond number, the shape of the drop that is initially close to a sphere first transforms to an elongated prolate, but later becomes an oblate ellipsoid with spiky peaks. Careful analysis at small Bond numbers indicate that there are small but notable differences between behavior at rotating and precessing fields and in both field configurations the drop becomes a 3D ellipsoid before undergoing the prolate instability. Additionally, it is evaluated that the shape of larger drops can be influenced by the gravitational effects, but in the conducted experiments these effects are around the order of measurement error and are expected to be negligible. Nevertheless, the phase separated magnetic fluids have a large number of effects yet to be studied, some of which have been indicated here, including labyrinth-like pattern formation in slightly precessing magnetic fields and the interesting relaxation of out-of-equilibrium system, which, when under field, can lead to solid-like magnetic objects.

Overall, it is possible to conclude that there is a large diversity of complex phenomena in magnetic fluids, many of which are connected to instabilities. They can be typically characterized with dimensionless quantities, which scale with the square of magnetic field. However, despite the small scale of these phenomena, gravitational effects can play an important, sometimes even dominant role and should be evaluated with a great care.

## Appendix A

# Source code of useful functions in MATLAB®

## A.1 Fitting functions

### A.1.1 Magnetization

```
0 function MM=magCurve(H,d0,Sd,T,ms,Phi)
  %Fit for H and M in CGS units, d in nm
  % H - Magnetic field (Oe)
  % d0 - log-normal distribution characteristic diameter in nm
  % ln(d0) is the mean of ln(d)
 5 % Sd - polydispersity factor
  % T - temperature in K
  % Ms - saturation magnetization of the bulk material
  % Phi - volume fraction
  mu=@(d,ms) ms*pi.*d.^3.*1e-21/6;
10 ksi=@(d,H,T,ms) mu(d,ms).*H./1.38e-16./T;
  L=@(d,H,T,ms) coth(ksi(d,H,T,ms))-1./ksi(d,H,T,ms);

  Q=@(d,d0,Sd) 1./(d*Sd*sqrt(2*pi)).*exp(-(log(d/d0)).^2/(2*Sd^2));

15 M=@(T,ms,d0,Sd,Phi,H) Phi*ms*integral(@(d) d.^3.*L(d,H,T,ms).*...
  Q(d,d0,Sd),0,Inf)/...
  integral(@(d) d.^3.*Q(d,d0,Sd),0,Inf);

  MM=zeros(length(H),1);
20 for i=1:length(H)
  MM(i)=M(T,ms,d0,Sd,Phi,H(i));
end
end
```

### A.1.2 Birefringence

```

0 function dn=birefCurve(H,d0,Sd,T,ms,dns)
  % in CGS units
  % H - magnetic field in Oe
  % d0 - characteristic diameter in nm
  % Sd - polydispersity
5  % T - temperature in K
  % ms - saturation magnetization of the material in G
  % dns - saturation dn of the birefringence
  % d in nm
mu=@(d,ms) ms*pi.*d.^3.*1e-21/6;
10 ksi=@(d,H,T,ms) mu(d,ms).*H/(1.38e-16*T);
n=@(d,H,T,ms) 1-3./ksi(d,H,T,ms).*coth(ksi(d,H,T,ms))+3./(ksi(d,H,T,ms)).^2;

Q=@(d,d0,Sd) 1./(d*Sd*sqrt(2*pi)).*exp(-(log(d/d0)).^2/(2*Sd^2));

15 M=@(T,ms,d0,Sd,H,ns) dns*integral(@(d) d.^3.*n(d,H,T,ms).*...
    Q(d,d0,Sd),0,Inf)./integral(@(d) d.^3.*Q(d,d0,Sd),0,Inf);

dn=zeros(length(H),1);
for i=1:length(H)
20   dn(i)=M(T,ms,d0,Sd,H(i),dns);
end
end

```

### A.1.3 Elongation of a magnetic droplet

```

0 function xx=elongation(x,a,b)
h2r=x;
mju=a;
sig=b;
xx=zeros(size(h2r));
5 for i=1:length(h2r)
f=@(x) eq_4_31(sqrt(1-1/x^2),mju,sig)-h2r(i);
xx(i)=fzero(f,[1.0000001 100]); %finding a solution
end
end
10 function f=eq_4_31(e,mju,sig)
f=sig*(4*pi/(mju-1)+4*pi*(1-e.^2)./(2*e.^3).*log((1+e)./(1-e))-2*e).^2/...
2/pi.*((3-2*e.^2)./e.^2-(3-4*e.^2).*asin(e)./(e.^3.*sqrt(1-e.^2)))./...
((1-e).^2/3).*(3-e.^2).*log((1+e)./(1-e))./e.^5-6./e.^4);
15 end

```

## Appendix B

# Essentials of the used experimental systems

## B.1 Essentials for using cameras in microscopy

### B.1.1 Testing the camera linearity

As mentioned in § 2.1.2, the linearity of the camera [54] is essential for quantitative measurements. The linear regime in which the recorded intensity is proportional to the number of photons can be found as follows.

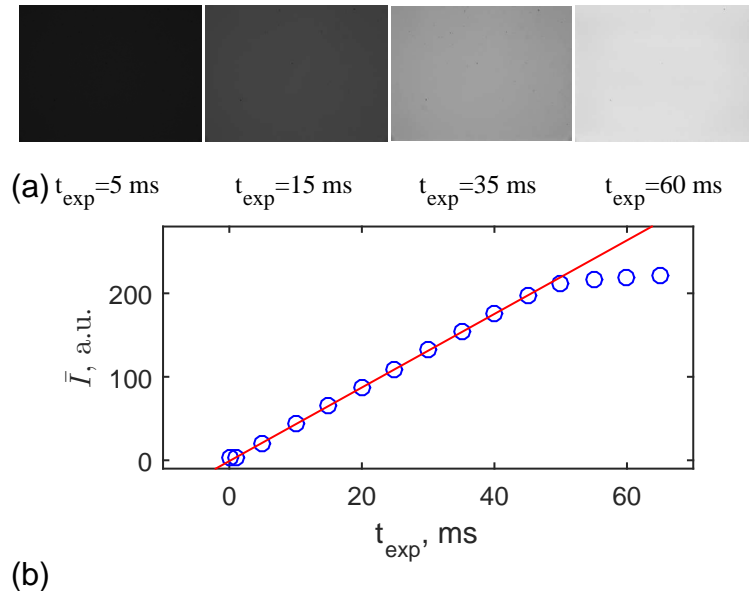


Figure B.1: An example of a linearity test for *Lumenera LU165C* camera. (a) Images of bright field at several exposure times. (b) The mean intensity dependence on the exposure time. Data are marked with blue circles, while the red line is a fit for the linear region.

A bright field of a constant illumination is imaged with the camera. Images  $I(i, j)$  are recorded at different exposure times  $t_{\text{exp}}$ . An example for *Lumenera LU165C* 8-bit camera can be seen in figure B.1 (a). Afterwards, the mean image intensity  $\bar{I}$  in each of these images is calculated and plotted against  $t_{\text{exp}}$ . Exposure time is proportional to the incoming intensity, as the illumination is kept constant. Regions in this graph where the mean image intensity increases linearly with the exposure time indicate the linear regions of the camera that are useful for quantitative analysis. The example of *Lumenera* camera,

visible in figure B.1 (b), shows that the linear region is wide and corresponds to a range of intensity values  $I \in (5 : 210)$  of the total 256 intensity levels.

### B.1.2 Spatial calibration for two cameras

Camera initial alignment is done using a stage micrometer. Simultaneously, the spatial resolution is then measured.

The previous step allows to reduce the spatial calibration to finding the translation between images that are simultaneously acquired. This can be achieved with cross-correlation them and finding the displacement of the peak, which corresponds. It is more precise for images with peculiar pattern, hence the same image pair of stage micrometers is preferred.

### B.1.3 Image acquisition using LabView

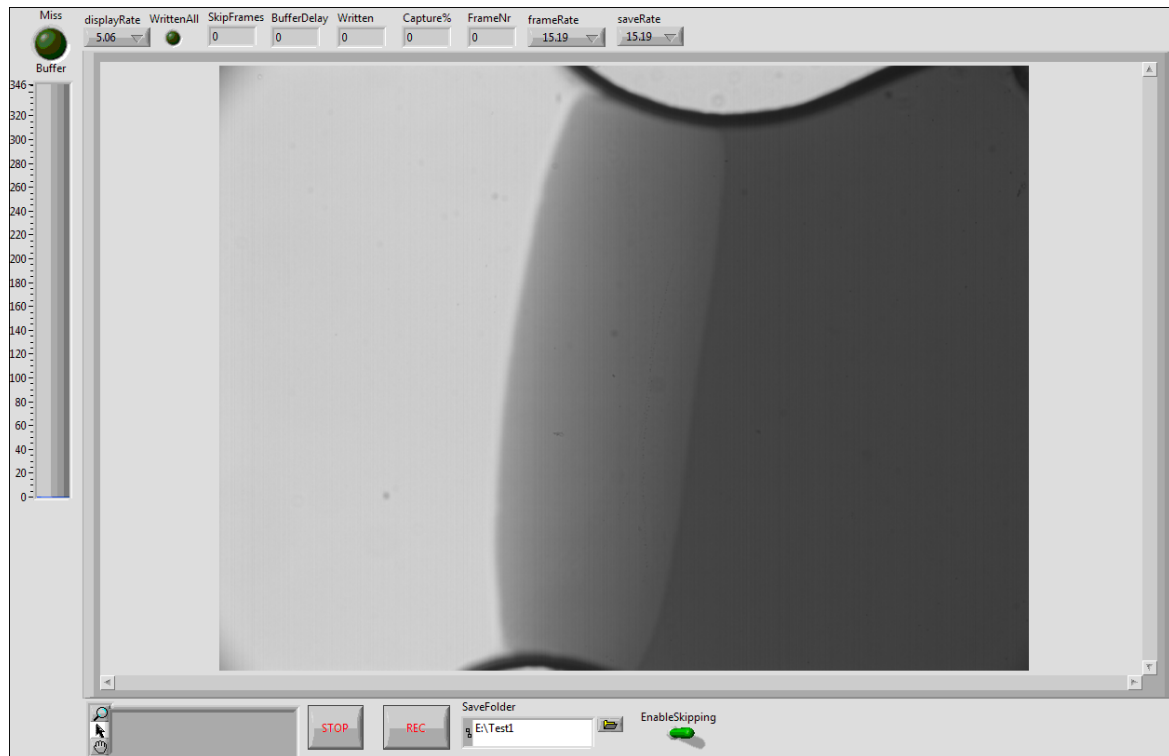


Figure B.2: Front panel of a program made in Labview for image acquisition with *Lumenera LU165C* camera.

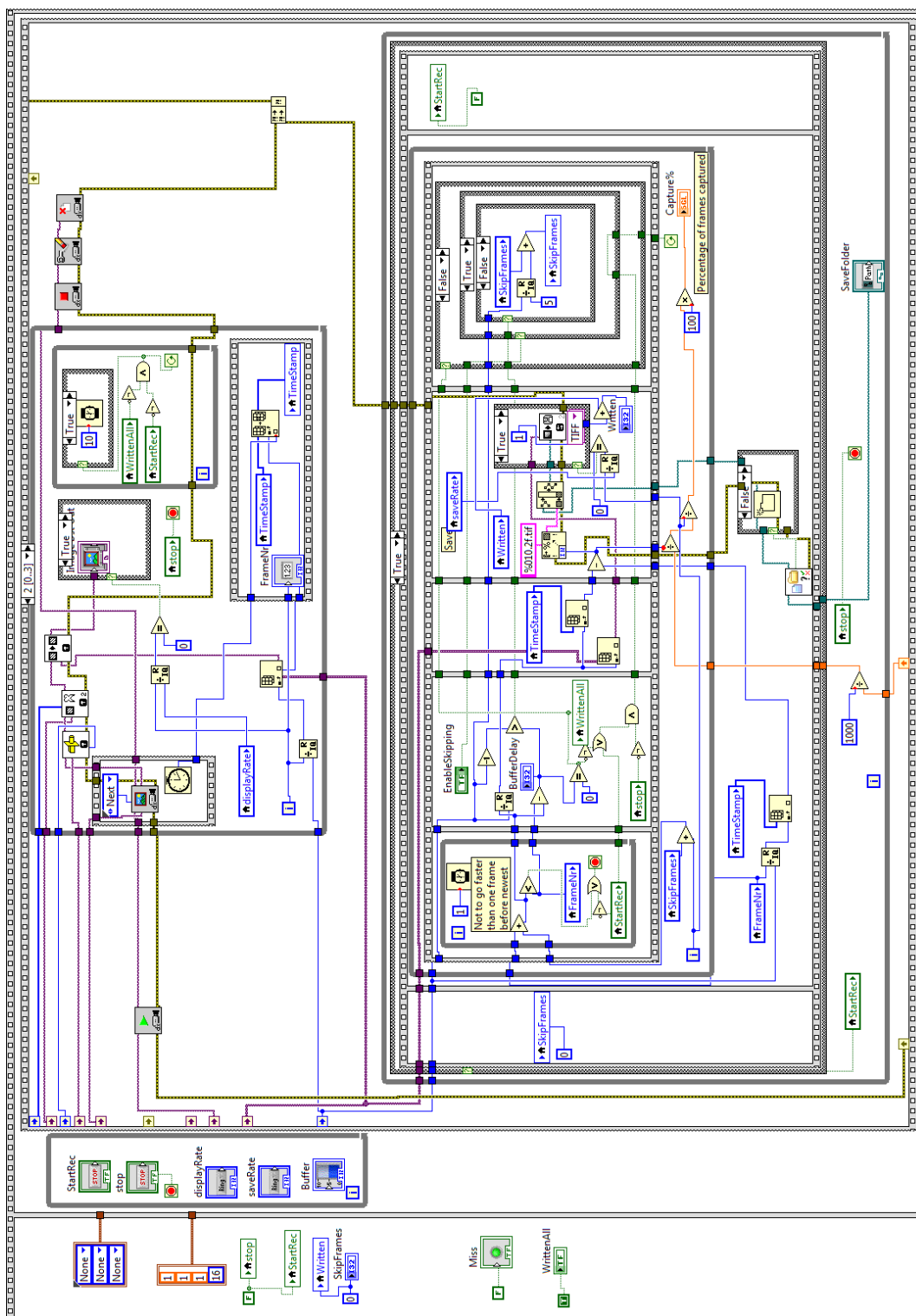


Figure B.3: Main view of the block diagram of a program made in Labview for image acquisition with *Lumenera LU165C* camera. Independent cycles for image acquisition and image saving are shown, including the frame verification algorithm to detect lost frames.

## B.2 LabView program for coil system control

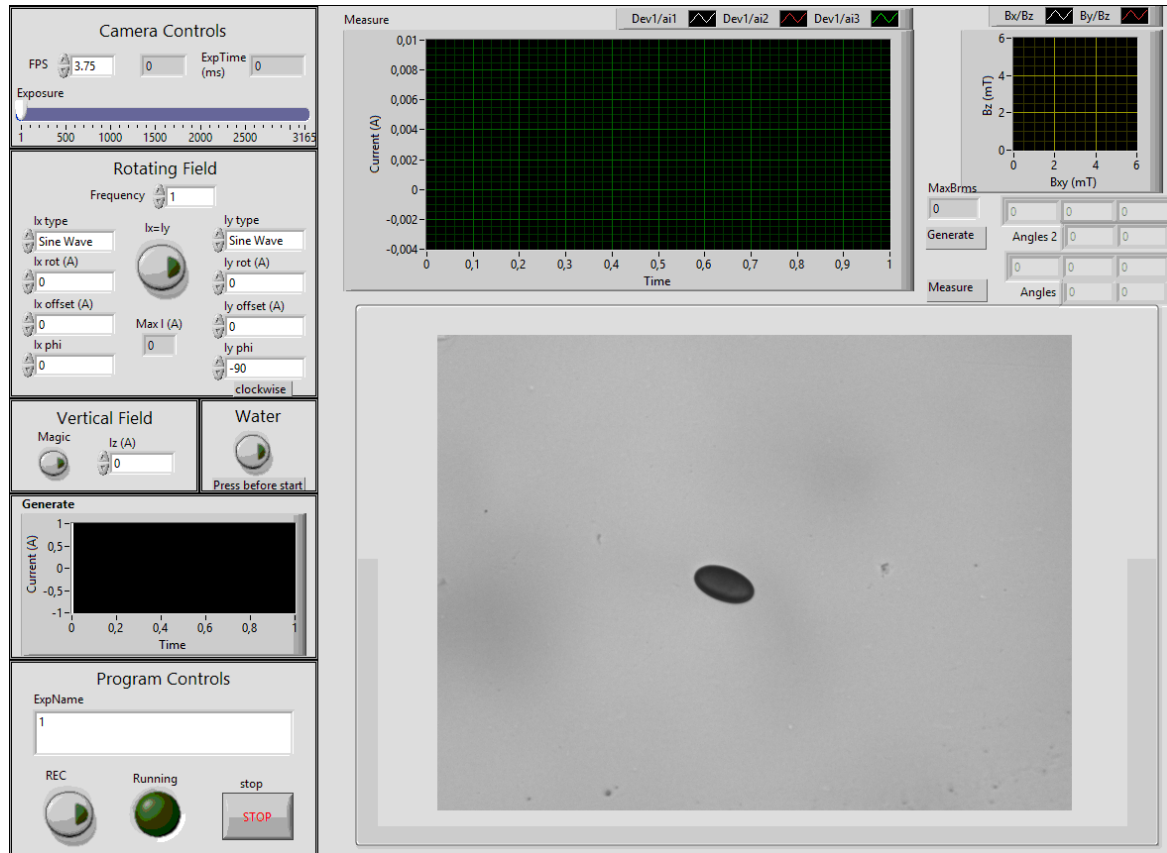


Figure B.4: Front panel of a program made in Labview for experiment control in coil system, described in § 4.2.1.

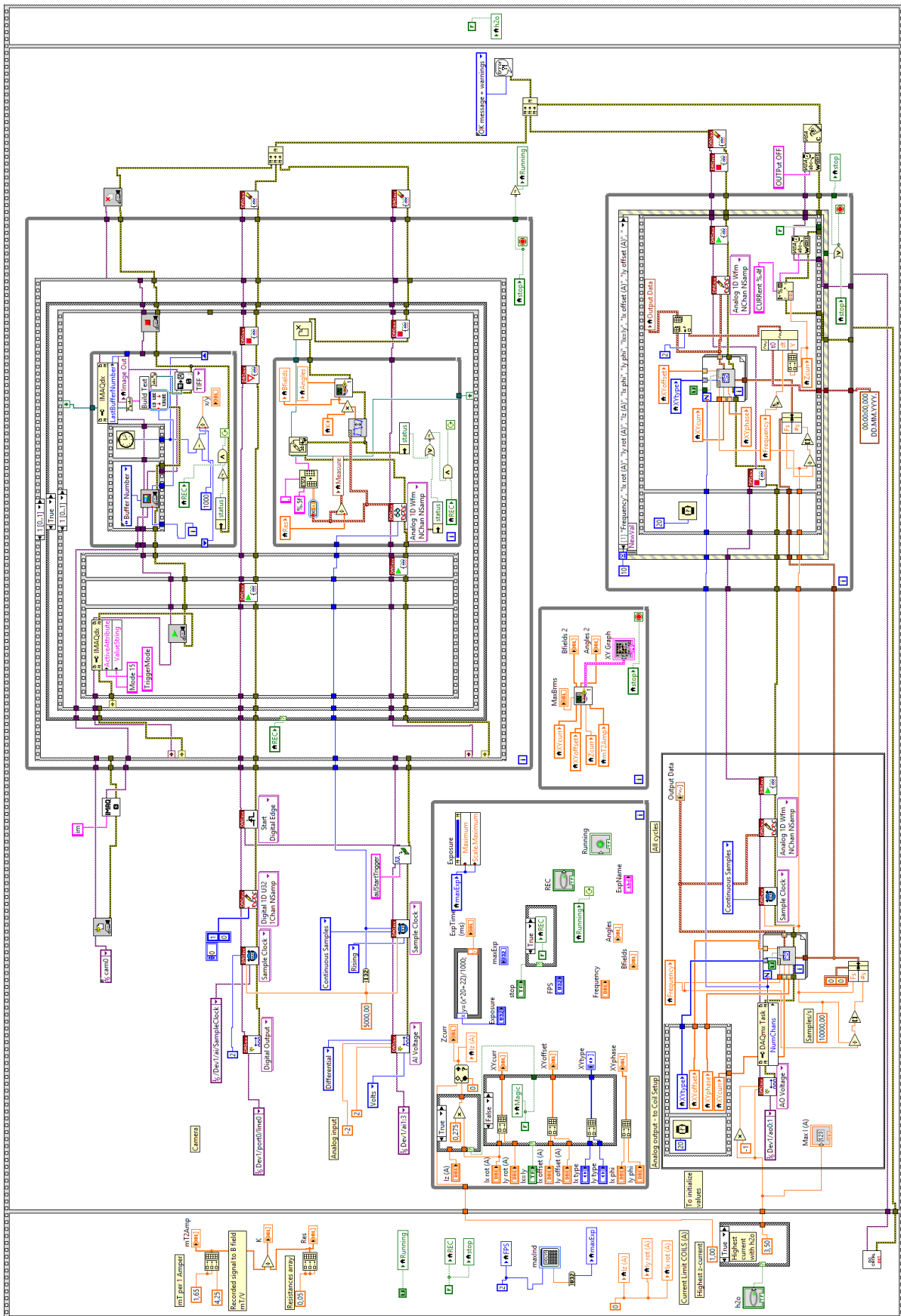


Figure B.5: Main view of the block diagram of a program made in Labview for experiment control in coil system. Independent cycles for process parameter control, signal generation and synchronized data acquisition are shown.



## *Appendix C*

# Description of the used software

## C.1 FEMM - Finite Element Method Magnetics

Finite Element Method Magnetics is a free software for performing numerical simulations in magnetic systems, developed by Ph.D. David Meeker. Here it is used to calculate magnetic fields obtainable with particular coils, during coil development. The software can be found in <http://www.femm.info/>.

## C.2 MATLAB®

This software is a numerical computing environment with its own programming language. Its syntax, being a fourth-generation programming language, is intuitive and easy to learn with basic knowledge in C or Pascal. It is particularly interesting for the many built-in functions useful for data and image processing, fitting and plotting. The extensive documentation with precise function description and multiple examples allows rapid learning while coding.

MATLAB® is developed by *MathWorks* and a license is necessary. More information can be found in <https://www.mathworks.com/products/matlab/>.

## C.3 COMSOL Multiphysics® Modeling Software

It is a finite element analysis, solver and simulation software for physics and engineering, which is particularly useful to couple multiple physical phenomena in a single model simultaneously. Most of the interactions can be done through a user-friendly interface, making it intuitive to use. A small drawback is the short documentation of its functionality, which requires more time for an unexperienced user.

COMSOL Multiphysics® is a license based software developed by *COMSOL* and more information can be found in <http://www.comsol.com/>.

## C.4 LabVIEW System Design Software

This system design platform is a very useful tool for developing computer controlled experimental system, that can link and synchronize data and image acquisition, processing, displaying and exporting, as well as instrument control. It uses a visual programming language, which is extremely intuitive to use. The main elements are small building blocks that are interconnected with wires. Each building block hides a function inside for which wires as inputs and outputs have to be connected with the specific data type only.

Software is developed by *National Instruments* and requires a license. More information can be found in <http://www.ni.com/labview/> It is widely used in the scientific and industrial communities, hence a large number of equipment allows a LabVIEW integration with suitable building blocks developed by the device manufacturer. However, separate software add-ons can be necessary. For example, DAQ complements the *National Instruments* data acquisition devices, while IMAQ is needed to use cameras.

## Appendix D

# Additional figures

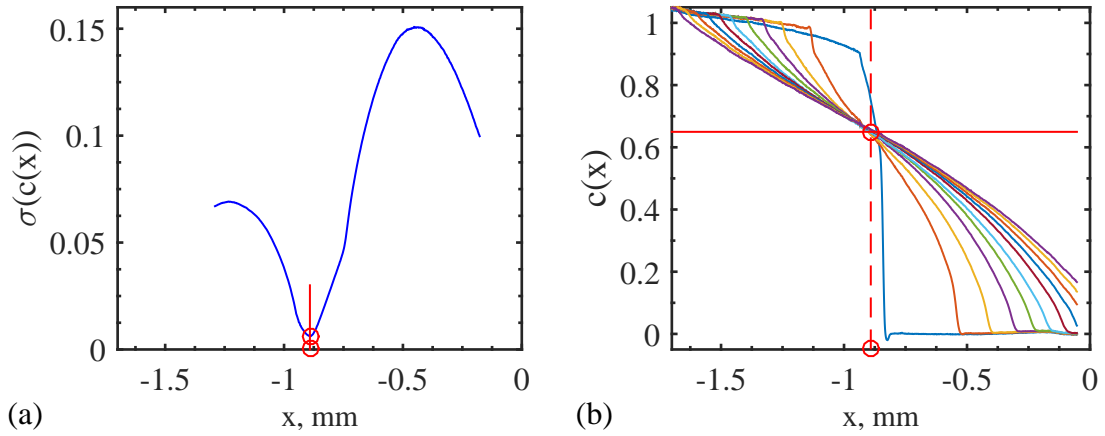
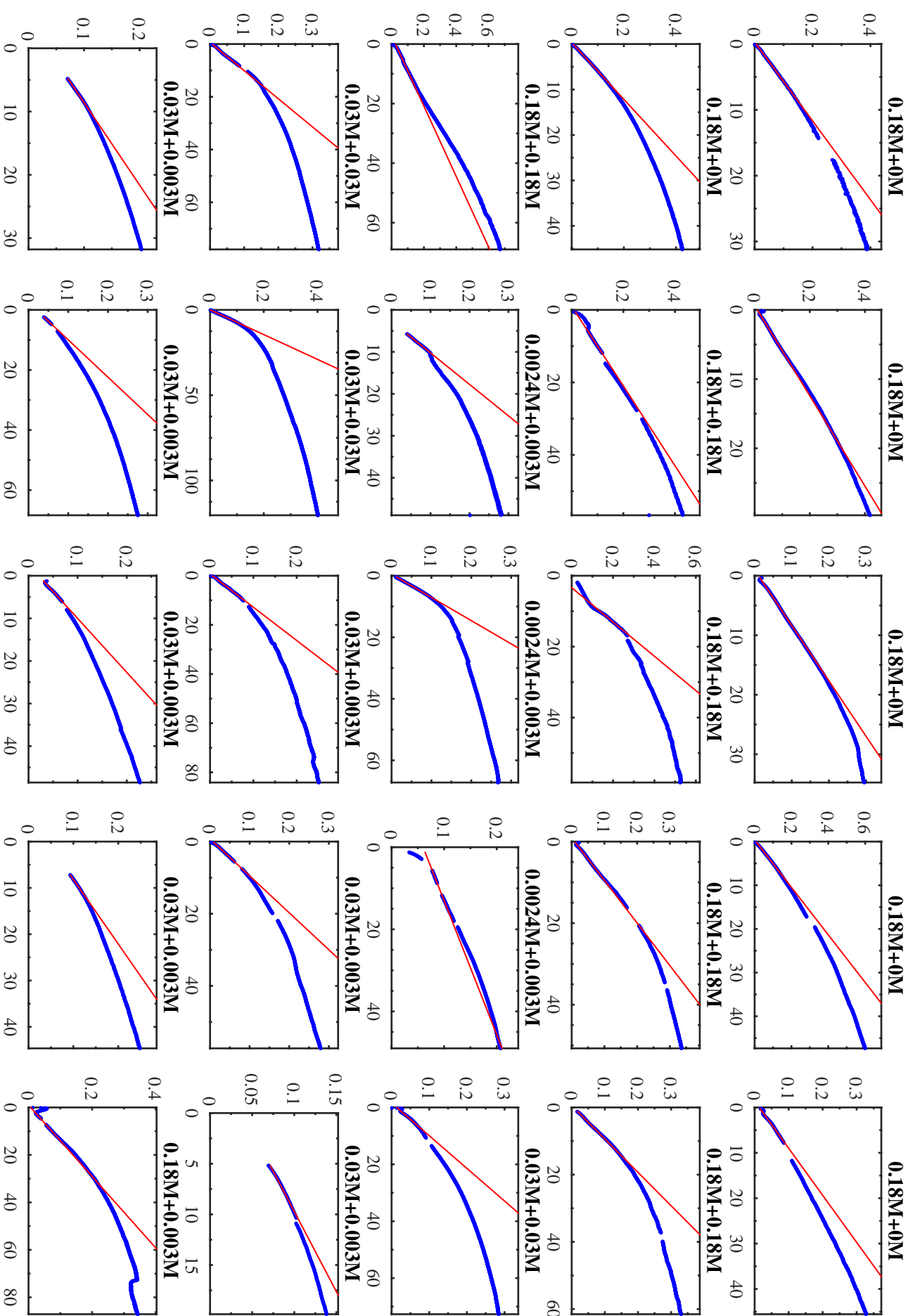


Figure D.1: The algorithm used to estimate the coordinate  $x_0$  of the interface is intended to remove the possible interface formation artifacts. It assumes that concentration profile during diffusion or other mixing has a point  $x_0$  where the concentration  $c_{\text{fix}}$  is not changing (as  $c_{\text{fix}} = 0.5$  at  $x = 0$  for the solution of a step-like diffusion in (3.5)). This point  $x_0$  is found by locating the minimum of the standard deviation  $\min(\sigma(c(x)))$ , showed in (a), which is calculated for each  $x$  across multiple  $t$  values. The corresponding concentration value is found  $c_{\text{fix}} = \bar{c}(x_0)$ , where  $\bar{c}$  is the average concentration values for each  $x$  position over all times  $t$ . A visual inspection of concentration profiles at several measurement times together with a comparison of  $c_{\text{fix}}$  in (b) show that the interface coordinate  $x_0$  is found correctly.



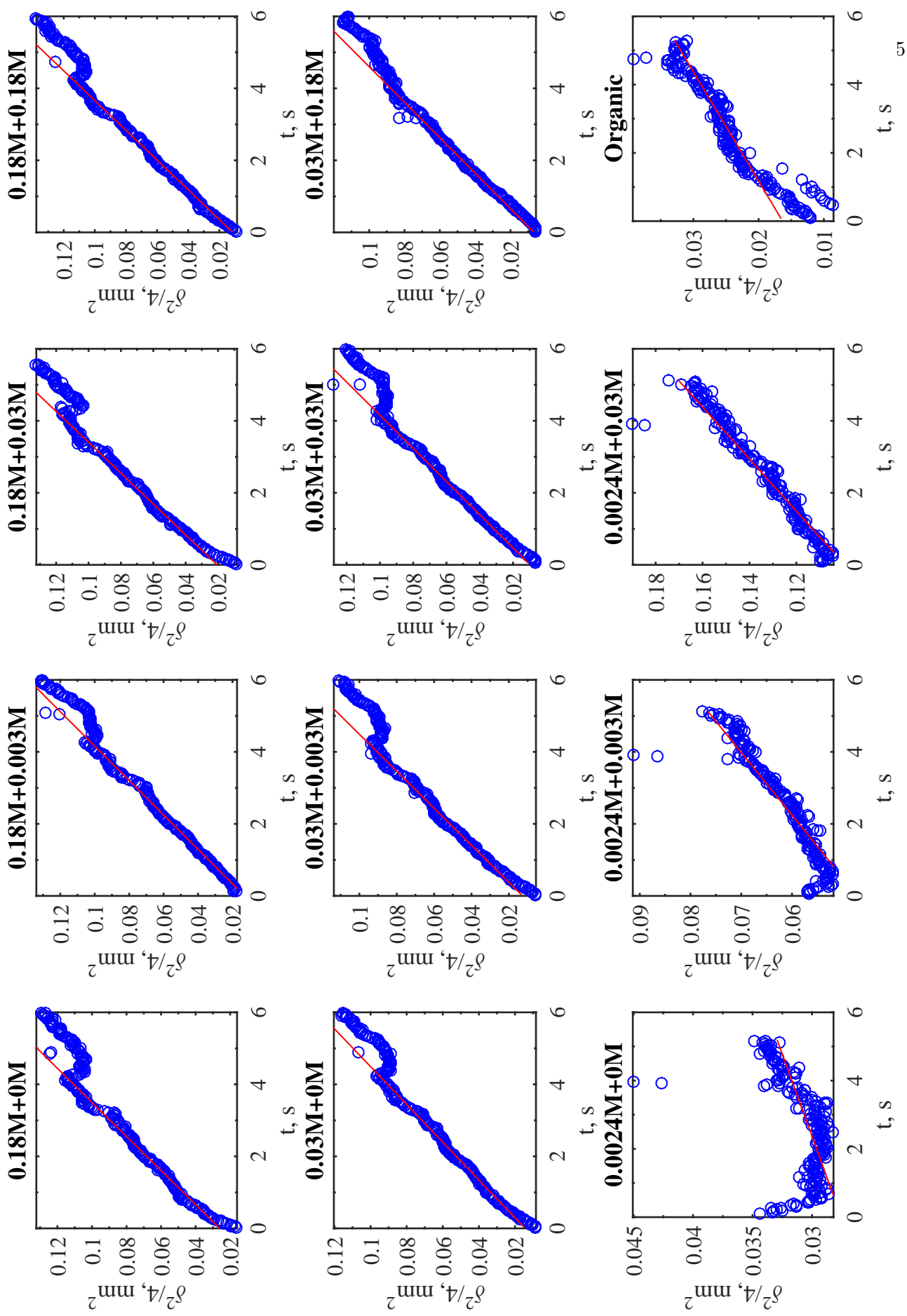


Figure D.3: Determination of the effective diffusion coefficients  $D_{\text{eff}}$  in microfluidics experiments. Blue circles show measurement data and red lines are fits of manually selected representative regions. Title of each plot shows the free citrate concentration in magnetic fluid and citrate solution in water.



## *Appendix E*

# Authors' publications

Results of this study are included as a part of three publications, which mainly concern the magnetic micro-convection, discussed in chapter 2. Many important conclusions made here arise from comparisons with numerical simulation results and theoretical predictions, for which suitable references are present in the text.

To ease the reading of this work, these publications are included hereafter, with permission of the copyright holders. Including the relevant number in bibliography and places of use in the text, they are listed here:

- [48] - K. Ērglis, A. Tatulcenkov, G. Kitenbergs, O. Petrichenko, F.G. Ergin, B.B. Watz and A. Cēbers, "Magnetic field driven micro-convection in the Hele-Shaw cell", *Journal of Fluid Mechanics*, **714**, 612-633, 2013  
In § 2.1, parts of it, including figures 2.3, 2.4, 2.5, 2.7 and 2.8, are reproduced with permission from Cambridge University Press.
- [49] - G. Kitenbergs, A. Tatulcenkovs, K. Ērglis, O. Petrichenko, R. Perzynski and A. Cēbers, "Magnetic field driven micro-convection in the Hele-Shaw cell: Brinkman model and its comparison with experiment", *Journal of Fluid Mechanics*, **774**, 170-191, 2015  
In § 2.2, parts of it, including figures 2.15, 2.16, 2.17, 2.18, 2.19, 2.20, 2.21, 2.22 and 2.23, are reproduced with permission from Cambridge University Press.
- [50] - G. Kitenbergs, K. Ērglis, R. Perzynski, A. Cēbers, "Magnetic particle mixing with magnetic micro-convection for microfluidics", *Journal of Magnetism and Magnetic Materials*, **380**, 227-230, 2015  
Mostly in § 2.3.1, parts of it, including figures 2.12, 2.25, 2.26, 2.27, 2.28 and 2.29, are reprinted with permission from Elsevier.

# Magnetic field driven micro-convection in the Hele-Shaw cell

K. Ērglis<sup>1</sup>, A. Tatulcenkov<sup>1</sup>, G. Kitenbergs<sup>1</sup>, O. Petrichenko<sup>1</sup>, F. G. Ergin<sup>2</sup>,  
B. B. Watz<sup>2</sup> and A. Cēbers<sup>1,†</sup>

<sup>1</sup>Department of Theoretical Physics, University of Latvia, Riga, Zellu 8, LV-1002, Latvia

<sup>2</sup>Dantec Dynamics A/S, Tonsbakken 16-18, Skovlunde, 2740, Denmark

(Received 2 March 2012; revised 27 September 2012; accepted 11 October 2012)

Micro-convection caused by ponderomotive forces of the self-magnetic field of a magnetic fluid in the Hele-Shaw cell under the action of a vertical homogeneous magnetic field is studied both experimentally and numerically. It is shown that a non-potential magnetic force at magnetic Rayleigh numbers greater than the critical value causes fingering at the interface between the miscible magnetic and non-magnetic fluids. The threshold value of the magnetic Rayleigh number depends on the smearing of the interface between fluids. Fingering with its subsequent decay due to diffusion of particles significantly increases the mixing at the interface. Velocity and vorticity fields at fingering are determined by particle image velocimetry measurements and qualitatively correspond well to the results of numerical simulations of the micro-convection in the Hele-Shaw cell carried out in the Darcy approximation, which account for ponderomotive forces of the self-magnetic field of the magnetic fluid. Gravity plays an important role at the initial stage of the fingering observed in the experiments.

**Key words:** Hele-Shaw flows, MHD and electrohydrodynamics, magnetic fluids

---

## 1. Introduction

Magnetic-field-driven micro-convection was found in the early 1980s (Maiorov & Cebers 1983) extending the previous work on magnetostatic instabilities of magnetic liquids in the Hele-Shaw cell (Cebers & Maiorov 1980) for miscible fluids. Since the ponderomotive force on the magnetizable fluid is proportional to the concentration of magnetic particles and the local gradient of the magnetic field strength, it is potential only when the concentration and magnetic field strength gradients are collinear. The field strength gradient in a homogeneous applied field results from the self-magnetic field of the liquid. Any concentration perturbations that destroy this collinearity cause the liquid to start to flow. An important issue that is absent in gravitational convection is the dependence of the field gradient on the concentration field. It should be mentioned that the equivalent of the thermal expansion coefficient, which in liquids has an order of magnitude of  $10^{-3}$ , is much larger in this case because of the strong dependence of the magnetization of a liquid on the particle concentration.

In view of these considerations, the theoretical model of the magnetic micro-convection considers the Hele-Shaw flow under the action of the ponderomotive forces

† Email address for correspondence: [aceb@tesla.sal.lv](mailto:aceb@tesla.sal.lv)

due to the self-magnetic field of the fluid, the equations for the magnetostatic field, and the diffusion equation for the concentration of the magnetic nanoparticles (Cebers 1997). The theoretical analysis shows that there is a threshold value of the critical magnetic field strength determined by the magnetic Rayleigh number.

Later, magnetic-field-driven micro-convection has attracted the interest of researchers both from an experimental and a theoretical point of view. Magnetic-field-driven fingering was observed in micro-channels using the methods of microfluidics (Derec *et al.* 2008) and on the interface of a circular region concentrated by magnetic particles (Wen, Chen & Kuan 2007). The concept of the magnetic-field-driven micro-convection was experimentally studied for the case of the time evolution of gratings of magnetic particles induced by thermophoresis at non-homogeneous illumination of the magnetic colloids (Mezulis & Blums 2005). The theoretical analysis of the last problem was given by Igonin & Cebers (2003).

The theoretical analysis of the growth increments of the fingering instability in the case of plane interface between miscible magnetic and non-magnetic fluids was given by Igonin & Cebers (2003). Numerical analysis of the magnetic-field-driven micro-convection in the frame of the described model was carried out by Chen & Wen (2002). In the work of Chen (2003) the effect of the Korteweg stress was taken into account in the numerical simulation of magnetic micro-convection.

In spite of various efforts, the quantitative information on the main characteristics of the micro-convection that develops is rather poor. Even the occurrence of fluid flow during the formation of the fingers at the interface between two miscible fluids has not yet been confirmed. Here we obtain quantitative information on the micro-flow driven by the self-magnetic field of the magnetic colloid by applying particle image velocimetry (PIV) methods with specially designed algorithms for processing images with poor contrast (Ergin *et al.* 2010). The main obstacles for quantitative comparison with the theoretical analysis and numerical simulations given in the first part of the work are discussed, and it is shown that in spite of small density differences between the magnetic fluid and its solvent gravity plays an important role in the smearing of the concentration distribution, which essentially determines the critical field strength for the development of the magnetic micro-convection. Nevertheless, we illustrate that, in general, the numerical simulation and experimental data are in good qualitative agreement.

## 2. Mathematical formulation

### 2.1. Model

We consider two miscible fluids where the first is a magnetic fluid and the second is a simple non-magnetic fluid. Fluids are confined in a horizontal Hele-Shaw cell and a magnetic field is applied perpendicular to the cell, the sketch of the cell is shown in figure 1. The viscosities of the fluids are equal. The ponderomotive forces of the non-homogeneous self-magnetic field on the interface between fluids cause fingering instability. Its growth is described by the set of equations, which includes the Darcy equation, the convection–diffusion equation and equations for the magnetostatic field (Cebers 1997; Igonin & Cebers 2003) and reads

$$-\nabla p - \frac{12\eta}{h^2} \mathbf{u} - \frac{2M(c)}{h} \nabla \psi_m(c) = 0, \quad \nabla \cdot \mathbf{u} = 0, \quad (2.1)$$

$$\frac{\partial c}{\partial t} + (\mathbf{u} \cdot \nabla)c = D\nabla^2 c, \quad (2.2)$$

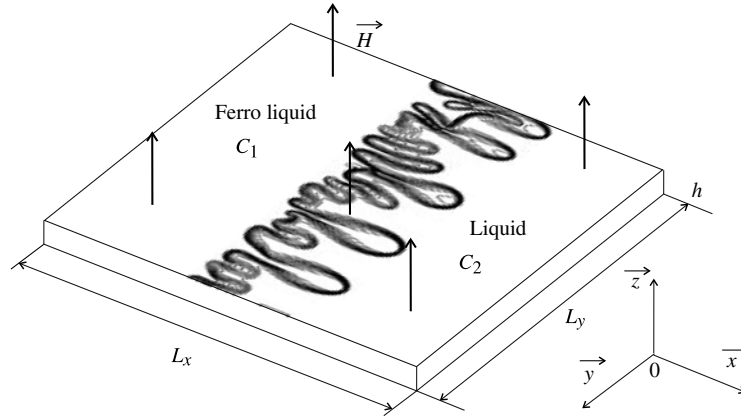


FIGURE 1. The Hele-Shaw cell sketch.

where  $p$  is pressure,  $\mathbf{u} = (u_x(x, y), u_y(x, y))$  is the depth averaged velocity,  $\eta$  is the viscosity of the fluid,  $h$  is the thickness of the Hele-Shaw cell,  $D$  is isotropic constant diffusion coefficient and  $c$  is the concentration of magnetic fluid normalized by its value far from the interface. The magnetization  $M(c)$  is taken to be proportional to the concentration of the magnetic fluid  $c$  ( $M = M_0 c$ ) and the value of the magnetostatic potential  $\psi_m$  on the boundary of the Hele-Shaw cell is given by Cebers (1981) and Jackson, Goldstein & Cebers (1994)

$$\psi_m(\mathbf{r}, t) = M_0 \int c(\mathbf{r}', t) K(\mathbf{r} - \mathbf{r}', h) dS', \quad (2.3)$$

where the integration is performed over the boundary of the Hele-Shaw cell,  $K(\mathbf{r}, h) = 1/|\mathbf{r}| - 1/\sqrt{|\mathbf{r}|^2 + h^2}$ .

Equations (2.1) and (2.2) extend in the Darcy approximation the model which is usually applied for the study of the displacements of miscible, non-magnetic fluids in the Hele-Shaw cell (Goyal & Meiburg 2006).

The boundary conditions for the velocity components and the concentration of the fluid are as follows:

$$u_x(0, y) = u_y(0, y) = 0, \quad c(0, y) = 1, \quad (2.4a)$$

$$u_x(L_x, y) = u_y(L_x, y) = 0, \quad c(L_x, y) = 0, \quad (2.4b)$$

and the conditions of the periodicity across the Hele-Shaw cell are

$$\mathbf{u}(x, 0, t) = \mathbf{u}(x, L_y, t), \quad c(x, 0, t) = c(x, L_y, t). \quad (2.5)$$

The boundary conditions (2.4) require that the fluid is motionless at both ends of the cell. The motion of the liquid arises from a non-potential magnetic force  $-2M(c)\nabla\psi_m/h$ .

The equations are put in dimensionless form by introducing the following scales: length  $h$ , time  $h^2/D$ , velocity  $D/h$  and magnetostatic potential  $M_0 h$ . As a result the set of dimensionless equations reads

$$-\nabla p - \mathbf{u} - 2Ra_m c \nabla \psi_m = 0, \quad \nabla \cdot \mathbf{u} = 0, \quad (2.6)$$

$$\frac{\partial c}{\partial t} + (\mathbf{u} \cdot \nabla) c = \nabla^2 c. \quad (2.7)$$

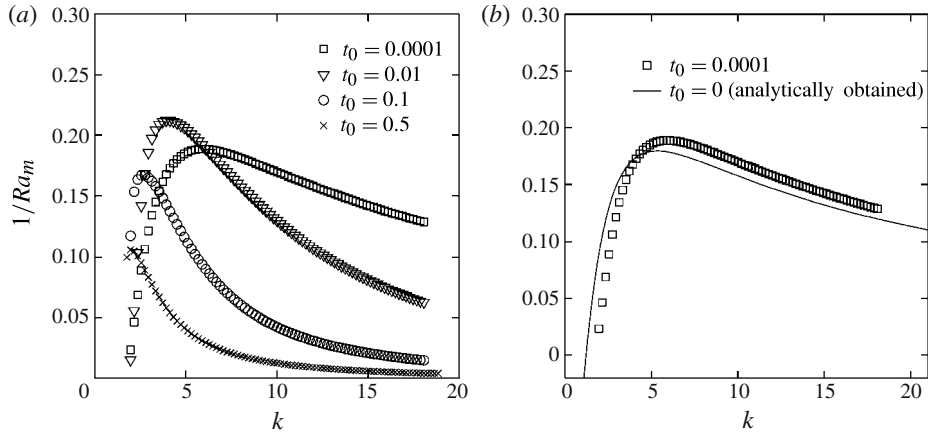


FIGURE 2. (a) The neutral curves of the magnetic micro-convection for different values of the smearing parameter ( $t_0 = 0.5$ ,  $t_0 = 0.1$ ,  $t_0 = 0.01$ ,  $t_0 = 0.0001$ ). (b) The theoretical neutral curve (solid line) and the neutral curve calculated numerically (dashed line).

Here  $Ra_m = M_0^2 h^2 / 12 \eta D$  is the magnetic Rayleigh number determined by the ratio of the characteristic time of the diffusion  $\tau_D = h^2 / D$  and the characteristic time of motion due to non-homogeneous self-magnetic field of the fluid  $\tau_M = 12 \eta / M_0^2$ .

### 2.1.1. The linear stability analysis

In order to test the numerical algorithm, we compare the theoretical results of a linear stability analysis with the numerical results. The solution of the quasi-steady linear stability problem for miscible magnetic fluid in the Hele-Shaw cell is found in Igonin & Cebers (2003). An analytical solution may be found for the value of the smearing parameter  $t_0 = 0$ . The linear perturbation of a quiescent base state is represented by  $\{v_x, v_y, c, \psi_m\}(x, y, t) = \{0, 0, c_0, \psi_{m0}\}(x) + \{v'_x, v'_y, c', \psi'_m\}(x) e^{iky + \lambda t}$  ( $c_0 = 0.5(1 - \text{erf}(x/2\sqrt{t_0}))$ ), where the parameter  $t_0$  characterizes the thickness of the interfacial region. We focus on the linear analysis of the stability of the interface in the formal limit  $t_0 = 0$  when the concentration distribution is step-like. The dispersion relation reads

$$ks + Ra_m[2J(s, k) - kf(k(s+1))] = 0, \quad (2.8)$$

where the parameter  $s$  is  $s = \sqrt{1 + \lambda/k^2}$  and the functions  $J(p, q)$  and  $f(p)$  are defined by the integrals

$$J(p, q) = \int_0^\infty e^{-pz} (K_0(z) - K_0(\sqrt{z^2 + q^2})) dz, \quad (2.9)$$

$$f(p) = \int_0^\infty e^{-pz} \ln(1 + z^{-2}) dz. \quad (2.10)$$

Here  $K_0$  is the modified Bessel function of the second kind (McDonald function).

Neutral curves shown in figure 2(a) are calculated numerically as follows. The Fourier coefficients  $\hat{c}_n$  for the concentration field averaged along the  $x$ -axis  $\langle c' \rangle(y) = \int_{L_x} c'(x, y) dx / L_x = \sum_{n=0}^{N_y} \langle \hat{c}_n(t) \rangle e^{ik_n y}$  are fitted by  $\langle \hat{c}_n \rangle = \langle \hat{c}_n^0 \rangle e^{\lambda_n t}$ , and the growth increments  $\lambda_n$  are found in dependence on the wavenumber  $k_n$ . The neutral

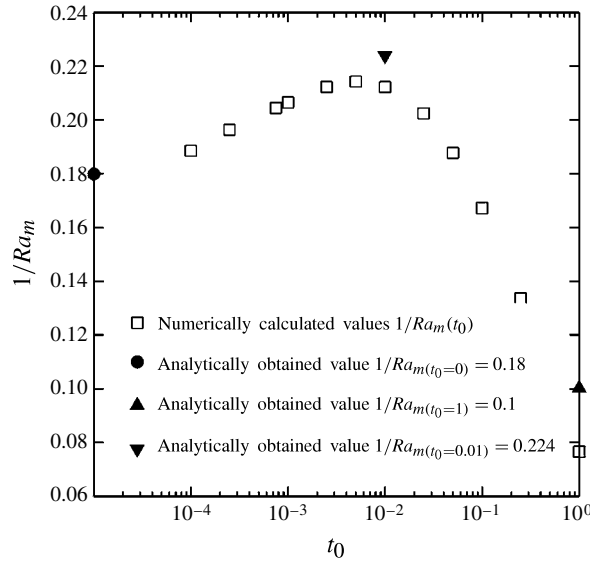


FIGURE 3. The inverse values of the critical magnetic Rayleigh number in dependence on the smearing parameter  $t_0$ . Both triangles shown are analytical results from Igonin (2004), and the black circle shows analytical results for the sharp front.

curves for definite values of the smearing parameter  $t_0$  are found by solving the equation  $\lambda_n(Ra_m^c, k_n) = 0$  by a spline interpolation.

To reproduce in the simulations growth increments theoretically calculated for a sharp diffusion front it is necessary to take the concentration perturbation corresponding to the theoretically found eigenfunction. The critical values of the magnetic Rayleigh number in dependence on the wavenumber for  $t_0 = 0.0001$  with perturbation corresponding to the eigenfunction for a sharp front are shown in figure 2(b) by the dashed line. They agree reasonably well with the theoretical values obtained from (2.8) for  $t_0 = 0$  and shown in figure 2(b) by the solid line. Their small difference is due to difference of eigenfunctions for sharp and smeared fronts.

The inverse values of the critical magnetic Rayleigh number obtained numerically are shown in figure 3 in semi-logarithmic coordinates as a function of  $t_0$ . They show agreement with the available theoretical results (Igonin 2004) for sharp and smeared fronts. These tests validate the numerical algorithm.

The numerical algorithm described in appendix A is applied further to study fingering at magnetic micro-convection in the nonlinear regime.

## 2.2. Numerical results

The initial concentration perturbation at the interface is introduced by applying relation (A 6) with  $\zeta(y)$  taken to be random. In long-time numerical calculations typically  $512 \times 512$  collocation points are used for the space discretization. The time step  $\Delta t$  typically is  $\Delta t = 10^{-5}$ .

Typical fingering patterns for three values of  $Ra_m$  and the smearing parameter  $t_0 = 0.05$  are shown in figure 4. The pattern formation has several stages as may be seen in figure 4. At first ( $t = 0.0014$  and  $t = 0.002$ ) well-resolved fingers are formed that later coarsen with time ( $t = 0.0035$  and  $t = 0.009$ ). Finally, the finger pattern smears out because of diffusion of the magnetic particles ( $t = 0.013$ ).

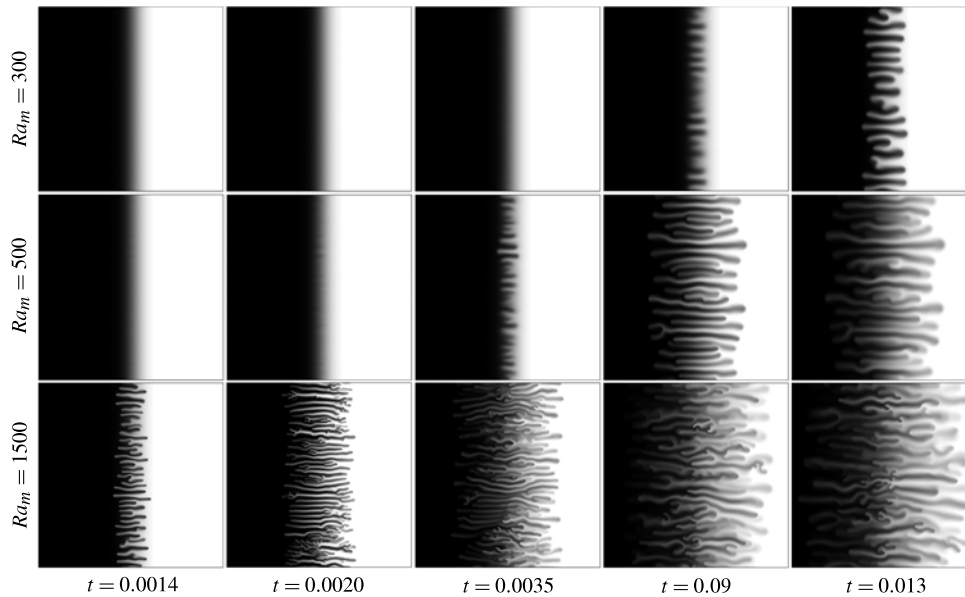


FIGURE 4. Concentration images for magnetic Rayleigh number  $Ra_m = 300$ ,  $Ra_m = 500$ ,  $Ra_m = 1500$ , at time  $t = 0.0014$ ,  $t = 0.002$ ,  $t = 0.0035$ ,  $t = 0.009$ ,  $t = 0.013$ , with  $L_x = 6$ ,  $L_y = 6$  and  $t_0 = 0.05$ .

Snapshots of the concentration, vorticity, stream function and velocity fields for  $t_0 = 0.05$  and  $Ra_m = 500$  at time moment  $t = 0.013$  are shown in figure 5. The velocity field is visualized by using the line integral convolution technique. Line integral convolution (LIC) is a powerful technique for generating striking images from vector data and for visualizing vector fields. Introduced by Cabral & Leedom (1993), the method has rapidly found many application areas, ranging from computer art to scientific visualization. Given a vector field and an input texture, line integral convolution produces an output texture in which the data values are highly correlated in the direction of the flow. LIC produces an intensity output image, which is reproduced as a greyscale picture. This image includes tangential information of vector field as well as information on its magnitude. The formation of alternating array of vortices may be seen at figure 5(b,c).

To make a qualitative comparison with the experimental data, described in the next part, the time dependence of the maximal vorticity for several values of the magnetic Rayleigh number is calculated and shown in figure 6. The characteristic maximum corresponds to the transition from the development of the magnetic micro-convection to its decay due to particle diffusion. The spiky character of the curve at larger values of the magnetic Rayleigh number is due to the emerging vortices, which intensify the mixing.

### 3. Experimental demonstration

Magnetic micro-convection is studied on the interface between two miscible fluids. The first fluid is distilled water which contains 0.1% fluorescent tracer micro-particles with diameter  $1\ \mu\text{m}$  for PIV measurements. The second is a water-based magnetic fluid with  $\gamma\text{-Fe}_2\text{O}_3$  particles of average radius 14 nm, saturation

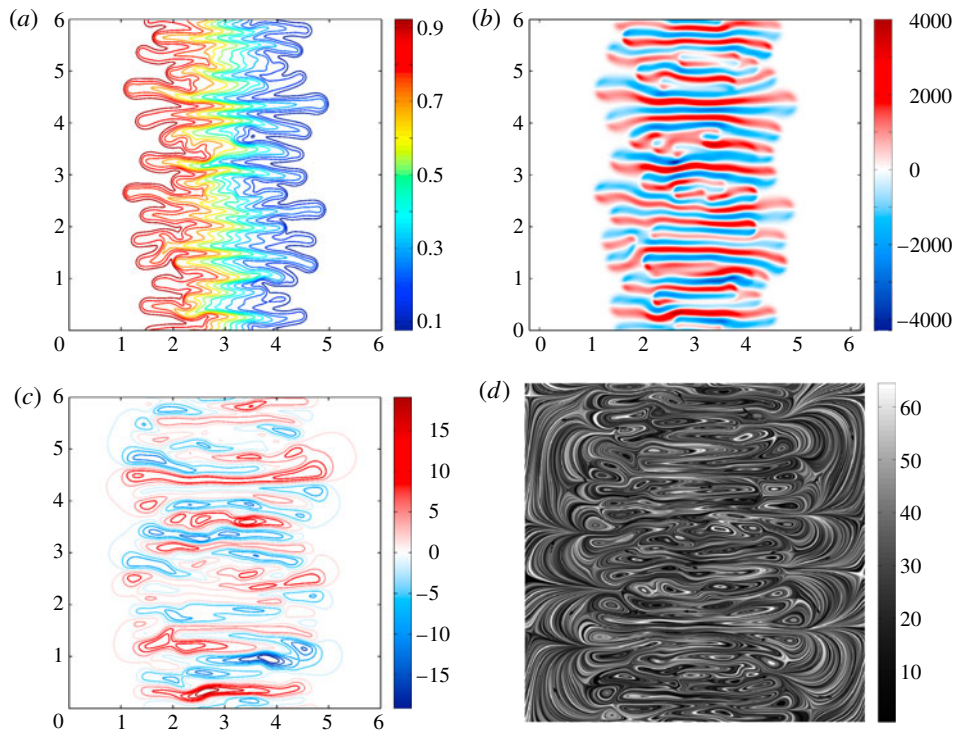


FIGURE 5. Snapshots of concentration (a), vorticity (b), stream function (c) and velocity field (d) for miscible magnetic and non-magnetic fluids in the Hele-Shaw cell. Snapshots correspond to the magnetic Rayleigh number  $Ra_m = 500$  at time  $t = 0.013$ , with  $L_x = 6$ ,  $L_y = 6$  and  $t_0 = 0.05$ .

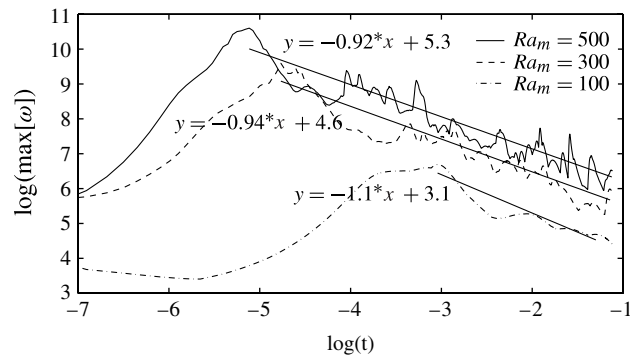


FIGURE 6. The relaxation of the maximal value of vorticity field  $\omega_{max}$  for different values of magnetic numbers  $Ra_m$  on a logarithmic scale.

magnetization 10 G and initial susceptibility 0.064, as determined by the vibrating sample magnetometer measurements. The density of the liquid is  $\rho = 1.077 \text{ g cm}^{-3}$ . The diffusion coefficient of the particles is determined by diffusion light scattering and equals  $D = 5.5 \times 10^{-8} \text{ cm}^2 \text{ s}^{-1}$ . Magnetic nanoparticles of  $\gamma\text{-Fe}_2\text{O}_3$  are synthesized

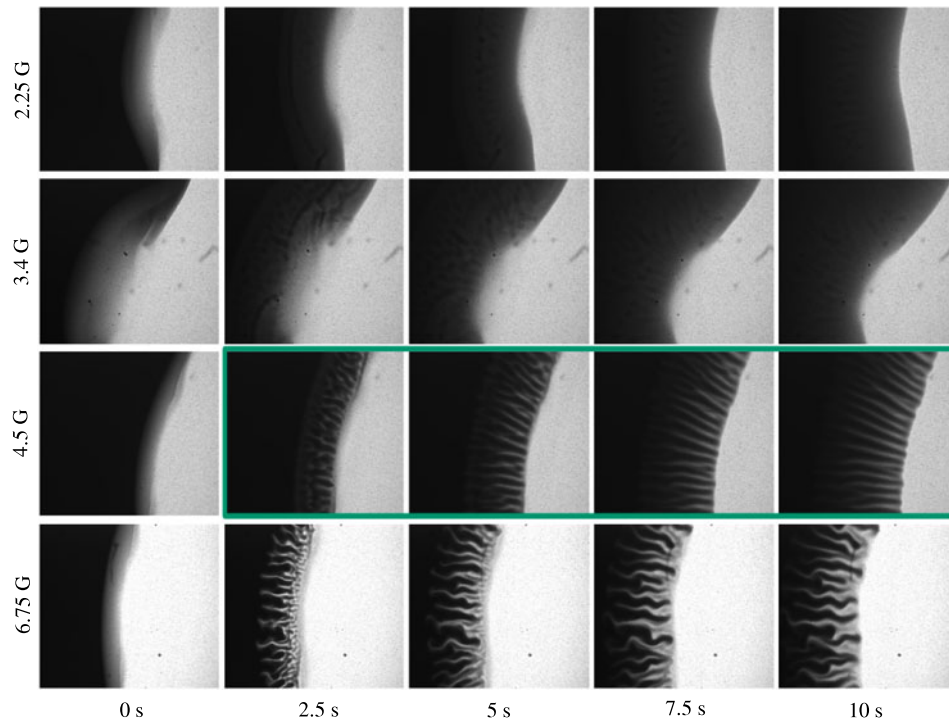


FIGURE 7. Determination of the threshold value of the magnetic field for finger-like pattern development.

by a precipitation reaction (Massart). The Hele-Shaw cell is prepared from two microscope cover glasses separated by a  $127\ \mu\text{m}$  thick Parafilm. The Parafilm is cut to form channels for air and fluids. The horizontal dimensions of the fluid channel are  $18\ \text{mm} \times 6\ \text{mm}$ . After assembly the cell is heated to weld the cover glasses. A few drops of magnetic fluid are placed on one side of the cell and one half of the cell is filled with magnetic fluid because of capillary forces. Then the magnetic field is switched on, and a small amount of the non-magnetic fluid is added to the other side of the cell using a small tube and a syringe with a microscrew until the solvent comes into contact with the magnetic fluid.

The homogeneous magnetic field with strength  $H \in (0-300)\ \text{Oe}$  is created in the central part of the coil where the Hele-Shaw cell is placed. The coil with diameter  $34\ \text{mm}$  and height  $16\ \text{mm}$  consists of 38 turns of  $0.7\ \text{mm}$  wire.

The theoretical analysis (Cebers 1997; Igonin & Cebers 2003) and numerical calculations described in Part 2 show that the smearing of the diffusion front between the two miscible fluids plays an important role in the development of the magnetic micro-convection.

The experimental data shown in figure 7 clearly confirm the existence of the critical value of the field strength below which the fingering due to the magnetic micro-convection is not observed. If we estimate the critical field strength according to the data shown in figure 7 to be  $3.4\ \text{G}$ , the magnetic Rayleigh number for the fluid with the given physical properties is  $Ra_m = 1150$ , a value much larger than the critical value corresponding to  $t_0 = 0$  and shown in figure 3. Figure 3 shows that such large values of the critical magnetic Rayleigh number correspond to large values of the smearing

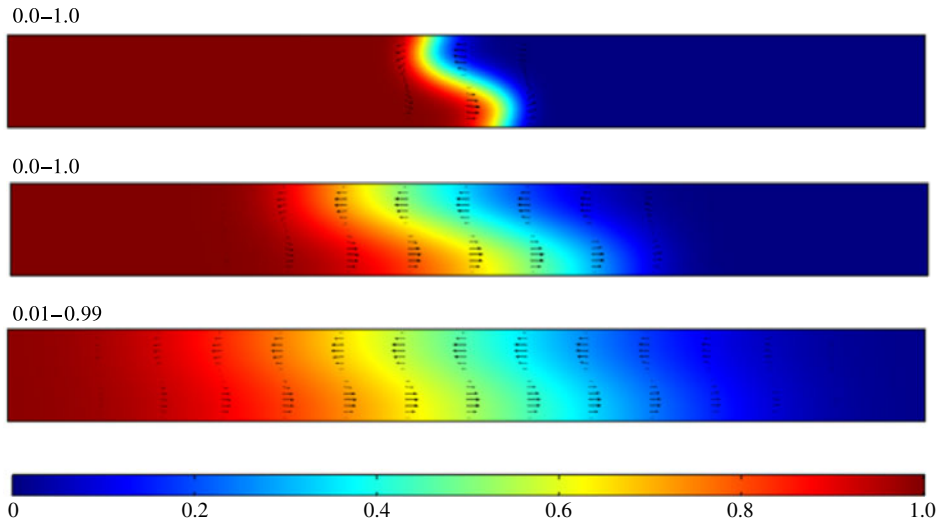


FIGURE 8. Concentration field at  $t = 0.1, 1, 5$  and  $Ra = 400$ .

parameter, which should not be expected if the particle diffusion were dominant. Large smearing may be explained by the effect of the gravitational force. Although the densities of the magnetic and carrier liquids are similar, nevertheless a simple estimate shows that the gravitational Rayleigh number  $Ra = \Delta\rho gh^3/8D\eta$  at a density difference of  $0.077 \text{ g cm}^{-3}$  is quite large and exceeds  $3.5 \times 10^4$ . As a result, after the liquids make contact counterflows arise in the lower and upper parts of the Hele-Shaw cell. Their role in the smearing of the interface may be illustrated by the Stokes model with the concentration  $c$  dependent gravity force and the diffusion equation. Scaling time by  $h^2/4D$ , length by  $h/2$  and the velocity by  $\Delta\rho gh^2/4\eta$  ( $h$  is the thickness of the Hele-Shaw cell), the dimensionless set of partial differential equations (PDEs) reads

$$-\nabla p + \nabla^2 \mathbf{v} - c \mathbf{e}_y = 0, \quad (3.1)$$

$$\frac{\partial c}{\partial t} + Ra(\mathbf{v} \cdot \nabla)c = \nabla^2 c. \quad (3.2)$$

The evolution of the concentration field and the liquid flow are calculated by using the Comsol software with the initial concentration distribution given by  $c_0(x, t_0)$  at  $t_0 = 0.025$ :

$$c_0(x, 0) = \frac{1}{2} \left( 1 - \frac{2}{\sqrt{\pi}} \int_0^{x/(2\sqrt{t_0})} \exp(-y^2) dy \right). \quad (3.3)$$

The results for  $Ra = 400$  (the results for other values of the Rayleigh number are qualitatively the same) in the cell  $x \in [-10 : 10]$  and  $y \in [-1 : 1]$  are shown in figures 8 and 9. The calculated concentration distribution in the middle of the cell ( $y = 0$ ) at different time moments and the evolution of the horizontal component of the velocity in the middle cross-section of the cell ( $x = 0$ ) are shown in figures 10 and 11, respectively. We see that the flow due to gravity smears out the concentration distribution and, after some transition time, the concentration distribution with a much wider transition layer is established, as may be seen in figure 8. The time dependence of the maximal value of the velocity of the arising flow for different values of the

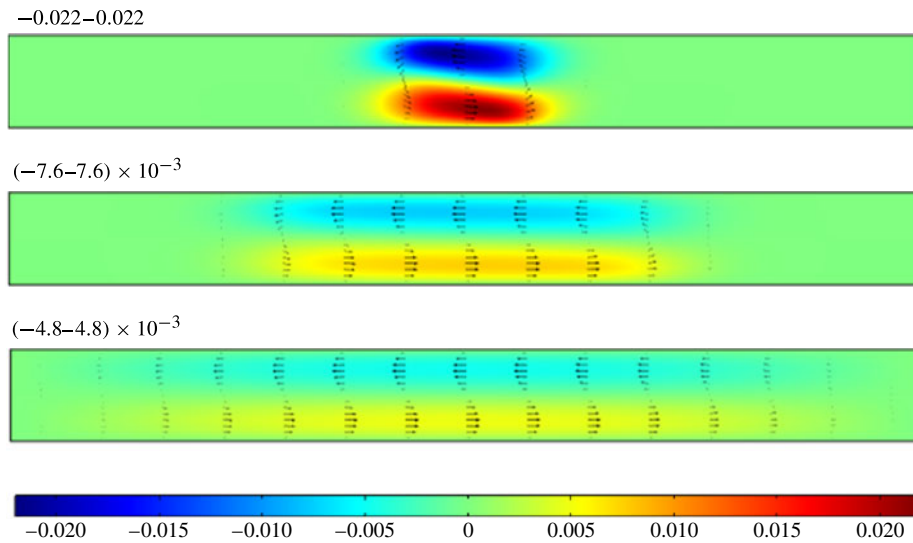


FIGURE 9. Evolution of the horizontal velocity field at  $t = 0.1, 1, 5$  and  $Ra = 400$ .

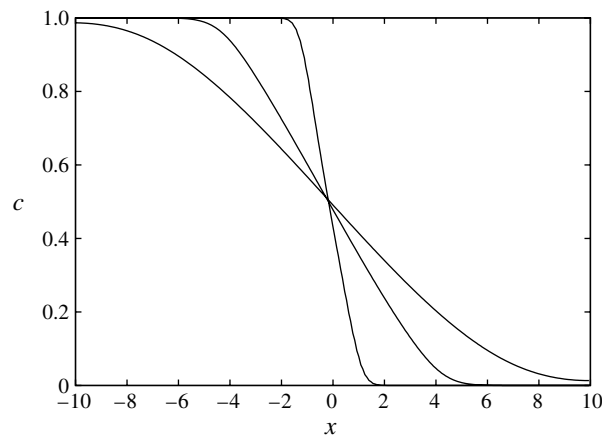


FIGURE 10. Smearing of the concentration distribution due to the flow caused by gravity at  $t = 0.1, 1, 5$  and  $Ra = 400$ .

Rayleigh number is shown in figure 12. Thus, we see that gravity causes considerable smearing of the interface before the fingering due to the magnetic micro-convection starts. This result explains the rather large values of the magnetic Rayleigh number necessary for its initiation.

Estimating the characteristic velocity of the flow caused by gravity according the data in figure 12 by  $v = 10^{-2} \Delta \rho g h^2 / 4 \eta$  in dimensional units that give the characteristic velocity of flow as  $31 \mu\text{m s}^{-1}$ , we see that it is close to the values determined from the contrast variation of the interface observed in the experiment and shown in figure 13. The characteristic times of the decay of the flow caused by gravity  $0.1 h^2 / 4 D \simeq 70 \text{ s}$  are also in agreement.

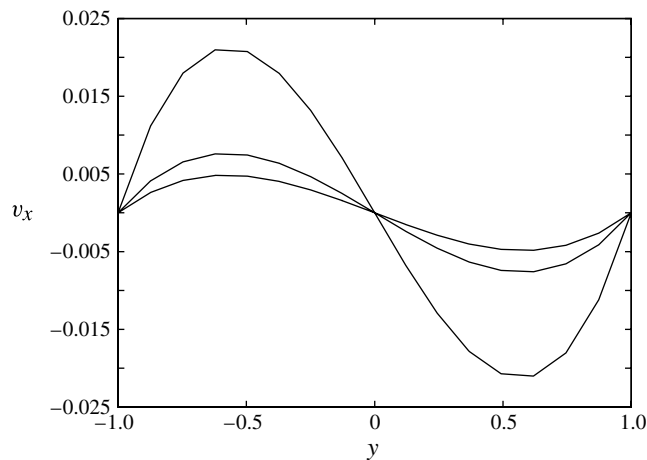


FIGURE 11. Horizontal component of velocity in the middle cross-section of the cell for different dimensionless time moments  $t = 0.1, 1, 5$  and  $Ra = 400$ .

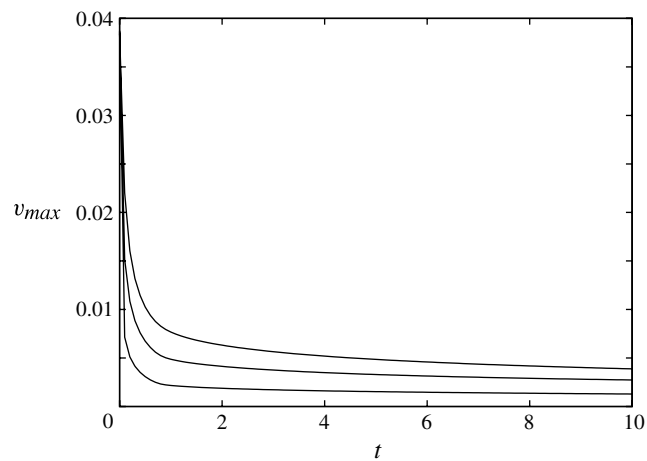


FIGURE 12. Time dependence of the maximal horizontal velocity with  $Ra = 400, 1000, 5000$ .

The experimental results of the development of magnetic micro-convection for several values of the magnetic field strength are shown in figure 14. The patterns are similar to those observed in numerical experiments for moderate values of the magnetic Rayleigh number and shown in figure 4. The grainy structure of the interface, which may be seen in figure 14 for larger values of the field (18 and 27 G), is caused by the normal field instability (Rosensweig 1985) of the layer of magnetic fluid formed by the gravitational convection.

The estimates that confirm that the grainy structure, which may be seen in figure 14 for larger values of the field is caused by the normal field instability are given in appendix B. The results for the critical field strength and the structure period given the physical parameters of liquids described above are in good agreement with the

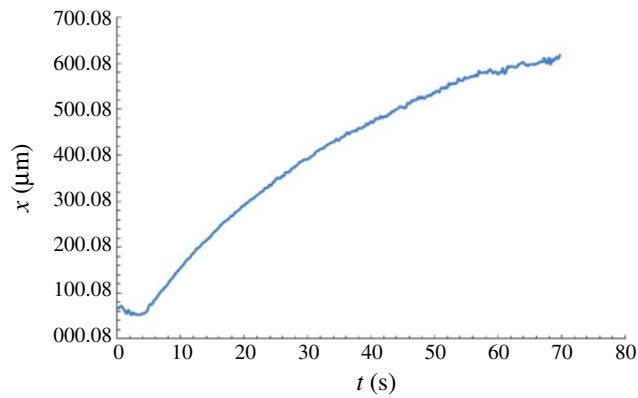


FIGURE 13. (Colour online) Experimental data of the propagation of the interface at a magnetic field value of 2.25 G.

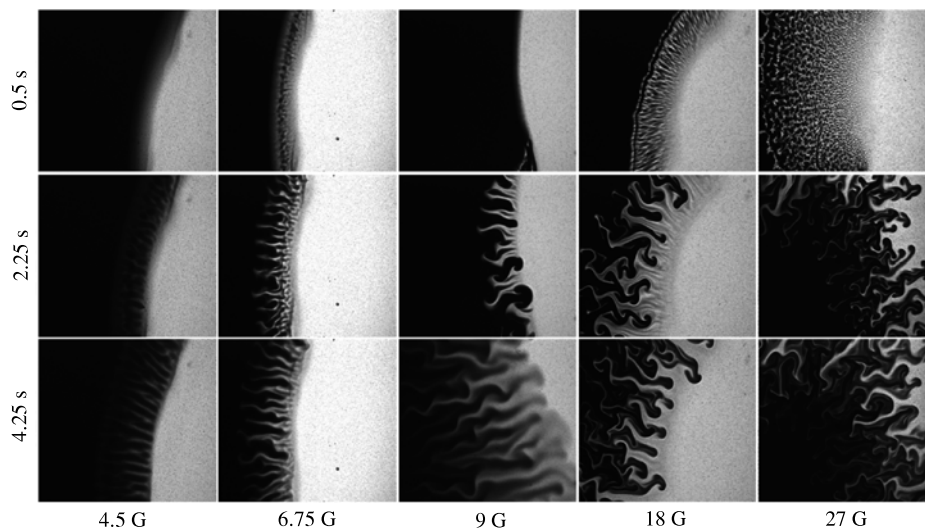


FIGURE 14. Fingering instability development in dependence on the magnetic field strength.

experiment (figure 14). In order to check that the stratification resulting from the flow due to gravity and subsequent normal field instability indeed cause the grainy structure, a glycerol–water mixture with density matched to the density of the magnetic fluid was prepared. The fingering at the interface of magnetic and non-magnetic fluids with matched densities for field of 27 G is shown in figure 15. We clearly see that the grainy structure is absent now. This result and the estimates given in appendix B confirm that the grainy structure is caused by the normal field instability on the interface between two miscible fluids. It should be mentioned here that matching the density of the magnetic fluid is a subtle issue since it is impossible to use salt solution which causes the coagulation of the electrostatically stabilized magnetic fluid. Using the glycerol–water solution creates another problem: the viscosity of the glycerol–water solution is higher than the viscosity of the ferrofluid. Nevertheless,

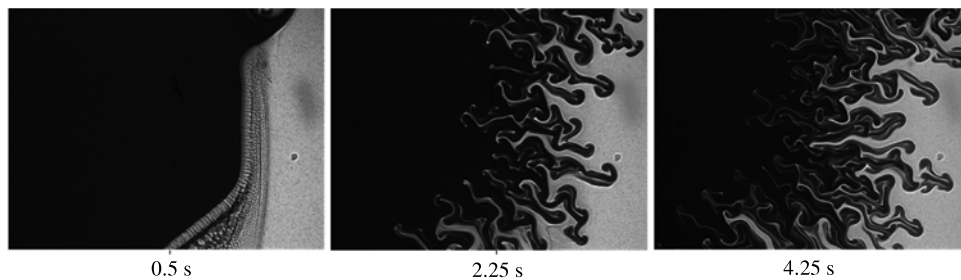


FIGURE 15. Fingering at the interface between the fluids with matched densities, with  $B = 27$  G.

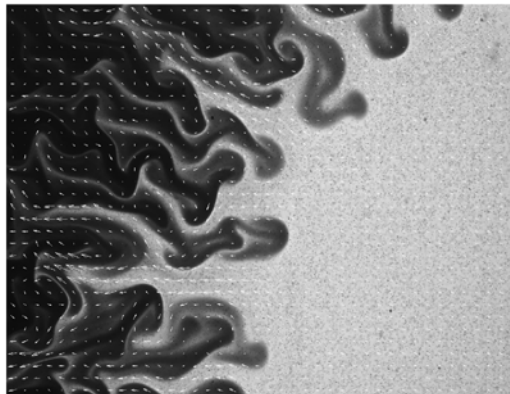


FIGURE 16. Vector field at time 8.5 s and  $B = 18$  G.

we believe that the reason of the grainy structure formation now is confirmed both theoretically and experimentally. Some small-scale stripe-like structure which may be seen in figure 15 is caused by the fingering phenomenon on the borders of the Hele-Shaw cell wetted by the ferrofluid.

Thus, the full model of the magnetic micro-convection is much more complicated as considered here and should incorporate three-dimensional equations for the magnetic field, concentration and flow.

Quantitative information about the velocity field of the micro-convection is obtained by PIV measurements. The main problem of using PIV algorithms for magnetic micro-convection is that it is impossible to determine the fluid flow in the darker regions because of poor image contrast. Therefore, special image-processing algorithms had been developed to improve the contrast (Ergin *et al.* 2010). This algorithm includes image preprocessing for local image normalization and a Gaussian filter in order to reduce noise. The vector field after preprocessing is obtained by an adaptive correlation algorithm with 2 refined steps, 2 passes per step, 32-pixel-wide interrogation windows with 50% overlap. The velocity field of the fingering pattern obtained at  $H = 180$  Oe and  $t = 8.5$  s is shown in figure 16. Vortices formation similar to that observed in numerical experiments (figure 5) is visible.

The values of the fingering velocity for one value of the field strength are shown in figure 17. Maximal value of the fingering velocity may be compared

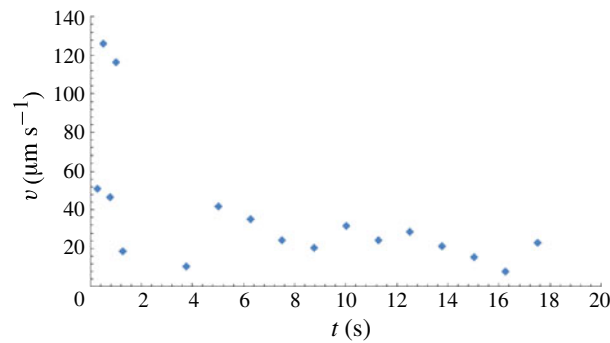


FIGURE 17. (Colour online) Finger velocity in dependence on time at a magnetic field value of 6.75 G.

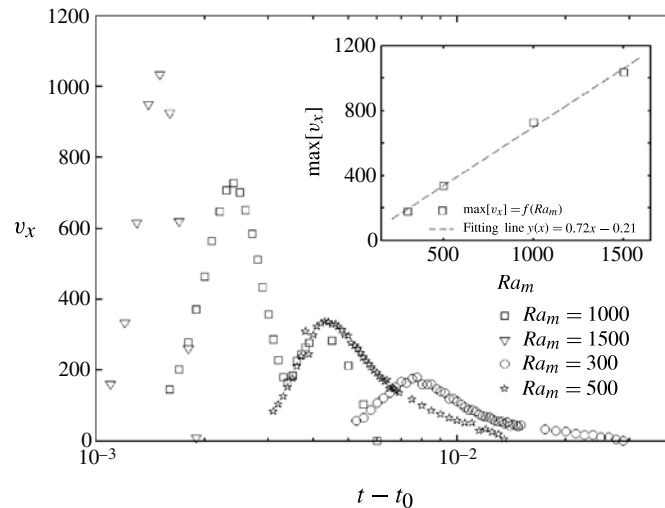


FIGURE 18. Finger velocity in dependence on time at different values of the magnetic Rayleigh number  $Ra_m = 300, 500, 1000$  and  $1500$ , with  $t_0 = 0.05$ .

with data obtained from numerical calculations. Finger velocities in dependence on time obtained from the numerical simulations at several values of the magnetic Rayleigh number are shown in figure 18. Its maximal value may be fitted by  $\max(v_x) = 0.72Ra_m$ . As a result, the dimensional velocity of fingering for the physical parameters of the ferrofluid given above at field strength 6.75 G is equal to  $142 \mu\text{m s}^{-1}$ : a value very close to that obtained in the experiments (figure 17).

By using the obtained velocity field, vorticity values are calculated with the Dantec dynamics software, which uses the neighbouring window velocity value difference to find the vorticity for each window. Afterwards we export the vorticity field values and post process them using MATLAB to extract the necessary information, e.g. the maximum absolute vorticity time dependence, shown in figure 19. Thus, the developed algorithm allows us to obtain the evolution of the vorticity field during the development of the magnetic micro-convection and its decay due to the diffusion of the magnetic nanoparticles. It may be characterized by a rapid increase of the vorticity

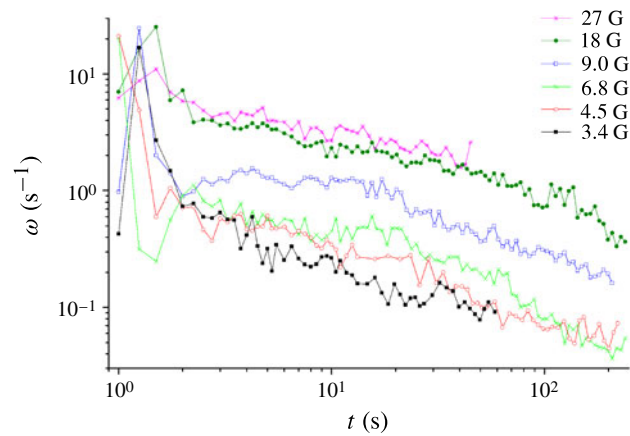


FIGURE 19. Vorticity dependence on time for different magnetic field values.

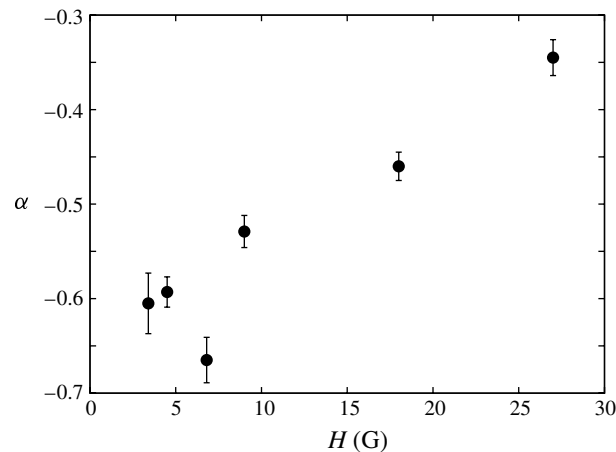


FIGURE 20. The exponent of the power law  $\alpha$  for different magnetic field values.

followed by its slow decay. Again a qualitative similarity between the numerical data figure 6 and experimental data figure 19 is observed. Experimental data for the vorticity decay may be fitted by the power law  $\omega_{max} \sim t^\alpha$ . The values of the exponent  $\alpha$  obtained are shown in figure 20. This figure illustrates the increase of the exponent with the field strength, which corresponds to the slower decay of the fingering at larger fields. This trend correlates with the increase of the exponent obtained in the numerical simulations at several values of the magnetic field strength shown in figure 6.

#### 4. Conclusions

The proposed model of the magnetic micro-convection qualitatively describes the experimental data on the development and decay of the magnetic micro-convection as shown by the results of numerical simulations. The characteristic feature of the magnetic-field-driven micro-convection is an initial fast development of the fingering

with a subsequent decay of the flow due to the diffusion of the nanoparticles. As a result considerable enhancement of the mixing is achieved, which may be interesting for some applications of the magnetic nanoparticles in microfluidics. The smearing of the diffusion front caused by the action of gravity force because of the small density difference between the magnetic colloid and its solvent plays an important role in the threshold value of the magnetic field strength for the development of the magnetic micro-convection. Stratification caused by gravitational convection is the reason for the development of the normal field instability. The theoretical analysis of the normal field instability on the interface between two miscible fluids shows good agreement with the experimental observations.

### Acknowledgement

This work was supported by the ESF project 2009/0223/1DP/1.1.1.2.0/APIA/VIAA/008.

### Appendix A. Numerical algorithm

In order to apply spectral methods and the fast Fourier transform (FFT) we represent the concentration by a sum of two parts:

$$c(x, y, t) = c_D(x, t) + c'(x, y, t), \quad (\text{A } 1)$$

where  $c_D(x, t)$  is given by the solution of the one-dimensional convection–diffusion equation as  $c_D(x, t) = 0.5(1 - \text{erf}(x/\sqrt{4t}))$  and corresponds to a step-like concentration at  $t = 0$ . The concentration perturbation  $c'$  is a periodic function in the  $x, y$  directions ( $c'(x, y) = c'(x + L_x, y + L_y)$ ). As a result, the numerical solution should be found for the periodic function  $c'(x, y)$ .

Similarly, the magnetostatic potential is split into two contributions

$$\psi_m(x, y, t) = \psi_m^D(x, t) + \psi_m'(x, y, t), \quad (\text{A } 2)$$

here

$$\psi_m^D(x, t) = \int_{-\infty}^{+\infty} c_D(x - \zeta, t) \ln(1 + \zeta^{-2}) d\zeta, \quad (\text{A } 3a)$$

$$\psi_m'(\mathbf{r}) = \int_S c'(\mathbf{r}', t) \mathbf{K}(\mathbf{r} - \mathbf{r}', 1) dS'. \quad (\text{A } 3b)$$

Integration in (A 3a) is carried out through all of the infinite region occupied by the magnetic fluid. The fast decay of the field strength  $\partial\psi_m^D/\partial x$  with the distance from the diffusion front justify the use of periodic boundary conditions. Integration in (A 3b) is carried out along the cell with dimensions  $L_x$  and  $L_y$ .

The Fourier component of  $\partial\psi_m^D/\partial x$  is obtained by using the convolution theorem according to the relation:

$$\frac{\partial \hat{\psi}_m^D}{\partial x}(k_n) = 2\pi \frac{\partial \hat{c}_D}{\partial x}(k_n) \frac{1 - e^{-|k_n|}}{|k_n|}, \quad (\text{A } 4)$$

where the Fourier coefficients  $\partial \hat{c}_D/\partial x$  are calculated by a one-dimensional FFT (the domain size is increased in the  $x$  direction from  $L_x$  to  $4L_x$  to eliminate the Gibbs phenomenon).

The perturbation of the concentration at the initial time is introduced by a small displacement  $\zeta(y)$  of the isoline  $c = 0.5$  at  $x = x_0$  (for all numerical

calculations  $x_0 = L_x/2$ ) according to the relation

$$c(x, y, t_0) = \frac{1}{2} \left( 1 - \operatorname{erf} \left( \frac{x - x_0 + \zeta(y)}{\sqrt{4t_0}} \right) \right), \quad (\text{A } 5)$$

where  $t_0$  is the parameter that characterizes the smearing.

The small perturbation  $\zeta$  is defined by the Fourier series  $\zeta(y) = \sum_{n=1}^N [a_n \cos(qyn) + b_n \sin(qyn)]$  ( $q = 2\pi/L_y$ ).

For the test of the results of linear analysis

$$c(x, y, t_0) = \frac{1}{2} \left( 1 - \operatorname{erf} \left( \frac{x - x_0}{\sqrt{4t_0}} \right) \right) + \zeta(x, y), \quad (\text{A } 6)$$

where the amplitudes of perturbation modes  $a_n$ ,  $b_n$  are defined by eigenfunctions found theoretically and read  $\{a_n, b_n\} = \{\varepsilon_a, \varepsilon_b\} e^{-qn\sqrt{1+\lambda/(n^2q^2)}|x-x_0|}$  ( $\lambda$  is given by the dispersion relation (2.8) for fixed value of magnetic Rayleigh number  $Ra_m$ ).

Equations (2.6) and (2.7) are solved numerically by the spectral method in the vorticity stream function formulation (Tan & Homsy 1988; Zimmerman & Homsy 1992). The stream function  $\psi$  is defined as  $u_x = \partial\psi/\partial y$  and  $u_y = -\partial\psi/\partial x$ , and the vorticity  $\omega$  is

$$\omega = -\nabla^2\psi. \quad (\text{A } 7)$$

Taking into account (A 1) the convection–diffusion equation (2.7) can be written as follows

$$\frac{\partial c'}{\partial t} = \frac{\partial^2 c'}{\partial x^2} + \frac{\partial^2 c'}{\partial y^2} - \frac{\partial\psi}{\partial y} \left( \frac{\partial c_D}{\partial x} + \frac{\partial c'}{\partial x} \right) + \frac{\partial\psi}{\partial x} \frac{\partial c'}{\partial y}. \quad (\text{A } 8)$$

Equation (2.6) gives the vorticity equation

$$\omega = -2Ra_m \left( \frac{\partial\psi_m}{\partial y} \left[ \frac{\partial c_D}{\partial x} + \frac{\partial c'}{\partial x} \right] - \frac{\partial\psi_m}{\partial x} \frac{\partial c'}{\partial y} \right). \quad (\text{A } 9)$$

In order to solve numerically (A 8) and (A 9) the Fourier spectral method is used. The concentration perturbation  $c'$ , stream function  $\psi$  and vorticity  $\omega$  are presented by the Fourier series

$$c'(x, y, t) = \sum_{n=0}^{N-1} \sum_{m=0}^{M-1} \hat{c}_{nm}(t) e^{i(k_n x + q_m y)}, \quad (\text{A } 10a)$$

$$\psi(x, y, t) = \sum_{n=0}^{N-1} \sum_{m=0}^{M-1} \hat{\psi}_{nm}(t) e^{i(k_n x + q_m y)}, \quad (\text{A } 10b)$$

$$\omega(x, y, t) = \sum_{n=0}^{N-1} \sum_{m=0}^{M-1} \hat{\omega}_{nm}(t) e^{i(k_n x + q_m y)} \quad (\text{A } 10c)$$

where  $k_n = 2\pi n/L_x$ ,  $q_m = 2\pi m/L_y$  are wavenumbers ( $n, m = 0, 1, 2, \dots$ ). Functions  $\hat{c}_{nm}$ ,  $\hat{\psi}_{nm}$  and  $\hat{\omega}_{nm}$  are calculated by using FFT in collocation points  $x_n = (L_x/N)n$  and  $y_m = (L_y/N)m$  ( $n = 0, 1, 2, \dots, N-1$ ,  $m = 0, 1, 2, \dots, M-1$ ). The total number of collocation points  $N, M$  is proportional to  $2^p$ ,  $p = 1, 2, 3, \dots$  and depend on the concrete case.

The nonlinear terms in (A 8) and (A 9) are given by applying a FFT:

$$J(x, y, t) = \frac{\partial \psi}{\partial y} \left( \frac{\partial c_D}{\partial x} + \frac{\partial c'}{\partial x} \right) - \frac{\partial \psi}{\partial x} \frac{\partial c'}{\partial y} = \sum_{n=0}^{N-1} \sum_{m=0}^{M-1} \hat{J}_{nm}(t) e^{i(k_n x + q_m y)}, \quad (\text{A } 11a)$$

$$Q(x, y, t) = \frac{\partial \psi_m}{\partial y} \left( \frac{\partial c_D}{\partial x} + \frac{\partial c'}{\partial x} \right) - \frac{\partial \psi_m}{\partial x} \frac{\partial c'}{\partial y} = \sum_{n=0}^{N-1} \sum_{m=0}^{M-1} \hat{Q}_{nm}(t) e^{i(k_n x + q_m y)}. \quad (\text{A } 11b)$$

As a result, the equations for the amplitudes of the Fourier modes read

$$\hat{\omega}_{nm} = (k_n^2 + q_m^2) \hat{\psi}_{nm}, \quad (\text{A } 12)$$

$$\hat{\omega}_{nm} = -2Ra_m \hat{Q}_{nm}, \quad (\text{A } 13)$$

$$\frac{\partial \hat{c}_{nm}}{\partial t} = -(k_n^2 + q_m^2) \hat{c}_{nm} - \hat{J}_{nm}. \quad (\text{A } 14)$$

The values of the stream function  $\psi(t_j)$  for given values of the concentration  $c(t_j)$  are found from (A 12) and (A 13). Since  $\psi'_m$  is periodic in both the  $x$  and  $y$  directions,  $\hat{\psi}'_m(\mathbf{k})$  is obtained as follows:

$$\hat{\psi}'_m(\mathbf{k}) = 2\pi \hat{c}_{nm}(\mathbf{k}) \hat{T}_{nm}(\mathbf{k}), \quad (\text{A } 15)$$

where  $\mathbf{k} = (k_n, q_m)$  is the two-dimensional wave vector and  $|\mathbf{k}| = \sqrt{k_n^2 + q_m^2}$ . The Fourier coefficients  $\hat{c}_{nm}$  are calculated using a two-dimensional FFT algorithm and  $\hat{T}_{nm}(\mathbf{k}) = (1 - e^{-|\mathbf{k}|})/|\mathbf{k}|$  is the Fourier transform of  $K(\mathbf{r}, 1)$ . All derivatives of  $\psi'_m$  are calculated spectrally from the obtained values of  $\hat{\psi}'_m(\mathbf{k})$ .

The linear equation (A 14) is solved for the known stream function by applying the linear propagator method, which factors out the leading-order linear term prior to the discretization. Introducing  $\hat{\chi}_{nm} = e^{(k_n^2 + q_m^2)t} \hat{c}_{nm}$  the equation  $\partial \hat{\chi}_{nm} / \partial t = -e^{(k_n^2 + q_m^2)t} \hat{J}_{nm}$  is discretized by using the three-step Adams–Bashforth method (Samarskij & Gulin 1989). The result reads

$$\hat{c}_{nm}^{(j+1)*} = \hat{c}_{nm}^j \gamma - \frac{\Delta t}{12} (23 \hat{J}_{nm}^j \gamma - 16 \hat{J}_{nm}^{(j-1)} \gamma^2 + 5 \hat{J}_{nm}^{(j-2)} \gamma^3), \quad (\text{A } 16)$$

$$\gamma = e^{-(k_n^2 + q_m^2) \Delta t}. \quad (\text{A } 17)$$

Further, corrected values of  $\hat{\psi}_{nm}^{(j+1)*}$  and  $\hat{J}_{nm}^{(j+1)*}$  are found from (A 12), (A 13) and (A 11a), respectively. As a result, the Fourier components of the concentration are obtained for the next time step

$$\hat{c}_{nm}^{(j+1)} = \hat{c}_{nm}^j - \frac{\Delta t}{2} (\hat{J}_{nm}^{(j+1)*} + \hat{J}_{nm}^j) - \frac{\Delta t}{2} (k_n^2 + q_m^2) (\hat{c}_{nm}^{(j+1)*} + \hat{c}_{nm}^j). \quad (\text{A } 18)$$

The concentration field is obtained by applying the inverse FFT to  $\hat{c}_{nm}^{(j+1)}$  and adding  $c_D(t)$ . Since the numerical scheme used is not fully implicit in time, the solution may show numerical instability.

## Appendix B. Normal field instability at the interface of miscible magnetic and non-magnetic fluids

Normal field instability of the free horizontal surface of a magnetic liquid is well understood. However, this instability has not been considered yet in the case of the interface between two miscible fluids. In this appendix it is shown that in the case

when  $t_0 \rightarrow 0$  it is possible to obtain analytically the dispersion equation for the growth increment of the instability.

The Stokes equation in the case of miscible liquids and the diffusion equation for the particle concentration read

$$-\nabla p + \eta \nabla^2 \mathbf{v} + \chi_0 c \nabla \left( \frac{H^2}{2} \right) - \Delta \rho c g \mathbf{e}_z = 0, \quad \nabla \cdot \mathbf{v} = 0, \quad (\text{B } 1)$$

$$\frac{\partial c}{\partial t} + \mathbf{v} \cdot \nabla c = D \nabla^2 c, \quad (\text{B } 2)$$

where the  $z$ -axis is along the vertical direction,  $c$  is the concentration of magnetic particles normalized to 1 by the concentration far from the interface, and  $\Delta \rho$  is the density difference of the magnetic and non-magnetic liquids.

At equilibrium when the magnetic field is parallel to the gradient of the concentration  $c_0$  it reads

$$\mathbf{H} = \mathbf{H}_0 = (0, 0, H_\infty / (1 + 4\pi \chi_0 c_0)). \quad (\text{B } 3)$$

Here  $H_\infty$  is the magnetic field strength far from the interface in the non-magnetic liquid and  $\chi_0$  is the magnetic susceptibility.

The equation for the magnetic field in the case of small perturbations around  $c = c_0(z)$  reads (with  $c = c_0 + c'$ ,  $\mathbf{H} = \mathbf{H}_0 + \mathbf{H}'$  and  $\mathbf{H}' = \nabla \psi'$ )

$$\frac{\partial}{\partial x} ((1 + 4\pi \chi_0 c_0) H'_x) + \frac{\partial}{\partial z} (4\pi \chi_0 c' H_{0z}) + \frac{\partial}{\partial z} ((1 + 4\pi \chi_0 c_0) H'_z) = 0. \quad (\text{B } 4)$$

In the limit when  $c_0$  is step-like, it follows from (B 4) that

$$H = (1 + 4\pi \chi_0 c_0) H'_z + \frac{4\pi \chi_0 c' H_\infty}{1 + 4\pi \chi_0 c_0} \quad (\text{B } 5)$$

is continuous on the interface where  $c_0(0^+) = 0$  and  $c_0(0^-) = 1$ .

The equations for the velocity and concentration perturbations read

$$-\nabla p' + \eta \nabla^2 \mathbf{v} + \chi_0 c_0 \nabla (\mathbf{H}_0 \cdot \mathbf{H}') - \Delta \rho c' g \mathbf{e}_z = 0 \quad (\text{B } 6)$$

and

$$\frac{\partial c'}{\partial t} + v_z \frac{dc_0}{dz} = D \nabla^2 c'. \quad (\text{B } 7)$$

Looking for perturbations periodic in the horizontal direction

$$(\mathbf{v}', c', \psi') = (\mathbf{v}(z), c(z), \psi(z)) \exp(ikx), \quad (\text{B } 8)$$

we have

$$\frac{\partial c}{\partial t} + v_z \frac{dc_0}{dz} = D \left( \frac{d^2 c}{dz^2} - k^2 c \right), \quad (\text{B } 9)$$

$$\eta \left( \frac{d^2}{dz^2} - k^2 \right)^2 v_z = - \frac{\chi_0 k^2 H_\infty}{1 + 4\pi \chi_0 c_0} \frac{dc_0}{dz} H - \Delta \rho c g k^2, \quad (\text{B } 10)$$

$$\frac{d}{dz} \left( (1 + 4\pi \chi_0 c_0) \frac{d\psi}{dz} \right) - (1 + 4\pi \chi_0 c_0) k^2 \psi + \frac{d}{dz} (4\pi \chi_0 c H_{0z}) = 0. \quad (\text{B } 11)$$

For step-like  $c_0(z)$  the boundary conditions are obtained by integration  $\int_{-\delta}^{\delta} dz(\dots)$  of (B 9)–(B 11) across the diffusion layer and taking the limit  $\delta \rightarrow 0$ . They

read ( $\mu_\infty = 1 + 4\pi\chi_0$ )

$$\left. \begin{aligned} c(0^+) &= c(0^-), \\ D \frac{dc}{dz}(0^+) - D \frac{dc}{dz}(0^-) &= -v_z(0), \\ v_z(0^+) &= v_z(0^-), \\ \frac{dv_z}{dz}(0^+) &= \frac{dv_z}{dz}(0^-), \\ \frac{d^2v_z}{dz^2}(0^+) &= \frac{d^2v_z}{dz^2}(0^-), \\ \frac{d^3v_z}{dz^3}(0^+) - \frac{d^3v_z}{dz^3}(0^-) &= \frac{(\mu_\infty - 1)k^2 H_\infty}{4\pi\eta\mu_\infty} H(0), \\ \psi(0^+) &= \psi(0^-), \\ \frac{d\psi_z}{dz}(0^+) + (\mu_\infty - 1)c(0)H_\infty &= \mu_\infty \frac{d\psi_z}{dz}(0^-) + \frac{(\mu_\infty - 1)c(0)H_\infty}{\mu_\infty}. \end{aligned} \right\} \quad (\text{B } 12)$$

Equations (B 9)–(B 11) at boundary conditions (B 12) are analysed in the quasi-stationary case when  $v, c, \psi \sim \exp(\lambda t)$ . The solutions of (B 9)–(B 11) that satisfy the condition  $v, c, \psi \rightarrow 0$  at  $|z| \rightarrow \infty$  and the boundary conditions for the magnetostatic potential and concentration read

$$\left. \begin{aligned} c &= E \exp(-\sqrt{\lambda/D + k^2}z) \quad (z > 0), \\ c &= E \exp(\sqrt{\lambda/D + k^2}z) \quad (z < 0), \\ \psi &= -\frac{(\mu_\infty - 1)H_\infty E}{\lambda/D\mu_\infty(\mu_\infty + 1)} (\sqrt{\lambda/D + k^2}(\mu_\infty^2 + 1) + (\mu_\infty - 1)k) \exp(-kz) \\ &\quad + \frac{(\mu_\infty - 1)H_\infty}{\lambda/D} \sqrt{\lambda/D + k^2} \exp(-\sqrt{\lambda/D + k^2}z) E \quad (z > 0), \\ \psi &= \frac{(\mu_\infty - 1)H_\infty E}{\lambda/D\mu_\infty(\mu_\infty + 1)} (\sqrt{\lambda/D + k^2}(\mu_\infty^2 + 1) - (\mu_\infty - 1)k) \exp(kz) \\ &\quad - \frac{(\mu_\infty - 1)H_\infty}{\lambda/D\mu_\infty^2} \sqrt{\lambda/D + k^2} \exp(\sqrt{\lambda/D + k^2}z) E \quad (z > 0), \\ v_z &= C \exp(-kz) + Dz \exp(-kz) - \frac{\Delta\rho g k^2 E}{\eta(\lambda/D)^2} \exp(-\sqrt{\lambda/D + k^2}z) \quad (z > 0), \\ v_z &= A \exp(kz) + Bz \exp(kz) - \frac{\Delta\rho g k^2 E}{\eta(\lambda/D)^2} \exp(\sqrt{\lambda/D + k^2}z) \quad (z < 0). \end{aligned} \right\} \quad (\text{B } 13)$$

The remaining five boundary conditions give the set of five equations for the unknown set of constants  $A, B, C, D, E$ . Its solubility condition gives the dispersion equation for the growth increment of small perturbations

$$\begin{aligned} &\frac{4\sqrt{\lambda/D + k^2}}{k} - \frac{(\mu_\infty - 1)^2(\mu_\infty^2 + 1)H_\infty^2}{8\pi\eta D\mu_\infty^2(\mu_\infty + 1)} \frac{\sqrt{\lambda/D + k^2} - k}{\lambda/Dk} \\ &= \frac{\Delta\rho g \sqrt{\lambda/D + k^2}(2k^2 - \lambda/D) - 2k^3}{D\eta k(\lambda/D)^2}. \end{aligned} \quad (\text{B } 14)$$

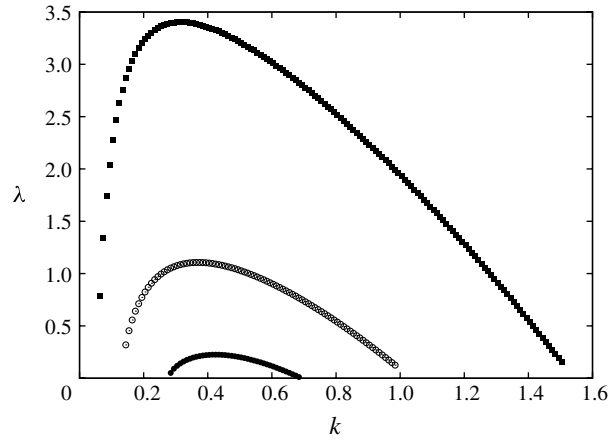


FIGURE 21. Growth increments of the normal field instability at the interface of two miscible fluids in dependence on the wavenumber at different values of the magnetic Rayleigh number. Here  $Ra_m^c = 6$  (black circles),  $Ra_m^c = 10$  (open circles) and  $Ra_m^c = 20$  (squares).

There are two characteristic lengths in the problem: the magnetic length,

$$l_H^{-2} = \frac{(\mu_\infty - 1)^2(\mu_\infty^2 + 1)H_\infty^2}{8\pi\eta D\mu_\infty^2(\mu_\infty + 1)}, \quad (\text{B } 15)$$

and the gravitational length,

$$l_G^{-3} = \frac{\Delta\rho g}{D\eta}. \quad (\text{B } 16)$$

On the scales  $l_H$  and  $l_G$ , the magnetic and gravitational Rayleigh numbers, respectively, are equal to one. Choosing as the characteristic scale of the wavenumber  $(\Delta\rho g/(D\eta))^{1/3}$ , the dispersion equation in dimensionless form reads ( $\tilde{\lambda} = \lambda l_G^2/D$ , where  $Ra_m = (l_G/l_H)^2$  is the magnetic Rayleigh number defined by the characteristic gravitational length, tildes are further omitted)

$$\frac{4\sqrt{\lambda + k^2}}{k} - Ra_m \frac{\sqrt{\lambda + k^2} - k}{k\lambda} = \frac{\sqrt{\lambda + k^2}(2k^2 - \lambda) - 2k^3}{k^2\lambda^2}. \quad (\text{B } 17)$$

In the limit  $\lambda \rightarrow 0$ , equation (B 17) gives

$$Ra_m = \frac{3}{2k} + 8k^2. \quad (\text{B } 18)$$

This gives for the critical magnetic Rayleigh number  $Ra_m^c$  and wavenumber  $k_*$

$$Ra_m^c = 24k_*^2, \quad k_* = (3/32)^{1/3}. \quad (\text{B } 19)$$

The dependence of the growth increment on the dimensionless wavenumber for several values of the magnetic Rayleigh number is shown in figure 21.

The obtained results give values for the characteristic period of the pattern arising at the normal field instability and the critical magnetic field strength, which have the same order of magnitude as observed in the experiment. The critical value of the magnetic Rayleigh number for the critical field in the case of the physical properties

of the magnetic liquid and the density difference of the liquids for the critical magnetic field strength and the period of the pattern give the values  $H_c = 2.47$  G and  $2\pi/k_* = 27$   $\mu\text{m}$ , respectively. These values are close to those observed in the experiment. As one can see, the formation of the grainy structure on the interface already appears at field strength of 6.75 G: a value quite close to our estimates. The period of the structure 20  $\mu\text{m}$  estimated by counting the number of black dots 20 which are seen in figure 14 on the length scale  $4 \times 10^{-2}$  cm also is close to our estimate.

It should be remarked that scales of this phenomenon are completely different from the classical normal field instability, whose scale is determined by the capillary length and is of the order of centimetres.

## REFERENCES

- CABRAL, B. & LEEDOM, L. 1993 Imaging vector fields using line integral convolution. *Proc. ACM* **93**, 263–270.
- CEBERS, A. 1981 Dynamics of magnetostatic instabilities. *Magnetohydrodynamics* **17**, 113–121.
- CEBERS, A. 1997 Stability of diffusion fronts of magnetic particles in porous media under the action of external magnetic field. *Magnetohydrodynamics* **33**, 48–55.
- CEBERS, A. & MAIOROV, M. M. 1980 Magnetostatic instabilities in plane layers of magnetizable fluids. *Magnetohydrodynamics* **16**, 21–27.
- CHEN, C.-Y. 2003 Numerical simulations of fingering instabilities in miscible magnetic fluids in a Hele-Shaw cell and the effect of Korteweg stress. *Phys. Fluids* **15**, 1086–1089.
- CHEN, C.-Y. & WEN, C.-Y. 2002 Numerical simulations of miscible magnetic flows in a Hele-Shaw cell. Radial flows. *J. Magnetism Magnetic Mater.* **252**, 296–298.
- DEREC, C., BOLTENHAGEN, P., NEVEU, S. & BACRI, J.-C. 2008 Magnetic instability between miscible fluids in a Hele-Shaw cell. *Magnetohydrodynamics* **44**, 135–142.
- ERGIN, F. G., WATZ, B. B., ERGLIS, K. & CEBERS, A. 2010 Poor-contrast particle image processing in micro scale mixing. *Proceedings of the ASME 10th Biennial Conference on Engineering Systems Design and Analysis*, pp. 1–5. ASME.
- GOYAL, N. & MEIBURG, E. 2006 Miscible displacements in Hele-Shaw cells: two-dimensional base states and their linear stability. *J. Fluid Mech.* **558**, 329–355.
- IGONIN, M. 2004 Hydrodynamic instabilities of miscible and immiscible magnetic fluids in a Hele-Shaw cell. PhD thesis, D. Diderot University Paris 7.
- IGONIN, M. & CEBERS, A. 2003 Labyrinthine instability of miscible magnetic fluids. *Phys. Fluids* **15**, 1734–1744.
- JACKSON, D. P., GOLDSTEIN, R. E. & CEBERS, A. O. 1994 Hydrodynamics of fingering instabilities in dipolar fluids. *Phys. Rev. E* **50**, 298–307.
- MAIOROV, M. & CEBERS, A. 1983 Magnetic microconvection on the diffusion front of ferroparticles. *Magnetohydrodynamics* **19**, 376–380.
- MEZULIS, A. & BLUMS, E. 2005 Experimental investigations of the microconvective instability in optically induced gratings. *Magnetohydrodynamics* **41**, 341–348.
- ROSENSWEIG, R. E. 1985 *Ferrohydrodynamics*. Cambridge University Press.
- SAMARSKIJ, A. A. & GULIN, A. V. 1989 *Numerical Methods*. Nauka.
- TAN, C. T. & HOMSY, G. M. 1988 Simulation of nonlinear viscous fingering in miscible displacement. *Phys. Fluids* **31**, 1330–1338.
- WEN, C.-Y., CHEN, CHING-YAO & KUAN, D.-C. 2007 Experimental studies of labyrinthine instabilities of miscible ferrofluids in a Hele-Shaw cell. *Phys. Fluids* **19**, 084101.
- ZIMMERMAN, W. B. & HOMSY, G. M. 1992 Viscous fingering in miscible displacements: unification of effects of viscosity contrast, anisotropic dispersion, and velocity dependence of dispersion on nonlinear finger propagation. *Phys. Fluids* **4** (11), 2348–2359.

# Magnetic field driven micro-convection in the Hele-Shaw cell: the Brinkman model and its comparison with experiment

G. Kitenbergs<sup>1,2,3</sup>, A. Tatulcenkovs<sup>4</sup>, K. Ērglis<sup>1</sup>, O. Petrichenko<sup>1</sup>,  
R. Perzynski<sup>2,3</sup> and A. Cēbers<sup>4,†</sup>

<sup>1</sup>MMML Lab, Faculty of Physics and Mathematics, University of Latvia, Riga, LV-1002, Latvia

<sup>2</sup>Sorbonne Universités, UPMC Univ. Paris 06, UMR 8234, PHENIX, Paris, F-75005, France

<sup>3</sup>CNRS, UMR 8234, PHENIX, Paris, F-75005, France

<sup>4</sup>Department of Theoretical Physics, University of Latvia, Riga, LV-1002, Latvia

(Received 6 February 2015; revised 8 April 2015; accepted 27 April 2015)

The micro-convection caused by the ponderomotive forces of the self-magnetic field in a magnetic fluid is studied here both numerically and experimentally. The theoretical approach based on the general Brinkman model substantially improves the description with respect to the previously proposed Darcy model. The predictions of both models are here compared to finely controlled experiments. The Brinkman model, in contrast to the Darcy model, allows us to describe the formation of mushrooms on the plumes of the micro-convective flow and the width of the fingers. In the Brinkman approach, excellent quantitative agreement is also obtained for the finger velocity dynamics and the velocity maximal values as a function of the magnetic Rayleigh number. The diffusion coefficient of particles of the water-based magnetic colloid determined by the threshold field strength value of the micro-convection is significantly larger than the diffusion coefficient of individual particles. This result is confirmed by independent measurements of the diffusion coefficient at the smearing of the diffusion front.

**Key words:** colloids, Hele-Shaw flows, magnetic fluids

## 1. Introduction

Magnetic field driven micro-convection was discovered in the early 1980s (Maiorov & Cebers 1983), extending the concept of self-magnetic field driven instabilities (Cebers & Maiorov 1980) for miscible fluids. Magnetic micro-convection is caused by the ponderomotive force of the non-homogeneous self-magnetic field of a magnetic fluid which, if the concentration gradient is not collinear to the magnetic field gradient, is non-potential and creates a flow. The phenomenon of magnetic micro-convection has attracted the attention of researchers from different points of view. Magnetic field driven micro-convection for various Hele-Shaw cell thicknesses was observed in Derec *et al.* (2008). The instability of a circular interface between miscible magnetic and non-magnetic fluids was studied in Chen & Wen (2002). The role

† Email address for correspondence: [aceb@tok.sal.lv](mailto:aceb@tok.sal.lv)

of three-dimensional effects was studied in Wen, Chen & Kuan (2007). Convective motion in the concentration gratings induced by non-homogeneous illumination under the action of a magnetic field was studied in Mezulis & Blums (2005) and Zablotsky (2012). The theoretical models are based on the equation of motion of the magnetic liquid, the diffusion equation for magnetic particles and the Maxwell equations for a magnetostatic field (Cebers 1997). On this basis different characteristics of magnetic micro-convection were found by linear stability analysis (Igonin & Cebers 2003). It is interesting to note that more complex models were applied for the description of magnetic micro-convection, including the Korteweg stress (Chen 2003), which has long been of interest in the physics of miscible fluids (Truzzolillo *et al.* 2014). It should be remarked that fingering phenomena in miscible fluids (Bischofberger, Ramachandran & Nagel 2014) are still of general scientific interest.

The magnetic micro-convection studied here has already been explored in Erglis *et al.* (2013). In particular, velocity fields were experimentally determined using particle image velocimetry. The results obtained were interpreted according to a theoretical model of the flow based on a simple Darcy approximation, which was unable to describe all the features of micro-convection observed experimentally. For example, the formation of mushrooms on the plumes of the micro-convective flow, the width of the fingers, and the enhanced particle diffusion of ionic water-based ferrofluids, were not explained. Further, in the experimental system of Erglis *et al.* (2013), poor control of interface formation affected the smearing of the diffusion front, which is an important parameter defined below in § 2.2.

Here we substantially improve the experimental set-up for the measurement of the velocities of fingers in micro-convection, where particular attention is paid to the formation of the interface between miscible fluids. Moreover, a much more complete model for magnetic micro-convection, based on the Brinkman equation for the fluid flow instead of the Darcy model, is employed. The main characteristics of micro-convection, such as the characteristic size of the primary fingers or their velocity dynamics, are calculated and compared with experiment. We show that the Brinkman model gives much better quantitative and qualitative agreement with the experimental data than the previous Darcy model.

We organize the paper as follows. In § 2 we formulate the Brinkman model for magnetic micro-convection. Dimensionless quantities are introduced and it is shown that the magnetic micro-convection is determined by the magnetic Rayleigh number. Linear stability analysis is carried out and the wavenumber of the fastest growing mode is calculated as a function of the magnetic Rayleigh number. These results are compared with those of the Darcy model. The numerical algorithm and the numerical results obtained are described in § 3; in particular (unlike the Darcy model), the Brinkman model predicts the formation of mushrooms on the developing fingers. For a further comparison, the primary finger velocity and the Fourier spectrum dynamics are analysed in the framework of both models. In § 4 the experimental set-up is introduced, together with the experimental observations, including determination of the critical field and the subsequent image analysis. It allows us to retrieve comparable data on the Fourier coefficient dynamics of the primary fingers and velocities. Comparison between experiment and simulation, together with extensive discussion, is carried out in § 5.

## 2. Mathematical formulation

### 2.1. The model

We consider two miscible fluids where the first is a magnetic fluid and the second is a simple non-magnetic fluid. Fluids are confined in a horizontal Hele-Shaw cell and

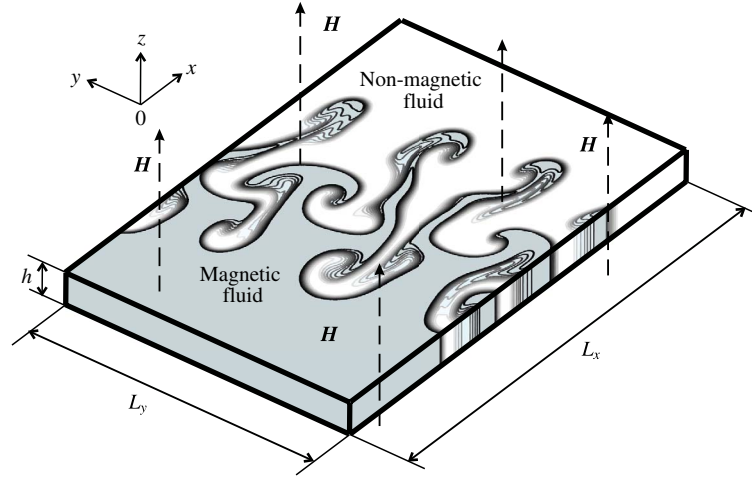


FIGURE 1. Sketch of the Hele-Shaw cell. The interface is formed between a magnetic fluid (a colloidal solution of magnetic nanoparticles) and a carrier fluid.

a magnetic field is applied perpendicular to the cell; a sketch of the cell is shown in figure 1. The viscosities of the fluids are equal. The ponderomotive forces of the non-homogeneous self-magnetic field near the fluid interface cause a fingering instability. Its growth is described by a set of equations, which includes the Brinkman equation, where the ponderomotive magnetic force is taken into account, the continuity equation, and the convection–diffusion equation (Cebers 1997; Igonin & Cebers 2003), and reads as follows:

$$-\nabla p - \frac{12\eta}{h^2}\mathbf{u} - \frac{2M(c)}{h}\nabla\psi_m + \eta\Delta\mathbf{u} = 0, \quad \nabla \cdot \mathbf{u} = 0, \quad (2.1a,b)$$

$$\frac{\partial c}{\partial t} + (\mathbf{u} \cdot \nabla)c = D\Delta c, \quad (2.2)$$

where  $\Delta = \partial^2/\partial x^2 + \partial^2/\partial y^2$ ,  $\nabla = (\partial/\partial x, \partial/\partial y)$ . Note that a viscous term  $\eta\Delta\mathbf{u}$  is added, with respect to the Darcy model in the equation of motion. It describes the horizontal diffusion of vorticity, absent from the Darcy model, which takes into account only the friction with walls  $-12\eta\mathbf{u}/h^2$ , and allows us to obtain more coarse fingers in agreement with experiment. Here  $p$  is the pressure,  $\mathbf{u} = (u_x(x, y), u_y(x, y))$  is the depth-averaged velocity,  $\eta$  is the viscosity of the fluid,  $h$  is the thickness of the Hele-Shaw cell,  $D$  is the constant isotropic diffusion coefficient, and  $c$  is the concentration of the magnetic fluid normalized by its value far from the interface. The magnetization  $M(c)$  is taken to be proportional to the concentration of the magnetic fluid  $c$  ( $M = M_0c$ ) and the value of the magnetostatic potential  $\psi_m$  on the boundary of the Hele-Shaw cell is given by (Cebers 1981; Jackson, Goldstein & Cebers 1994)

$$\psi_m(\mathbf{r}, t) = M_0 \int c(\mathbf{r}', t) K(\mathbf{r} - \mathbf{r}', h) dS', \quad (2.3)$$

where the integration is performed over the boundary of the Hele-Shaw cell:  $K(\mathbf{r}, h) = 1/|\mathbf{r}| - 1/\sqrt{|\mathbf{r}|^2 + h^2}$ .

Equations (2.1) and (2.2) extend the model that is usually applied for the study of the displacements of miscible, nonmagnetic fluids in the Hele-Shaw cell (Goyal & Meiburg 2006), via the Brinkman approximation.

The boundary conditions for the velocity components and the concentration of the fluid are

$$u_x(0, y) = u_y(0, y) = 0, \quad c(0, y) = 1, \quad (2.4a,b)$$

$$u_x(L_x, y) = u_y(L_x, y) = 0, \quad c(L_x, y) = 0, \quad (2.5a,b)$$

and the conditions of periodicity across the Hele-Shaw cell are

$$\mathbf{u}(x, 0, t) = \mathbf{u}(x, L_y, t), \quad c(x, 0, t) = c(x, L_y, t). \quad (2.6a,b)$$

The boundary conditions (2.4) require that the fluid is motionless at both ends of the cell. The motion of the liquid arises from a non-potential magnetic force  $-2M(c)\nabla\psi_m/h$ .

The equations are put into dimensionless form by introducing the following scales: length  $h$ , time  $h^2/D$ , velocity  $D/h$ , pressure  $12\eta D/h^2$ , magnetostatic potential  $M_0h$ . The set of dimensionless equations therefore reads

$$-\nabla p - \mathbf{u} - 2Ra_m c \nabla \psi_m + \frac{\Delta \mathbf{u}}{12} = 0, \quad \nabla \cdot \mathbf{u} = 0, \quad (2.7a,b)$$

$$\frac{\partial c}{\partial t} + (\mathbf{u} \cdot \nabla)c = \Delta c. \quad (2.8)$$

Here  $Ra_m = M_0^2 h^2 / 12\eta D$  is the magnetic Rayleigh number determined by the ratio of the characteristic time of diffusion  $\tau_D = h^2/D$  and the characteristic time  $\tau_M = 12\eta/M_0^2$  of the motion due to a non-homogeneous self-magnetic field of the fluid.

## 2.2. The linear stability analysis

The development of small perturbations of the interface depends on the smearing of the diffusion front between the miscible liquids (Cebers 1997; Igonin & Cebers 2003). In the case when the smearing occurs due to the diffusion of the particles their concentration distribution is described by  $c_0 = 0.5(1 - \text{erf}(x/2\sqrt{t_0}))$ , where  $t_0$  is the smearing time. An analytical solution may be found in the limit  $t_0 = 0$ , when the concentration distribution is step-like. Development of small perturbations is considered in the quasi-stationary approximation. It is valid when the characteristic time of the perturbation evolution is smaller than the characteristic time of the evolution of the concentration field.

The linear perturbation of a quiescent base state is represented by  $\{u_x, u_y, c, \psi_m\}(x, y, t) = \{0, 0, c_0, \psi_{m0}\}(x) + \{u'_x, u'_y, c', \psi'_m\}(x)e^{iky+\lambda t}$ , where  $k$  is the wavenumber and  $\lambda$  is the growth increment of perturbation. In the motionless state the ponderomotive force due to the self-magnetic field is balanced by the pressure gradient

$$-\frac{\partial p_0}{\partial x} - 2Ra_m c_0 \frac{\partial \psi_{m0}}{\partial x} = 0, \quad (2.9)$$

where

$$\psi_{m0} = \int_{-\infty}^{+\infty} c_0(x - \xi, t_0) \ln(1 + \xi^{-2}) d\xi. \quad (2.10)$$

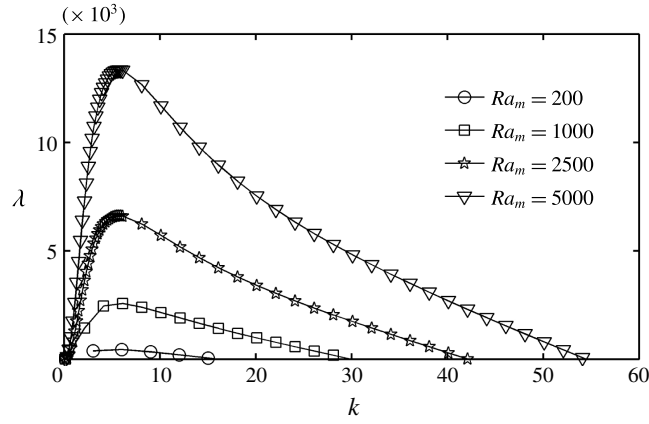


FIGURE 2. Growth increments  $\lambda$  as a function of the wavenumber for different values of the magnetic Rayleigh number,  $Ra_m = 200, 1000, 2500, 5000$ .

Equations (2.7) and (2.8) for small perturbations of the velocity  $u'_x$  and the concentration  $c'$  gives

$$\left(\frac{d^2}{dx^2} - k^2\right)^2 u'_x - 12 \left(\frac{d^2}{dx^2} - k^2\right) u'_x - 24k^2 Ra_m \left(\frac{dc_0}{dx} \psi'_m - c' \frac{d\psi_{m0}}{dx}\right) = 0, \quad (2.11)$$

$$(\lambda + k^2)c' + u'_x \frac{dc_0}{dx} - \frac{d^2 c'}{dx^2} = 0, \quad (2.12)$$

where

$$\psi'_m = 2 \int_{-\infty}^{+\infty} c'(x - \xi) \left( K_0(k|\xi|) - K_0\left(k\sqrt{\xi^2 + 1}\right) \right) d\xi \quad (2.13)$$

and  $K_0$  is the modified Bessel function of the second kind (a Macdonald function). Equations (2.11) and (2.12) and boundary conditions  $c'(\pm\infty, y) = u'_x(\pm\infty, y) = 0$  yield the eigenvalue problem for the growth rate of the perturbations  $\lambda$ . Its solution in the limit  $t_0 \rightarrow 0$  is straightforward and is given in appendix A. The growth increments in this limit are calculated according to (A 27) given in appendix A.

The growth increment as a function of the wavenumber  $k$  for different values of the magnetic Rayleigh number,  $Ra_m = 200, 1000, 2500$  and  $5000$  at  $t_0 = 0$ , is shown in figure 2. We see that the maximal growth increment for all tested values of the magnetic Rayleigh number in figure 2 corresponds to the wavenumber approximately equal to  $k \simeq 5$ . For comparison, figure 3 shows the neutral curves of the magnetic micro-convection for the Brinkman model and the Darcy model at  $t_0 = 0$ . With the Brinkman model the onset of the instability corresponds to a critical value of the magnetic Rayleigh number  $Ra_m^{cr} = 6.6$  associated with a critical wavenumber  $k^{cr} = 1.8$ . These numbers can be compared with the Darcy model (Erglis *et al.* 2013):  $Ra_m^{cr} = 5.7$  and  $k^{cr} = 5.2$  at  $t_0 = 0$ . We thus see that while increasing the magnetic Rayleigh number the fingers develop with very different widths in the framework of the two models at the same value of  $t_0$ . The finger width predicted by the Darcy model (Erglis *et al.* 2013) produces fingers of significantly smaller width (larger  $k^{cr}$ ) than the Brinkman model (smaller  $k^{cr}$ ), the latter model producing fingers with a width close to the experimental observations (see below).

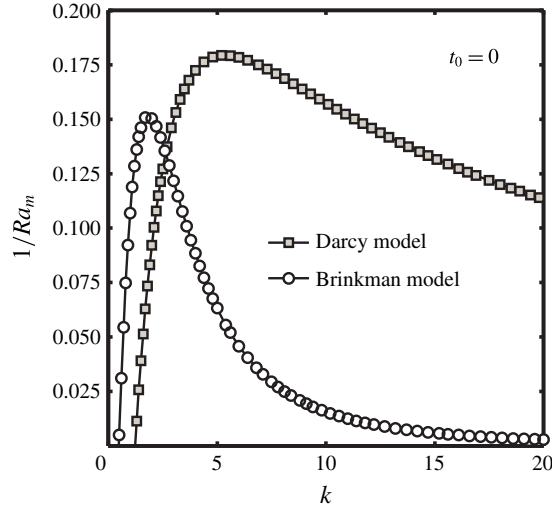


FIGURE 3. Neutral curves ( $\lambda=0$ ) of magnetic micro-convection at  $t_0=0$  for the Brinkman model (circles) and Darcy model (squares) as obtained by linear stability analysis.

### 3. Numerical simulation

#### 3.1. Numerical algorithm

The evolution of magnetic micro-convection is studied numerically in the non-linear stage. Equations (2.7a,b) and (2.8) are solved by the spectral method in the vorticity–stream function formulation (Tan & Homsy 1988; Zimmerman & Homsy 1992). In order to apply the spectral method, the concentration and magnetostatic potential are presented as

$$c(x, y, t) = c_0(x, t) + c'(x, y, t), \quad (3.1)$$

and

$$\psi_m(x, y, t) = \psi_{m0}(x, t) + \psi'_m(x, y, t), \quad (3.2)$$

where

$$\psi_{m0}(x, t) = \int_{-\infty}^{+\infty} c_0(x - \xi, t) \ln(1 + \xi^{-2}) d\xi, \quad (3.3a)$$

$$\psi'_m(\mathbf{r}) = \int_S c'(\mathbf{r}', t) K(\mathbf{r} - \mathbf{r}', 1) dS'. \quad (3.3b)$$

The details of the numerical algorithm are described in appendix B.

The numerical algorithm is checked by the calculation of neutral curves of the magnetic micro-convection for several values of the characteristic smearing time  $t_0$ . To this end, the concentration perturbation is introduced by a small displacement  $\zeta(x, y)$  of isoline  $c = 0.5$  at  $x_0 = 0$ ,

$$c(x, y, t=0) = \frac{1}{2} \left( 1 - \operatorname{erf} \left( \frac{x - x_0}{\sqrt{4t_0}} \right) \right) + \zeta(x, y), \quad (3.4)$$

where

$$\zeta(x, y) = \sum_{n=1}^N \varepsilon_a e^{-k_n \sqrt{1 + \lambda_n / (k_n^2)} |x - x_0|} \cos(k_n y), \quad k_n = 2\pi n / L_y, \quad \varepsilon_a = 10^{-3}, \quad (3.5)$$

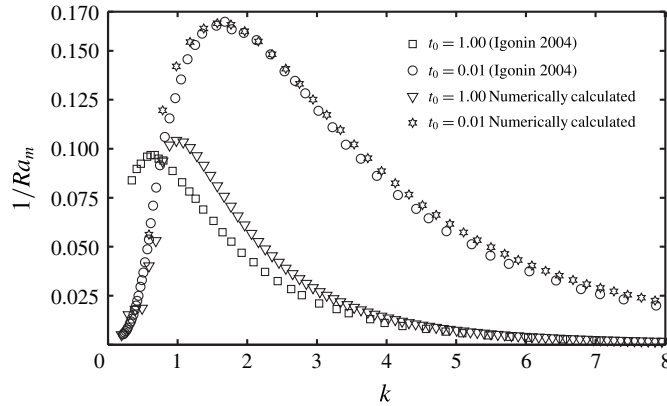


FIGURE 4. Neutral curves ( $\lambda = 0$ ) of the magnetic micro-convection for different values of the smearing parameters ( $t_0 = 0.01$  and  $t_0 = 1$ ). Triangles and stars show the present numerical results, while circles and squares are Igonin's numerical solution of the eigenvalue problem (Igonin 2004).

and  $\lambda_n$  is given by the dispersion relation (A 27) of appendix A for a fixed value of the magnetic Rayleigh number  $Ra_m$ . The concentration perturbation corresponds to the eigenfunction calculated in appendix A (relations (A 9), (A 10) for the zero smearing time). In order to calculate the neutral curves numerically, the Fourier coefficients  $\hat{c}_{mn}$  in (B 4a) of appendix B are calculated by two-dimensional fast Fourier transform of the concentration field and the growth increments  $\lambda$  are found as a function of the wavenumber  $k$  by matching the time dependence with  $\hat{c}_{0n}(t) = \hat{c}_{0n}(0)e^{\lambda t}$ . The neutral curves for definite values of the smearing parameter  $t_0$  are found by solving the equation  $\lambda(Ra_m^c, k) = 0$  by spline interpolation.

Figure 4 shows the numerically calculated neutral curves for two values of the smearing time  $t_0 = 0.01$  and  $t_0 = 1$ , together with those obtained in Igonin (2004) by numerical solution of the eigenvalue problem ((2.11) and (2.12)) at the same  $t_0$  value. From figure 4 we may conclude that the present numerical algorithm gives neutral curves in good agreement with the numerical calculations of (Igonin 2004) despite the small deviation at  $t_0 = 1$ , since eigenfunctions for sharp and smeared fronts for  $t_0 = 1$  are different.

### 3.2. Numerical results

The initial concentration perturbation at the interface is introduced by applying the relation (3.4) with  $\zeta(y)$  taken to be random. In numerical calculations over long times, typically  $1024 \times 512$  collocation points are used for the space discretization. The time step is typically  $\Delta t = 10^{-5}$  for  $Ra_m < 2000$  and  $\Delta t = 10^{-6}$  for  $Ra_m > 2000$ .

Fingering patterns for three values of magnetic Rayleigh numbers  $Ra_m = 500, 1500, 5000$  with a smearing parameter  $t_0 = 0.025$  are shown in figure 5. Initially, depending on the magnetic field intensity, well-resolved fingers are formed for  $Ra_m = 500$  at  $t = 0.02$  and for  $Ra_m = 5000$  at  $t = 0.002$ . Fingers expand due to the magnetic interaction between particles forming a stable boundary between the magnetic and non-magnetic phases. Simultaneously the bending instability of fingers develops at  $Ra_m = 500$  ( $t = 0.035$ ),  $Ra_m = 1500$  ( $t = 0.013$ ) and  $Ra_m = 5000$  ( $t = 0.002$ ). Finally the finger pattern smears out due to diffusion of magnetic particles, and in a strong magnetic field,

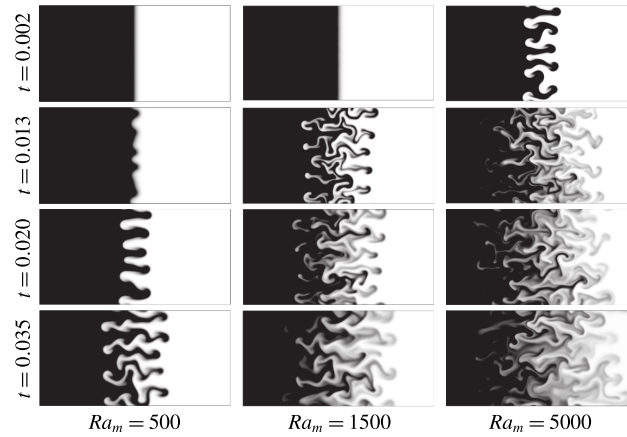


FIGURE 5. Concentration images for the magnetic Rayleigh number  $Ra_m = 500$ ,  $Ra_m = 1500$ ,  $Ra_m = 5000$  at time  $t = 0.002$ ,  $t = 0.013$ ,  $t = 0.02$ ,  $t = 0.035$  with  $L_x = 16$ ,  $L_y = 8$  and  $t_0 = 0.025$ .

$Ra_m = 1500$  ( $t = 0.02$ ,  $t = 0.035$ ) and  $Ra_m = 5000$  ( $t = 0.013$ ,  $t = 0.02$ ,  $t = 0.035$ ), the formation of new well-resolved larger fingers is observed. Fingering pattern dynamics, limited to the primary fingers, for  $Ra_m = 318$  and  $t_0 = 0.005$  can be seen in movie 1 in the supplementary material available at <http://dx.doi.org/10.1017/jfm.2015.255>.

The peculiarities of magnetic micro-convection in the non-linear stage are characterized via its Fourier spectrum dynamics. It is obtained from concentration plots with an ‘in-house’ data-processing algorithm, described in § 2 of the supplementary material. The characteristic size of the fingers is verified with a peak finding algorithm, described in § 3 of the supplementary material. The analysis is limited to the development of the primary fingers. To ease the comparison, the numerical simulation data are analysed in the same way as the experimental data in § 4.1.

Figures 6(a) and 6(b) show the Fourier spectrum dynamics of the magnetic micro-convection for the Brinkman and Darcy models, respectively, at  $Ra_m = 318$  and  $t_0 = 0.005$ , along with the experimental data (figure 6c), which will be discussed in § 4.1.1. We see that the spectrum of the wavenumbers in the pattern stays around a constant value  $\simeq 5$  at all times in the case of the Brinkman model. In comparison, the concentration pattern dynamics, as obtained in the framework of the Darcy model, has a much smaller scale at the beginning and shows different behaviour. Only around  $t = 0.1$  does it approach  $k \simeq 5$ .

A special algorithm is developed in order to calculate the velocity of fingers as a function of the magnetic Rayleigh number. A regular concentration perturbation by (3.4) with  $\zeta(y) = 0.25 \cos(ky)$  and the characteristic value of the wavenumber  $k = 4.19$  is used and its evolution with time is calculated. The finger velocity is found from the largest concentration gradient displacement over time. Figure 7 shows the velocity of the fingers as a function of time, calculated in the framework of both the Brinkman model and the Darcy model for two values of  $Ra_m$  (181 and 318), chosen for an easy comparison with the experiments considered below. It presents growth with subsequent decay due to the smearing out of the concentration pattern. Both the growth and the following decay are faster in Darcy’s framework. The emergence and decay of instability observed in numerical and physical experiments is similar to the development of normal field instability at the interface between the miscible magnetic

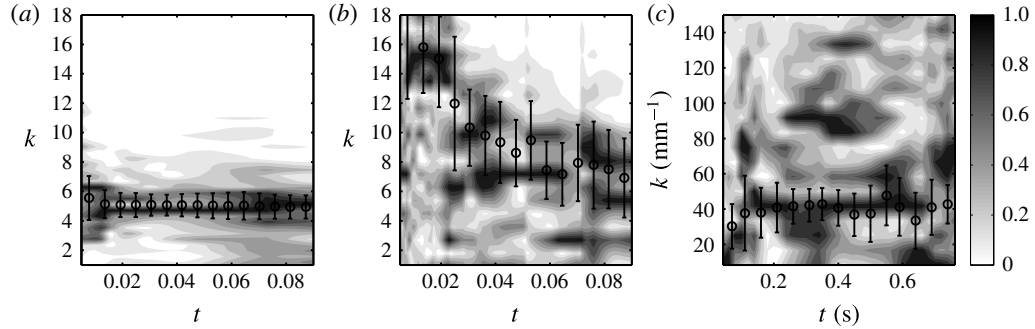


FIGURE 6. Analysis of the fingering pattern dynamics. The graphs show colour-coded greyscale contour plots of the Fourier coefficient dynamics. The average wavenumbers found by the peak finding algorithm are marked as circles with error bars. Results are shown for numerical simulation data at  $Ra_m = 318$  and  $t_0 = 0.005$  of (a) the Brinkman model, (b) the Darcy model and (c) the experimental data at  $H = 138$  Oe. The sizes of graphs are equal with respect to dimensionless quantities.

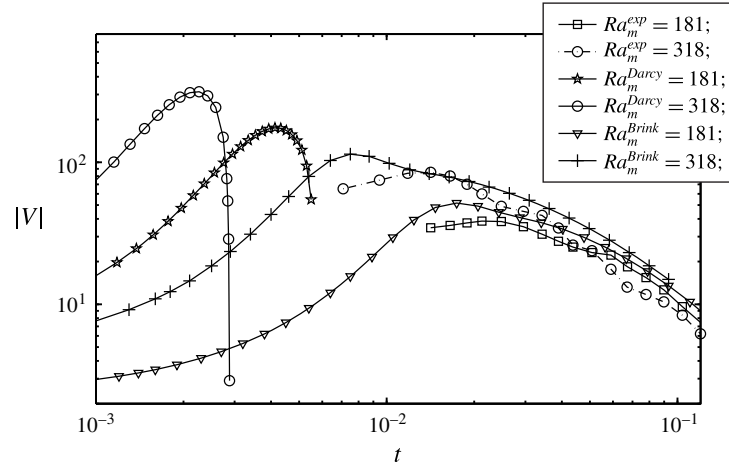


FIGURE 7. Finger velocity  $|V|$  as a function of time for two values of the magnetic Rayleigh number  $Ra_m$ . Data according to the Brinkman model: triangles,  $Ra_m = 181$ ; crosses,  $Ra_m = 318$ . Data according to the Darcy model: stars,  $Ra_m = 181$ ; open circles,  $Ra_m = 318$ . Experimental data: squares,  $Ra_m = 181$ ; open circles on a dot-dashed line,  $Ra_m = 318$ .

and non-magnetic fluids (Chen, Tsai & Miranda 2008). A peak initially formed on the interface after reaching its maximal amplitude further disappears due to the diffusion of magnetic particles. The maximum in Chen *et al.* (2008) was also obtained for the normalized mixing length in the case of confined liquids, which after reaching a maximum, decays due to the diffusion of magnetic nanoparticles.

It is interesting to remark that, for a regular concentration perturbation, a definite value of the magnetic Rayleigh number may be found at which the finger pattern exhibits chevron instability. The development of this zigzag pattern is shown in figure 8.

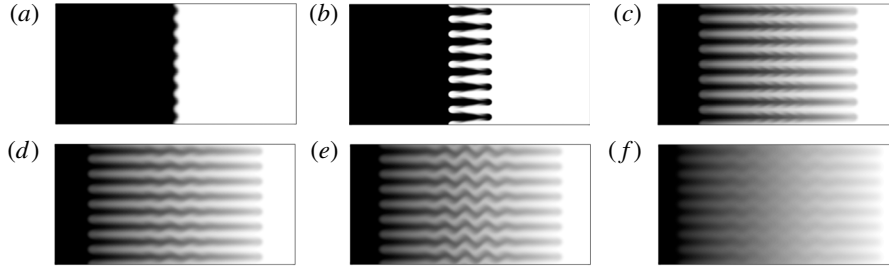


FIGURE 8. Development of chevron instability at a regular concentration perturbation for magnetic Rayleigh number  $Ra_m = 1200$ ,  $L_x = 24$ ,  $L_y = 12$ ,  $t_0 = 0.0137$ ,  $\Delta t = 0.00001$ , and (a)  $t = 0.001$ , (b)  $t = 0.007$ , (c)  $t = 0.085$ , (d)  $t = 0.12$ , (e)  $t = 0.145$ , (f)  $t = 0.27$ .

Numerical simulation makes it possible to study the finger formation between two miscible magnetic and non-magnetic fluids in detail. Figure 9 compares the concentration images, the velocity vector field, the absolute value of the concentration gradient and the vorticity distribution during the formation of two fingers. The initial concentration perturbation at the interface is introduced by random perturbation, the magnetic Rayleigh number being  $Ra_m = 500$ . The convection is caused by the ponderomotive forces due to the non-collinearity of the gradient of magnetic field and the gradient of concentration on the interface between fluids. Initially, at  $t = 0.00025$  (figure 9) a periodic system of vortices with different intensities is formed. The pair of (+, -) vortices increases the absolute value of the gradient of concentration, and as a result also increases the absolute value of the fluid velocity ( $t = 0.0025$ ). The velocity of fluids is maximal and fingers are formed ( $t = 0.01$ ) between the pairs of (+, -) vortices. The concentration gradient increases on the side boundaries of fingers ( $t = 0.0135$ ), causing rearrangement of the vorticity ( $t = 0.0175$ ) and formation of mushrooms on the plumes of the convective motion ( $t = 0.0275$ ).

#### 4. Experimental observation

The experimental study of magnetic micro-convection is performed by observing the instability dynamics at the interface of two miscible fluids in a Hele-Shaw cell with an optical microscope. The first fluid is distilled water. The second is a water-based magnetic fluid with maghemite ( $\gamma\text{-Fe}_2\text{O}_3$ ) particles that have an average diameter  $d = 7.0$  nm (polydispersity PDI = 0.33), saturation magnetization  $M_{sat} = 8.4$  G and an initial magnetic susceptibility  $\chi_m = 0.016$ , as determined by vibrating sample magnetometer magnetization measurements. Magnetic particles are synthesized by a coprecipitation method (Massart 1981) and stabilized with citrate ions, leading to a fluid density  $\rho_{mf} = 1.147$  g cm<sup>-3</sup> and particle volume fraction  $\phi = 2.9\%$ . An additional study in zero field of this water-magnetic fluid system with a jump of concentration (G. Kitenbergs, unpublished) shows that the effective diffusion coefficient is  $D = 5.4 \times 10^{-5}$  cm<sup>2</sup> s<sup>-1</sup>.

The experimental set-up, which is described in more detail in our recent publication (Kitenbergs *et al.* 2015), can be seen in figure 10. A Hele-Shaw cell (A) is made of two microscope glass slides and Parafilm M<sup>®</sup> spacers to form channels for fluids and air. The top glass slide has two drilled holes in which metallic tubes are glued for tubing connections (B) that come from syringes. Heating welds the glass slides and forms a Hele-Shaw cell with  $h = 120$   $\mu\text{m}$  thickness and  $5 \times 20$  mm

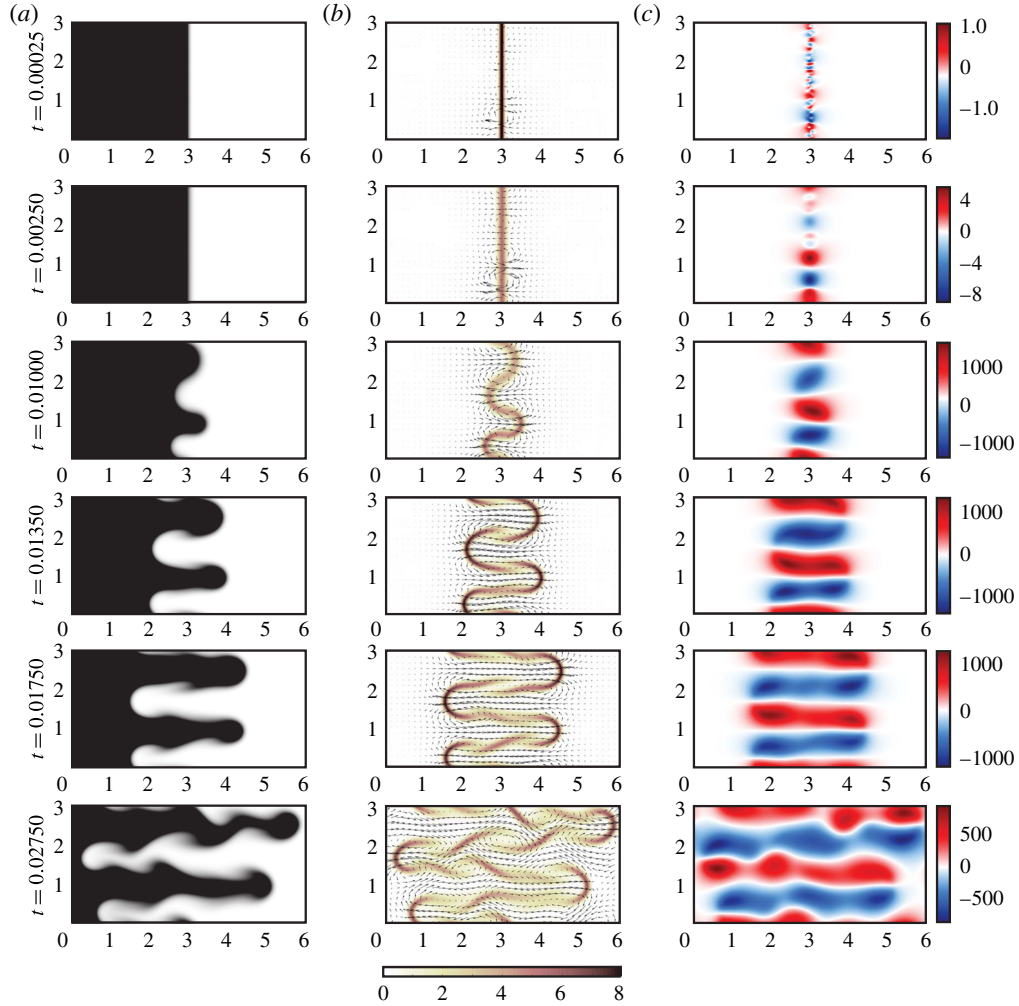


FIGURE 9. (Colour online) (a) Concentration images, (b) vector plots of the velocity field and absolute values of the concentration gradient, and (c) vorticity fields for a miscible magnetic and non-magnetic fluid in the Hele-Shaw cell. Numerical simulation snapshots correspond to the magnetic Rayleigh number  $Ra_m = 500$  at times  $t = 0.00025$ ,  $t = 0.0025$ ,  $t = 0.01$ ,  $t = 0.0135$ ,  $t = 0.0175$ ,  $t = 0.0275$ , with  $L_x = 6$ ,  $L_y = 3$  and  $t_0 = 0.025$ .

lateral size. The cell is placed on a microscope stage equipped with a coil system (C) made up of two identical coils, creating a homogeneous magnetic field up to  $H = 150$  Oe in the  $z$  direction. Water (D) is introduced into the cell with a syringe through tubing to fill the cell halfway. Magnetic fluid (E) is slowly introduced with a syringe pump until it meets the water and an interface is formed. This has significantly improved the control of interface formation, allowing us to keep the initial concentration smearing as small as possible. The initial concentration smearing corresponds to the smearing parameter  $t_0$ , which is crucial in numerical simulations. From a corresponding diffusion experiment (G. Kitenbergs, unpublished) performed in the same experimental set-up, we can estimate it to be  $t_0 \approx 0.05$  s, as it is impossible to extract it directly for each experiment. Instability development is observed with

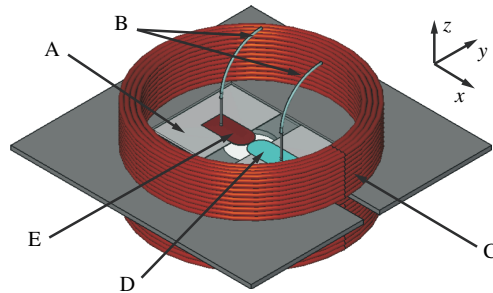


FIGURE 10. (Colour online) Scheme of the experimental set-up with (A) a Hele-Shaw cell, (B) tubing connections, (C) a coil system, (D) water and (E) magnetic fluid droplets.

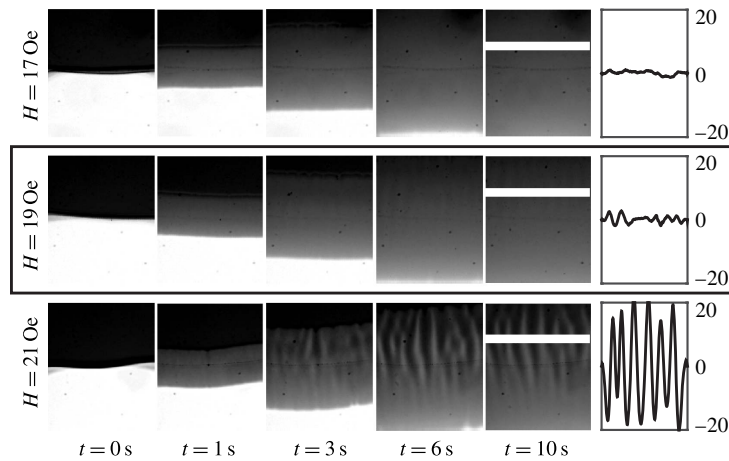


FIGURE 11. Experimental determination of the critical field (marked with a rectangle). Plots on the right-hand side show intensity values along the white lines at  $t = 10.0$  s in a.u., after applying two moving average filters to remove background and noise. At  $H = 19$  Oe a small but marked fingering pattern is visible, as compared to intensity fluctuations around the noise level at  $H = 17$  Oe. At  $H = 21$  Oe a well-developed fingering pattern is already visible.

an inverted microscope (Leica DMI 3000B,  $10\times$ , bright-field) and recorded with fast (Mikrotron MC1363, 50 Hz) and regular (Lumenera Lu165c, 15 Hz) cameras simultaneously.

Experiments are performed for various magnetic field values. The critical field at which the fingering pattern appears is here estimated to be  $H_{crit} = 19 \pm 1$  Oe, justified by the experimental images in figure 11. Further increase of the field, as can be seen in figure 12, at first leads to straight fingers becoming more pronounced. Above a less obvious second threshold ( $H \approx 40$  Oe), finger bending and splitting is observed. A further increase of the magnetic field causes the instability to develop more rapidly. At  $H = 138$  Oe, which is the largest magnetic field used in experiments, the primary fingers develop completely in less than a second (see also movie 3 in the supplementary material).

To describe the process quantitatively, several characteristics are retrieved with image analysis methods, and are explained below.

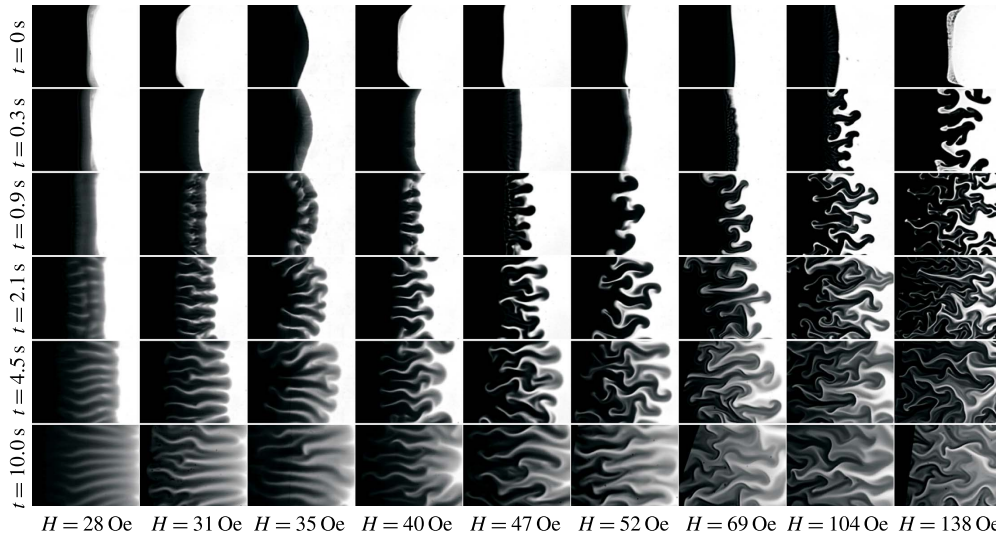


FIGURE 12. Experimental images of the magnetic micro-convection development for various magnetic field values. Each image is  $0.7 \text{ mm} \times 0.9 \text{ mm}$  in size.

#### 4.1. Experimental image analysis

The experimental snapshots in figure 12 clearly indicate a field dependence. We perform an analysis of the experimental data comparable to that of the numerical simulations, and we retrieve the characteristic Fourier coefficients and wavenumber of the instability pattern and also the primary finger velocities. This is done with ‘in-house’ image processing algorithms written in MATLAB.

To allow direct comparison with numerical simulations, the images from the two cameras are transformed into concentration fields. As cameras are used in the linear regime, where intensity is proportional to the number of photons, and magnetic particles absorb optical light, the conversion is done with the Beer–Lambert law. The intensities of initial concentrations that are needed for the calculation are found in the first images of each image series, separately for both cameras. The concentrations are also normalized with respect to the initial magnetic fluid concentration, so setting  $c_0 = 1$ . The coordinate systems of images from two cameras are linked via spatial calibration, which is done by cross-correlation of images of a fixed stage micrometer.

##### 4.1.1. Analysis of fingering pattern dynamics

An obvious parameter of the fingering instability is its spatial periodicity. We quantify it by finding the dynamics of the characteristic Fourier coefficients of the concentration profile along the initial fluid interface, using the algorithm explained in §2 of the supplementary material. As a result we get a colour-coded contour plot for each magnetic field value. The dynamics during the primary finger development at  $H = 138 \text{ Oe}$  is shown next to numerical simulation data in figure 6(c) and for several other magnetic fields in figure SM.2 in the supplementary material.

To verify the Fourier coefficient accuracy, an additional algorithm finds the average wavenumber dynamics in the same concentration profiles. It is based on peak finding and is explained in §3 in the supplementary material. The average wavenumbers are plotted as circles with error bars on the Fourier coefficient contour plots in figure 6(c) and SM.2 in the supplementary material.

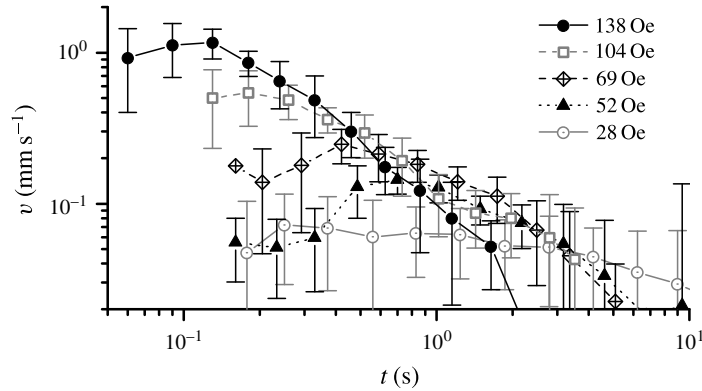


FIGURE 13. Finger velocity dynamics for several magnetic field values.

Three points are worth noting. First, the dominant Fourier coefficients and average wavenumbers match well, confirming that the two algorithms are working accurately. Second, the characteristic wavenumber stays constant during the development of the primary fingers. Deviations from this constant value are visible only at the very beginning of each experiment, due to the time needed for the formation of the fluid interface and the first notable finger tips. Most importantly, the characteristic wavenumbers are close to the same value,  $k \simeq 40\text{--}50 \text{ mm}^{-1}$ , for a wide range of magnetic fields ( $H = 19\text{--}138 \text{ Oe}$ ).

This wavenumber  $k$  corresponds to a characteristic wavelength  $\lambda \simeq 125\text{--}160 \text{ }\mu\text{m}$ . It is close to the cell thickness  $h$  and therefore consistent with earlier observations in Derec *et al.* (2008).

#### 4.1.2. Analysis of the finger velocities

To characterize the instability dynamics across the initial interface, we choose to find the primary finger velocity dynamics. Velocities are found by locating the displacement of the maximal concentration gradient on the primary finger trajectories. The algorithm is described in § 5 of the supplementary material.

In each experiment the velocity dynamics is retrieved for several fingers. Averaging over these fingers and logarithmic time spans gives the average velocity dynamics and its standard deviation as the error for each magnetic field. Several of them are shown in figure 13. Data indicate that for fields larger than  $H = 40 \text{ Oe}$  (corresponding to the second magnetic micro-convection threshold) the velocity first increases, reaching a maximum value  $v_{max}$  which is followed by a slower decay. For lower fields (data shown only for  $H = 28 \text{ Oe}$ ) the primary finger velocity first remains roughly constant without any well-pronounced maximum, and later slowly decreases.

We quantify the field dependence by comparing the average maximal velocities. We find the maximal velocity  $v_{max}$  for each finger and calculate the average value  $\bar{v}_{max}$  and its standard deviation for all magnetic fields. The average maximal velocity increases as a function of the magnetic field. It scales as  $H^2$ , thus as the Rayleigh number  $Ra_m$ . Data are shown in figure 14(a) as a function of the square of the magnetic field strength.

## 5. Discussion and comparison of experimental and theoretical results

Let us now compare the numerical simulations with the experimental results. The development of micro-convection depends on the magnetic Rayleigh number,

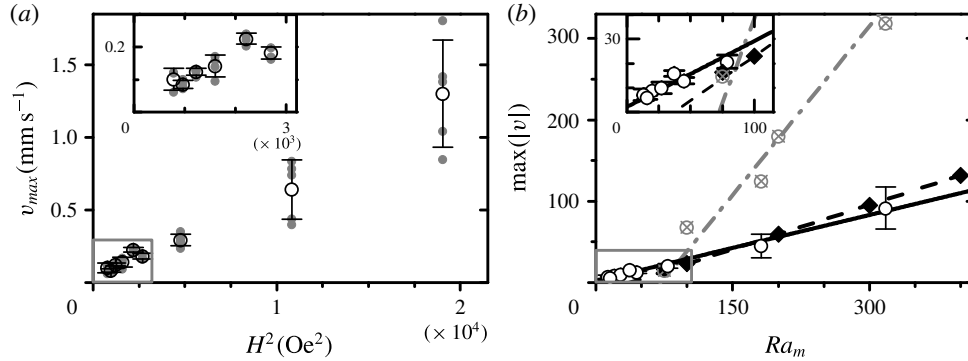


FIGURE 14. Maximal finger velocity. (a) Experimental data of the maximal finger velocity (grey dots) and average maximal velocity (empty circles with error bars) as a function of the square of the magnetic field strength. (b) Numerical simulation and experimental data with linear fits: the Brinkman model (black diamonds and a dashed line), the Darcy model (grey crossed open circles and a dash-dot line) and experimental data in dimensionless units (empty circles with error bars and a straight line) as a function of  $Ra_m$ . Fitted slopes and their uncertainties are  $0.36 \pm 0.01$ ,  $1.39 \pm 0.15$  and  $0.27 \pm 0.03$ . The two insets show the parts of the graphs marked with grey boxes in the main figures.

$Ra_m = M_0^2 h^2 / 12 \eta D$ . The threshold value of the field strength at the development of the magnetic micro-convection (figure 11) allows us to estimate the diffusion coefficient of the particles. For the critical magnetic Rayleigh number, given the maximum of data in figure 3, we choose the value  $Ra_m^{cr} = 6$  corresponding to  $t_0 = 0$ ; we obtain  $D = 1.7 \times 10^{-5} \text{ cm}^2 \text{ s}^{-1}$  for the diffusion coefficient of the particles – a value of the same order of magnitude as that found above from the independent measurements of the diffusion profile in zero field. Note that it is much larger than the value calculated according to Einstein’s formula  $k_B T / 3 \pi \eta d \simeq 6 \times 10^{-7} \text{ cm}^2 \text{ s}^{-1}$ . It may be related to an electric field originating from the gradient of ionic species at the interface and able to modify the diffusion process. This will be studied in a separate publication (G. Kitenbergs, unpublished). Taking  $t_0 = 0$  for this estimate corresponds to experimental observations with a smearing time of the diffusion front equal to 0.05 s, which in dimensionless units is approximately  $5.7 \times 10^{-3}$  and is close to zero.

A qualitative visual comparison can be done by watching the three movies in the supplementary material, which correspond to the Brinkman model (movie 1), the Darcy model (movie 2) and the experimental data (movie 3) at  $Ra_m = 318$ . The movies are created so that the fields of view and the durations are the same with respect to dimensionless quantities. More details can be found in § 1 in the supplementary material.

The Fourier spectra dynamics of the concentration perturbations are shown in figure 6. To simplify the comparison, the plot sizes are equalized with respect to the dimensionless quantities. For the experimental data (figure 6c), the characteristic pattern wavenumber gives  $k \simeq 40 \text{ mm}^{-1}$ . Multiplying it by the thickness of the Hele-Shaw cell  $h = 120 \text{ }\mu\text{m}$ , we find  $kh \simeq 5$  in dimensionless units, which is in good agreement with the numerical simulation data in the frame of the Brinkman model, visible in figure 6(a) and with the linear analysis. In contrast, the Darcy model figure 6(b) predicts an initial pattern with a much smaller scale and faster dynamics.

Finger velocities and their time dependence also agree well. Both numerical and experimental data in figure 7 show non-monotonic time dependence of the finger velocity. The Darcy model predicts faster growth and decay of the finger velocity than observed experimentally and found in the framework of the Brinkman model.

A quantitative comparison of the magnetic micro-convection field-dependence is done by comparing the maximal primary finger velocity as a function of the magnetic Rayleigh number. The experimental data (figure 14a), after conversion to non-dimensional units, show good agreement with the numerical data obtained in the framework of the Brinkman model (figure 14b). The slope 0.27 obtained experimentally for the linear dependence of  $\max(|v|)$  as a function of  $Ra_m$  is close to the value 0.36 for the Brinkman model and quite far from the value 1.39 in the frame of the Darcy model. The numerical values of the finger velocities are also similar. For example, the characteristic value of the finger velocity at  $H = 104$  Oe is  $0.64 \text{ mm s}^{-1}$ . In dimensionless units, it corresponds to 45 at  $Ra_m = 181$ , which is close to the value 59 obtained with the Brinkman model and very different from the value 180 obtained with the Darcy model for  $Ra_m = 200$  (see figure 14b).

Both in numerical simulation and experiment (data not shown), if the magnetic Rayleigh number is large enough, the relation  $v_{max}t_{max} \simeq 1$  (in dimensionless units) holds with good accuracy, where  $t_{max}$  is the time interval at which the maximal finger velocity is established. This corresponds to the scaling  $v_{max} = h\tau_D^{-1}Ra_m$  and  $t_{max} = \tau_D/Ra_m$ .

The development of micro-convection as shown by the numerical simulations (see figure 5,  $t = 0.035$ ,  $Ra_m = 500$ ) has the same features as those observed in experiments (figure 12,  $35 \text{ Oe} < H < 40 \text{ Oe}$ ). In both numerical simulations and experiments we observe the formation of mushrooms, which, as shown by numerical calculation, are connected with the dynamics of vortices at the development of micro-convection (figure 9). We should point out that this feature was not observed in the numerical simulations carried out in the Darcy approximation (Erglis *et al.* 2013).

Another interesting feature observed both in numerical simulations (figure 5) and in experiments (figure 12) is the bending instability of fingers, which leads to the formation of chevron patterns in the numerical simulations (figure 8). Formation of chevron patterns in thin ferromagnetic films (Seul & Wolfe 1992) and stripe patterns of ferrofluids (Flament *et al.* 1996) occur if the distance between the stripes is larger than the equilibrium one. Development of chevrons in the case shown in figure 8 occurs by rearrangement of vortices responsible for the formation of fingers. The field strength  $H_{ch}$  at which the chevron formation is observed in numerical simulation is  $H_{ch}/H_c \simeq 5.5$ ; this ratio is slightly larger than that observed in the experiment  $\simeq 2.5$  (figure 12).

## 6. Conclusions

The numerical simulation and experimental study of the magnetic micro-convection carried out here show good qualitative and quantitative agreement. The application of the Brinkman model allows us to explain several quantitative and qualitative features of the magnetic micro-convection, which was not possible with the Darcy model. Rearrangements of the vortex patterns at the development of magnetic micro-convection are responsible for the formation of mushrooms on the plumes of micro-convective flows and their chevron-like instabilities. The non-monotonic time dependence of the finger velocities, which exhibits the development of micro-convection when the magnetic field strength is larger than the threshold value, and its subsequent decay due to particle diffusion, may be quantitatively described by the Brinkman model. The Darcy model predicts much faster growth and decay

of instability than observed in the experiments. The dependence of the maximal finger velocity on the magnetic Rayleigh number calculated in the framework of the Brinkman model is in better quantitative agreement with experimental data than that calculated according to the Darcy model. A similar conclusion is valid with respect to the Fourier spectrum dynamics of the concentration field. The estimate of the particle diffusion coefficient from the experimentally determined threshold value of the field strength gives a value larger than expected for thermally driven diffusion processes by two orders of magnitude. This could be connected to the charge of the magnetic particles and other free species in the water-based fluid used, which will be studied in detail separately.

### Acknowledgements

G.K.'s research was supported by European Social Fund Project 2013/0028/1DP/1.1.1.2.0/13/APIA/VIAA/054. The authors are grateful to M. M. Maiorov for magnetic measurements.

### Supplementary movies

Supplementary movies are available at <http://dx.doi.org/10.1017/jfm.2015.255>.

### Appendix A

In the limit  $t_0 \rightarrow 0$ ,  $\partial \psi_{m0}(x, 0)/\partial x = -\ln(1+x^{-2})$  and the equations for the velocity component  $u'_x$  and concentration perturbations (2.11), (2.12) read

$$\left(\frac{d^2}{dx^2} - k^2\right)^2 u'_x - 12 \left(\frac{d^2}{dx^2} - k^2\right) u'_x - 24k^2 Ra_m \ln(1+x^{-2})c' = 0, \quad (\text{A } 1)$$

$$(\lambda + k^2)c' - \frac{d^2 c'}{dx^2} = 0. \quad (\text{A } 2)$$

The boundary conditions at the discontinuity of the concentration  $c_0$  are given by continuity of the concentration perturbation, tangential and normal to the front velocity components and their derivatives:

$$c'(0^+) - c'(0^-) = 0, \quad (\text{A } 3)$$

$$u'_x(0^+) - u'_x(0^-) = 0, \quad (\text{A } 4)$$

$$\frac{du'_x}{dx}(0^+) - \frac{du'_x}{dz}(0^-) = 0, \quad (\text{A } 5)$$

$$\frac{d^2 u'_x}{dx^2}(0^+) - \frac{d^2 u'_x}{dx^2}(0^-) = 0. \quad (\text{A } 6)$$

The two remaining boundary conditions at the discontinuity are obtained by integration  $\int_{-\delta}^{\delta} (\dots) dx$  of (A 1) and (A 2) across the diffusion layer and taking the limit  $\delta \rightarrow 0$ , which gives

$$\frac{dc'}{dx}(0^+) - \frac{dc'}{dx}(0^-) = -c_0 u'_x(0), \quad (\text{A } 7)$$

$$\frac{d^3 u'_x}{dx^3}(0^+) - \frac{d^3 u'_x}{dx^3}(0^-) = -24k^2 Ra_m \psi'_m(0). \quad (\text{A } 8)$$

From (A 2), boundary condition (A 3) for concentration  $c'$ , and taking into account conditions at infinity  $c'(\infty) = 0$ ,  $c'(-\infty) = 0$ , it follows that

$$c'|_{x<0} = Qe^{\sqrt{\lambda+k^2}x}, \quad (\text{A } 9)$$

$$c'|_{x>0} = Qe^{-\sqrt{\lambda+k^2}x}. \quad (\text{A } 10)$$

The general solution of (A 1) reads

$$u'_x = \tilde{A}_1(x)e^{kx} + \tilde{B}_1(x)e^{-kx} + \tilde{C}_1(x)e^{\sqrt{k^2+12}x} + \tilde{D}_1(x)e^{-\sqrt{k^2+12}x}, \quad (\text{A } 11)$$

where the functions  $\tilde{A}_1$ ,  $\tilde{B}_1$ ,  $\tilde{C}_1$ ,  $\tilde{D}_1$  are given by the solution of the set of linear differential equations

$$\frac{d\tilde{A}_1}{dx}e^{kx} + \frac{d\tilde{B}_1}{dx}e^{-kx} + \frac{d\tilde{C}_1}{dx}e^{kmx} + \frac{d\tilde{D}_1}{dx}e^{-kmx} = 0, \quad (\text{A } 12)$$

$$\frac{d\tilde{A}_1}{dx}e^{kx} - \frac{d\tilde{B}_1}{dx}e^{-kx} + m\frac{d\tilde{C}_1}{dx}e^{kmx} - m\frac{d\tilde{D}_1}{dx}e^{-kmx} = 0, \quad (\text{A } 13)$$

$$\frac{d\tilde{A}_1}{dx}e^{kx} + \frac{d\tilde{B}_1}{dx}e^{-kx} + m^2\frac{d\tilde{C}_1}{dx}e^{kmx} + m^2\frac{d\tilde{D}_1}{dx}e^{-kmx} = 0, \quad (\text{A } 14)$$

$$\frac{d\tilde{A}_1}{dx}e^{kx} - \frac{d\tilde{B}_1}{dx}e^{-kx} + m^3\frac{d\tilde{C}_1}{dx}e^{kmx} - m^3\frac{d\tilde{D}_1}{dx}e^{-kmx} = \frac{24}{k}Ra_m \ln(1+x^{-2})c'(x). \quad (\text{A } 15)$$

Its solution reads

$$\tilde{A}_1|_{x<0} = -kRa_mQg(-k(s-1), x) + A_1, \quad (\text{A } 16)$$

$$\tilde{A}_1|_{x>0} = -kRa_mQg(k(s+1), x) + A_2, \quad (\text{A } 17)$$

$$\tilde{B}_1|_{x<0} = kRa_mQg(-k(s+1), x) + B_1, \quad (\text{A } 18)$$

$$\tilde{B}_1|_{x>0} = kRa_mQg(k(s-1), x) + B_2, \quad (\text{A } 19)$$

$$\tilde{C}_1|_{x<0} = \frac{k}{m}Ra_mQg(-k(s-m), x) + C_1, \quad (\text{A } 20)$$

$$\tilde{C}_1|_{x>0} = \frac{k}{m}Ra_mQg(k(s+m), x) + C_2, \quad (\text{A } 21)$$

$$\tilde{D}_1|_{x<0} = -\frac{k}{m}Ra_mQg(-k(s+m), x) + D_1, \quad (\text{A } 22)$$

$$\tilde{D}_1|_{x>0} = -\frac{k}{m}Ra_mQg(k(s-m), x) + D_2, \quad (\text{A } 23)$$

where  $m = \sqrt{1+12/k^2}$ ,  $s = \sqrt{1+\lambda/k^2}$  and

$$g(a, z) = \int_0^z e^{-a\zeta} \ln(1+\zeta^{-2}) d\zeta, \quad g(a, -z) = -g(-a, z). \quad (\text{A } 24a,b)$$

As a result,

$$\begin{aligned} u'_x|_{x<0} &= A_1 e^{kx} + B_1 e^{-kx} + C_1 e^{kmx} + D_1 e^{-kmx} \\ &\quad - kRa_m Qg(-k(s-1), x)e^{kx} + kRa_m Qg(-k(s+1), x)e^{-kx} \\ &\quad + \frac{k}{m} Ra_m Qg(-k(s-m), x)e^{kmx} - \frac{k}{m} Ra_m Qg(-k(s+m), x)e^{-kmx}, \end{aligned} \quad (\text{A } 25)$$

$$\begin{aligned} u'_x|_{x>0} &= A_2 e^{kx} + B_2 e^{-kx} + C_2 e^{kmx} + D_2 e^{-kmx} \\ &\quad - kRa_m Qg(k(s+1), x)e^{kx} + kRa_m Qg(k(s-1), x)e^{-kx} \\ &\quad + \frac{k}{m} Ra_m Qg(k(s+m), x)e^{kmx} - \frac{k}{m} Ra_m Qg(k(s-m), x)e^{-kmx}. \end{aligned} \quad (\text{A } 26)$$

Boundary conditions (A 3) and the vanishing perturbation conditions at infinity give the set of linear algebraic equations, of which the condition of solubility gives the dispersion equation for the growth increment of perturbations:

$$sk + Ra_m \left( 2 \frac{m-1}{m} J(s, k) + k \left[ \frac{g(k(s+m), \infty)}{m} - g(k(s+1), \infty) \right] \right) = 0, \quad (\text{A } 27)$$

where the function  $J(p, q)$  is defined by the integral

$$J(p, q) = \int_0^\infty e^{-pz} \left( K_0(z) - K_0 \left( \sqrt{z^2 + q^2} \right) \right) dz. \quad (\text{A } 28)$$

## Appendix B

Introducing the stream function  $\psi$  via  $u_x = \partial\psi/\partial y$  and  $u_y = -\partial\psi/\partial x$ , and the vorticity  $\omega = -\Delta\psi$  allows us to rewrite the convection–diffusion equation (2.8) as

$$\frac{\partial c'}{\partial t} = \frac{\partial^2 c'}{\partial x^2} + \frac{\partial^2 c'}{\partial y^2} - \frac{\partial\psi}{\partial y} \left( \frac{\partial c_0}{\partial x} + \frac{\partial c'}{\partial x} \right) + \frac{\partial\psi}{\partial x} \frac{\partial c'}{\partial y}. \quad (\text{B } 1)$$

Equation (2.7a,b) gives the vorticity equation

$$\omega = -\frac{1}{12} \Delta^2 \psi - 2Ra_m \left( \frac{\partial\psi_m}{\partial y} \left[ \frac{\partial c_0}{\partial x} + \frac{\partial c'}{\partial x} \right] - \frac{\partial\psi_m}{\partial x} \frac{\partial c'}{\partial y} \right). \quad (\text{B } 2)$$

Integration in (3.3a) is carried out through all of the infinite region occupied by the magnetic fluid. The fast decay of the field strength  $\partial\psi_{m0}/\partial x$  with distance from the diffusion front justifies the use of periodic boundary conditions. Integration in (3.3b) is carried out along the cell with dimensions  $L_x$  and  $L_y$ .

The Fourier component of  $\partial\psi_{m0}/\partial x$  is obtained using the convolution theorem:

$$\frac{\partial \hat{\psi}_{m0}}{\partial x}(q_m) = 2\pi \frac{\partial \hat{c}_0}{\partial x}(q_m) \frac{1 - e^{-|q_m|}}{|q_m|}, \quad (\text{B } 3)$$

where the Fourier coefficients  $\partial \hat{c}_0/\partial x$  are calculated by a one-dimensional fast Fourier transform (the domain size is increased in the  $x$  direction from  $L_x$  to  $4L_x$  to eliminate the Gibbs phenomenon).

The concentration perturbation  $c'$ , the stream function  $\psi$  and the vorticity  $\omega$  are presented by the Fourier series

$$c'(x, y, t) = \sum_{m=0}^{M-1} \sum_{n=0}^{N-1} \hat{c}_{mn}(t) e^{i(q_m x + k_n y)}, \quad (\text{B } 4a)$$

$$\psi(x, y, t) = \sum_{m=0}^{M-1} \sum_{n=0}^{N-1} \hat{\psi}_{mn}(t) e^{i(q_m x + k_n y)}, \quad (\text{B } 4b)$$

$$\omega(x, y, t) = \sum_{m=0}^{M-1} \sum_{n=0}^{N-1} \hat{\omega}_{mn}(t) e^{i(q_m x + k_n y)}, \quad (\text{B } 4c)$$

where  $q_m = (2\pi m)/L_x$ ,  $k_n = (2\pi n)/L_y$  are wavenumbers ( $m, n = 0, 1, 2, \dots$ ). Functions  $\hat{c}_{mn}$ ,  $\hat{\psi}_{mn}$  and  $\hat{\omega}_{mn}$  are calculated by using fast Fourier transform in collocation points  $x_m = (L_x/M)m$  and  $y_n = (L_y/N)n$  ( $m = 0, 1, 2, \dots, M-1$ ,  $n = 0, 1, 2, \dots, N-1$ ). The total number of collocation points  $N, M$  is proportional to  $2^p$ ,  $p = 1, 2, 3, \dots$ , and depend on the concrete case.

The non-linear terms in (B 1) and (B 2) are given by applying the fast Fourier transform:

$$J(x, y, t) = \frac{\partial \psi}{\partial y} \left( \frac{\partial c_0}{\partial x} + \frac{\partial c'}{\partial x} \right) - \frac{\partial \psi}{\partial x} \frac{\partial c'}{\partial y} = \sum_{m=0}^{M-1} \sum_{n=0}^{N-1} \hat{J}_{mn}(t) e^{i(q_m x + k_n y)}, \quad (\text{B } 5a)$$

$$Q(x, y, t) = \frac{\partial \psi_m}{\partial y} \left( \frac{\partial c_0}{\partial x} + \frac{\partial c'}{\partial x} \right) - \frac{\partial \psi_m}{\partial x} \frac{\partial c'}{\partial y} = \sum_{m=0}^{M-1} \sum_{n=0}^{N-1} \hat{Q}_{nm}(t) e^{i(q_m x + k_n y)}. \quad (\text{B } 5b)$$

As a result, the equations for the amplitudes of the Fourier modes read

$$\hat{\omega}_{mn} = (q_m^2 + k_n^2) \hat{\psi}_{mn}, \quad (\text{B } 6)$$

$$\hat{\omega}_{mn} = -\frac{(q_m^2 + k_n^2)^2}{12} \hat{\psi}_{mn} - 2R a_m \hat{Q}_{mn}, \quad (\text{B } 7)$$

$$\frac{\partial \hat{c}_{mn}}{\partial t} = -(q_m^2 + k_n^2) \hat{c}_{mn} - \hat{J}_{mn}. \quad (\text{B } 8)$$

The values of the stream function  $\psi(t_j)$  for given values of the concentration  $c(t_j)$  are found from (B 6) and (B 7). Since  $\psi'_m$  is periodic in both the  $x$  and  $y$  directions,  $\hat{\psi}'_m(\mathbf{k})$  is obtained as follows:

$$\hat{\psi}'_m(\mathbf{k}) = 2\pi \hat{c}_{mn}(\mathbf{k}) \hat{T}_{mn}(\mathbf{k}), \quad (\text{B } 9)$$

where  $\mathbf{k} = (q_m, k_n)$  is the two-dimensional wavevector and  $|\mathbf{k}| = \sqrt{q_m^2 + k_n^2}$ . The Fourier coefficients  $\hat{c}_{mn}$  are calculated by a two-dimensional fast Fourier transform algorithm, and  $\hat{T}_{mn}(\mathbf{k}) = (1 - e^{-|\mathbf{k}|})/|\mathbf{k}|$  is the Fourier transform of  $K(\mathbf{r}, 1)$ . All derivatives of  $\psi'_m$  are calculated spectrally from the obtained values of  $\hat{\psi}'_m(\mathbf{k})$ .

The linear equation (B 8) is solved for the known stream function by applying the linear propagator method, which factors out the leading-order linear term prior to the discretization. Introducing  $\hat{\chi}_{mn} = e^{(q_m^2 + k_n^2)t} \hat{c}_{mn}$ , the equation  $(\partial \hat{\chi}_{mn})/(\partial t) = -e^{(q_m^2 + k_n^2)t} \hat{J}_{mn}$

is discretized by using the three-step Adams–Bashforth method (Samarskij & Gulin 1989). The result reads

$$\hat{c}_{mn}^{(j+1)*} = \hat{c}_{mn}^j \gamma - \frac{\Delta t}{12} (23\hat{J}_{mn}^j \gamma - 16\hat{J}_{mn}^{(j-1)} \gamma^2 + 5\hat{J}_{mn}^{(j-2)} \gamma^3), \quad (\text{B } 10)$$

$$\gamma = e^{-(q_m^2 + k_n^2)\Delta t}. \quad (\text{B } 11)$$

Further, corrected values of  $\psi_{mn}^{(j+1)*}$  and  $\hat{J}_{mn}^{(j+1)*}$  are found from (B 6), (B 7) and (B 5a), respectively. As a result the Fourier components of the concentration are obtained for the next time step:

$$\hat{c}_{mn}^{(j+1)} = \hat{c}_{mn}^j - \frac{\Delta t}{2} (\hat{J}_{mn}^{(j+1)*} + \hat{J}_{mn}^j) - \frac{\Delta t}{2} (q_m^2 + k_n^2) (\hat{c}_{mn}^{(j+1)*} + \hat{c}_{mn}^j). \quad (\text{B } 12)$$

The concentration field is obtained by applying the inverse fast Fourier transform to  $\hat{c}_{mn}^{(j+1)}$  and adding  $c_0(t)$ . Since the numerical scheme used is not fully implicit in time, the solution may show numerical instability.

#### REFERENCES

- BISCHOFBERGER, I., RAMACHANDRAN, R. & NÄGEL, S. R. 2014 Fingering versus stability in the limit of zero interfacial tension. *Nat. Commun.* **5**, 5265.
- CEBERS, A. 1981 Dynamics of magnetostatic instabilities. *Magnetohydrodynamics* **17**, 113–121.
- CEBERS, A. 1997 Stability of diffusion fronts of magnetic particles in porous media under the action of external magnetic field. *Magnetohydrodynamics* **33**, 48–55.
- CEBERS, A. & MAIOROV, M. M. 1980 Magnetostatic instabilities in plane layers of magnetizable liquids. *Magnetohydrodynamics* **16** (1), 21–27.
- CHEN, C.-Y. 2003 Numerical simulations of fingering instabilities in miscible magnetic fluids in a Hele-Shaw cell and the effects of Korteweg stresses. *Phys. Fluids* **15** (4), 1086–1089.
- CHEN, C.-Y., TSAI, W. K. & MIRANDA, J. A. 2008 Hybrid ferrohydrodynamic instability: coexisting peak and labyrinthine patterns. *Phys. Rev. E* **77**, 056306.
- CHEN, C.-Y. & WEN, C.-Y. 2002 Numerical simulations of miscible magnetic flows in a Hele-Shaw cell: radial flows. *J. Magn. Magn. Mater.* **252**, 296–298.
- DEREC, C., BOLTENHAGEN, P., NEVEU, S. & BACRI, J.-C. 2008 Magnetic instability between miscible fluids in a Hele-Shaw cell. *Magnetohydrodynamics* **44** (2), 135–142.
- ERGLIS, K., TATULCENKOV, A., KITENBERGS, G., PETRICHENKO, O., ERGIN, F. G., WATZ, B. B. & CEBERS, A. 2013 Magnetic field driven micro-convection in the Hele-Shaw cell. *J. Fluid Mech.* **714**, 612–633.
- FLAMENT, C., BACRI, J.-C., CEBERS, A., ELIAS, F. & PERZYNSKI, R. 1996 Parallel stripes of ferrofluid as a macroscopic bidimensional smectic. *Europhys. Lett.* **34** (3), 225–230.
- GOYAL, N. & MEIBURG, E. 2006 Miscible displacements in Hele-Shaw cells: two-dimensional base states and their linear stability. *J. Fluid Mech.* **558**, 329–355.
- IGONIN, M. 2004 Hydrodynamic instabilities of miscible and immiscible magnetic fluids in a Hele-Shaw cell. PhD dissertation, Université Paris 7 – Denis Diderot.
- IGONIN, M. & CEBERS, A. 2003 Labyrinthine instability of miscible magnetic fluids. *Phys. Fluids* **15**, 1734–1744.
- JACKSON, D. P., GOLDSTEIN, R. E. & CEBERS, A. O. 1994 Hydrodynamics of fingering instabilities in dipolar fluids. *Phys. Rev. E* **50**, 298–307.
- KITENBERGS, G., ERGLIS, K., PERZYNSKI, R. & CEBERS, A. 2015 Magnetic particle mixing with magnetic micro-convection for microfluidics. *J. Magn. Magn. Mater.* **380**, 227–230.
- MAIOROV, M. M. & CEBERS, A. 1983 Magnetic microconvection on the diffusion front of ferroparticles. *Magnetohydrodynamics* **19** (4), 376–380.

- MASSART, R. 1981 Preparation of aqueous magnetic liquids in alkaline and acidic media. *IEEE* **17**, 1247–1248.
- MEZULIS, A. & BLUMS, E. 2005 Experimental investigations of the microconvective instability in optically induced gratings. *Magnetohydrodynamics* **41** (4), 341–348.
- SAMARSKIJ, A. A. & GULIN, A. V. 1989 *Numerical Methods*. Nauka.
- SEUL, M. & WOLFE, R. 1992 Evolution of disorder in magnetic stripe domains. Part I. Transverse instabilities and disclination unbinding in lamellar patterns. *Phys. Rev. A* **46**, 7519–7533.
- TAN, C. T. & HOMSY, G. M. 1988 Simulation of nonlinear viscous fingering in miscible displacement. *Phys. Fluids* **31**, 1330–1338.
- TRUZZOLILLO, D., MORA, S., DUPAS, C. & CIPELLETTI, L. 2014 Off-equilibrium surface tension in colloidal suspensions. *Phys. Rev. Lett.* **112**, 128303.
- WEN, C.-Y., CHEN, C.-Y. & KUAN, D. C. 2007 Experimental studies of labyrinthine instabilities of miscible ferrofluids in a Hele-Shaw cell. *Phys. Fluids* **19**, 084101.
- ZABLOTSKY, D. 2012 Microconvective effects in non-isothermal and inhomogeneous dispersions of magnetic nanoparticles. PhD dissertation, University of Latvia.
- ZIMMERMAN, W. B. & HOMSY, G. M. 1992 Viscous fingering in miscible displacements: unification of effects of viscosity contrast, anisotropic dispersion, and velocity dependence of dispersion on nonlinear finger propagation. *Phys. Fluids* **4** (11), 2348–2359.



## Magnetic particle mixing with magnetic micro-convection for microfluidics



Guntars Kitenbergs<sup>a,b,c,\*</sup>, Kaspars Ērglis<sup>a</sup>, Régine Perzynski<sup>b,c</sup>, Andrejs Cēbers<sup>a</sup>

<sup>a</sup> MML Lab, Department of Theoretical Physics, University of Latvia, Zeļļu 8, LV-1002 Rīga, Latvia

<sup>b</sup> Sorbonne Universités, UPMC Univ Paris 06, UMR 8234, PHENIX, 4 place Jussieu, F-75005 Paris, France

<sup>c</sup> CNRS, UMR 8234, PHENIX, 4 place Jussieu, F-75005 Paris, France

### ARTICLE INFO

#### Article history:

Received 30 June 2014

Received in revised form

29 September 2014

Accepted 4 October 2014

Available online 18 October 2014

#### Keywords:

Microfluidics

Mixing

Magnetic fluid

Ferrofluid

Magnetic micro-convection

Diffusion

### ABSTRACT

In this paper we discuss the magnetic micro-convection phenomenon as a tool for mixing enhancement in microfluidics systems in cases when one of the miscible fluids is a magnetic particle colloid. A system of a water-based magnetic fluid and water is investigated experimentally under homogeneous magnetic field in a Hele–Shaw cell. Subsequent image analysis both qualitatively and quantitatively reveals the high enhancement of mixing efficiency provided by this method. The mixing efficiency dependence on the magnetic field and the physical limits is discussed. A suitable model for a continuous-flow microfluidics setup for mixing with magnetic micro-convection is also proposed and justified with an experiment. In addition, possible applications in improving the speed of ferrohydrodynamic sorting and magnetic label or selected tracer mixing in lab on a chip systems are noted.

© 2014 Elsevier B.V. All rights reserved.

### 1. Introduction

Over the last 15 years the field of microfluidics has continuously advanced, providing an interesting framework for various applications and scientific studies. As these systems typically have a small Reynolds number, a lot of effort has been devoted to enhance mixing, which is otherwise limited by diffusion speed [1], causing long channel lengths. Mixers in microfluidics can be divided into passive and active, where the latter need an external energy supply [2]. A convenient energy source for active mixing systems is an external magnetic field, as the energy can be transmitted to the microfluidics chip or cell without direct connectors. It is particularly interesting for systems with magnetic particles. Magnetic fluid, being a colloidal dispersion of magnetic particles, can be used as a model system for future applications. Several examples of magnetic and non-magnetic fluid mixing have already been demonstrated [3,4]. Here we evaluate the possible use of the magnetic micro-convection phenomenon for mixing applications, applying the knowledge obtained in previous theoretical and experimental studies [5,6].

### 2. Theory, materials and methods

Magnetic micro-convection, first described in 1980s [7], is caused by a ponderomotive force of the non-homogeneous self-magnetic field of the magnetic fluid. Above a certain magnetic field threshold, an instability forms on the magnetic/non-magnetic fluid interface. A characteristic fingering pattern results from the magnetic particle flow induced by the acting force, pushing magnetic particles into the non-magnetic liquid. This force depends on particle concentration gradient, which decreases with mixing time as a result of the ongoing particle diffusion. Here we will focus on the practical application of the magnetic micro-convection, whereas more information on the fundamental aspects can be found in our previous studies [5,6].

Experimentally magnetic micro-convection is tested in a Hele–Shaw cell as a microfluidics model system. It is placed on a stage with a coil system in an inverted microscope (Leica DMI3000B) with a 10× magnification (see Fig. 1). The coil system (Fig. 1(1)) consists of two identical coils that are 19 mm high and have inner and outer diameters of  $d_{in} = 45$  mm and  $d_{out} = 57$  mm, respectively. Each coil has 200 turns of copper wire with a diameter  $d = 0.7$  mm. Coils are fixed on both sides of a microscope stage (1 mm thick, Fig. 1(2)) so that their axes and the optical axis of the microscope coincide. A current (up to 3 A) flowing through the coils that are connected in series ( $R_{tot} = 2.9\Omega$ ) creates a  $\approx 25$  mm<sup>2</sup> large area with a homogeneous magnetic field in  $z$  direction (up to

\* Corresponding author at: MML Lab, Department of Theoretical Physics, University of Latvia, Zeļļu 8, LV-1002 Rīga, Latvia.

E-mail addresses: [guntars.kitenbergs@lu.lv](mailto:guntars.kitenbergs@lu.lv) (G. Kitenbergs), [kaspars.erglis@lu.lv](mailto:kaspars.erglis@lu.lv) (K. Ērglis), [regine.perzynski@upmc.fr](mailto:regine.perzynski@upmc.fr) (R. Perzynski), [aceb@tok.sal.lv](mailto:aceb@tok.sal.lv) (A. Cēbers).

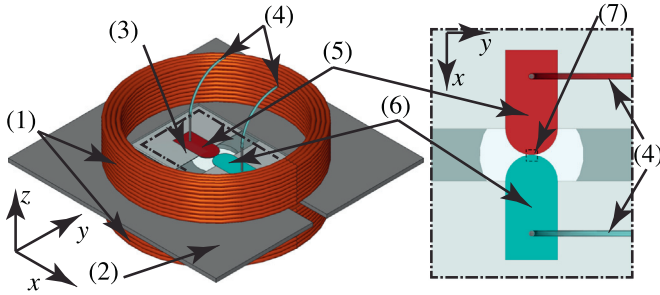


**Fig. 1.** Experimental setup consists of a coil system (1) fitted on a microscope stage (2). A Hele-Shaw cell (3) with tubing connections for fluid introduction (4) is placed in the center. A closer view of the cell displays how magnetic fluid (5) and water (6) droplets are brought to a contact in the center of the Hele-Shaw cell. Camera is recording only the central part of the cell (7) where droplets merge.

$B=20$  mT) where the center of the cell is placed. The cell (Fig. 1(3)) is made of two Parafilm M<sup>®</sup> spacers, cut in 'U' shapes, that are put opposite to each other between two glass slides to form a rectangular cell leaving two outlets for air on the sides. Two metal tubes, glued in drilled holes in the upper glass slide, provide tubing connections (Fig. 1(4)) to a syringe pump. After assembly, glass slides with spacers are welded together on a hot plate (75 °C, 5 min), creating a cell with a  $5 \times 20 \times 0.12$  mm<sup>3</sup> size. The process is filmed in the bright-field mode with a fast camera (Mikrotron MC1363, maximum resolution  $1280 \times 1024$  px). It is recording true color images at  $f=50$  Hz and its white balance is calibrated for the tungsten halogen lamp used for illumination. Color images are later converted to 8-bit grayscale images ( $I_{\text{GRAY}} = 0.2989 \times I_{\text{R}} + 0.5870 \times I_{\text{G}} + 0.1140 \times I_{\text{B}}$ ) for subsequent analysis.

The miscible fluids are water based magnetic fluid (Fig. 1(5)) and distilled water (Fig. 1(6)). The magnetic fluid is made by Massart's coprecipitation method [8] and results in maghemite particles that are stabilized with citrate ions and have a mean diameter  $d=7.0$  nm, saturation magnetization  $M_{\text{sat}} = 8.4$  kA/m at  $B_{\text{sat}} = 1$  T, susceptibility  $\chi_0 = 0.2$  (SI units) in the range up to  $B=20$  mT and volume fraction  $\phi = 2.9\%$  (from magnetization measurements).

Both fluids are slowly brought into contact inside the cell through the tubing connections by a syringe pump, while the magnetic field is already present. When droplets touch and an interface is formed along the  $y$ -axis, the pump is turned off, stopping the flow of fluids. The magnetic micro-convection is recorded for further analysis in  $0.5 \times 0.5$  mm<sup>2</sup> area (Fig. 1(7)) with the microscope camera, forming images  $I_t(i, j)$ , where  $t$  is the time, and  $i$  and  $j$  denote spatial indices with the total length  $N=360$  px for both  $x$  and  $y$  axes (see Fig. 2(a)).

To characterize a mixing system quantitatively, information on concentration distribution is necessary. As we use bright field microscopy and magnetic fluid is absorbing light, we find normalized concentration plots  $c_t(i, j)$  from images  $I_t(i, j)$  via the Beer–

Lambert law (see Fig. 2(b))

$$c_t(i, j) = \frac{\lg I_t(i, j) - \lg I_{\text{H}_2\text{O}}}{\lg I_{\text{FF}} - \lg I_{\text{H}_2\text{O}}}, \quad (1)$$

where  $I_{\text{H}_2\text{O}}$  and  $I_{\text{FF}}$  are the intensities of initial water and magnetic fluid concentrations, found in images at  $t=0$ . A spatially averaged concentration  $\bar{c}_t(i)$  is then calculated from concentration data, to characterize concentration in the mixing direction along the  $x$ -axis (see Fig. 2(c))

$$\bar{c}_t(i) = \frac{1}{N} \sum_{j=1}^N c_t(i, j). \quad (2)$$

To quantify mixing dynamics, we define mixing efficiency  $M_{\text{eff}}(t)$  as follows:

$$M_{\text{eff}}(t) = 1 - \frac{\sqrt{\frac{1}{N} \sum_{i=1}^N (\bar{c}_t(i) - c_{\infty}(i))^2}}{\sqrt{\frac{1}{N} \sum_{i=1}^N (c_0(i) - c_{\infty}(i))^2}}, \quad (3)$$

where  $c_0$  and  $c_{\infty}$  are theoretical concentration distributions before mixing starts ( $t=0$ ) and when mixing has finished ( $t \rightarrow \infty$ ) (see Fig. 2(c)). Definition of  $M_{\text{eff}}$  is a slight variation of other measurements from the literature, e.g. mixing ratio [3] and percentage mixed [9], adjusted for better representation of the experimental data.

The experiment involves an interface formation, which creates a slightly mixed state that differs from one time to another, due to the experimental limitations instead of a theoretical step like concentration distribution  $c_0$ . We remove this influence by introducing a relative mixing efficiency  $M_r(t)$  for  $t > t_0$ , which subtracts the mixing efficiency that has been made due to the interface formation. This value  $M_{\text{eff}}(t_0)$  is taken at a manually chosen time  $t_0$ , when it can be seen that the interface formation is finished (typically  $t_0=0.04$  s)

$$M_r(t) = M_{\text{eff}}(t) - M_{\text{eff}}(t_0). \quad (4)$$

### 3. Results and discussion

The experiments are performed for various magnetic field values. Snapshots of magnetic micro-convection development at several time moments can be seen in Fig. 3(a). Larger field provokes a faster evolution of the instability, enhancing mixing. It becomes more apparent, when one observes the spatially averaged concentration  $\bar{c}_t$  dynamics, shown in Fig. 3(b) contour plots. In the case of diffusion ( $B=0$ ), more than 2 s are needed for mixing to change the initial concentrations  $c_0$  near the edges of the  $x$ -axis 0.5 mm field of view, whereas for the largest field  $B=13.3$  mT it happens in less than 0.5 s. Clearly, an increase in the field strength increases the mixing development, although interface formation influence makes it less notable.

A more quantitative result of the magnetic micro-convection influence can be seen in Fig. 4(a), where relative mixing efficiency  $M_r(t)$  is shown for the magnetic field values. Achieved  $M_r$  values might seem small, but it is important to remember its definition (Eqs. (3) and (4)) and the experimental cell, which is much larger than the considered field of view ( $0.5 \times 0.5$  mm<sup>2</sup>) and accordingly has two large basins of the original concentrations, making it very long to reach completely mixed state. Overall, small fields ( $B < 7$  mT) seem to enhance mixing over diffusion only slightly, while further increase of magnetic field boosts mixing. This can be explained by Fig. 4(b), where relative mixing efficiency is plotted as a function of magnetic field squared for several time values. Data points in graph agree well with the fitted lines, implying

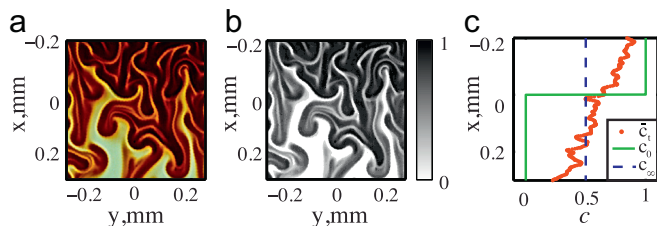


**Fig. 2.** Example of image analysis sequence for finding concentration distribution. (a) Original image  $I$ . (b) Concentration plot  $c$ , found via the Beer–Lambert law (Eq. (1)). (c) Spatially averaged concentration  $\bar{c}$  calculated with Eq. (2) is marked with dots, while theoretical initial state  $c_0$  and final mixed state  $c_{\infty}$  are marked with solid and dashed lines.

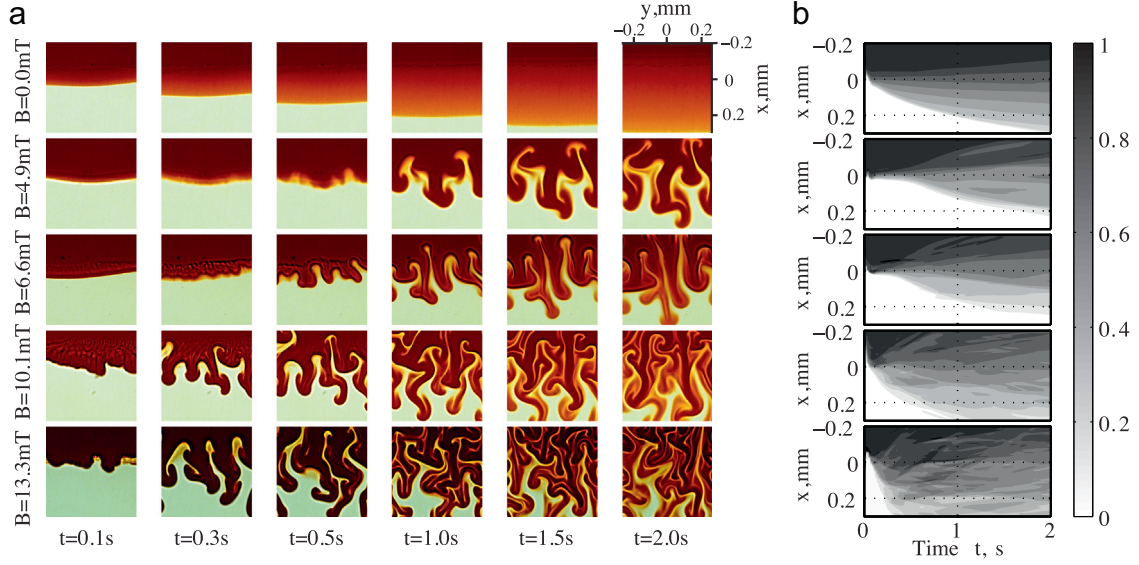


**Fig. 3.** (a) Snapshots of the magnetic micro-convection development at several times for various magnetic fields. The field of view is  $0.5 \times 0.5 \text{ mm}^2$ . (b) Spatially averaged concentration time dependence for the same magnetic fields as in (a) qualitatively revealing mixing enhancement and dynamics.

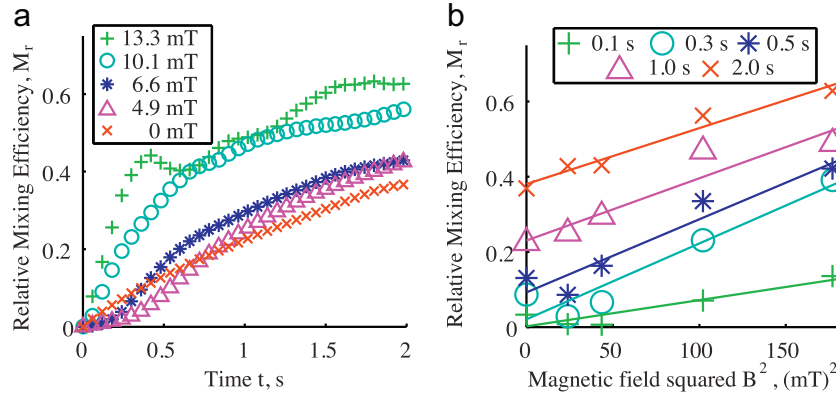


**Fig. 4.** (a) Relative mixing efficiency as a function of time for various magnetic fields. A clear mixing enhancement is visible. (b) Relative mixing efficiency as a function of magnetic field squared for various time moments.

mixing efficiency to be square dependent on the field. This result is consistent with previous findings of the field dependence of magnetic micro-convection characteristics [6].

Magnetic field influence on mixing can be analyzed by observing the change in slopes of the fitted lines in Fig. 4(b). The slopes are  $0.7$ ,  $2.0$ ,  $2.0$ ,  $1.7$  and  $1.5 \times 10^{-3} \text{ mT}^{-2}$  for  $0.1$ ,  $0.3$ ,  $0.5$ ,  $1.0$  and  $2.0 \text{ s}$  time values respectively. The variation in slopes for different times arises from the phenomenon and diffusion interplay. At small, but finite times ( $t = 0.1 \text{ s}$ ,  $t = 0.3 \text{ s}$ ), the instability forms and enhances mixing, increasing the slope until a maximum. Afterwards ( $t > 0.5 \text{ s}$ ), a slow decrease of the slope can be seen, as the concentrations tend to equate. In addition, these fits offer an estimate of the relative mixing efficiency after a selected time as a function of magnetic field. For example, after  $t = 0.5 \text{ s}$  (linear fit for data marked with asterisk in Fig. 4(b))

$$M_r(t = 0.5 \text{ s}) = 0.002 \times (B[\text{mT}])^2 + 0.092, \quad (5)$$

which is valid for this particular system with  $B < 20 \text{ mT}$ .

A direct comparison between the magnetic micro-convection and other active mixing methods for magnetic/non-magnetic fluid systems is difficult due to the different geometries and fluids used. Wen et al. [3], where mixing in a microchannel is achieved with an AC magnetic field, has mentioned that the characteristic fingers reach both channel walls, which are  $\Delta x = 0.15 \text{ mm}$  apart, after

$t = 0.5 \text{ s}$  at  $B = 14.6 \text{ mT}$ . In comparison, after the same time and a similar field strength, we have observed that fingers created by micro-convection are  $\Delta x = 0.5 \text{ mm}$  long, which is three times more, although the particle concentration and the initial susceptibility for our magnetic fluid are smaller. Partly this comes from the differences in thicknesses. In Zhu et al. [4] mixing with an in-plane DC field is achieved in a reservoir with a  $0.5 \text{ mm}$  radius. The mixing efficiency in this paper is insufficiently explained, allowing us only to surmise that magnetic micro-convection creates instabilities in similar length and time scales for alike magnetic fields.

The results showed above clearly indicate the advantages of using magnetic micro-convection for mixing. It is very simple to realize it in an already existing microfluidics setup, by adding small coils in the desired place of mixing, as proposed in Fig. 5.

To test this concept, we have made a preliminary experiment in a simple continuous flow microfluidics setup as similar as possible to the proposed concept. The flow cell is made of a 'Y' shape cut in a single Parafilm M<sup>®</sup> layer ( $20 \times 50 \text{ mm}^2$ ) with two inlet channels ( $\approx 5 \times 20 \text{ mm}^2$ ) with a  $\approx 15^\circ$  angle between them that join in a common outlet channel ( $\approx 10 \times 20 \text{ mm}^2$ ). Two glass slides are welded together with this layer as described previously in Section 2, making a flow cell with a  $0.12 \text{ mm}$  thickness. The upper glass slide has glued metal tubing connections for inlets (magnetic fluid

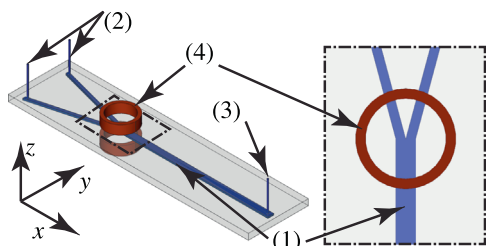


Fig. 5. A proposed test setup with microfluidics channel (1), inlets (2), outlet (3) and small coils (4).

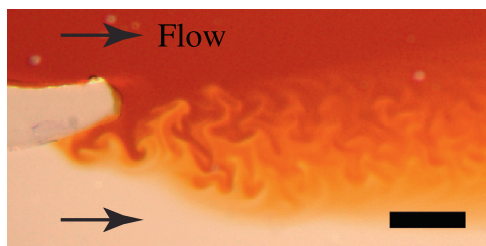


Fig. 6. A preliminary test of mixing with magnetic micro-convection in a simple microfluidics flow cell. Scale bar is 0.5 mm.

and water) and outlet. Syringe pump produces a  $v=0.15$  mm/s flow in the  $x$  direction over the field of view, as determined with a micro-Particle Image Velocimetry (Dantec) setup.

Magnetic micro-convection in the flow cell test (see Fig. 6) creates a similar pattern as seen above, most likely inducing a comparable mixing enhancement. A more detailed study in a specially designed microfluidics channels should be performed to characterize the applicability of the phenomenon in specific systems, but the concept and its benefit have been showed.

In these experiments the magnetic field is created with a coil system, because it can be easily installed on a microscope stage, without blocking the observation ability of the microscope. Besides, the field strength is adjustable with a power supply and does not involve any moving parts on the microscope stage. However, a homogeneous magnetic field needed for evoking magnetic micro-convection can also be obtained differently. For example, permanent magnets can be advantageous in applications where a connection to a power supply is impossible and a flexible adjustment of the used field is not needed. In addition, they can provide high fields while having a small size. Another apparent method is micro-fabrication, where micro-coil or permanent magnet systems can be implemented in the microfluidics chip during its production. In fact, the magnetic field source should be selected after considering the requirements of the desired application and the critical field [6] needed for the magnetic micro-convection.

A limitation of boosting mixing by increasing the magnetic field strength comes from the saturation of magnetic fluid particle magnetization. It is efficient to increase the field only during the linear regime, which can be found from the magnetic fluid magnetization curve and is  $B_{\text{sat}} \approx 20$  mT for this particular magnetic fluid, as mentioned before (magnetization curve is not showed).

Magnetic nanoparticles are well known in many scientific and clinical applications [10]. As magnetic fluid is a colloid that consists of magnetic nanoparticles, it should be possible to realize magnetic micro-convection with any magnetic particle ensemble, if colloidal, magnetic and setup properties are properly combined. For example, we can consider a colloidal dispersion of magnetic particles that is functionalized with antibodies. Mixing it with an analyte in a microfluidics flow cell by using the magnetic micro-

convection should decrease the time needed for cell or biomolecule magnetic labeling. Together with a consecutive magnetic sorting and subsequent analysis, an accelerated immunoassay test in a lab on a chip system can be achieved. Other possible applications are in speeding up sorting mechanisms based on ferrohydrodynamics [11] or increasing the mixing speed of selected tracers that are suspended in the magnetic fluid.

#### 4. Conclusions

We have shown that the magnetic micro-convection is a convenient method to enhance mixing in microfluidics systems that use magnetic particle colloids. Comparing to other methods proposed in the literature, it is better or of similar efficiency. In addition, it is easy to implement due to the simple requirements of a homogeneous magnetic field in the place wanted. The experiments show the capability to achieve  $M_r \approx 45\%$  over a large 0.5 mm distance in 0.4 s with a magnetic field  $B < 15$  mT, which is four times more and 10 times faster than with diffusion. Mixing efficiency quickly grows with an increasing magnetic field, following a square law, but it is limited by the magnetization saturation. A simple microfluidics test measurement proves the concept. But further measurements in a specially designed microfluidics setup are necessary for full characterization of the magnetic microconvection usage capabilities, including determining the influence of channel size, flow-rate and colloidal properties and reducing the interface formation effect.

#### Acknowledgments

This research is supported by a European Social Fund Project no. 2013/0028/1DP/1.1.1.2.0/13/APIA/VIAA/054

#### References

- [1] Y.K. Suh, S. Kang, A review on mixing in microfluidics, *Micromachines* 1 (3) (2010) 82–111. <http://dx.doi.org/10.3390/mi1030082>.
- [2] V. Hessel, H. Löwe, F. Schönfeld, Micromixers—a review on passive and active mixing principles, *Chem. Eng. Sci.* 60 (8–9) (2005) 2479–2501. <http://dx.doi.org/10.1016/j.ces.2004.11.033>.
- [3] C.-Y. Wen, C.-P. Yeh, C.-H. Tsai, L.-M. Fu, Rapid magnetic microfluidic mixer utilizing AC electromagnetic field, *Electrophoresis* 30 (24) (2009) 4179–4186. <http://dx.doi.org/10.1002/elps.200900400>.
- [4] G.-P. Zhu, N.-T. Nguyen, Rapid magnetofluidic mixing in a uniform magnetic field, *Lab Chip* 12 (22) (2012) 4772–4780. <http://dx.doi.org/10.1039/c2lc40818j>.
- [5] K. Erglis, A. Tatulcenkov, G. Kitenbergs, O. Petrichenko, F.G. Ergin, B.B. Watz, A. Cebers, Magnetic field driven micro-convection in the Hele–Shaw cell, *J. Fluid Mech.* 714 (2013) 612–633. <http://dx.doi.org/10.1017/jfm.2012.512>.
- [6] A. Tatulcenkovs, G. Kitenbergs, K. Erglis, O. Petrichenko, R. Perzynski, A. Cebers, Magnetic field driven micro-convection in the Hele–Shaw cell: Brinkman model and its comparison with experiment, Submitted to *Phys. Fluids*.
- [7] M.M. Maiorov, A. Cebers, Magnetic microconvection on the diffusion front of ferroparticles, *Magneto hydrodynamics* 19 (1983) 376–380.
- [8] R. Massart, Preparation of aqueous magnetic liquids in alkaline and acidic media, *IEEE* 17 (1981) 1247–1248.
- [9] T.J. Johnson, D. Ross, L.E. Locascio, Rapid microfluidic mixing, *Anal. Chem.* 74 (1) (2002) 45–51. <http://dx.doi.org/10.1021/ac010895d>.
- [10] A. Ito, M. Shinkai, H. Honda, T. Kobayashi, Medical application of functionalized magnetic nanoparticles, *J. Biosci. Bioeng.* 100 (1) (2005) 1–11, doi:<http://dx.doi.org/10.1263/jbb.100.1>.
- [11] T. Zhu, R. Cheng, S. Lee, E. Rajaraman, M. Eiteman, T. Querec, E. Unger, L. Mao, Continuous-flow ferrohydrodynamic sorting of particles and cells in microfluidic devices, *Microfluid. Nanofluid.* 13 (4) (2012) 645–654. <http://dx.doi.org/10.1007/s10404-012-1004-9>.



# Bibliography

- [1] G. M. Whitesides, “The origins and the future of microfluidics.,” *Nature*, vol. 442, no. 7101, pp. 368–373, 2006.
- [2] J.-C. Bacri, R. Perzynski, and D. Salin, “Magnetic liquids,” *Endeavour*, vol. 12, no. 2, pp. 76–83, 1988.
- [3] M. M. Maiorov and A. Cēbers, “Magnetic microconvection on the diffusion front of ferroparticles,” *Magnetohydrodynamics*, vol. 19, no. 4, pp. 376–380, 1983.
- [4] J.-C. Bacri, A. Cēbers, and R. Perzynski, “Behavior of a magnetic fluid microdrop in a rotating magnetic field,” *Physical Review Letters*, vol. 72, no. 17, pp. 2705–2708, 1994.
- [5] A. Wu, P. Ou, and L. Zeng, “Biomedical Applications of Magnetic Nanoparticles,” *Nano*, vol. 5, no. 5, pp. 245–270, 2010.
- [6] A. H. Lu, E. L. Salabas, and F. Schüth, “Magnetic nanoparticles: Synthesis, protection, functionalization, and application,” *Angewandte Chemie - International Edition*, vol. 46, pp. 1222–1244, 2007.
- [7] N. Carron, “Babel of Units. The Evolution of Units Systems in Classical Electromagnetism,” *ArXiv:physics.hist-ph/1506.01951*, 2015.
- [8] J. de Vicente, D. J. Klingenberg, and R. Hidalgo-Alvarez, “Magnetorheological fluids: a review,” *Soft Matter*, vol. 7, pp. 3701–3710, 2011.
- [9] Q. A. Pankhurst, J. Connolly, S. K. Jones, and J. Dobson, “Applications of magnetic nanoparticles in biomedicine,” *Journal of Physics D: Applied Physics*, vol. 36, pp. R167–R181, 2003.
- [10] P. Tartaj, M. D. P. Morales, S. Veintemillas-Verdaguer, T. Gonzalez-Carreno, and C. J. Serna, “The preparation of magnetic nanoparticles for applications in biomedicine,” *Journal of Physics D: Applied Physics*, vol. 36, pp. R182–R197, 2003.
- [11] E. Blūms, A. Cēbers, and M. Maiorov, *Magnetic Fluids*. Walter de Gruyter, 1997.
- [12] R. Rosensweig, *Ferrohydrodynamics*. Dover Books on Physics, Dover Publications, 2014.
- [13] S. Odenbach, *Colloidal Magnetic Fluids: Basics, Development and Application of Ferrofluids*. Lecture Notes in Physics, Springer, 2009.
- [14] K. Ērglis, Q. Wen, V. Ose, A. Zeltins, A. Sharipo, P. A. Janmey, and A. Cēbers, “Dynamics of magnetotactic bacteria in a rotating magnetic field.,” *Biophysical journal*, vol. 93, no. 4, pp. 1402–1412, 2007.

- [15] R. Massart, "Preparation of aqueous magnetic liquids in alkaline and acidic media," *IEEE Transactions on Magnetics*, vol. 17, no. 2, pp. 1247–1248, 1981.
- [16] E. Dubois, V. Cabuil, F. Boue, and R. Perzynski, "Structural analogy between aqueous and oily magnetic fluids," *The Journal of Chemical Physics*, vol. 111, pp. 7147–7160, 1999.
- [17] F. Cousin, E. Dubois, and V. Cabuil, "Tuning the interactions of a magnetic colloidal suspension.," *Physical Review E*, vol. 68, p. 021405, 2003.
- [18] R. Massart, E. Dubois, V. Cabuil, and E. Hasmonay, "Preparation and properties of monodisperse magnetic fluids," *Journal of Magnetism and Magnetic Materials*, vol. 149, pp. 1–5, 1995.
- [19] U. Kubitscheck, *Fluorescence Microscopy: From Principles to Biological Applications*. Wiley, 2013.
- [20] M. Liong, J. Lu, M. Kovichich, T. Xia, S. G. Ruehm, A. E. Nel, F. Tamanoi, and J. I. Zink, "Multifunctional inorganic nanoparticles for imaging, targeting, and drug delivery," *ACS Nano*, vol. 2, no. 5, pp. 889–896, 2008.
- [21] O. Petrichenko, *Ferromagnetic nanoparticles and their application for the functionalization of the soft matter (organic compounds like dihydropyridine-type lipids, polymers)*. PhD thesis, University of Latvia, 2014.
- [22] V. Sints, E. Blūms, M. Maiorov, and G. Kronkalns, "Diffusive and thermodiffusive transfer of magnetic nanoparticles in porous media," *The European Physical Journal E*, vol. 38, no. 5, p. 35, 2015.
- [23] S. Budavari, A. Smith, P. Heckelman, J. Kinneary, and M. O'Neill, *Merck Index: An Encyclopedia of Drugs, Chemicals, and Biologicals (12th Edition)*. Merck & Company, 1996.
- [24] J.-C. Bacri, R. Perzynski, D. Salin, V. Cabuil, and R. Massart, "Magnetic colloidal properties of ionic ferrofluids," *Journal of Magnetism and Magnetic Materials*, vol. 62, no. 1, pp. 36–46, 1986.
- [25] P. A. Hassan, S. Rana, and G. Verma, "Making Sense of Brownian Motion: Colloid Characterization by Dynamic Light Scattering.," *Langmuir*, vol. 31, pp. 3–12, 2015.
- [26] L. H. Hanus and H. J. Ploehn, "Conversion of intensity-averaged photon correlation spectroscopy measurements to number-averaged particle size distributions. 1. Theoretical development," *Langmuir*, vol. 15, no. 12, pp. 3091–3100, 1999.
- [27] J.-C. Bacri, R. Perzynski, D. Salin, and J. Servais, "Magnetic transient birefringence of ferrofluids : particle size determination," *Journal de Physique*, vol. 48, pp. 1385–1391, 1987.
- [28] E. Hasmonay, E. Dubois, J.-C. Bacri, R. Perzynski, Y. Raikher, and V. Stepanov, "Static magneto-optical birefringence of size-sorted  $\gamma$ -Fe<sub>2</sub>O<sub>3</sub> nanoparticles," *The European Physical Journal B - Condensed Matter and Complex Systems*, vol. 5, no. 4-6, pp. 859–867, 1998.

- [29] A. Cēbers and M. M. Maiorov, “Magnetostatic instabilities in plane layers of magnetizable liquids,” *Magnetohydrodynamics*, vol. 16, no. 1, pp. 21–27, 1980.
- [30] A. Cēbers, “Stability of diffusion fronts of magnetic particles in porous media under the action of external magnetic field,” *Magnetohydrodynamics*, vol. 33, p. 48, 1997.
- [31] A. Cēbers, “Dynamics of magnetostatic instabilities,” *Magnetohydrodynamics*, vol. 17, pp. 113–121, 1981.
- [32] D. P. Jackson, R. E. Goldstein, and A. Cēbers, “Hydrodynamics of fingering instabilities in dipolar fluids,” *Physical Review E*, vol. 50, pp. 298–307, 1994.
- [33] M. Igonin and A. Cēbers, “Labyrinthine instability of miscible magnetic fluids,” *Journal of Magnetism and Magnetic Materials*, vol. 252, pp. 293 – 295, 2002. Proceedings of the 9th International Conference on Magnetic Fluids.
- [34] M. Igonin and A. Cēbers, “Labyrinthine instability of miscible magnetic fluids,” *Physics of Fluids*, vol. 15, pp. 1734–1744, 2003.
- [35] M. Igonin, *Hydrodynamic instabilities of miscible and immiscible magnetic fluids in a Hele-Shaw cell*. PhD dissertation, Universite Paris 7 - Denis Diderot, 2004.
- [36] C.-Y. Chen and C.-Y. Wen, “Numerical simulations of miscible magnetic flows in a Hele–Shaw cell: Radial flows ,” *Journal of Magnetism and Magnetic Materials*, vol. 252, pp. 296 – 298, 2002.
- [37] C.-Y. Chen, “Numerical simulations of fingering instabilities in miscible magnetic fluids in a Hele-Shaw cell and the effects of Korteweg stresses,” *Physics of Fluids*, vol. 15, no. 4, pp. 1086–1089, 2003.
- [38] C.-Y. Wen, C.-Y. Chen, D.-C. Kuan, and S.-Y. Wu, “Labyrinthine instability of a miscible magnetic drop,” *Journal of Magnetism and Magnetic Materials*, vol. 310, no. 2, Part 3, pp. e1017 – e1019, 2007. Proceedings of the 17th International Conference on Magnetism The International Conference on Magnetism.
- [39] C.-Y. Wen, C.-Y. Chen, and D. Kuan, “Experimental studies of labyrinthine instabilities of miscible ferrofluids in a Hele-Shaw cell,” *Physics of Fluids*, vol. 19, p. 084101, 2007.
- [40] C.-Y. Chen, W. K. Tsai, and J. A. Miranda, “Hybrid ferrohydrodynamic instability: Coexisting peak and labyrinthine patterns,” *Physical Review E*, vol. 77, pp. 1–7, 2008.
- [41] C. Derec, P. Boltenhagen, S. Neveu, and J.-C. Bacri, “Magnetic instability between miscible fluids in a Hele-Shaw cell,” *Magnetohydrodynamics*, vol. 44, no. 2, pp. 135–142, 2008.
- [42] A. Mezulis and E. Blūms, “Experimental investigations of the microconvective instability in optically induced gratings,” *Magnetohydrodynamics*, vol. 41, no. 4, pp. 341–348, 2005.
- [43] D. Zablotzky, *Microconvective effects in non-isothermal and inhomogeneous dispersions of magnetic nanoparticles*. PhD dissertation, University of Latvia, 2012.

- [44] T. T. Al-Housseiny, P. A. Tsai, and H. A. Stone, “Control of interfacial instabilities using flow geometry,” *Nature Physics*, vol. 8, no. October, pp. 747–750, 2012.
- [45] E. O. Dias and J. A. Miranda, “Taper-induced control of viscous fingering in variable-gap Hele-Shaw flows,” *Physical Review E*, vol. 87, pp. 1–6, 2013.
- [46] I. Bischofberger, R. Ramachandran, and S. R. Nagel, “An island of stability in a sea of fingers: emergent large-scale features of the viscous flow instability,” *ArXiv:physics.flu-dyn/1410.7623*, 2015.
- [47] I. Bischofberger, R. Ramachandran, and S. R. Nagel, “Fingering versus stability in the limit of zero interfacial tension,” *Nature Communications*, vol. 5, pp. 1–6, 2014.
- [48] K. Ērglis, A. Tatulcenkov, G. Kitenbergs, O. Petrichenko, F. G. Ergin, B. B. Watz, and A. Cēbers, “Magnetic field driven micro-convection in the Hele-Shaw cell,” *Journal of Fluid Mechanics*, vol. 714, pp. 612–633, 2013.
- [49] G. Kitenbergs, A. Tatulcenkovs, K. Ērglis, O. Petrichenko, R. Perzynski, and A. Cēbers, “Magnetic field driven micro-convection in the Hele-Shaw cell: Brinkman model and its comparison with experiment,” *Journal of Fluid Mechanics*, vol. 774, pp. 170–191, 2015.
- [50] G. Kitenbergs, K. Ērglis, R. Perzynski, and A. Cēbers, “Magnetic particle mixing with magnetic micro-convection for microfluidics,” *Journal of Magnetism and Magnetic Materials*, vol. 380, pp. 227–230, 2015.
- [51] M. Raffel, C. E. Willert, S. T. Wereley, and J. Kompenhans, *Particle Image Velocimetry: A Practical Guide*. Experimental Fluid Mechanics, Springer Berlin Heidelberg, 2007.
- [52] DantecDynamics, “Micro PIV system,” 2015. URL: [http://www.dantecdynamics.com/docs/products-and-services/microfluidics/PI103\\_Microfluidics.PIV.pdf](http://www.dantecdynamics.com/docs/products-and-services/microfluidics/PI103_Microfluidics.PIV.pdf). Accessed: 2015-05-25.
- [53] F. G. Ergin, B. B. Watz, K. Ērglis, and A. Cēbers, “Poor-contrast particle image processing in micro scale mixing,” *Proceedings of the ASME 10th Biennial Conference on Engineering Systems Design and Analysis*, pp. 1–5, 2010.
- [54] D. B. Murphy, *Fundamentals of Light Microscopy and Electronic Imaging*. Wiley-Liss, 2001.
- [55] J. Russ, *The Image Processing Handbook, Fifth Edition*. CRC Press, 2006.
- [56] A. Einstein, *Investigations on the Theory of the Brownian Movement*. Dover Books on Physics Series, Dover Publications, 1956.
- [57] T. M. Squires and S. R. Quake, “Microfluidics: Fluid physics at the nanoliter scale,” *Reviews of Modern Physics*, vol. 77, no. July, pp. 977–1026, 2005.
- [58] Y. Temiz, R. D. Lovchik, G. V. Kaigala, and E. Delamarche, “Lab-on-a-chip devices: How to close and plug the lab?,” *Microelectronic Engineering*, vol. 132, pp. 156–175, 2015.

- [59] C. D. Chin, V. Linder, and S. K. Sia, "Lab-on-a-chip devices for global health: past studies and future opportunities.," *Lab on a chip*, vol. 7, no. Section 2, pp. 41–57, 2007.
- [60] Y. K. Suh and S. Kang, "A Review on Mixing in Microfluidics," *Micromachines*, vol. 1, no. 3, pp. 82–111, 2010.
- [61] V. Hessel, H. Löwe, and F. Schönfeld, "Micromixers - a review on passive and active mixing principles," *Chemical Engineering Science*, vol. 60, no. 8-9, pp. 2479–2501, 2005.
- [62] C.-Y. Wen, C.-P. Yeh, C.-H. Tsai, and L.-M. Fu, "Rapid magnetic microfluidic mixer utilizing AC electromagnetic field.," *Electrophoresis*, vol. 30, no. 24, pp. 4179–4186, 2009.
- [63] G.-P. Zhu and N.-T. Nguyen, "Rapid magnetofluidic mixing in a uniform magnetic field.," *Lab on a chip*, vol. 12, no. 22, pp. 4772–4780, 2012.
- [64] T. J. Johnson, D. Ross, and L. E. Locascio, "Rapid microfluidic mixing.," *Analytical chemistry*, vol. 74, no. 1, pp. 45–51, 2002.
- [65] A. Ito, M. Shinkai, H. Honda, and T. Kobayashi, "Medical application of functionalized magnetic nanoparticles," *Journal of Bioscience and Bioengineering*, vol. 100, no. 1, pp. 1 – 11, 2005.
- [66] T. Zhu, R. Cheng, S. Lee, E. Rajaraman, M. Eiteman, T. Querec, E. Unger, and L. Mao, "Continuous-flow ferrohydrodynamic sorting of particles and cells in microfluidic devices," *Microfluidics and Nanofluidics*, vol. 13, no. 4, pp. 645–654, 2012.
- [67] L. Borlido, A. Azevedo, A. Roque, and M. Aires-Barros, "Magnetic separations in biotechnology," *Biotechnology Advances*, vol. 31, no. 8, pp. 1374 – 1385, 2013.
- [68] E. Cussler, *Diffusion: Mass Transfer in Fluid Systems*. Cambridge Series in Chemical Engineering, Cambridge University Press, 2009.
- [69] E. M. Huisman, Q. Wen, Y.-H. Wang, K. Cruz, G. Kitenbergs, K. Ērglis, A. Zeltins, A. Cēbers, and P. A. Janmey, "Gelation of semiflexible polyelectrolytes by multivalent counterions.," *Soft matter*, vol. 7, no. 16, pp. 7257–7261, 2011.
- [70] P. Cicuta and A. M. Donald, "Microrheology: a review of the method and applications," *Soft Matter*, vol. 3, no. 12, pp. 1449–1455, 2007.
- [71] J.-C. Bacri, A. Cēbers, A. Bourdon, G. Demouchy, B. Heegaard, B. Kashevsky, and R. Perzynski, "Transient grating in a ferrofluid under magnetic field: Effect of magnetic interactions on the diffusion coefficient of translation," *Physical Review E*, vol. 52, no. 4, pp. 3936–3942, 1995.
- [72] B. Bokstein, M. Mendeleev, and D. Srolovitz, *Thermodynamics and Kinetics in Materials Science : A Short Course: A Short Course*. Thermodynamics and Kinetics in Materials Science: A Short Course, Oxford University Press, 2005.
- [73] J. L. Anderson, "Colloid Transport By Interfacial Forces," *Annual Review of Fluid Mechanics*, vol. 21, no. 1969, pp. 61–99, 1989.

- [74] B. Abécassis, C. Cottin-Bizonne, C. Ybert, A. Ajdari, and L. Bocquet, “Boosting migration of large particles by solute contrasts,” *Nature materials*, vol. 7, no. 10, pp. 785–789, 2008.
- [75] B. Abécassis, C. Cottin-Bizonne, C. Ybert, A. Ajdari, and L. Bocquet, “Osmotic manipulation of particles for microfluidic applications,” *New Journal of Physics*, vol. 11, no. 7, p. 075022, 2009.
- [76] T. Cosgrove, *Colloid Science: Principles, Methods and Applications*. Wiley, 2005.
- [77] J. C. McDonald, D. C. Duffy, J. R. Anderson, D. T. Chiu, H. Wu, O. J. Schueller, and G. M. Whitesides, “Fabrication of microfluidic systems in poly(dimethylsiloxane).,” *Electrophoresis*, vol. 21, pp. 27–40, 2000.
- [78] D. Qin, Y. Xia, and G. M. Whitesides, “Rapid prototyping of complex structures with feature sizes larger than 20  $\mu\text{m}$ ,” *Advanced Materials*, vol. 8, no. 11, pp. 917–919, 1996.
- [79] D. C. Duffy, J. C. McDonald, O. J. Schueller, and G. M. Whitesides, “Rapid Prototyping of Microfluidic Systems in Poly(dimethylsiloxane).,” *Analytical chemistry*, vol. 70, no. 23, pp. 4974–4984, 1998.
- [80] G. Batchelor, *An Introduction to Fluid Dynamics*. Cambridge Mathematical Library, Cambridge University Press, 2000.
- [81] K. Griesbaum, A. Behr, D. Biedenkapp, H.-W. Voges, D. Garbe, C. Paetz, G. Collin, D. Mayer, and H. Höke, *Hydrocarbons*. Cambridge Mathematical Library, Wiley-VCH Verlag GmbH & Co. KGaA, 2000.
- [82] O. Söhnel and P. Novotný, *Densities of aqueous solutions of inorganic substances*. Physical sciences data, Elsevier, 1985.
- [83] R. H. Webb, “Confocal optical microscopy,” *Reports on Progress in Physics*, vol. 59, no. 3, pp. 427–471, 1996.
- [84] S. N. Yakovenko, T. G. Thomas, and I. P. Castro, “Transition through rayleigh–taylor instabilities in a breaking internal lee wave,” *Journal of Fluid Mechanics*, vol. 760, pp. 466–493, 2014.
- [85] F. H. C. Heussler, R. M. Oliveira, M. O. John, and E. Meiburg, “Three-dimensional navier–stokes simulations of buoyant, vertical miscible hele-shaw displacements,” *Journal of Fluid Mechanics*, vol. 752, pp. 157–183, 2014.
- [86] J.-C. Bacri, A. Cēbers, A. Bourdon, G. Demouchy, B. M. Heegaard, and R. Perzynski, “Forced rayleigh experiment in a magnetic fluid,” *Physical Review Letters*, vol. 74, pp. 5032–5035, 1995.
- [87] E. A. Peterson and D. A. Krueger, “Reversible, field induced agglomeration in magnetic colloids,” *Journal of Colloid and Interface Science*, vol. 62, no. 1, pp. 24 – 34, 1977.
- [88] J.-C. Bacri, R. Perzynski, D. Salin, V. Cabuil, and R. Massart, “Phase diagram of an ionic magnetic colloid: Experimental study of the effect of ionic strength,” *Journal of Colloid and Interface Science*, vol. 132, no. 1, pp. 43–53, 1989.

- [89] E. Dubois, R. Perzynski, F. Boué, and V. Cabuil, “Liquid–gas transitions in charged colloidal dispersions: small-angle neutron scattering coupled with phase diagrams of magnetic fluids,” *Langmuir*, vol. 16, no. 13, pp. 5617–5625, 2000.
- [90] B. Frka-Petesic, E. Dubois, L. Almasy, V. Dupuis, F. Cousin, and R. Perzynski, “Structural probing of clusters and gels of self-aggregated magnetic nanoparticles,” *Magnetohydrodynamics*, vol. 49, no. 3, pp. 328–338, 2013.
- [91] A. Cēbers, “Thermodynamic stability of magnetofluids,” *Magnetohydrodynamics*, vol. 18, pp. 137–142, 1982.
- [92] J.-C. Bacri and D. Salin, “Instability of ferrofluid magnetic drops under magnetic field,” *Journal de Physique Lettres*, vol. 43, pp. 649–654, 1982.
- [93] J.-C. Bacri and D. Salin, “Bistability of ferrofluid magnetic drops under magnetic field,” *Journal of Magnetism and Magnetic Materials*, vol. 39, no. 1–2, pp. 48 – 50, 1983.
- [94] J.-C. Bacri and D. Salin, “Optical scattering on ferrofluid agglomerates,” *Journal de Physique Lettres*, vol. 43, pp. 771–777, 1982.
- [95] E. Janiaud, F. Elias, J.-C. Bacri, V. Cabuil, and R. Perzynski, “Spinning ferrofluid microscopic droplets,” *Magnetohydrodynamics*, vol. 36, pp. 300–311, 2000.
- [96] S. Afkhami, A. J. Tyler, Y. Renardy, M. Renardy, T. G. St. Pierre, R. C. Woodward, and J. S. Riffle, “Deformation of a hydrophobic ferrofluid droplet suspended in a viscous medium under uniform magnetic fields,” *Journal of Fluid Mechanics*, vol. 663, pp. 358–384, 2010.
- [97] G.-P. Zhu, N.-T. Nguyen, R. V. Ramanujan, and X.-Y. Huang, “Nonlinear deformation of a ferrofluid droplet in a uniform magnetic field,” *Langmuir*, vol. 27, no. 24, pp. 14834–14841, 2011.
- [98] A. Zakinyan and Y. Dikansky, “Drops deformation and magnetic permeability of a ferrofluid emulsion,” *Colloids and Surfaces A: Physicochemical and Engineering Aspects*, vol. 380, no. 1–3, pp. 314–318, 2011.
- [99] Y. Dikansky and A. Zakinyan, “Dynamics of a nonmagnetic drop suspended in a magnetic fluid in a rotating magnetic field,” *Technical Physics*, vol. 55, no. 8, pp. 1082–1086, 2010.
- [100] A. Cēbers, “Virial method of investigation of statics and dynamics of drops of magnetizable liquids,” *Magnetohydrodynamics*, vol. 21, pp. 19–26, 1985.
- [101] Y. Dikansky, A. Cēbers, and V. P. Shatsky, “Magnetic emulsion properties in electric and magnetic fields. 1. statics,” *Magnetohydrodynamics*, vol. 26, no. 1, pp. 25–30, 1990.
- [102] N. V. Plechkova and K. R. Seddon, “Applications of ionic liquids in the chemical industry,” *Chemical Society Reviews*, vol. 37, pp. 123–150, 2008.
- [103] M. Mamusa, J. Sirieix-Plénet, F. Cousin, R. Perzynski, E. Dubois, and V. Peyre, “Microstructure of colloidal dispersions in the ionic liquid ethylammonium nitrate: influence of the nature of the nanoparticles’ counterion,” *Journal of Physics: Condensed Matter*, vol. 26, no. 28, p. 284113, 2014.

- [104] K. S. Neto, A. Bakuzis, G. Gonçalves, F. Pelegrini, and P. Morais, “Evidence of phase separation in magnetic colloids using magnetic resonance,” *Journal of Magnetism and Magnetic Materials*, vol. 289, pp. 129 – 132, 2005. Proceedings of the 10th International Conference on Magnetic Fluids.
- [105] K. Ērglis, *Experimental study of properties and motion of flexible magnetic microfilaments*. PhD thesis, University of Latvia, 2010.
- [106] O. Gal, “MATLAB® File Exchange function *fit\_ellipse*,” 2003. URL: <http://www.mathworks.com/matlabcentral/fileexchange/3215-fit-ellipse>. Accessed: 2014-04-30.
- [107] K. Morozov and A. Lebedev, “The effect of magneto-dipole interactions on the magnetization curves of ferrocolloids,” *Journal of Magnetism and Magnetic Materials*, vol. 85, pp. 51–53, 1990.
- [108] A. O. Ivanov and O. B. Kuznetsova, “Magnetic properties of dense ferrofluids: an influence of interparticle correlations.,” *Physical Review E*, vol. 64, p. 041405, 2001.
- [109] E. W. Weisstein, “Oblate spheroid,” 2015. From MathWorld—A Wolfram Web Resource. URL: <http://mathworld.wolfram.com/OblateSpheroid.html>. Accessed: 2015-06-10.
- [110] S. Elborai, D. K. Kim, X. He, S. H. Lee, S. Rhodes, and M. Zahn, “Self-forming, quasi-two-dimensional, magnetic-fluid patterns with applied in-plane-rotating and dc-axial magnetic fields,” *Journal of Applied Physics*, vol. 97, p. 10Q303, 2005.
- [111] S. Rhodes, X. He, S. Elborai, S. H. Lee, and M. Zahn, “Magnetic fluid behavior in uniform DC, AC, and rotating magnetic fields,” *Journal of Electrostatics*, vol. 64, pp. 513–519, 2006.



---

## Sujet : Instabilités hydrodynamiques de fluides magnétiques en écoulements microfluidiques

---

**Résumé :** Ce travail explore expérimentalement en géométrie microfluidique, des instabilités sous champ de fluides magnétiques aqueux, aux propriétés bien caractérisées et dont les nanoparticules sont stabilisées électrostatiquement. La micro-convexion magnétique observée à l'interface miscible entre le fluide magnétique et l'eau est étudiée quantitativement dans une cellule de Hele-Shaw sous champ magnétique homogène, en particulier par vélocimétrie par image de particules. Les résultats sont comparés aux prédictions théoriques et à des simulations numériques. Au delà de la caractérisation des champs critiques, il est observé qu'une augmentation du champ  $H$  accélère la croissance des doigts, comme  $H^2$ , tandis que la figure de digitation n'est pas modifiée. Une application au mélange en microfluidique est ici envisagée. L'étude de la micro-convexion a révélé une diffusion effective de coefficient beaucoup plus grand que celui des nanoparticules, tel que prédit par la formule de Stokes-Einstein ou obtenu par des mesures directes. Des explorations expérimentales montrent que cette diffusion effective provient d'un écoulement lié à la différence de densité des deux fluides. La diffusion semble influencée par les agents qui stabilisent les nanoparticules. Des gouttes de liquide magnétique concentré co-existant avec une phase diluée sont obtenues par séparation de phase induite par ajout de sel et/ou application d'un champ magnétique. Leur déformation sous champ permet de suivre l'évolution temporelle de la phase concentrée métastable. Dans un champ magnétique précessant à l'angle magique, les gouttes se comportent comme en champ tournant, sauf en ce qui concerne leur déformation initiale.

**Mots clés :** Fluides magnétiques, Ecoulements de Hele-Shaw, Colloïdes, Gouttes magnétiques, Instabilités, Micro-convexion

---

## Subject : Hydrodynamic instabilities in microfluidic magnetic fluid flows

---

**Abstract :** Magnetic field induced instabilities of magnetic fluids in microfluidic environment are investigated experimentally. Electrically stabilized water-based magnetic nanocolloids are used and throughout characterized. Magnetic micro-convexion, observed at a miscible magnetic fluid-water interface in a Hele-Shaw cell in homogeneous field, is studied quantitatively and compared with theoretical predictions and numerical simulations, micro-convective flows being characterized by particle image velocimetry. Besides the critical field determination, it is shown that an increase of the magnetic field  $H$  speeds up the finger growth, which scales as  $H^2$ , while the size of the fingering pattern is not changed. An application towards mixing enhancement in microfluidics is considered. The micro-convexion study reveals a much larger effective diffusion coefficient of the nanoparticles than expected from Stokes - Einstein relation and standard determinations. Investigations with the same setup and with continuous microfluidics show that the effective diffusion mostly arises from a flow induced by the density difference between the miscible fluids. Additionally, the diffusion coefficient seems to be influenced by the particle stabilizing agents. Drops of a concentrated magnetic phase in co-existence with a dilute one are formed by phase separation after salt addition to the magnetic fluid and/or the application of a magnetic field. Their under-field shape deformations allow investigating the time evolution of the concentrated phase. Experiments show that in a precessing field at magic angle, the drops behave as in a rotating field except the initial shape deformation before quick elongation.

**Keywords :** Magnetic fluids, Hele-Shaw flows, Colloids, Magnetic drops, Instabilities, Micro-convexion

---